July 2020

ELUCIDATING MECHANISMS OF METASTASIS WITH IMPLANTABLE BIOMATERIAL NICHES

Ryan Adam Carpenter
University of Massachusetts Amherst

ELUCIDATING MECHANISMS OF METASTASIS WITH IMPLANTABLE BIOMATERIAL NICHES

A Dissertation Presented

by

RYAN ADAM CARPENTER

Submitted to the Graduate School of the
University of Massachusetts Amherst in partial fulfillment
of the requirements for the degree of

DOCTOR OF PHILOSOPHY

May 2020

Chemical Engineering

ELUCIDATING MECHANISMS OF METASTASIS WITH IMPLANTABLE BIOMATERIAL NICHES

A Dissertation Presented

by

RYAN ADAM CARPENTER

Approved as to style and content by:

_____
Jungwoo Lee, Chair

_____
Shelly Peyton, Member

_____
Lisa Minter, Member

_____
John Klier, Department Head
Department of Chemical Engineering

ACKNOWLEDGMENTS

I want to first acknowledge my advisor, Dr. Jungwoo Lee. Joining a new lab has been quite the journey. I thank Jungwoo for putting trust in me to make influential decisions and involve me at nearly every step of the processes of building the lab from the ground up. These experiences have been greatly beneficial beyond the traditional research skills gained from dissertation work. I appreciate Jungwoo's ability to guide me through this challenging and ambitious research direction and for laying the foundation for the implantable biomaterial platform used in this work.

I also want to thank my dissertation committee for helping me with various aspects of this dissertation. Dr. Shelly Peyton was very helpful in the early stages of my project and I thank her for the time and effort she put in guiding my first publication, presented here in Chapter 4. I am grateful for her permission to use her spinning disk confocal microscope. This equipment greatly enhanced the imaging throughout of my project and enabled more in-depth tissue characterization. Dr. Lisa Minter has taught me a lot about immunology in, and out of the classroom. I want to specifically thank her for the time and effort taken to help me implement bone marrow transplantation experiments highlighted in Chapter 2.

There have been many undergraduate students, graduate students, and postdoctoral fellows that work in the Life Science Laboratories that have greatly helped in experimental and day-to-day operation of my project. First, I would like to thank all the former and present members of the Lee lab. Specifically, Abhinav Sharma, Yongkuk Park, and Jun-Goo Kwak have all played a large part in bringing unique insight and providing feedback during group meetings and daily discussions. There have been several undergraduate

students that have contributed to this work, most notably Taylor Smart, Emma Durkee, Lauren Timmins, Hyun-Woo Sung, Justinne Guarin, Matthew Fernez, and Nicolas Thomas. I would specifically like to acknowledge the efforts made by Dalton Macres and Katherine Daniel in supporting the work presented in Chapter 6. Beyond the Lee lab, several UMass researchers have taken time to teach me new techniques, provided experimental materials, and participated in the discussion of research ideas. I would like to thank Dr. Lauren Barney, Dr. Lauren Jansen, Dr. Alyssa Schwartz, Dr. Kerianne Dobosz, Dr. Chris Hall, Dr. Nele Van Dessel, Vishnu Raman, Carey Dougan, and Yen Tran for their contributions to supporting this dissertation work.

I also want to acknowledge collaborators that have co-authored manuscripts and provided useful feedback and research materials. Dr. Hoon Hur, Dr. Daeyoung Kim, Hye Jeong Oh, and In-Hye Ham provided invaluable patient-derived xenograft experiments and statistical analysis for the work presented in Chapter 3. There have been several other collaborative projects that are not discussed in detail within this dissertation, however I appreciate their time and resources in shaping my project and expanding the scope of my knowledge including Dr. Young-Cheul Kim, Seok-Yeong Yu, Dr. Joseph Bergan, Dr. M. Soledad Sosa, Dr. Miles Miller, Dr. Mikala Egeblad, and Dr. Ashish Kulkarni.

I want to thank the Department of Chemical Engineering for their administrative support. Much of this work would not be possible without the funding sources and facilities at UMass. Lab funding was provided by National Institute of Health (R01CA237171 and R00CA163671) and the Institute for Applied Life Sciences. I am grateful for the year of funding and travel grant provided by the National Science Foundation Soft Materials for Life Sciences National Research Traineeship (1545399). I greatly appreciate the Bristol

Myers Squibb Scholar-in-Training award that allowed me to attend the 2019 American Association for Cancer Research Annual Meeting. I want to thank Dr. Amy Burnside, director of the flow cytometry and animal imaging core facilities, and Dr. James Chambers, director of the light microscope facility, for their training, insight, and assistance in using various equipment. I greatly appreciate all of the work done by the Animal Care Services, specifically Dr. J. Paul Spurlock, Christie Hart, Cathy Cervi, Elizabeth Nadeau, Elizabeth Ortiz, Billye Davis, and Alison Miller.

Lastly, I would like to thank my family and friends for supporting me at every step of this endeavor. I specifically want to thank my parents, Richard and Linda, for instilling the mentality to never stop learning and for pushing me to achieve my dreams.

ABSTRACT

ELUCIDATING MECHANISMS OF METASTASIS WITH IMPLANTABLE BIOMATERIAL NICHES

MAY 2020

RYAN ADAM CARPENTER, B.A., UNIVERSITY AT BUFFALO

B.S., UNIVERSITY AT BUFFALO

Ph.D., UNIVERSITY OF MASSACHUSETTS AMHERST

Directed by: Professor Jungwoo Lee

Metastasis is the leading cause of cancer related deaths, yet it remains the most poorly understood aspect of tumor biology. This can be attributed to the lack of relevant experimental models that can recapitulate the complex and lengthy progression of metastatic relapse observed in patients. Mouse models have been widely used to study cancer, however they are critically limited to study metastasis. Most models generate aggressive metastases in the lung without the use of unique cell lines or specialized injection techniques. This limits the ability to study disseminated tumor cells (DTCs) in other relevant metastasis prone tissues. Prolonged observation of the post-dissemination phase of cancer cell biology and the dormant-to-active transition are additional challenges to study in mouse models due to the rapid onset of actively growing primary and secondary tumors that shorten the experimental timeframe. These limitations have left a critical gap in the understanding of metastasis, specifically the long-term bi-directional crosstalk between DTCs and their local microenvironment. Previous findings have demonstrated that subcutaneously implanted inverted colloidal crystal (ICC) hydrogel scaffolds recruit circulating tumor cells and capture metastatic progression. Here, I introduce new

implantable tissue engineered metastasis models that overcome the fundamental restrictions of existing mouse models and substantiate the role of the tumor niche in the reactivation of dormant DTCs with molecular and cellular detail.

Throughout my dissertation work I engineered DTC niches leveraging ICC scaffolds to identify critical niche components that enable metastatic progression. Changing the anatomical location of the implant yielded unique microenvironments with varying levels of metastatic potential. In a secondary approach, I utilized the immunomodulatory properties of ICC scaffolds to assist the transplantation of adult lung and liver tissues into the subcutaneous space for prolonged study of metastasis-relevant tissues. Next, I leveraged the transplantable nature of scaffold niches to investigate DTC dormancy and potential triggers of metastatic relapse. I developed a fully humanized mouse model to explore local niche evolution as human DTCs progress from single cells to small colonies and overt metastases. The local vasculature and $Ly6G^{+}$ cells were observed to play important roles during each step of the transition to aggressive proliferation. The effect of adjuvant chemotherapy and surgical disruption on DTCs and their niche was also explored by using a fully immunocompetent mouse model. Lastly, I improved the fabrication of ICC hydrogel scaffolds to make the process more scalable for widespread use. The use of expanded polystyrene beads enabled cheaper, faster, and safer production of ICC hydrogel scaffolds.

Tissue engineering approaches to recreate *in vivo* DTC microenvironments represent an exciting opportunity to better understand metastasis. The presented models and techniques may be enabling tools to aid in the development of anti-metastasis therapies that significantly benefit patient health.

TABLE OF CONTENTS

Page

LIST OF TABLES

Table Page

LIST OF FIGURES

Figure Page

CHAPTER 1

CANCER METASTASIS AND EXPERIMENTAL MODELS

1.1 Introduction

Cancer is a disease whereby cells in the body divide uncontrollably. Cancer is caused by genetic changes that alter genes that are involved in cell growth, division, and DNA repair[1]. During cancer progression, cells can gain a malignant phenotype characterized by the ability to invade local tissues and spread to distant tissues. Metastatic disease occurs once the cancer spreads to a distant site and proliferates. Patient survival rates dramatically decline as cancers spread from the local organ of origin to distant organs **(Figure 1.1)**. For example, the five-year relative survival rate for breast cancer is 99% when diagnosed locally, and only 27% when diagnosed in distant organs. This phenomenon is further amplified during aging with five-year survival rates in breast cancer diagnosed in distant organs dropping to 22% and 15% for patients 65-84 and 85+, respectively[2].

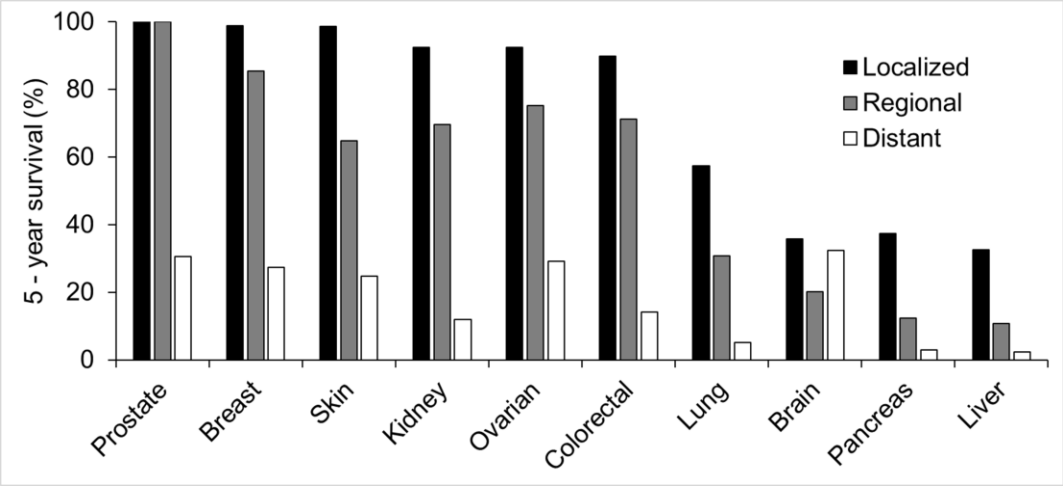

Figure 1.1. 5-year patient survival rate based on stage at time of diagnosis.
Data adapted from National Cancer Institute Cancer Statistics Review[2].

Metastatic disease presents several clinical challenges[3]. First, detection of disseminated tumor cells (DTCs) is not practical and even secondary tumor colonies can be challenging to find. Some patients may remain asymptomatic until metastatic disease reaches an advanced stage. Second, treatment options for patients diagnosed with metastatic disease are severely limited. In most cases there is no cure for metastatic disease. Instead treatment is used to slow tumor growth and reduce symptoms. Most metastatic cancer treatment strategies are similar to the primary tumor of origin, however cancer cells can gain new genetic alterations that make them resistant to therapy.

Although several aspects of metastasis have been uncovered, treatment for patients has only marginally improved[4-7]. Current experimental models of metastasis are limited in their ability to fully recapitulate the metastatic cascade and it remains unclear if these models provide accurately represent human metastasis. The work of this dissertation aimed to provide new experimental models to study DTC biology and the evolution of the local microenvironment during metastatic progression. In this chapter, the current understanding of metastatic disease progression are highlighted as well as the experimental models to study circulating, disseminated, and metastatic cancer cells.

1.2 The Metastatic Cascade

The initial step of the metastatic cascade is invasion into nearby normal tissue or blood and lymphatic vessels. As cancer cells proliferate and form a primary tumor they may gain additional phenotypic traits that enable eventual metastatic disease. This hypothesized event is commonly referred to as an epithelial-mesenchymal transition (EMT). In the early-stage carcinomas cancer cells are generally in an epithelial-like state

characterized by maintenance of cell-cell junctions, apical-basal polarity, and interaction with the underlying basement membrane. The transition to the mesenchymal state is characterized by loss of cell-cell junctions, loss of cellular polarity, degradation of the basement membrane and reorganization of the surrounding extracellular matrix. Activation of EMT programs via EMT related transcription factors like ZEB1 and SNAIL in non-metastatic cells has been shown to increase their metastatic potential[8]. The phenomenon of EMT is still not fully understood and evidence of metastases that appear to not undergo such a transition have been presented.

Invasion into draining lymph nodes is generally the first clinical identification of potential metastatic disease, however the spread to distant anatomical locations is widely believed to occur through the blood circulation. Entrance into the blood system presents cancer cells new challenges including hemodynamic forces[9]. Circulating tumor cells (CTCs) are one of the most challenging aspects of the metastatic cascade to study due to their relative rarity in the blood, inability to detect via platelet shielding, and limited success in expansion once purified. While in circulation, cancer cells home to new locations via passive mechanical trapping and active processes such as cell-mediated adhesion. While this phenomenon is traditionally viewed as the circulation of singular CTCs, recent findings suggest that CTCs with the highest metastatic potential exist as clusters[10]. Once extravasated from systemic circulation, CTCs are considered disseminated. Like CTCs, DTCs are exposed to a new set of microenvironment pressures present in the secondary tissue. The microenvironment plays an important role in determining the proliferative state of the DTCs and are explained in further detail below.

In the nineteenth century organ specific patterns of metastatic growth were identified[11]. A study of 735 breast cancer patients and their resulting metastatic disease revealed a preference to form in the liver and lungs. These observations initiated research into the apparent pre-disposition of certain organs to undergo metastasis. Metastatic organotropism is largely observed in the liver, bone, lung, and brain **(Figure 1.2)**. The liver is the most common distant site of metastasis from solid tumors. The liver is anatomically situated to capture many CTCs that enter portal circulation. Additionally, hepatic blood vessels are fenestrated, providing a low barrier of entry into the parenchymal tissue. The bone marrow vasculature also consists of fenestrated sinusoidal capillaries that normally facilitate trafficking of hematopoietic cells[12]. Besides anatomical and physical features, several cellular and molecular mechanisms have been uncovered in each tissue microenvironment that are important for CTC homing and metastasis formation. In the liver, claudin-2, MIF, CCL2, and IL-6 have been shown to promote metastasis[13-15]. CXCL12, RANKL, OPN, and BMPs are important in CTC recruitment to the bone marrow[16]. Osteolytic metastasis is characterized by a "vicious cycle" whereby growth factors, such as TGF-β, embedded in the bone matrix are released and further metastatic growth occurs. Cancer cells that extravasate into lung tissue can stimulate local fibroblasts which ultimately increases WNT signaling and promotion of colonization[17]. DTCs in the brain can induce astrocytes to establish Notch signaling and endothelin production for favorable metastasis conditions[18-19]. In addition to microenvironment features, cancer cells themselves can develop intrinsic mechanisms that can be identified to predict relapse in specific tissues. One example of this is breast cancer cells with high expression of CXCR4, IL-11, osteopontin, and CTGF have been shown to have prometastatic effects in the

formation of bone metastases[20]. Although organ specific mechanisms have been identified, targeting these individual pathways may prove to be impractical. Rather, understanding potential shared mechanisms of metastatic outgrowth could yield targetable pathways for more effective treatment.

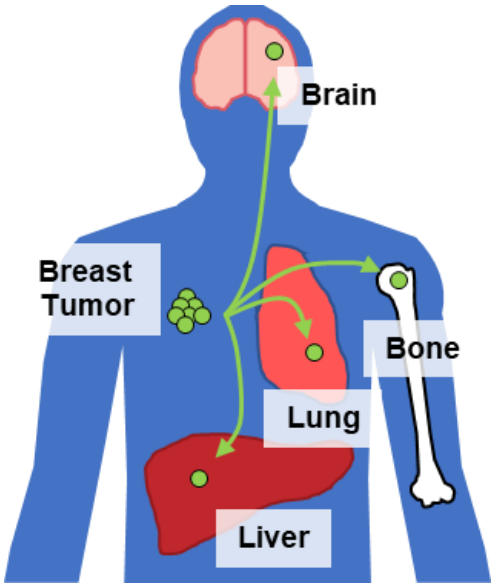

Figure 1.2. Organotropic behavior of tumor cell dissemination to distant tissues. Metastatic tumor development primarily occurs in a subset of organs. Here a primary breast tumor is shown to generated disseminated tumor cells in the brain, bone, lung, and liver.

In the early 2000s, the pre-metastatic niche hypothesis was developed based on the finding that the presence of non-cancer cells can predict a future metastatic site[21]. Findings by Kaplan *et al.* revealed that soluble factors derived from the primary tumor can activate VLA-4^+ (integrin $\alpha_4\beta_1$) $VEGFR1^+$ hematopoietic bone marrow progenitors, changing their phenotype to be more mobile and supportive of metastatic growth in visceral organs. Additionally, tumor derived factors upregulated fibronectin expression in lung fibroblasts to improve homing of these bone marrow derived cells. Removal of these bone marrow derived cells prevented metastasis, however their function and the precise mechanism of soluble factor activation were unknown[21]. Since these findings, work has been expanded

to identify the role of the primary tumor has on changing normal host tissue and hematopoietic response **(Figure 1.3)**. In addition to cytokines, exosomes, small membrane vesicles that contain functional biomolecules including proteins, lipids, RNA, and DNA, have been identified as key drivers of pre-metastatic niche development[22]. Exosomes have been shown to interact with bone marrow cells and organ-specific niche cells to prepare pre-metastatic niches. One of the first exosome-mediated steps in the pre-metastatic niche formation is believed to be the induction of vascular leakiness. Delivery of microRNAs through exosomes can disrupt the blood-brain barrier and enable the formation of brain metastases[23]. Additionally, vascular integrity is decreased in the lung following upregulation of Angpt2, MMP3, and MMP10 early in pre-metastatic niche development and prior to tumor dissemination[24]. The next step in pre-metastatic niche evolution is activation of resident stroma. Aside from interfering with vascular cells, exosomes have been shown to increase S100 protein upregulation in lung fibroblasts and liver-specific Kupffer cells through integrin-mediated binding[25]. Interestingly, the site of pre-metastatic niche formation was defined by the integrin expression pattern on the exosome. S100 proteins have been shown to be strong chemoattractants of myeloid and endothelial cells and appear at several stages of cancer[26-27]. As explained above, activation of local fibroblasts has been shown to increase fibronectin deposition in the lung and liver. Tumor derived exosomes were recently shown to alter perivascular cells to a less differentiated state, with enhanced extracellular matrix production[28]. The LOX family of proteins, involved in collagen crosslinking have also been shown to prime the pre-metastatic niche, however the source is believed to be from the primary tumor rather than activated fibroblasts. LOX accumulates with fibronectin, crosslinks collagen IV and enables

adhesion of myeloid cells. The recruited myeloid cells break down the matrix and create a feed-forward loop of increased bone marrow derived cell recruitment [29]. The final step and hallmark of pre-metastatic niche formation is the systemic recruitment of immune cells. Bone marrow derived cells and myeloid derived suppressor cells play an important role in repressing IFN-γ-mediated immune responses and increasing proinflammatory signaling to make the microenvironment more permissive for immune evasion, extravasation, survival, and proliferation of DTCs[30]. The secretion of MMP9 from recruited hematopoietic cells aids in additional matrix remodeling. Neutrophils respond strongly to chemokines, CXCL1, CXCL2, CXCL5, CXCL12 (SDF-1), secreted by stromal cells activated by exosomes[31]. A recent study found that recruited neutrophils secrete leukotrienes, that can convert cancer cell populations into metastasis-initiating cells[32].

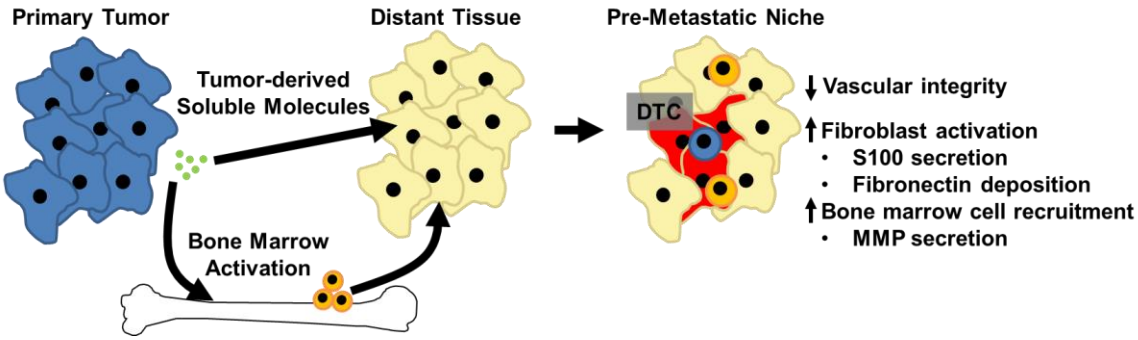

Figure 1.3. Schematic of pre-metastatic niche formation.
Soluble molecules released from the primary tumor act on CTC-recipient tissue fibroblasts and the bone marrow to generate a metastasis-prone microenvironment.

Although the pre-metastatic niche hypothesis is an exciting direction to uncover potential therapeutic targets it does not explain all potential avenues for metastatic relapse. Once a cancer cell has disseminated it generally does not immediately proliferate. A period of cellular dormancy can exist for periods ranging from months to years before relapse into a proliferative metastatic tumor. Clinically, DTCs can be found in the bone marrow years

after primary tumor removal[33-35]. CTCs and cell-free DNA can also be found in circulation in patients in remission[36-38]. There are three hypothesized mechanisms of dormancy: cellular, angiogenic, and immunologic[39]. Cellular dormancy refers to cells that remain in a singular state due to intrinsic signaling. This is the least understood mechanism of DTC dormancy due to challenges in identifying single cells and their proliferative state through histological characterization. Traditionally cellular dormancy was evaluated by negative Ki67, a marker for proliferation, signal. The ratio of ERK and p38 activity has been found to also signal dormancy. High ERK:p38 ratio is required for proliferation, whereas low ERK:p38 ratio is seen in a dormant state[40]. Dormancy can also be induced by downregulation of the PI3K-AKT pathway[41]. NR2F1 upregulation plays a critical role in driving growth arrest via SOX9, RARβ, and NANOG[42]. The microenvironment can play a key role in regulating the dormant phenotype in DTCs. In the bone marrow, GAS6 produced by osteoblasts induces dormancy through Axl, Tyro3, and Mer[43]. BMP7 secreted from bone stromal cells causes cancer cells to activate p38 MAPK, p21, and NDRG1 [44]. The p38 pathway and associated dormancy was also found to be activated by TGFβ2 signaling in the bone marrow[45]. Angiogenic dormancy arises from a lack of vasculature to continually sustain the initial growth of a micrometastasis. Without adequate nutrients, the tumors fail to become metastases and can undergo apoptosis[46]. This mechanism of dormancy is challenged by findings of non-proliferative tumors in direct contact with endothelial cells[47-48]. Finally, immunological dormancy describes a hypothesis whereby immune cells control the growth of proliferating tumors but do not eliminate them. Clinical observations of patients with transplanted organs containing donor tumor cells have developed metastasis after immunosuppression suggesting the host immune system was

keeping the tumor in check[49]. A preclinical model found that maintenance of metastatic dormancy was halted once $CD8^+$ T cells were selectively removed[50]. Adaptive immune cells may also inhibit pro-angiogenic pathways to prevent growth[51]. The dual nature of the immune system in tumor progression have made the mechanisms for potential immunological dormancy unclear.

1.3 Experimental Models of Metastasis

Despite success in treating primary tumors, metastatic relapse remains a challenging disease to treat. A great emphasis has been placed in better understanding the fate of tumor cells that escape the primary lesion. Considerable efforts have been made in understanding the biology of CTCs and early stage DTCs to identify targets that may prevent metastatic outbreak. Although limited in study for ethical reasons, human samples remain the best samples for understanding metastasis and the development of effective therapies. Alternatively, mouse models provide an invaluable intermediate between reductionist *in vitro* approaches and human patients. However, mouse models are often imperfect and do not always produce translational findings to human patients. There is a critical need to generate new methods and models to better simulate and investigate disease progression for translatable outcomes. In this section various techniques are highlighted that improve understanding of CTC and DTC biology **(Figure 1.4)**.

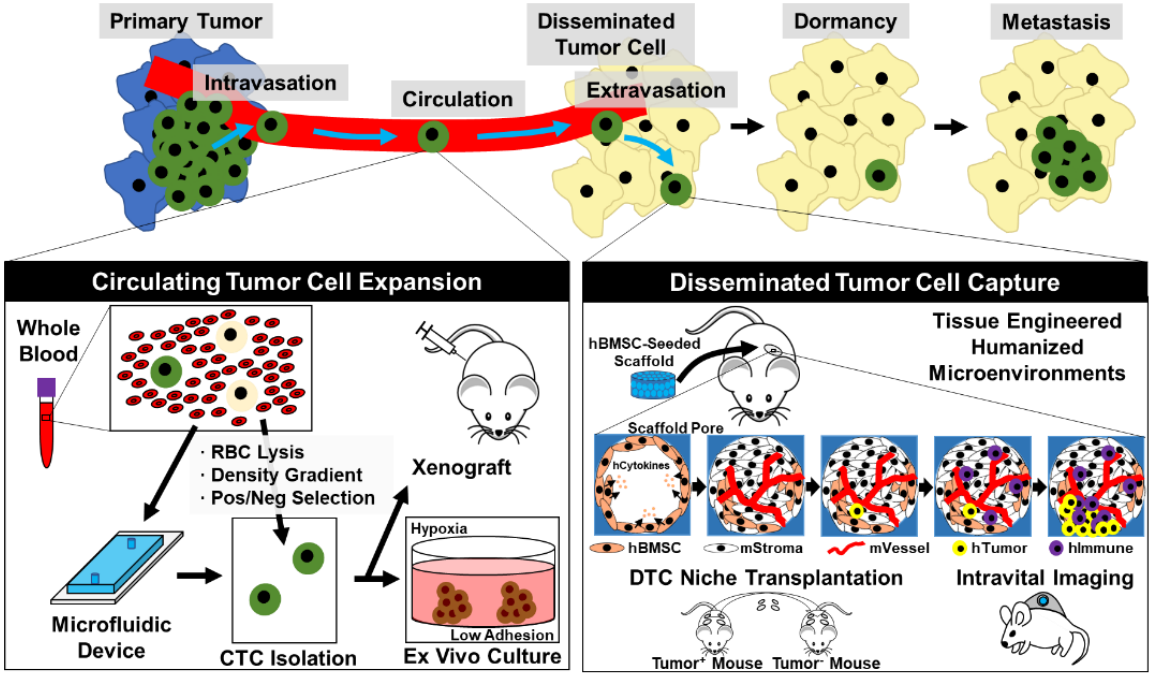

Figure 1.4. Schematic of the metastatic cascade and advanced techniques developed to elucidate the biology of circulating and disseminated tumor cells
Circulating tumor cells can be isolated via microfluidic devices and traditional cell separation techniques. Captured circulating tumor cells are kept viable in optimized *ex vivo* culture conditions and transplantation into mice. Disseminated tumor cells can be captured in tissue engineered microenvironments for long-term monitoring of progression to metastases. Intravital imaging windows have been used to visualize extravasation into scaffold niches.

1.3.1 Isolation and Culture of Circulating Tumor Cells

CTCs are rare cells within the diverse population of cells in the blood. Red blood cells, leukocytes, myeloid cells, endothelial cells, and various epithelial cells can be found in the blood. Early research in the field of CTCs utilized existing cell sorting techniques via antibody targeting [52]. EpCAM and cytokeratin are prevalent markers to isolate CTCs from whole blood samples. CellSearch, the only FDA approved diagnostic tool for clinical use, detects $EpCAM^{+}/Cytokeratin^{+}$ CTCs [53]. However, these methods require a cell-fixation step preventing subsequent functional assays. Additionally, selection of $EpCAM^{+}/Cytokeratin^{+}$ cell populations has been shown to be limited in its ability to

capture all tumor-derived cells as CTCs may have undergone an epithelial-to-mesenchymal transition during intravasation into the blood stream and no longer display epithelial markers.

Due to the rarity of CTCs there have been efforts to culture captured cells *ex vivo* to increase the yield and accuracy of analytical characterization. Additionally, new techniques have been developed to isolate CTCs. Several microfluidic devices have been developed to streamline the isolation process and minimally damage cell populations. In general, these devices are constructed with PDMS with the flow chambers coated with EpCAM antibodies [54]. Utilizing the unique flow properties of different blood components, devices have been made to separate CTCs with minimal exogenous processing such as red blood cell lysis buffers [55]. An additional solution to separate CTCs that has shown success in microfluidic platforms and more traditional immunomagnetic separation techniques is the depletion of the non-CTC populations mainly composed of immune cells [56]. Due to the heterogenous population of CTCs and the potential for an epithelial-to-mesenchymal transition, this approach attempts to capture a more complete population of CTCs in whole blood and minimize the potential for negative downstream side effects due to antibody binding. Lastly, a simplistic technique to capture CTCs involves the isolation of nucleated cells via density-based separation, such as Ficoll Paque. Although this does not separate immune cells from CTCs, during *ex vivo* culture these immune cells eventually die leaving an enriched CTC population [57].

Ex vivo culture of CTCs is a challenging endeavor, and very few studies have been successful. Stable cell lines can take months to develop with low yield. Several groups have seen success using a cocktail of growth factors including EGF and FGF among others

to culture CTCs *ex vivo* [55, 58]. Additionally, *ex vivo* CTC culture is commonly performed under hypoxic conditions of <5% O_2 [56]. Those cells that were successful during initial culture were capable of expansion without growth factors. Another approach to culture CTCs includes the addition of tumor associate fibroblasts and extracellular matrix proteins. Three-dimensional culture was still necessary for effective expansion [54]. Multiple reports indicate an enrichment of $CD44^+/CD24^-$ CTCs which have been previously classified as cancer stem cells, a highly tumorigenic subpopulation [59].

Even with advances in culture techniques, it is often challenging to expand primary cells *in vitro*. Drastic changes in nutrient availability, oxygen tension, cell-cell interaction, mechanical stiffness, extracellular matrix proteins can overwhelm cells and prevent proliferation. Human patient-derived xenografts in immunodeficient mice have yielded physiologically relevant maintenance of tumors. Similarly, CTCs have been xenotransplanted into murine hosts to enrich the population of cells that could form metastatic tumors [60]. Similarly to *in vitro* studies, CD44 was frequently observed in metastatic disease. Interestingly the CTCs developed markers that were not present in the primary tumor. This phenomenon is frequently observed in the clinic and is believed to be a major driver of drug resistance and poor patient prognosis.

In clinics, the capture of patient CTCs may be an important tool for diagnostics and aid in developing personalized therapeutic strategies to improve patient outcome. Current technology enables comprehensive CTC genotyping to identify mutations, however cells may not be fully receptive to drug candidates. CTC lines can be used to screen panels of single and combinatorial drug candidates. Additionally, better understanding of cells that can form metastases is also necessary. Data suggests that not all CTCs can form metastases.

Understanding the intrinsic factors that are unique to metastasis-initiating CTCs is another key area of study to prevent metastatic disease. Currently these approaches are limited by the lack of reliable methods to culture patient CTCs and the long periods of time required to generate cell lines.

1.3.2 *In Vitro* Models to Study Disseminated Tumor Cells and Dormancy

As techniques improve to isolate and characterize CTCs improve, there has also been considerable effort in understanding the DTC microenvironment. *In vitro* models have been developed to observe tumor cell behavior in controlled environments. Precise control of soluble molecules, cell ratios, substrate matrix, and external compressive, elastic, and shear forces can be applied reproducibly[61-62]. Additional benefits of *in vitro* systems include the high throughput nature, easy accessibility for real-time microscopic analysis, and fabrication with fully human cellular and extracellular components. A co-culture system of human stromal and endothelial cells was used to mimic lung and bone marrow microenvironments. Seeding with human cancer cells followed by a cocktail of laminin-rich extracellular matrix and supplement-free media created a dormant microenvironment[63]. Endothelial cell derived thrombospondin-1 kept cancer cells in a dormant state by suppressing neovasculature and associated TGF-β1 and periostin. Another *in vitro* model utilized a microfluidic system to study human breast cancer extravasation into a human bone marrow microenvironment[64]. This model consists of a fibrin gel, seeded with human mesenchymal stem cells and osteoblasts, surrounded by flow channels separated by a layer of human endothelial cells. Human cancer cells are introduced in the flow channel and microscopically observed as they extravasate into the bone marrow mimic. This model demonstrated potential as a drug screening assay for

compounds that prevent extravasation and metastatic outgrowth. Although complex *in vitro* models have been developed, generating fully physiologically relevant models is challenging *ex vivo*. Additionally, as highlighted above with the culture of patient CTCs, certain primary cells are challenging to culture *ex vivo*. *In vitro* models have unmet potential in fully modeling DTC biology and still need time to reach the predictive value of *in vivo* models.

1.3.3 *In Vivo* Models to Study Disseminated Tumor Cells and Dormancy

In vivo models encompass the full complexity and dynamics of a living system and provide great insight on tumor biology [65-67]. Mouse models have long been the gold standard to observe tumor progression from a primary tumor to a lethal metastasis. Mice are relatively cheap, easy to house and handle, and reproduce quickly. Due to the widespread use of mice in research laboratories a rich infrastructure of tools has been developed. Clinical imaging modalities such as x-ray, magnetic resonance imaging, and positron-emission tomography have all been adapted for use in preclinical studies[68-69]. In this section traditional mouse models and tissue engineering approaches to study metastasis are discussed **(Figure 1.5)**.

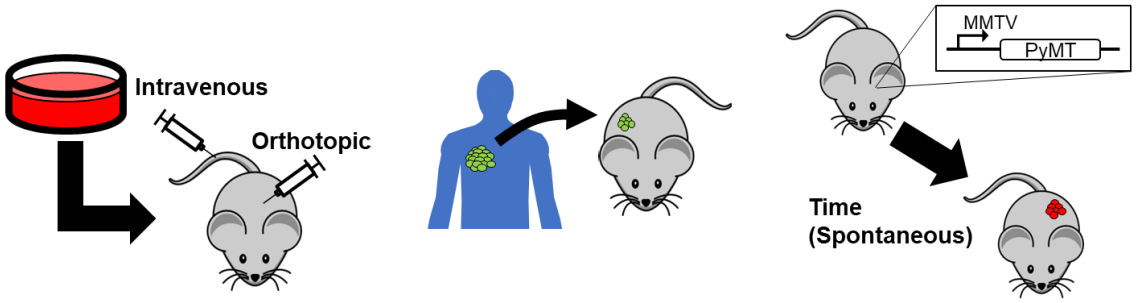

Cell Line Inoculation

Pros
- Rapid testing
- Human or mouse tumor cells

Cons
- Unnatural formation of metastasis
- Irreversible changes during ex vivo culture

Patient-Derived Xenograft

Pros
- Human cells in a living organism

Cons
- Immunodeficient hosts
- Low engraftment

Genetically Engineered

Pros
- Natural tumor progression
- Immune competent

Cons
- High primary tumor burden
- Low throughput (breeding)

Figure 1.5. Traditional methods to generate in vivo mouse models of metastasis. Primary tumors are commonly formed via cell line inoculation, patient-derived tissue transplantation, or genetic engineering to create spontaneous tumors. Each method presents its own unique benefits and drawbacks.

The most common approach to modeling cancer in mice is the inoculation of *in vitro* cultured tumor cell lines. Injection of these cells can occur orthotopically, at the site of original primary tumor, ectopically, not at the site of original primary tumor, or systemically by directly injecting into circulation. These models benefit from rapid tumor generation and low cost, an attractive platform for preclinical therapeutic screening. Allogeneic transplantation into syngeneic immunocompetent hosts have been used for preclinical drug development since the 1950 and 1960s[70-71]. However, these models have shown low predictive value when translated to humans[72]. The discovery and widespread use of immunocompromised mice enabled xenotransplantation of human tissues into mice without host rejection[73]. Although these models utilize human cells, they still have low

predictive value for clinical outcomes[74-75]. The use of tumor cell lines has come under recent scrutiny as observations of altered *in vivo* tissue microenvironment development and irreversible gene expression changes due to culturing *in vitro* have been made[76-77].

Rather than digest tumor tissues, culture and expand the cells on two-dimensional substrates, and then introduce them into mice several models simply take pieces of tumor and implant them into mice. Engrafted tumors can be expanded by passaging to new mice and conserve histological and gene-expression features of the originating tumor[78]. When taken from human patients, these models are referred to as patient-derived xenografts (PDX). Co-clinical trials have been performed assessing the differences between PDX and patient responses to treatment. PDX models have been shown to accurately model clinical outcomes 87% of the time, including both positive and negative clinical outcomes[79]. Due to the personalized nature of these models, they have been proposed as powerful screening platforms to predict patient response[80]. Engraftment rates of patient tumor samples depends on several factors including sample quality and tumor type. The rate of engraftment can be on the order of months, making them impractical for personalized care and are additionally limited by logistical difficulties[81]. Over time or as the tumor is passaged to new mice, patient stroma and non-cancerous cells are eventually replaced with host cells.

Another approach is to genetically engineer mice that develop *de novo* tumorigenesis in a spontaneous or controlled manner. In early models, oncogenes were inserted under control of a tissue-specific promoter[82]. One example of this is the MMTV-PyMT mouse that develops a spontaneous breast cancer[83]. More recently, conditional models based on site-specific recombinase systems, like Cre-loxP, and CRISPR/Cas9 have been developed[84]. Due to *de novo* tumor generation, these models more accurately model

immune responses, develop heterogeneity, and progress toward metastatic disease in a more physiologically relevant manner. The ability to accurately predict patient response has also been studied extensively[85]. Genetically engineered models are limited by aggressive primary tumor burden, limiting their ability in studying metastasis[84]. Additionally, generation of new mouse models is time consuming and expensive[81].

The efforts described above were developed mostly to study the primary tumor, and their utilization in metastasis research is not as straightforward or effective. Mouse and human biology are ultimately different. The high frequency of metastasis in the lung, liver, brain, and bone observed in humans is not conserved in mice. For example, mice and other rodent models rarely develop bone metastases spontaneously [86]. There have been various techniques developed to overcome the natural limitations of mouse models; however, these often involve direct injection into the tissue of interest such as intratibial injections for bone metastasis[86]. Although xenograft models have become more accessible and widespread, in the context of metastasis they lack relevant recipient human tissue stroma. Studying human DTCs in a mouse microenvironment may reduce the translational power of traditional mouse models. Although this is ultimately unavoidable when using a mouse host, strategies to incorporate human recipient tissue for CTCs have been successful.

Early efforts to produce human relevant stroma involved the transplantation of human fetal lung and bone tissue into immunodeficient mice [87]. These implanted tissues were successful in recruiting human tumor cells and displayed specific human-human cell interactions not observed in the native murine tissue. Of the nine human small cell lung carcinoma cell lines intravenously injected, only seven developed metastases and these only occurred in the human fetal lung implants. Additionally, these studies revealed that

the freshly implanted tissues were more receptive to generating metastases compared to implants that had been in the mice for 8-10 weeks. They attributed this to a decrease in cytokine secretion and expression of adhesion molecules over time. Interestingly, they were able to recover the ability to recruit CTCs by either sublethal irradiation or IL-1a treatment. Although this study provided early evidence that human-human cell interaction is an important factor with xenograft models, ethical considerations, and challenges in obtaining human samples have limited widespread adaptation of this technique.

In recent years, tissue engineering strategies have been implemented to recapitulate human stromal microenvironments that attract CTCs from more readily available human sources. As mentioned above, the lack of metastases in the bone of mice is a critical challenge faced by the field. Formation of ectopic human bone and marrow tissues has been achieved via a combination of degradable polymers loaded with bone-inducing growth factors and seeding of human osteoblast precursors [88-89]. Similar to the studies performed in fetal human tissues, human tumor cells homed to and proliferated within ectopic human bone implants [90-94]. Besides bone, human liver microenvironments have also been developed *in vivo*, however they have not been utilized to study cancer [95].

A secondary approach utilizes implantable biomaterials to study the metastatic niche [96-101]. Pre-metastatic niches are transiently formed through inflammatory signaling from the primary tumor, instigating the recruitment of bone marrow derived cells to tissue microenvironments, priming the niche for CTCs. Interestingly, the implantation of various biomaterials has yielded niches with similar metastasis forming potential as traditionally discovered pre-metastatic niches. Work in our lab has utilized polyacrylamide hydrogel with an inverted colloidal crystal geometry to generate a highly porous, transparent, and

non-degradable biomaterial scaffolds [96-97, 101]. When implanted subcutaneously these niches are receptive to CTCs derived from orthotopic and intravenously delivered tumors. These scaffolds are discussed in further detail in the following section. Similar efforts to engineer a pre-metastatic niche have been made with different biomaterial platforms. A porous poly-lactic and glycolic acid scaffold has been leveraged to identify haptoglobin as a key signaling molecule to recruit CTCs [99]. These scaffolds have also been fabricated with polycaprolactone and used to track the dynamic immune response during cancer progression[102]. Their study revealed a detectable gene signature within the implantable niches that corresponded with disease progression and an opportunity to better understand myeloid derived suppressor cells. Besides the biological findings of this work, an exciting translational opportunity for implantable niches was presented that would enable diagnostic monitoring of the dynamic immunological profiles that occur during metastatic progression. Additional translational potential for implantable biomaterial microenvironments has also been explored with the goal of reducing DTC burden in native tissues by capturing circulating tumor cells within the tissue engineered niche [103-105].

A secondary problem related to the use of mouse models is the challenge of studying DTC dormancy. Metastasis is inherently difficult to study regardless of model due to the nature of its single cell origin. Single DTCs and early stage metastases are difficult to detect and characterize in patients and mouse models. Following a DTC over long periods of time amplifies this challenge. Most cancer cell lines used in metastasis studies are generally aggressive and do not undergo dormancy for timescales observed in humans. In order to study disseminated cells in many models the primary tumor must be surgically removed. There have been reports that some primary tumors inhibit the

metastatic capability of DTCs, and removal activates proliferation[106]. This does not appear to affect all models, as several dormancy mechanisms have been discovered via primary tumor removal. One example is the discovery of p38α/β dormancy activation via TGFβ2 signaling in DTCs in the bone marrow, which utilized a cell line xenograft surgically resected after reaching 500 mm^3 [45]. The squamous cell carcinoma cell line, HEp3, used in this study and others, takes on a dormant phenotype after prolonged *in vitro* passage[42]. Another cell line commonly used in dormant DTC studies is the mouse breast cancer cell line D2.0R. When intravenously delivered these cells remain single and non-proliferative in the lungs for at least 240 days [107]. Genetically engineered mouse models have also been utilized to study DTC biology. The discovery of early DTCs was made using MMTV-HER2 and MMTV-PyMT mice[108]. As a larger emphasis is put on DTC biology, new tools and techniques are necessary to better understand dormancy and mechanisms that initiate proliferation. Implantable biomaterial scaffolds have demonstrated potential for being powerful tools to study DTCs. Engraftment of a dorsal skin-fold window chamber enabled imaging of CTCs extravasating into the scaffold niche[97]. The ectopic nature of the tissue engineered niche has been leveraged to transplant DTC containing scaffolds into secondary tumor-free hosts for long-term observation[96]. Together, the presented features of tissue engineered niches to study metastasis represent an exciting opportunity to better understand DTCs and their microenvironment in a new lens. One of the focuses of this dissertation is expanding the application of implantable biomaterial scaffolds for the investigation of DTCs as they progress from a single cell to an overt metastasis.

1.4 Inverted Colloidal Crystal Hydrogel Scaffolds and Implantable Biomaterial Niches

Colloidal crystals are three-dimensional structures of ordered particles found in opal gemstones, bird feathers, beetles, sea creatures, and butterfly wings. Also known as photonic crystals, the structural geometry drives unique optical properties such as iridescent color. In nature these colloidal crystals consist of spherical particles in the nanometer scale[109-110]. Besides their attractive photonic properties, colloidal crystals are easily self-assembled across a wide range of diameters. Inverse colloidal crystal (ICC) structures have also been heavily studied for their photonic properties and more recently as a biomaterial scaffolding for tissue engineering applications[111]. ICC scaffolds are fabricated by filling the interstitial space of an initial colloidal crystal material with a polymer followed by selective removal of the colloidal crystals. The resulting structure consists of a reproducible interconnected spherical pore array with large surface area (**Figure 1.6**). These biomaterial scaffolds have been used in the tissue engineering of cartilage, liver, bone, and bone marrow, as well as circulating tumor cell attracting niches *in vivo*.

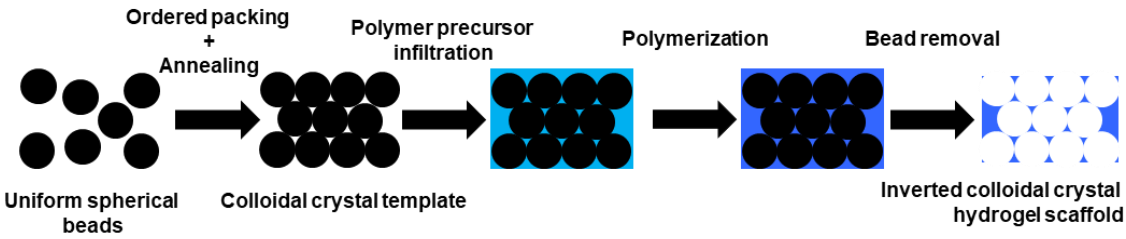

Figure 1.6. Inverted colloidal crystal hydrogel scaffold fabrication schematic.
Uniform spherical beads are orderly packed and partially annealed to create a free-standing colloidal crystal template. A hydrogel precursor solution is added to the template and polymerized around the template structure. The template material is selectively removed to create a hydrogel scaffold with an inverted colloidal crystal geometry.

1.4.1 *In Vivo* Tissue Development

Any material that enters the body undergoes a reaction known as the foreign body response. Initially soluble proteins in the host are adsorbed onto the material, accelerating the recruitment of innate immune cells such as macrophages. Prolonged exposure causes macrophages to form foreign body giant cells and recruit vasculature and fibroblasts to encapsulate the material with a fibrotic capsule that effectively seals the material off from the host. Experiments performed in the 1960s and 1970s found that subcutaneous implantation of porous poly(hydroxyethyl methacrylate) (pHEMA) sponges resulted in ingrowth of fibrous tissue, giant cells, blood vessels with a thin surrounding capsule[112-113]. Shortly after, an observation was made that pore size played a role in tissue infiltration, with 0.5 and 8 μm pores preventing infiltration while 40 μm allowing infiltration[114]. The introduction of sphere templated scaffolds enabled in depth analysis of tissue development within pHEMA and poly(methyl methacrylate) (PMMA) scaffolds as a function of tightly controlled pore size (20, 30, 40, 60, 80 μm)[115-116]. The effect of pore size on vascularization was further expanded when larger pore (79, 147, 224, 312 μm) poly (D, L-lactide-co-glycolide) (PLGA) scaffolds were implanted subcutaneously[116]. Smaller pores drove the formation of high blood vessel density with poor penetration into the scaffold, whereas larger pores had larger vessels at lower densities that fully infiltrated the scaffold. A follow up study using multiscale photoacoustic microscopy and optical coherence tomography confirmed these findings in a comparison of scaffolds with 80 μm pores 200 μm pores[117]. Non-hydrogel, β-tricalcium phosphate scaffolds have been explored with larger pore sizes; 300-400, 400-500, 500-600, and 600-700 μm[118]. Implantation of these scaffolds revealed that larger pore sizes are beneficial for blood vessel, however cellular infiltration is reduced

compared to scaffolds with smaller pores. Polyacrylamide ICC hydrogel scaffolds with 250-300 μm pores were shown to have the highest cellular infiltration and complete vascularization when implanted subcutaneously[97].

Another interesting feature of ICC hydrogel scaffold implantation is the unique immune microenvironments that form within the pores. $Lin^{-}Sca\text{-}1^{+}c\text{-}kit^{+}$ progenitor cells are recruited to polyacrylamide ICC scaffolds, and the number can be significantly enhanced by pre-seeding bone marrow stromal cells[97]. Investigation of the role of macrophages responding to ICC scaffolds has revealed specific cellular phenotypes arise at the material surface and within the pore[119]. Macrophages can be loosely categorized by their pro-inflammatory or alternative phenotypes. Pro-inflammatory, also referred to as M1 or classically activated, macrophages are characterized by secretion of pro-inflammatory cytokines, reactive oxygen species, and nitric oxide. Alternatively activated, M2, have several functions including immunomodulation, matrix deposition, tissue remodeling and are associated with wound healing. M1 macrophages were found on the pore and outer scaffold surfaces whereas M2 macrophages were observed in the foreign body capsule and the central region of larger pores. This phenomenon appears to be driven by direct adhesion to the biomaterial as these cells occupy adjacent spaces. Physical size has been shown in non-ICC biomaterial systems to play an important role in modulating the immune response[120]. Further study into the immune microenvironments that forms within porous materials is necessary to better understand the differences observed in the foreign body response compared to bulk materials. Collectively these results indicate a unique foreign body response against porous biomaterials **(Figure 1.7)**.

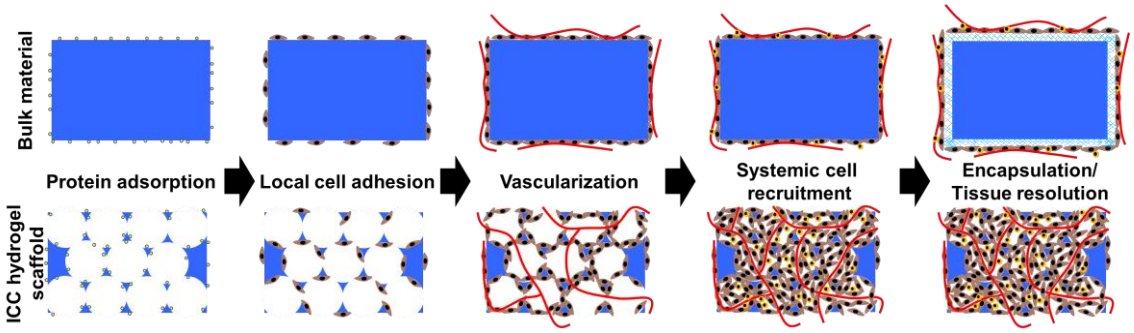

Figure 1.7. Host response to implanted biomaterials.
Once a biomaterial is implanted, soluble proteins are adsorbed onto the surface. Local myeloid cells are recruited to the surface of the material and secrete pro-angiogenic molecules. Additional immune cells are recruited from systemic circulation through the vasculature. As the wound healing response resolves, a dense fibrous capsule is formed around the material. ICC hydrogel scaffolds do not undergo encapsulation and remain fully vascularized.

My own observations with ICC scaffold implantation have aligned with previous studies in literature. However, the use of polyacrylamide has yielded some unique differences that warrant further investigation. Several factors change when altering the polymer composition and material properties. First, ICC scaffolds fabricated with polyacrylamide hydrogel yield more robust cell migration and infiltration within the pores compared to ICC scaffolds fabricated with polycaprolactone **(Figure 1.8)**. Second, ICC scaffolds made with varying percentages of polyacrylamide concentrations (5-50 wt%) revealed limitations in scaffold stability and cellular recruitment. There was no significant difference in tissue development from 30-50 wt%, however scaffolds made with 5-15 wt% polyacrylamide mechanically collapsed after subdermal implantation and inter-scaffold tissue development was incomplete **(Figure 1.9)**. Finally, 30 wt% polyacrylamide ICC scaffolds were examined with varying pore diameters from 75-500 μm. Blood vessel diameters increased with increasing pore sizes, but larger pores (400-500 μm) developed a more diverse range of vessels. Smaller pore sizes (75-150 μm) induced relatively

homogenous vascular development but restricted stromal and immune cell migration **(Figure 1.10)**. These results demonstrate the tunable nature of ICC hydrogel scaffolds to drive different host responses to generate unique tissue microenvironments.

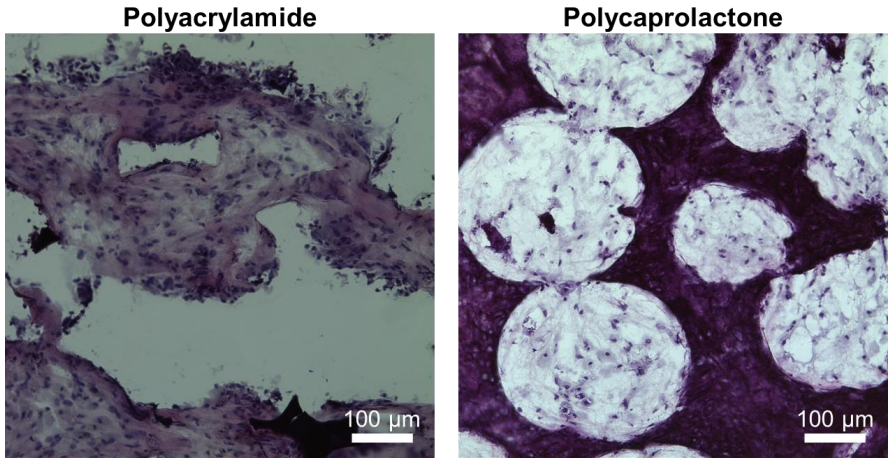

Figure 1.8. ICC scaffolds fabricated with polyacrylamide and polycaprolactone. Hematoxylin and eosin staining of scaffolds composed of 30 wt% polyacrylamide and polycaprolactone with the same bead size. Scaffolds were implanted for 4 weeks.

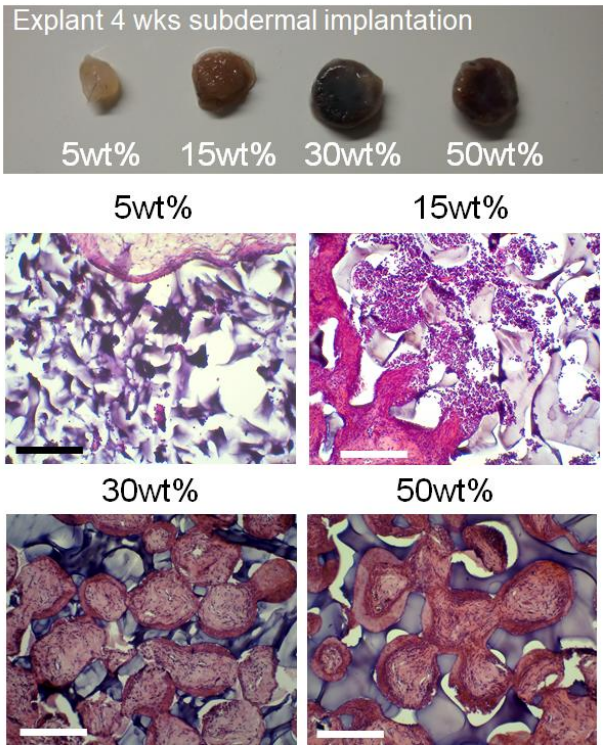

Figure 1.9. ICC polyacrylamide hydrogel scaffolds with four different polymer concentrations.
Gross images of scaffolds after 4 weeks implantation, and hematoxylin and eosin stained images. Scale bar 200 μm.

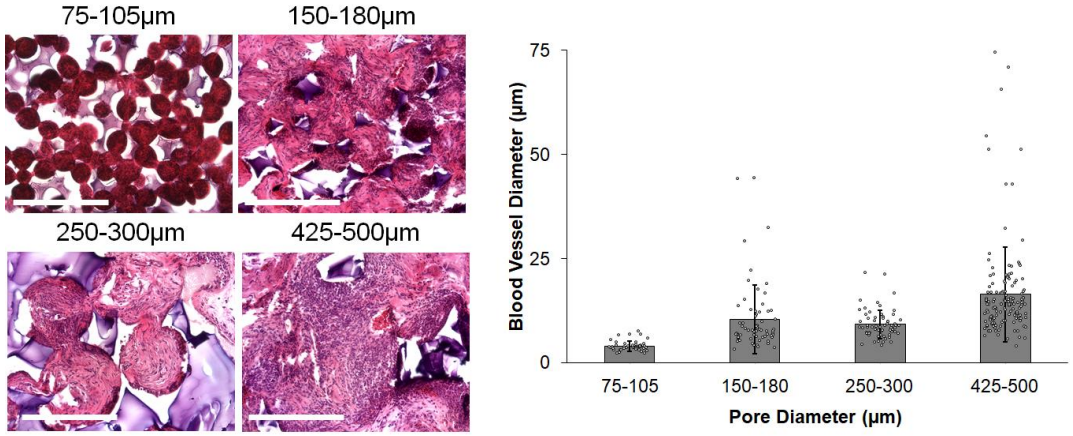

Figure 1.10. ICC polyacrylamide hydrogel scaffolds with four different pore sizes.
Hematoxylin and eosin staining of 30 wt% polyacrylamide scaffolds fabricated with different bead sizes. Scaffolds were implanted for 4 weeks. Increasing pore size, resulted in larger vascular diameter. Scale bar 250 μm.

1.4.2 Modelling the Metastatic Cascade

ICC scaffolds made with polyacrylamide have shown robust performance modeling multiple aspects of the metastatic cascade. The first usage of these scaffolds aimed to mimic the bone marrow microenvironment[97]. Human bone marrow stromal cell seeded scaffolds enhanced the marrow-like environment of the implant and increased recruitment of intravenously delivered TF-1a cells, a human leukemia cell line. Extravasation was observed in real-time by surgical engraftment of a skin-fold dorsal window chamber. In addition to the kinetics of adhesion and extravasation of CTCs, the blood vessel diameter associated with adhered CTCs was also determined **(Figure 1.11a)**. The second application of polyacrylamide ICC scaffolds in a metastasis study aimed to uncover cellular and molecular features of the early metastatic microenvironment[96]. In this model, scaffolds were subcutaneously implanted and allowed to fill with tissue before the orthotopic injection of human prostate cancer cells. Aggressive primary tumor growth required the removal of the scaffolds prior to the development of metastases. To prolong the study, scaffolds were transplanted to tumor-free hosts. Metastasis could be monitored noninvasively through luciferase imaging and showed a gradual increase in signal over a six week period **(Figure 1.11b)**. The stromal cells in metastasis-positive and metastasis-negative scaffolds was compared using a qPCR array and revealed upregulation in IL-1β, Mmp-9, Mmp-10, Mmp-13, Flt-4, Etv-4, and Mcam. The functional significance of stromal cell-derived IL-1β was confirmed in the same model using an FDA approved IL-1 receptor antagonist **(Figure 1.11c)**. ICC hydrogel scaffolds for application in understanding DTC biology remains largely unexplored. My dissertation work utilized ICC hydrogel scaffolds to uncover mechanisms of CTC recruitment and proliferative activation of dormant DTCs.

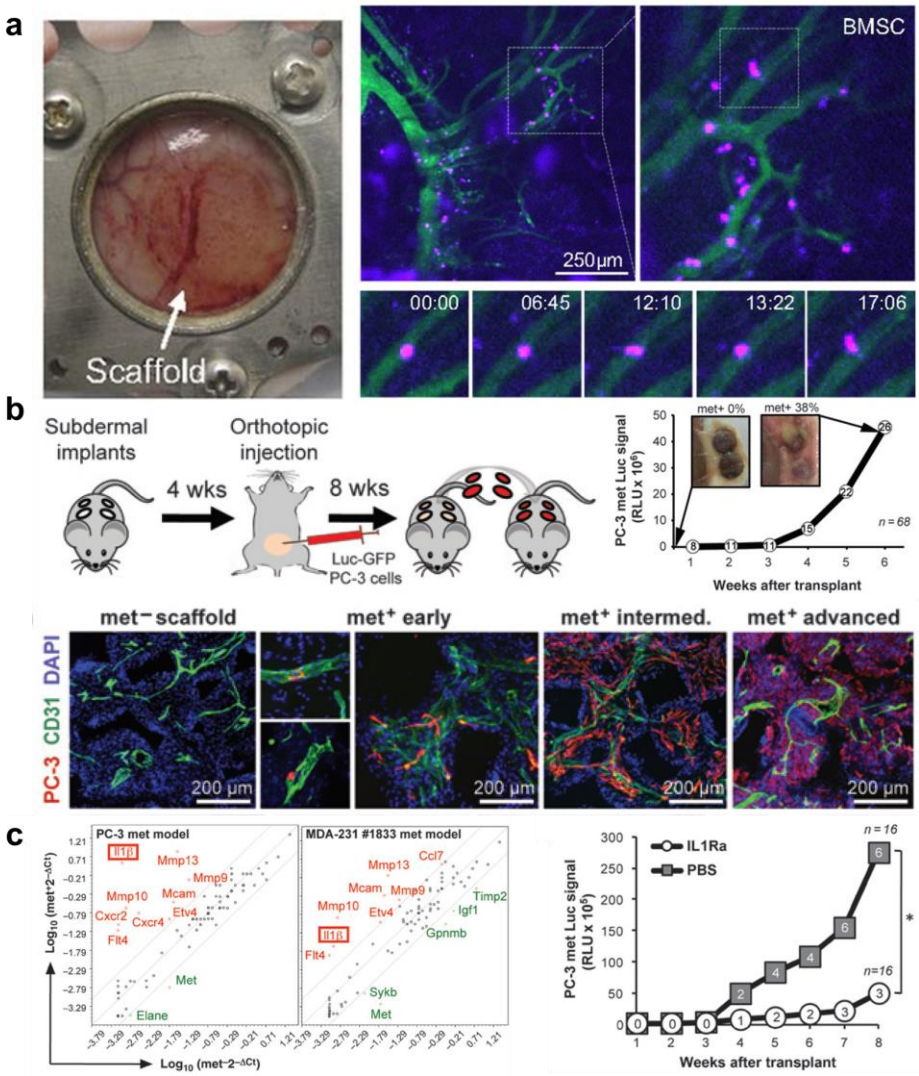

Figure 1.11 Foundational work using inverted colloidal crystal hydrogel scaffolds in a metastasis model.

a, Intravital imaging of extravasating cancer cells into scaffold microenvironment, adapted from Lee et al., *P.N.A.S (2012)*[96]. b, Long-term observation of DTCs and formation of advanced metastases, adapted from Cancer Research, 2014, 74/24, 7229-38, Bersani *et al.*, Bioengineered implantable scaffolds as a tool to study stromal-derived factors in metastatic cancer models, with permission from AACR[97]. c, Genetic analysis of stromal niche surrounding DTCs and functional reduction of metastatic relapse using ICC hydrogel scaffolds, adapted from Cancer Research, 2014, 74/24, 7229-38, Bersani *et al.*, Bioengineered implantable scaffolds as a tool to study stromal-derived factors in metastatic cancer models, with permission from AACR[97].

1.5 Dissertation Objectives

This dissertation aimed to provide new tools and techniques to study DTCs and metastatic relapse in mice. As described to this point, mouse models struggle to fully reproduce patient-relevant metastasis, specifically organotropism and long-term dormancy behaviors. This work builds upon the use of a highly porous ICC hydrogel scaffold to assess niche evolution during metastatic progression *in vivo*. The reproducible and standardized tissue formation provides a unique platform to study DTCs with high analytical power. First, I aimed to engineer new scaffold microenvironments that can be used to elucidate critical niche components for recruitment and DTC proliferation. Second, I aimed to leverage the transplantable nature of ectopic scaffold tissue to investigate long-term DTC niche evolution and potential activation mechanisms. Lastly, I aimed to improve the fabrication of ICC hydrogel scaffolds to make the process cheaper, safer, and faster. The aims of this dissertation are specified in further detail below.

1.5.1 Aim 1: Engineer unique niches that enable the study of disseminated tumor cells *in vivo*

Mouse models are generally limited to the study of lung metastasis without specialized cell lines or injection techniques. Tissue engineered approaches have opened the door as an exciting opportunity to study DTCs in controlled environments. Previous work in our group has utilized a porous scaffold implanted subcutaneously to study extravasation and niche evolution during metastatic progression. The first focus explored the potential of altering the implantation site of the hydrogel scaffold in different anatomical locations to generate unique microenvironments. The hypothesis was that each tissue niche will have differing CTC recruitment and metastatic potential, enabling the

elucidation of cellular and molecular signals critical for metastasis. The findings of this study are presented in Chapter 2.

A secondary approach to introduce new tissue microenvironments leveraging the unique tissue formation in ICC scaffolds is also presented. Here I aimed to transplant fully mature tissue from internal organs and transplant them subcutaneously. The rationale behind this approach was that the subcutaneous space provides greatly enhanced accessibility and transplantation can be leveraged for the study of human tissues in mice. The work corresponding to this sub-aim are presented in Chapter 3.

1.5.2 Aim 2: Investigate long term niche evolution and potential triggers of metastatic relapse in scaffold microenvironments

The evolution of DTCs and their niche are largely unknown following extravasation. It is widely accepted that DTCs undergo varying periods of dormancy prior to entering a proliferative state. Previous work with ICC scaffold microenvironments revealed the capability to expand the observation of DTCs in their niche by transplanting them into tumor-free mice. The objective of this aim was to further explore the changes to the local microenvironment that occur as DTCs change from singular dormant cells to small tumor colonies and eventual overt metastases.

The first study investigated a humanized model consisting of human cancer, immune cells, and DTC-niche stroma and is described in Chapter 4. Human bone marrow cell seeded scaffolds were implanted in immunodeficient mice prior to the formation of an orthotopic human prostate tumor. Peripheral blood mononuclear cells were injected to instigate inflammatory signaling from human cells. Scaffolds were transplanted to tumor-free mice and the niches were non-invasively monitored for 10 weeks. Histological

characterization revealed changes to local vascular and innate immune cells as DTCs progressed from singular cells to metastases.

Finally, a fully immunocompetent mouse model was used to investigate potential triggers of metastatic relapse. Recent reports have highlighted the possibility of enhanced risk of metastasis following adjuvant therapies. I aimed to explore the potential of biomaterial metastasis research to capture this phenomenon and uncover potential mechanisms of DTC activation. The corresponding work is found in Chapter 5.

1.5.3 Aim 3: Improve fabrication process of ICC hydrogel scaffolds to increase scalability

Although ICC hydrogel scaffolds have demonstrated great potential as a tool for metastasis research, the fabrication process is suboptimal. The process is laborious, taking up to a week to manufacture a batch of polyacrylamide scaffolds starting from soda lime glass beads. When using glass beads as a starting material safety becomes a major concern as dissolution of the glass template requires highly toxic hydrofluoric acid. Finally, cost of fabricating bioactive scaffolds requires the use of expensive crosslinking reagents to covalently bond collagen to the surface. In Chapter 6 I highlight the work performed to improve fabrication using expanded polystyrene beads as the starting material and a polymerization strategy to embed collagen within the polymer matrix.

1.6 Summary

As presented in this chapter, metastasis is a complex and dynamic process that stems from single cell interactions with their microenvironment and can take place over the course of months to years. Traditional mouse models designed to study cancer,

generally primary tumors, are poorly equipped to study the metastatic cascade due to technical limitations and human-mouse species differences. The work presented in this dissertation provides new tools to better understand metastasis. To achieve this, a biomaterial strategy was implemented to engineer receptive niches for circulating tumor cells. Specifically, inverted colloidal crystal scaffolds composed of polyacrylamide were used in a variety of ways to investigate circulating tumor cell recruitment, disseminated cell proliferation, and the cellular and soluble factor microenvironment changes that occur during the progression to metastases.

CHAPTER 2

DIVERSIFYING THE IMPLANTATION SITE OF POROUS BIOMATERIALS TO CREATE TISSUE-SPECIFIC MICROENVIRONMENTS

2.1 Abstract

The formation of metastatic tumors is the leading cause of cancer related deaths. Circulating tumor cells spread to several distal organs. However, disseminated tumor cells (DTCs) are reliant on their local tissue microenvironment to foster growth into overt metastases. Bone, brain, lung, and liver have been identified as favorable to metastatic growth, whereas tissues such as the muscle and intestine rarely develop metastases. Mouse models have been widely used to study various aspect of cancer biology, but they are limited to fully understand metastatic organotropism because metastasis mainly occurs in the lung. Identifying the common mechanisms that promote or suppress DTC growth across metastasis prone and resistive tissues is imperative to the development of better clinical strategies for metastatic disease. Recently, subdermally implanted porous biomaterials have demonstrated the ability to develop vascularized tissue microenvironments by recruiting near tissue cells and bone marrow derived cells. We have utilized these microenvironments to observe DTC progression from a single cell to an overt metastasis. Here, we report a new strategy to create tissue-specific microenvironment by altering the implantation site of porous biomaterials. In addition to subcutaneous implantation, porous scaffolds were inserted between liver lobes and within the intestinal mesentery. After 4 weeks *in vivo*, histological characterization confirmed recruitment of near tissue cells and significantly different immune cell profiles. Circulating tumor cells homed equally to the different implants, however metastasis was enhanced in scaffolds

implanted subcutaneously. High fibronectin and neutrophils in the subcutaneous scaffold microenvironment were identified as potential biomarkers of premetastatic niche signature, aligning with literature. We anticipate further microenvironment analysis using tissue engineered DTC niches may improve mechanistic understanding of metastatic development for the benefit of patient health.

2.2 Introduction

More than 90% of cancer-associated death is caused by metastasis. Circulating tumor cells released from a primary tumor disseminate into distal tissues where they often lay dormant until their surrounding microenvironments become favorable for re-growth. In theory, circulating tumor cells can disseminate into a wide variety of tissue sites but subsequent metastatic relapse occurs non-randomly. Regardless of primary tumor types, metastasis frequently occurs in brain, liver, lung, and bone. Metastasis seldom takes place in skin, intestine, and muscle. Even with this knowledge it is challenging to predict the eventual site of metastasis. Genetically distinct metastasis can also arise simultaneously in multiple organs. Thus, it is imperative to understand common mechanisms across metastasis-prone organs and identify key differences among supportive and restrictive niches to develop therapies that reduce the burden of metastasis and maintain disseminated tumor cells (DTCs) in an inactive state.

Mouse models are a critical tool for studying metastasis. Syngeneic, xenogeneic, and genetically engineered models are all limited by differences in their metastatic pattern compared to humans. The lung is a dominant site for metastasis while only a fraction of DTCs become metastases in the liver, bone, and brain. While these limitations can be addressed by directly injecting into target organs, the fidelity of these models is not clear.

There is a need for better models to study metastasis in mice in a variety of tissues. Recently, tissue engineering strategies have been exploited to address these limitations. Ectopic formation of bone containing human cells has had widespread success in recruiting human tumor cells in humanized mice. Additionally, several groups have identified the ability of implantable synthetic polymer biomaterials to recruit circulating tumor cells released from a primary tumor. Although there are reports of this phenomenon happening in both the subcutaneous and intraperitoneal cavity, the fate of the DTCs homed to implants located different anatomical sites has not been further investigated. Ultimately, the ability to monitor DTCs long-term has been challenging due to lethal tumor burden in the host. We have previously leveraged the ectopic nature of these DTC-containing niches and transplanted them to tumor-free mice for long-term observation and identified important niche components during evolution of early metastases.

Here we report a comparative analysis of tissue development, CTC recruitment, and DTC proliferation in inverted colloidal crystal (ICC) hydrogel scaffolds implanted in three different anatomical locations. ICC geometry is characterized by a three-dimensional structure consisting of interconnected ordered spherical pores. Polyacrylamide ICC scaffolds have shown robust and reproducible vascularized tissue formation and the ability to capture CTCs and monitor their eventual metastatic outgrowth when implanted in a subcutaneous pocket. During the foreign body response local and systemic cells are recruited to initiate a wound healing response. We hypothesized that implantation in different anatomical locations may capture unique local signatures that may alter the metastatic potential of the tissue. Due to surgical restrictions, expansion of implant locations was limited to the intraperitoneal cavity. The liver and intestinal mesentery were

selected because of their rich vascularization and differing natural metastatic potential. Unique tissue microenvironments were developed at each of the implant sites, and the metastatic potential of each niche was assessed using an MMTV-PyMT spontaneous breast tumor model. We envision that this side-by-side comparative biomaterial strategy will open the door to future study of local and systemic factors that influence metastasis development in a standardized manner.

2.3 Results

2.3.1 Implantation of ICC scaffold in subcutaneous, hepatic, and mesentery sites generates unique tissue microenvironments

ICC scaffolds are fabricated with a sacrificial bead-based template to produce a highly ordered porous matrix **(Figure 2.1A)**. In this study scaffolds were fabricated with polyacrylamide surface treated with rat tail collagen. Previous studies have identified scaffolds consisting of an average pore diameter of 300 ± 15 μm to have robust and reproducible tissue infiltration and vascular density[101]. Scaffolds were implanted in a dorsal subcutaneous pocket, sandwiched between the median and left caudate lobes of the liver, and wrapped within the small intestine in contact with the mesentery **(Figure 2.1B)**. Gross images of the scaffolds revealed recruitment of large blood vessels and infiltration of local tissue cells, embedding the scaffolds within their local microenvironment **(Figure 2.1C)**. Histological analysis was performed on the scaffolds at 1, 2.5, and 4 weeks post implantation **(Figure 2.1D)**. Implants followed a similar pattern of tissue infiltration: extracellular matrix polymerization, initial cellular infiltration, followed by complete tissue infiltration. Interestingly cells infiltrated the liver scaffold faster than subcutaneous and

intestine scaffolds. Hepatocyte tissue infiltration was also observed on the outermost pores of the liver scaffold.

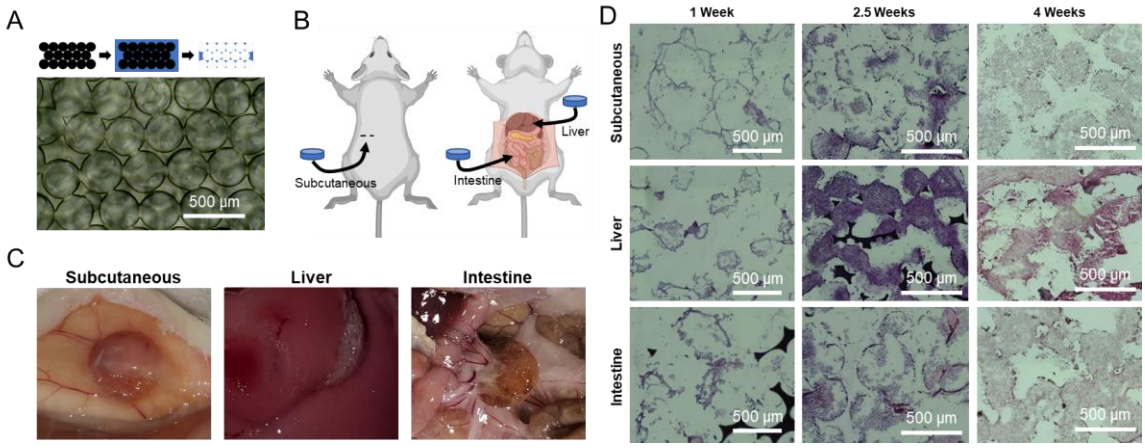

Figure 2.1. Tissue development within the pores of ICC hydrogel scaffolds implanted in different anatomical locations.
a, Fabrication schematic and brightfield image of ICC hydrogel scaffold. **b**, Schematic of implant locations. **c**, Gross images of ICC hydrogel scaffolds in subcutaneous, liver, and intestine sites four weeks after implantation. **d**, Hematoxylin and eosin staining of scaffolds implanted in different sites 1, 2.5, and 4 weeks after implantation.

2.3.2 Fibronectin and Ly6G rich microenvironments develop in subcutaneous implants

Scaffolds implanted for four weeks were screened with a panel of antibodies to evaluate the cellular and molecular components of the niche. Immunohistostaining was performed on scaffolds removed from the subcutaneous, liver, and intestine microenvironments **(Figure 2.2A)**. Cell markers, αSMA (myofibroblasts), CD31 (endothelial cell), Ly6G (neutrophils), F4/80 (macrophages), CD3 (T-lymphocytes), CD19 (B-lymphocytes), and molecular markers, fibronectin and MMP9, were selected to assess the local vasculature, immune, and tissue remodeling activity. Tissue development within each of the niches was significantly different from one another. Notably Ly6G and fibronectin were significantly increased in subcutaneous implants and MMP9 was

significantly higher in implants located near the liver **(Figure 2.2B)**. These results demonstrate that unique cellular and molecular microenvironments can be generated by changing the location of an implant.

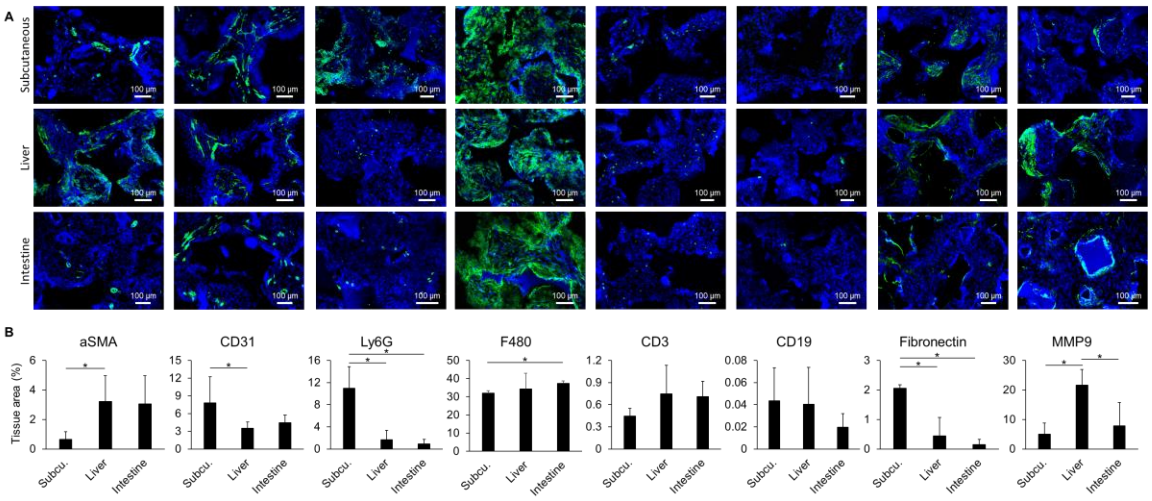

Figure 2.2. Immunohistological analysis of cellular and molecular niche components in subcutaneous, liver, and intestine implants.
a, Immunohistostaining comparison of ICC hydrogel scaffolds implanted in different anatomical locations. **b,** Quantitative analysis of immunohistostaining images (*P<0.05)**.**

2.3.3 Bone marrow derived cells are recruited to ICC implants

During the wound healing response bone marrow derived cells are activated and enter circulation to home to sites of inflammatory signaling. Parallels can be drawn between the inflammatory response that occurs at the site of a foreign object and that of a premetastatic niche. Previous studies with ICC scaffolds revealed the recruitment of bone marrow progenitor cells at the site of implantation, however the extent of other bone marrow derived cells was not investigated[97]. We hypothesized that bone marrow cells may be recruited to implants differently depending on the implant location. To test this hypothesis, we generated a chimeric mouse by performing a bone marrow transplant using eGFP bone marrow cells injected into a lethally irradiated C57BL/6 mouse. The bone

marrow was regenerated for 3.5 weeks before implantation of ICC hydrogel scaffolds in the subcutaneous, liver, and intestinal spaces **(Figure 2.3A)**. Three weeks after implantation scaffolds were removed and cryosectioned to assess the eGFP cell population **(Figure 2.3B)**. All implants recruited bone marrow derived eGFP^{+} cells, however liver implants had significantly higher tissue area coverage than implants in the subcutaneous and intestinal niches **(Figure 2.3C)**. The increase in bone marrow derived cells may correlate to the increased MMP9 secretion observed in the liver implants since MMP9 is believed to be secreted specifically from bone marrow cells and not local stroma[121].

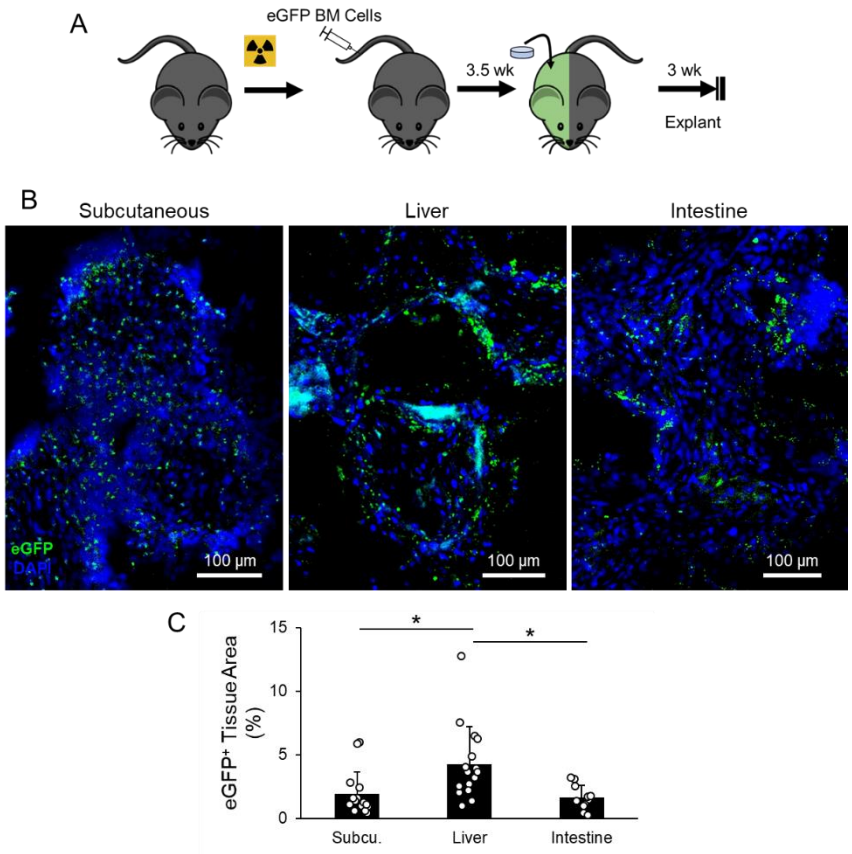

Figure 2.3. eGFP bone marrow cell recruitment to implantable biomaterial niches. **a,** Experimental schematic of eGFP bone marrow chimeric mouse generation and scaffold implantation. **b,** Fluorescent microscopy imaging of ICC hydrogel scaffolds for endogenous eGFP and DAPI. **c**, Quantitative image analysis of eGFP positive area in scaffold tissue (*P<0.05).

2.3.4 Circulating tumor cell recruitment comparable

Next, we examined the ability for the three different niches to recruit circulating tumor cells. A MMTV-PyMT spontaneous breast cancer model on the FVB background was used to generate CTCs in scaffold bearing mice. The MMTV-PyMT model was chosen because it is known to generate metastases and closely follow tumor progression observed in patients. Scaffolds were implanted at 4 weeks of age to maximize the CTC capture window. Eight weeks after implantation scaffolds were removed and analyzed via immunohistostaining **(Figure 2.4A)**. Both single DTCs and small metastatic colonies were observed in scaffolds regardless of implantation site **(Figure 2.4B)**. Quantification of DTCs revealed no significant difference in recruitment in the scaffolds from each of the tissues **(Figure 2.4C)**. In this analysis small colonies were considered a singular DTC event. DTCs were found as colonies more frequently in subcutaneous and intestine scaffolds compared to liver scaffolds. Analysis of the proliferative status of the DTCs revealed 6.7% (2/30), 7.8% (4/51), and 15.4% (4/26) were Ki-67^{+} in subcutaneous, liver, and intestine implants, respectively.

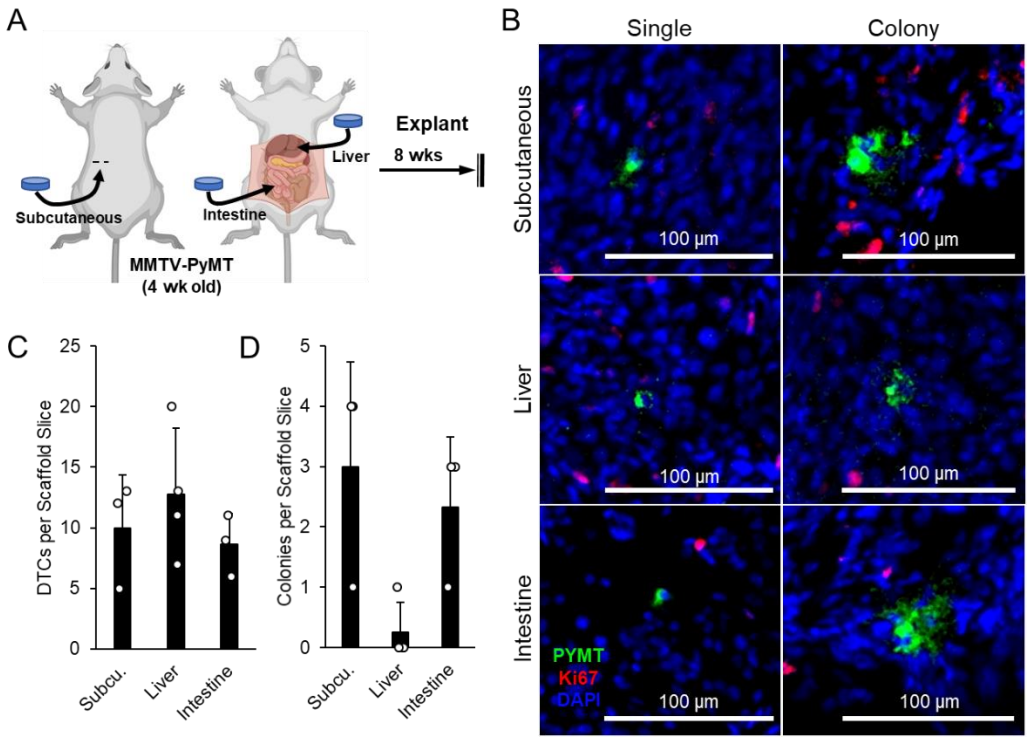

Figure 2.4. Tumor cell recruitment to ICC hydrogel scaffolds in an MMTV-PyMT spontaneous breast cancer model.
a, Experimental schematic of implantation strategy in MMTV-PyMT mice. **b,** Immunohistostaining of scaffold tissue reveals single DTCs and small micrometastases in subcutaneous, liver, and intestine scaffolds. **c,** Quantitative image analysis of DTC number in a single cryosection slice. **d,** Quantitative assessment of tumor colony number in a single cryosection slice.

2.3.5 Metastasis accelerated in subcutaneous microenvironment

Due to the high primary tumor burden in MMTV-PyMT mice, the maximum duration of scaffold implantation was limited to approximately 8 weeks. To prolong the observation window scaffolds were orthotopically transplanted into syngeneic tumor-free FVB mice **(Figure 2.5A)**. The implants were left in the mice for 5 weeks before they were removed for immunohistostaining. Single DTCs and tumor colonies were observed in all implants regardless of location **(Figure 2.5B)**. There were no significant differences in the number of DTCs or colonies in the implants **(Figure 2.5C and 2.5D)**. However, colonies in the subcutaneously implanted scaffolds were the only ones to become large proliferative colonies **(Figure 2.5E)**. These data suggest that unique microenvironments with different metastatic potential were generated by simply changing the site of the implanted ICC scaffold.

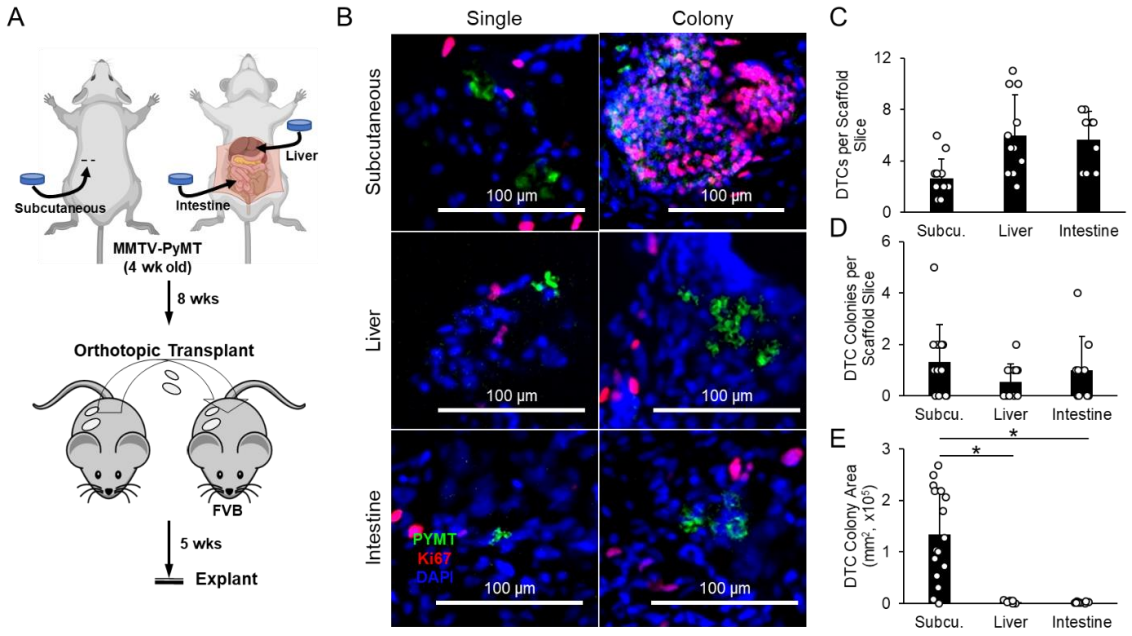

Figure 2.5. Investigation of DTC outgrowth in different anatomical locations.
a, Experimental schematic of transplantation model to extend experimental duration for the observation of DTC growth. **b,** Immunohistostaining of single DTCs and colonies in

scaffold niches. **c**, Quantitative analysis of DTC number in single cryosectioned tissue slice. **d,** Image analysis of tumor colony number in subcutaneous, liver, and intestine scaffolds. **e**, Quantitative analysis of tumor colony size in different scaffold tissues (*P<0.05).

2.4 Discussion

In vivo tissue engineered metastasis models have become an exciting area of research to probe hypotheses that traditional mouse models are inadequate to perform. For example, the generation of humanized ectopic bone has enabled the study of human cancer in a human bone-relevant microenvironment. Previously, we have demonstrated the potential of a porous ICC hydrogel scaffold to capture the long-term progression of DTCs and their local niche. Here we have provided a comprehensive analysis of the tissue formation, tumor cell recruitment, and DTC growth of three different tissue engineered niches generated by changing the implantation site of ICC hydrogel scaffolds. Although the scaffold microenvironment is driven by the foreign body response to the material, we found that the anatomical location drove unique tissue formation. Subcutaneous implants were characterized by high neutrophil recruitment and fibronectin. Liver and intestine scaffolds were similar in all markers analyzed except for MMP9, which was the highest in liver scaffolds. Interestingly bone marrow derived cells homed to the liver implants more than any other implant. Deeper analysis of the cellular niche via single cell RNA sequencing may provide additional information about the niche and reveal more intricate differences between the cellular populations.

Although it is believed that tissue engineered scaffolds enable metastatic tumor growth via premetastatic niche formation it has not been fully explored mechanistically.

Premetastatic niches are formed via systemic signaling derived from the primary tumor activation of bone marrow cells and priming of the local stroma to increase fibronectin secretion. Recruited bone marrow cells induce tissue remodeling by secreting matrix metalloproteinases. The foreign body response naturally induces several of these pathways without the need for priming by a primary tumor, including soluble fibronectin polymerization and recruitment of bone marrow derived cells. Here we provide evidence that metastatic growth in scaffold niches required fibronectin and Ly6G cells which were elevated in subcutaneous implants. Examination of the scaffold microenvironments over time may provide additional markers that correlate with metastatic niche development. The ability to tune the microenvironments by seeding engineered or tissue specific stromal cells onto the scaffolds prior to implantation may enable further mechanistic understanding of premetastatic niche development. Additionally, further examination of metastasis resistant scaffold niches may provide clues for keeping DTCs in a dormant state.

The results presented here demonstrate a new approach to engineer tissue microenvironments to study DTC biology and biomarkers for metastatic relapse. By utilizing a standardized ICC hydrogel scaffold reproducible tissues were generated and used for side-by-side analysis. This platform represents a high degree of control and tunability in tissue formation to address emerging hypotheses. Future studies may examine the role of biomaterial composition and physical features such as pore size have on driving tissue development. We believe this biomaterial driven approach will be an important tool in achieving mechanistic understanding of DTC behavior and yield therapies effective against metastasis.

2.5 Materials and Methods

All chemicals and materials were purchased from Sigma Aldrich or Fisher Scientific unless specified. All animal procedures were approved by the Institutional Animal Care and Use Committee at the University of Massachusetts-Amherst.

2.5.1 Porous hydrogel scaffold fabrication

ICC hydrogel scaffolds were fabricated as previously described[101]. Soda lime glass beads were sorted using an Advantech Sonic Sifter using 250 μm and 300 μm collection trays. Glass beads dispersed in deionized (DI) water were loaded into a 8 x 35 mm glass vial to a height of 2 mm. Vials were transferred to an oven set to 60 °C to remove the water. A glass template was made by annealing the beads in a 664 °C furnace for 4 hours. The annealed glass bead templates were infiltrated with a hydrogel precursor solution via centrifugation. The precursor solution was composed of 30 wt% acrylamide monomer, 1.5 wt% bis-acrylamide crosslinker, 0.2 vol% N,N,N',N'-tetramethylethylenediamine accelerator, and 0.2 vol% 2-hydroxy-2-methylpropiophenone photoinitiator in nitrogen purged DI water. The precursor solution was polymerized under a 15 W ultraviolet light source for 15 minutes. Glass beads were selectively dissolved in alternating washes of hydrofluoric and hydrochloric acid. Scaffolds were thoroughly washed with DI water to remove residual acid and lyophilized. Cracked or misshapen scaffolds were removed before proceeding. Scaffolds were sterilized with 70% ethanol and the scaffolds were surface treated with Sulpho-SANPAH to covalently crosslink rat-tail collagen. Scaffolds were stored at 4 °C in sterile phosphate buffered saline.

2.5.2 Mouse colony

MMTV-PyMT mice on the FVB/N background (002374) and eGFP mice on the C57BL/6 background (006567) were bred in house from a colony initially obtained from the Jackson Laboratory. Wild type FVB/N were acquired from MMTV-PyMT breeding and C57BL/6 (000664) mice were purchased from the Jackson Laboratory. Mice were housed in sterile conditions with unrestricted access to food and water.

2.5.3 Surgical implantation of scaffolds

Mice used in this study were between 4-8 weeks old at the time of implantation. Mice were anesthetized with 2% isoflurane before removing the dorsal and ventral hair with electric clippers and Nair. The skin was sterilized using 70% isopropyl alcohol prep wipes. Mice received 2 mg meloxicam/kg mouse weight subcutaneously prior to surgery. For subcutaneous implants a pocket was created by making a 2 mm horizontal incision in the dorsal space followed by expansion of surgical scissors into the incision and expansion. The implant was placed into the pocket and the incisions were closed with Reflex 7 mm wound clips. For liver and intestine implants, a 10 mm vertical incision was made in the lower abdomen and scaffolds were placed between the median and left caudate lobes of the liver,and wrapped within the small intestine in contact with the mesentery. The muscle layer was sutured and with polyglycolic acid sutures (Henry Schein), and the skin was closed with wound clips.

2.5.4 Frozen tissue preparation and sectioning

At the conclusion of the *in vivo* experiment, implants were frozen by embedding the tissue in Cryomatrix ^{TM} and snap-frozen in 2-methylbutane cooled on dry ice. Frozen

tissue was cut to 20 µm using a NX70 Cryostat. Frozen tissue blocks and sectioned slides were stored at -80 °C.

2.5.5 Histology

Hematoxylin and eosin staining was performed by fixing frozen tissue sections with 10% neutral buffered formalin for 10 minutes. After washing with DI water, sides were transferred to hematoxylin for 30 seconds. Slides were then washed with DI water until dye was no longer present in the effluent and then transferred to eosin Y for 45 seconds. Slides were serially dehydrated in 70, 85, and 100% ethanol before xylene. Samples were mounted in Shandon-Mount and covered with a glass cover slide. Images were taken with a color camera on an EVOS FL Auto microscope.

For immunohistostaining, frozen slides were fixed in -20 °C acetone for 10 minutes. Slides were washed with PBST solution 3 times before blocking in a solution containing 10% normal goat serum, and 1% bovine serum albumin for 1 hour. Following blocking primary antibodies diluted in blocking solution were added to the slides and left in a humidified chamber overnight at 4 °C. Slides were washed 3 times with PBST and then incubated with secondary antibodies diluted in blocking solution for 2 hours at room temperature. Prior to imaging, slides were washed 3 times in PBST and stained with a 10 ng/uL solution of DAPI. Fluorescent images were taken on a Zeiss Cell Observer SD. A-smooth muscle actin (ab5694), CD31 (550274), Ly6G (557445), F4/80 (565409), CD3 (550277), CD19 (550284), fibronectin (MA5-11981), MMP9 (PA513199), PyMT (ab15085), and Ki67 (ab16667) primary antibodies and anti-rabbit Alexa Fluor Plus 488 (A32731), anti-rat Alexa Fluor 647 (A21247), anti-hamster Alexa Fluor 488 (A21110),

and anti-mouse Alexa Fluor 660 (A21054), and anti-mouse Alexa Fluor 555 (A21424) secondary antibodies were used in this study.

2.5.6 Bone marrow transplantation

C57BL/6 mice were lethally irradiated with two doses of 6 Gy, four hours apart, from a cesium source. Twenty-four hours later, 20 x 10^6 bone marrow cells isolated from eGFP mice were intravenously injected. Engraftment was verified by microscopy for the presence of eGFP cells in blood collected via needle stick in the tail. Mice were given acidified antibiotic water (20 μg/mLtrimethoprim, 100μg/mL sulfamethoxazole, pH=3) for the duration of the experiment.

2.5.7 Orthotopic scaffold transplantation

Scaffolds were harvested from MMTV-PyMT mice and immediately transplanted to the same anatomical site in tumor-free FVB mice. The method for implantation was the same as initial surgery.

2.5.8 Image Analysis

All image processing and quantitative analysis was performed in ImageJ. Total tissue area was determined using the DAPI image for all relevant analysis. DTC counts were tabulated by assuming small colonies were formed from a single DTC.

2.5.9 Statistics

Unpaired Student's t tests were performed for comparison of the mean values between two groups. Statistical significance was determined if $p<0.05$ for two-tailed analysis. All quantitative data represent mean and standard deviation.

CHAPTER 3

SCAFFOLD-ASSISTED ECTOPIC TRANSPLANTATION OF INTERNAL ORGANS AND PATIENT-DERIVED TUMORS

Adapted with permission from Ryan Carpenter, Hye Jeong Oh, In-Hye Ham, Daeyoung Kim, Hoon Hur, and Jungwoo Lee. *ACS Biomaterials Science & Engineering*. **2019** 5(12), 6667-6678. DOI: 10.1021/acsbiomaterials.9b00978.

3.1 Abstract

Xenotransplantation of human tissues into immunodeficient mice has emerged as an invaluable preclinical model to study human biology and disease progression and predict clinical response. The most common anatomical site for tissue transplantation is the subcutaneous pocket due to simple surgical procedures and accessibility for gross monitoring and advanced imaging modalities. However, subcutaneously implanted tissues initially experience a sharp change in oxygen and nutrient supply and increased mechanical deformation. During this acute phase of tissue integration to the host vasculature, substantial cell death and tissue fibrosis occurs limiting the engraftment efficiency. Previously, we demonstrated the implantation of inverted colloidal crystal hydrogel scaffolds triggers pro-angiogenic and immunomodulatory functions without characteristic foreign body encapsulation. In this study we examine the use of this unique host response to improve the ectopic transplantation of tissues to the subcutaneous site. Scaffold-assisted tissues preserved morphological features and blood vessel density compared to native tissues, whereas Scaffold-free tissues collapsed and were less vascularized. Notably, the supporting biomaterial scaffold modulated the foreign body response to reduce localization of $Ly6G^+$ cells within the transplanted tissues. Co-transplantation of patient-derived gastric

cancer with a scaffold resulted in a comparable level of engraftment to conventional methods, however detailed immunehistological characterization revealed significantly better retention of proliferative cells ($Ki67^+$) and human immune cells ($CD45^+$) by the end of the study. We envision that leveraging the immunomodulatory properties of biomaterial interfaces can be an attractive strategy to improve functional engraftment of xenotransplants and accelerate individualized diagnostics and the development of novel therapeutic strategies.

3.2 Introduction

Mice have been used as an important model to understand the basic biology of health and disease and serve as a vital link in the preclinical development of therapies for human diseases[122-126]. The development and advancement of immunodeficient mouse models has enabled the xenotransplantation of human cells and tissues, significantly improving the clinical relevance of animal studies[127]. For example, xenotransplantation of human tumor cell lines, patient-derived immune cells, fetal tissue, organoids, and tumor fragments have been performed to understand human cell and tissue biology in health and disease[128-134]. In particular, patient-derived xenograft (PDX) tumor models have demonstrated their capability to reflect the human tumor microenvironment, predict patient response to chemotherapy, and accelerate discovery and validation of preclinical drugs[135-138]. A co-clinical trial in small lung cell cancer patients and corresponding PDX models showed consistency in responsiveness to cisplatin therapy, demonstrating the screening potential of PDX models[139]. Nevertheless, the fidelity, stability, engraftment efficiency, and engraftment kinetics of PDX tumors and mature tissues remain critical barriers to overcome for practical application[140]. For example, PDX models frequently fail to progress

to form metastatic lesions in mice[141]. Additionally, engraftment rates range widely between studies, from 10% to 95% depending on tumor type, and the time to reach initial engraftment can take several months to establish proliferative tumors[130].

Orthotopic transplantation of human tissues or tumors is most desirable but often limited by notable size difference between mouse and humans, and technical challenges to surgically access organs. The subcapsular region of the kidney is an attractive transplant site because of the richly vascularized environment, yet the small volume limits the size of transplanted tissues and requires technical expertise[142]. Alternatively, the subcutaneous space has been commonly used for transplantation because of the large tissue volume capacity, proximity to blood supply, simple surgical procedure and ease of accessibility for various imaging modalities[143-144]. However, engraftment efficiency of subcutaneously transplanted tissues remains suboptimal because of acute adaptation processes experienced by the donor tissue. First, the physical stresses beneath the skin caused by compressive forces from skin elasticity, and host motion can differ greatly from the donor tissue microenvironment[145-146]. This additional strain can cause soft tissue deformation and trigger abnormal mechano-transduction signaling[147]. Second, transplanted tissues suffer from limited oxygen and nutrient supply until blood vessels can reconnect to the host vasculature or neo-angiogenesis occurs. Delayed vascularization is accompanied by cell death and transformation of cellular phenotypes[148]. Third, the host wound response generates robust cellular recruitment from resident and systemic immune cells[149]. Acute local inflammation and fibrosis resultantly decreases donor tissue cell number and cellular heterogeneity as host cells infiltrate the graft and gradually replace donor tissue[150]. It is

imperative to develop strategies to overcome these acute detrimental effects on donor tissue to improve engraftment efficiency of current xenograft models to the subcutaneous space.

Accumulating data indicate that biomaterial implantation is a compelling route to modulate the host immune response[151-157]. Implant geometry, surface topology and chemistry, material composition, and bioactive delivery of drugs or cells have been explored to reduce fibrosis around implants and improve the longevity of biomedical devices[120, 158-161]. For example, implantation of medical grade polymers with circular, triangular, and pentagonal shaped cross sections revealed a circular rod had the lowest host response[162]. The degree of foreign body response against spherical biomaterials was shown to be modulated as a function of implant size[120]. Synthetic biomaterials composed of zwitterionic hydrogels that alternate positively and negatively charged functional groups significantly delayed the foreign body response and resultant fibrotic encapsulation[163]. Mechanical properties of synthetic zwitterionic hydrogels have been identified as a potent parameter to modulate the foreign body response after subcutaneous implantation[161]. Extracellular matrix scaffolds have shown to trigger a notably different pattern of local and systemic immune response compared to synthetic materials by switching from fibrotic encapsulation to wound healing and tissue repair mechanisms[164-165]. Hydrogels embedded with mesenchymal stem cells attenuated macrophage response and reduced fibrotic capsule thickness[166]. These results collectively indicate that implantable biomaterials represent an opportunity to modulate the fate of implanted human tissues to support better functional engraftment while retaining original tissue complexity.

In the presented work we hypothesized that an implantable biomaterial approach could be utilized to enhance the ectopic engraftment of mature tissue by improving

vascularization and altering the migration of immune cells. Furthermore, the biomaterial would act as a mechanical support to suppress mechanical deformation. We tested these hypotheses using inverted colloidal crystal (ICC) hydrogel scaffolds consisting of fully interconnected macroscale spherical pore arrays that have demonstrated mechanical robustness, and pro-angiogenic and immunomodulatory features after subdermal implantation[96-97, 101]. We first examined if co-implanted ICC hydrogel scaffolds promote the integration of liver and lung tissues retrieved from immunocompetent mice genetically engineered with DsRed fluorescent reporter protein to the immunodeficient NSG host mice. We also tested the impact of pre-seeded human bone marrow stromal cells (BMSCs) in ectopic tissue engraftment, which have been shown to further enhance angiogenesis and reduce inflammation[96-97, 101, 167]. Finally, we extended the study to examine the effects of stromal cell-seeded ICC hydrogel scaffolds on engraftment efficiency and cellular heterogeneity of human patient-derived gastric cancer samples. We envision this proof-of-concept study for biomaterial assisted ectopic tissue and tumor transplantation may improve the usage of mouse models for preclinical cancer research.

3.3 Results

3.3.1. Subdermal co-implantation of mature liver tissue within an ICC hydrogel scaffold reduces tissue deformation.

ICC scaffolds consist of an interconnected spherical pore array providing a high surface area-to-volume ratio and elicit a unique foreign body response that results in a vascularized tissue that does not undergo endogenous host rejection. We hypothesized that co-implantation of a mature tissue with an ICC hydrogel scaffold may improve the engraftment of transplanted tissues **(Figure 3.1a).** A 30 wt% polyacrylamide hydrogel

scaffold consisting of 300 ± 15 μm pores was used for this study, which has been shown to induce a richly vascularized tissue within 3 weeks of subdermal implantation[101]. To accommodate transplanted tissue samples, a cylindrical ICC scaffold (height = 2 mm and diameter = 6.5 mm) was modified by punching out a 3 mm diameter hole centrally. Human BMSCs were homogeneously seeded at a density of $5x10^5$ cells/scaffold **(Figure 3.1b)**. We employed DsRed immunocompetent mice as tissue donors and NSG immunodeficient mice as ectopic tissue recipients. Cells in DsRed mice ubiquitously express red fluorescence that facilitate rapid identification of surviving donor tissues in the recipient without staining. Immediately prior to surgery, a 3 mm piece of freshly harvested DsRed mouse liver tissue was collected using a biopsy punch and placed in the center of a scaffold prior to subcutaneous implantation. Three different groups of implants were used in the study, scaffold-free liver (Scaffold-free), unseeded scaffold-assisted liver (Blank-scaffold), and BMSC-seeded scaffold-assisted liver (BMSC-scaffold). Transplanted tissues were retrieved after one or two weeks of implantation **(Figure 3.1c).** Gross images of explanted tissue after 1 week implantation showed that the color of a liver tissue turned pale due to the significant loss of red blood cells whereas a liver tissue with a scaffold retained dark red color with a sign of vasculature **(Figure 3.1d)**. Hematoxylin and eosin (H&E) staining revealed that Blank-scaffold and BMSC-scaffold transplanted hepatic tissue retained morphological features present in native liver such as portal veins. A fibrotic capsule was observed around all sides of Scaffold-free transplants and the host-transplant interface of Blank-scaffold and BMSC-scaffold transplants. Interestingly, liver tissue at the interface of the biomaterial scaffold showed less fibrotic tissue formation **(Figure 3.1e-f)**. Characterization of albumin secretion via immunohistochemistry revealed maintenance of

liver function in all transplanted tissues **(Figure 3.2)**. We repeated the experiment with DsRed mouse lung tissue that has more than 25-fold weaker mechanical strength than the liver tissue [168]. The result revealed clear collapse of alveolar structures in Scaffold-free transplants **(Figure 3.3)**. Collectively these results indicate that co-implantation of mature mouse tissues with an ICC hydrogel scaffold better preserve intrinsic tissue structure by preventing tissue collapse and reduction of fibrotic capsule formation directly at the transplant interface compared to control scaffold-free transplants.

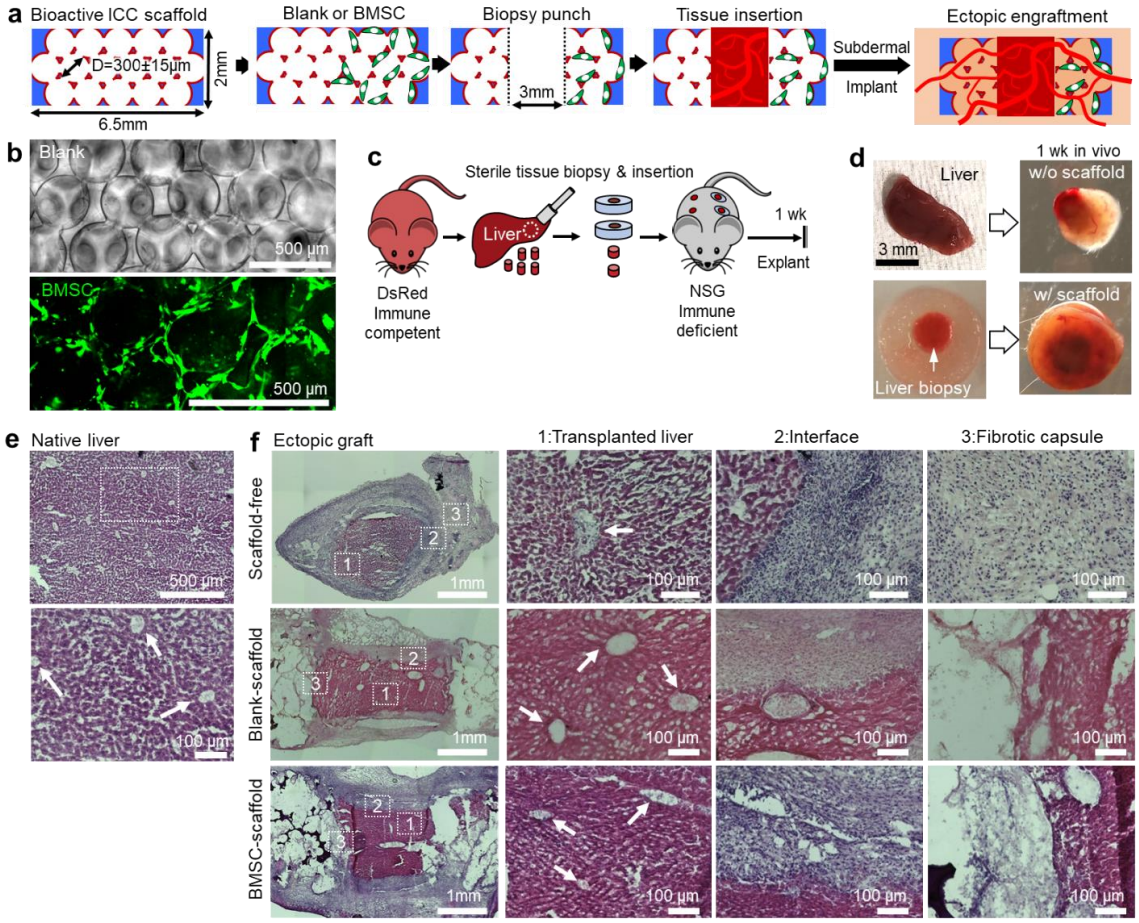

Figure 3.1. Scaffold-assisted transplants reduce tissue disruption.
a, Schematic of general strategy to improve ectopic engraftment of mature tissues using ICC hydrogel scaffolds. **b,** Representative brightfield (top) and fluorescence (bottom) microscopy images of ICC hydrogel scaffold pore structure and homogeneous seeding of fluorescently labelled hBMSCs on the surface of the scaffold pores. **c,** Experimental

schematic of DsRed mouse liver tissue transplantation into NSG immunodeficient mice with an ICC hydrogel scaffold. **d,** Gross images of a liver tissue and a liver tissue integrated with a hydrogel scaffold and after one week of subcutaneous transplantation. **e,** H&E images of native mouse liver tissue structure. **f,** H&E images Scaffold-free, Blank-scaffold, and BMSC-scaffold transplants after 1 week implantation. White arrows highlight large portal veins, a key anatomical structure in the liver**.**

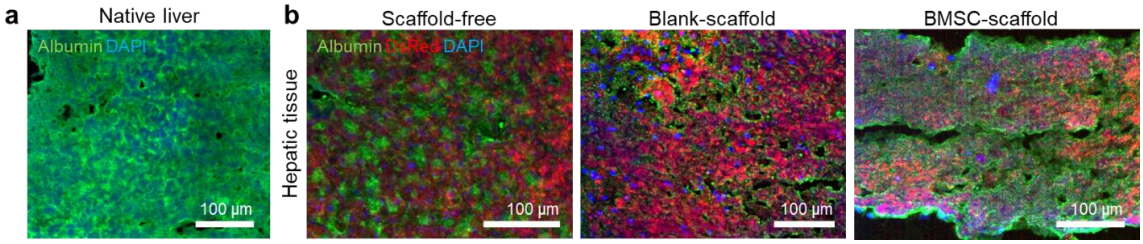

Figure 3.2. Albumin secretion in transplanted liver tissues.
a-b, IHS of mouse albumin in native liver **(a)** and transplanted liver tissues **(b)**.

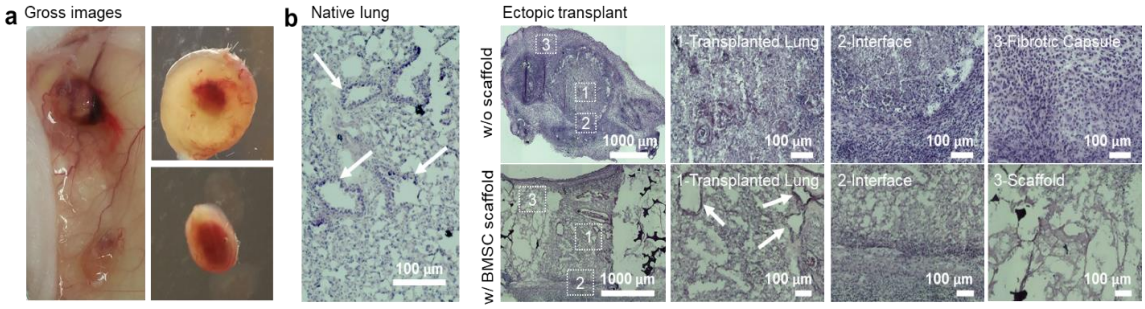

Figure 3.3. Ectopic engraftment of mature mouse lung tissue into NSG mice using ICC hydrogel scaffolds.
a, Gross images of ectopic subcutaneous lung tissue one week after transplantation. **b,** Low and high magnification images of mature lung tissue and transplanted tissues one week after transplantation. White arrows highlight large alveolar structures.

3.3.2. ICC hydrogel scaffold promotes vascularization to transplanted tissue.

We next examined if co-implanted ICC hydrogel scaffolds promote the formation of host blood vessels and vascular connection with the transplanted liver tissue. To validate functional vascular connection between transplanted liver tissue and the host, we intravenously perfused Evans Blue dye in mice carrying 1 week implants 20 minutes before sacrifice. Gross examination confirmed rich perfusion of Evans Blue dye in scaffold-assisted transplants whereas limited perfusion was evident in Scaffold-free transplants

(Figure 3.4a). Spatial distribution of the perfused dye was substantiated with IVIS fluorescent imaging. In scaffold-assisted transplants, strong fluorescence was localized to the area containing liver tissue **(Figure 3.4b)**. Quantitative analysis revealed scaffold assisted liver tissue implants showed at least 2.5-fold higher fluorescence signal than Scaffold-free implants. Blank-scaffolds showed 25% higher fluorescence than BMSC-scaffolds **(Figure 3.2c)**.

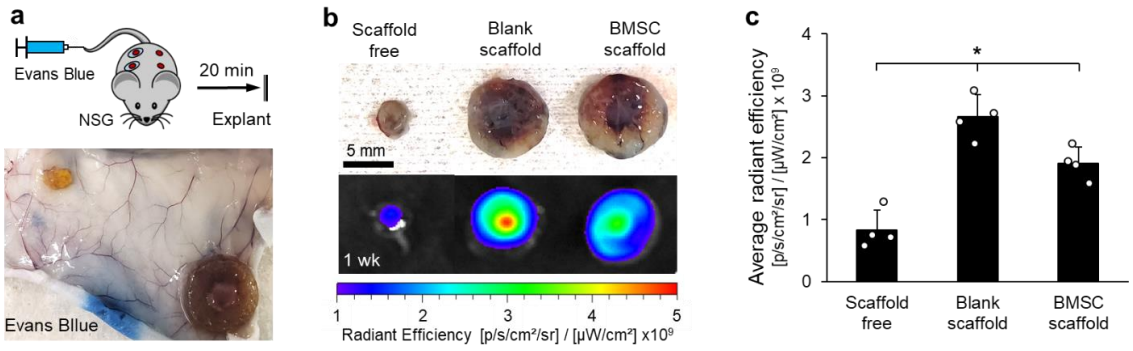

Figure 3.4. Characterization of vascular perfusion using Evans Blue.
a, Experimental schematic of Evans Blue perfusion experiment and gross image of transplanted liver tissue and surrounding subcutaneous tissue. **b,** Gross and fluorescent images of explanted tissues substantiating localized Evans Blue dye within transplanted liver tissue. **c,** Quantitative comparison of Evans Blue dye fluorescence in hepatic tissues one week after transplantation. (N=3 implants per group, *P<0.05)

Small sinusoidal blood vessels present in the transplanted liver tissues were visualized via endomucin antibody staining. In all transplants, intrinsic hepatic sinusoidal features were preserved. Blood vessels in the surrounding fibrotic capsule were less organized with branched morphology **(Figure 3.5a-d)**. Quantitative analysis of endomucin expression in the liver tissue revealed that the overlapping region of endomucin and endogenous DsRed fluorescence in BMSC-scaffolds was 63 % and 35 % higher compared to Scaffold-free and Blank-scaffold transplants, respectively **(Figure 3.5e)**. In the surrounding fibrotic tissue area, blood vessel density was significantly higher in scaffold

assisted transplants regardless of BMSCs and at least 2-fold higher than Scaffold-free controls **(Figure 3.5f)**. The discrepancy between Evans blue characterization and immunohistostaining results may be due to immature vasculature and increased leakiness in Blank-scaffold samples.

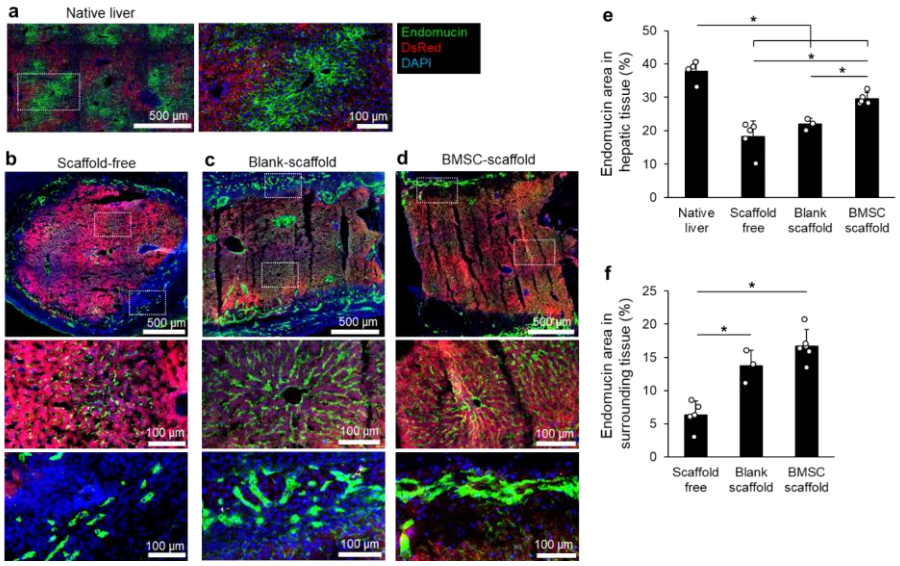

Figure 3.5. Vasculature staining in scaffold-free and scaffold assisted liver tissue. **a-d,** Immunohistostaining (IHS) images of native DsRed liver **(a),** Scaffold-free **(b),** Blank-scaffold **(c),** and BMSC-scaffold **(d)** transplanted tissues. Higher magnification images show hepatic sinusoids and newly generated blood vessels that surround the transplanted tissue. **e,** Quantitative comparison of endomucin^{+} hepatic sinusoid retention in ectopic tissue transplants. **f,** Quantitative comparison of endomucin^{+} blood vessel density in surrounding host tissue. (N=3-5 implants per group, *P < 0.05)

We further characterized vascular reconnection via injecting MDA-MB-231 human breast cancer cells that stably express eGFP into mice bearing transplanted liver tissues. Three days after injection, tissue was removed and analyzed for dissemination to the transplanted liver tissue **(Figure 3.6a)**. Imaging for endogenous eGFP disseminated tumor cells (DTCs) confirmed the presence of tail vein delivered human breast cancer cells in liver transplants in proximity to positively stained endomucin blood vessels **(Figure 3.6b)**. Scaffold-free tissues had significantly fewer DTCs compared to Blank-scaffold and

BMSC-scaffold hepatic tissues **(Figure 3.6c)**. Taken together these results demonstrated that BMSC-scaffolds improved preservation of intrinsic hepatic sinusoids and assisted in reaching stably reconnected vasculature compared to Scaffold-free and Blank-scaffold.

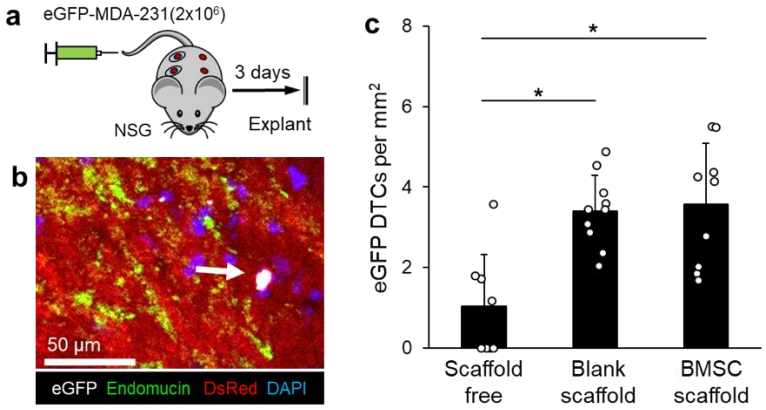

Figure 3.6. Circulating tumor cell dissemination to ectopic liver tissue.
a, Experimental schematic of functional vascular reconnection assay in scaffold-assisted ectopic transplant via intravenous delivery of human MDA-MB-231 cells. **b,** IHS of endogenous eGFP MDA-MB-231 cells, endomucin$^+$ hepatic sinusoids, and endogenous DsRed$^+$ hepatocytes. White arrow highlights DTC. **c,** Quantitative comparison of DTCs in transplanted liver tissues. (N=9 sections from 3 implants per group except Scaffold-free (N=2), *P < 0.05)

3.3.3. Biomaterial scaffold modulates innate immune cell migration.

Transplantation evokes a foreign body response, during which innate immune cells are recruited to the transplanted tissue and wound healing mechanisms act to resolve tissue disruption. We investigated the recruitment of mouse neutrophils and macrophages in the transplanted tissue microenvironments via IHS of Ly6G and F4/80, respectively (**Figure 3.7a-d)**. Ly6G$^+$ neutrophils are early responders in the foreign body response. Ly6G$^+$ cell infiltration was significantly higher in transplanted liver tissue compared to native liver regardless of the presence of a scaffold. However, Scaffold-free hepatic tissue had a 118-fold increase in Ly6G$^+$ cells over native tissue compared to 49-fold and 20-fold increase in Blank-scaffold and BMSC-scaffold groups, respectively. Samples collected two weeks

after transplantation had no significant differences in $Ly6G^+$ cell infiltration indicating potential resolution of acute response by $Ly6G^+$ cells. Interestingly, the surrounding tissue around Blank-scaffold and BMSC-scaffold transplants displayed a 10-fold and 21-fold increase in $Ly6G^+$ cells compared to Scaffold-free transplants after one week, respectively. The surrounding tissue of BMSC-scaffolds had the highest infiltration of $Ly6G^+$ cells one week after transplantation, however by week two the $Ly6G^+$ cell significantly decreased and was not significantly different from Scaffold-free and Blank-scaffold values **(Figure 3.7e).** Unlike neutrophils, macrophages are abundant in native liver tissue. Scaffold-free, Blank-scaffold, and BMSC-scaffold transplants contained at least 4-fold fewer $F4/80^+$ cells than native liver tissue. There were no differences in macrophage recruitment to the surrounding tissue in any of the experimental groups. The skewed distribution of $F4/80^+$ cells between the hepatic and the surrounding tissue remained in two weeks after transplantation **(Figure 3.7f)**. Examination of transplanted lung tissue in Scaffold-free and BMSC-scaffold transplants showed similar modulation of $Ly6G^+$ cell recruitment and macrophage response **(Figure 3.8)**. These results demonstrate that the presence of the scaffold altered the pattern of $Ly6G^+$ cell recruitment during the foreign body response, while increasing the vascular availability to the transplanted tissue **(Figure 3.7g)**.

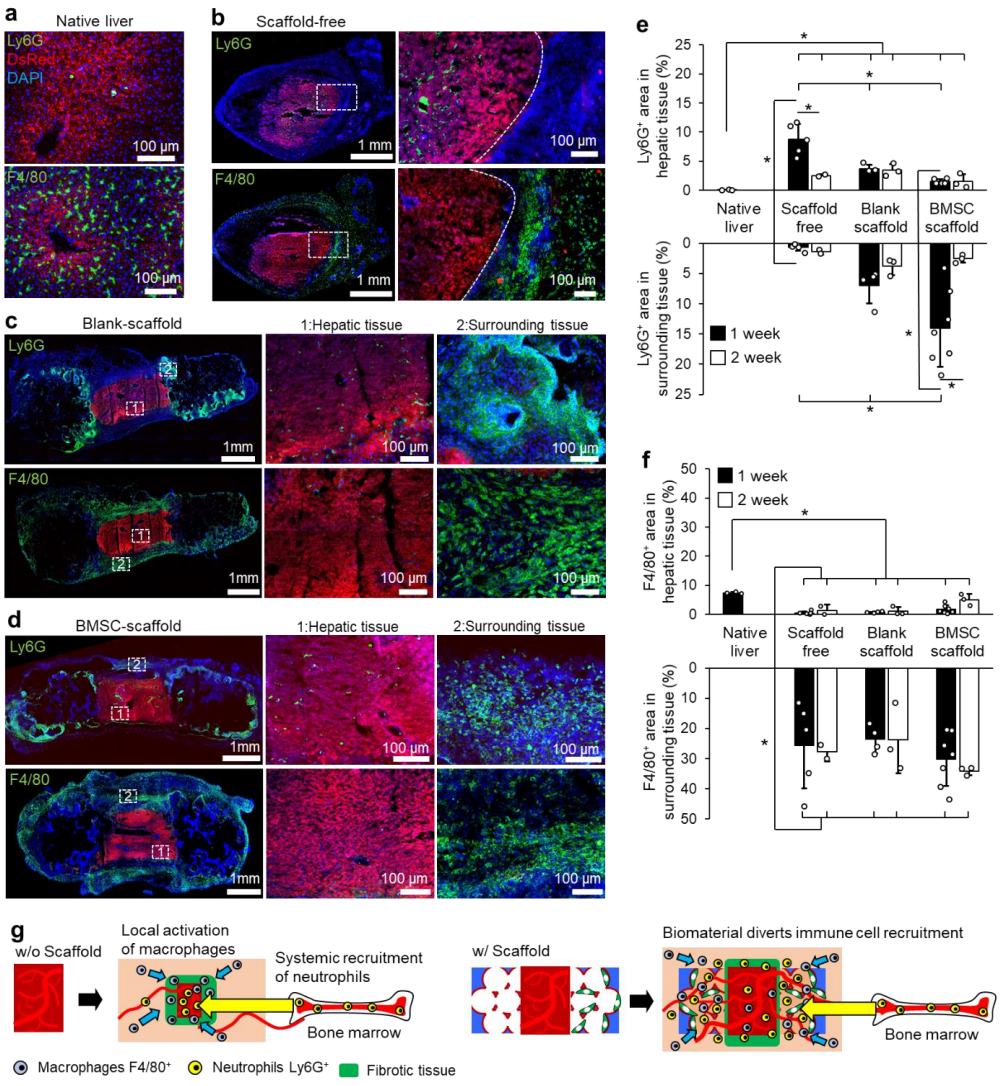

Figure 3.7. Scaffold derived immune modulation.
a-d, IHS images of Ly6G$^+$ neutrophils and F4/80$^+$ macrophages with nucleus (DAPI) and hepatic tissue (DsRed) in native **(a),** Scaffold-free **(b),** Blank-scaffold **(c),** and BMSC-scaffold **(d).** High magnification images show interface between hepatic tissue implant and host tissue. **e,** Quantitative comparison of Ly6G$^+$ neutrophil density in native liver tissue and ectopic tissue transplants and their spatial distribution between transplanted liver and surrounding biomaterials 1 and 2 weeks after transplantation. **f,** Quantitative comparison of F4/80$^+$ macrophage density in native liver tissue and ectopic tissue transplants and their spatial distribution between transplanted liver and surrounding biomaterials 1 and 2 weeks after transplantation. **g,** Proposed mechanism of improved ectopic tissue engraftment via pro-angiogenic and immunomodulatory scaffold that improves vascular reconnection while diverting immune cell recruitment to the biomaterial. (N=3-7 implants per group except Scaffold-free 2 week (N=2), *P < 0.05).

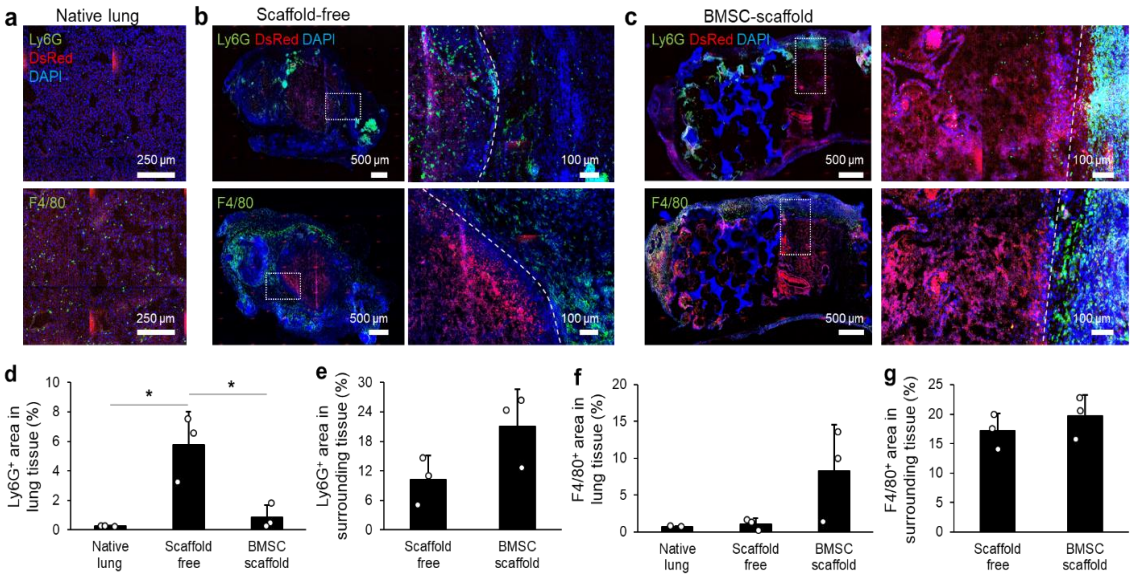

Figure 3.8. Immunomodulatory effects of ICC hydrogel scaffolds and immune cell migration on transplanted lung tissue.
a-c, IHS of $Ly6G^+$ and $F4/80^+$ cells within native DsRed lung **(a)** and transplanted lung tissue without **(b)** and with BMSC-seeded scaffold **(c)**. **d,** Quantitative analysis of $Ly6G^+$ distribution within transplanted tissue. **e,** Quantitative analysis of $Ly6G^+$ distribution in surrounding tissue. **f,** Quantitative analysis of $F4/80^+$ distribution within transplanted tissue. **g,** Quantitative analysis of $F4/80^+$ distribution in surrounding tissue. (N=3 implants, * $P<0.05$)

3.3.4. Scaffold-assisted transplantation of patient-derived gastric cancers aids maintenance of intrinsic tissue heterogeneity.

Next, we investigated the translational potential of scaffold-assisted xenotransplantation by transplanting seven human patient-derived gastric cancers into immunodeficient BALB/c nude mice. Patient-derived gastric cancer poorly engrafts when transplanted into immunocompromised mice with reported engraftment rates ranging from 15-28 %[169-171]. As with most PDX models, non-cancerous human cells are often lost during xenotransplantation into mice. We hypothesized that the co-implantation of patient-derived gastric cancers with a biomaterial scaffold would assist in tissue engraftment, and in doing

so maintain intratumoral cellular heterogeneity **(Figure 3.9a)**. To enhance the effect of the ICC scaffold, we seeded them with patient-derived cancer-associated fibroblasts (CAFs). CAFs have been documented to secrete numerous molecules that can stimulate cancer cells and non-cancerous cells in the tumor microenvironment[172-173]. The ICC scaffold described above was altered to accommodate larger tissue pieces by increasing the diameter to 12 mm while maintaining the same chemical composition, pore diameter and surface coating. Round, 2 cm pieces of gastric cancer tissue were removed from patients and stored in complete media with antibiotics. The tumor pieces were split into smaller 3-5 mm pieces, and then placed on top of the prepared scaffold. Scaffold material that exceeded the diameter of the tumor tissue was carefully removed using a razor blade. Placement on top of the scaffold rather than within the scaffold was chosen to increase the surface area between scaffold and PDX samples, increasing the effect of CAF-related soluble factors **(Figure 3.9b)**. One scaffold-assisted or scaffold-free tumor was implanted into 4-6 week old male BALB/c nude mice **(Figure 3.9c)**. In each PDX study, engraftment was checked after 2 weeks via palpation. If at least one tumor from the patient grew we continued the experiment for a maximum of 6 weeks **(Figure 3.9d)**. Engraftment was considered successful if tumors remained by the end of the study. At the end of the experiment mice were sacrificed and the samples were prepared for histological evaluation. Tumor morphology appeared to be conserved following transplantation in successfully engrafted tissues **(Figure 3.9e)**. Overall, 11 scaffold-free and 30 scaffold-assisted cancer pieces were transplanted into mice **(Figure 3.9f)**. The frequency of transplanted tumors that displayed incremental growth was slightly higher in scaffold-free xenografts than scaffold-assisted

xenografts (43.3% vs 36.4%) but statistical analysis using a logistic regression did not show a significant effect of scaffold on PDX engraftment (P=0.5965) **(Figure 3.6g)**.

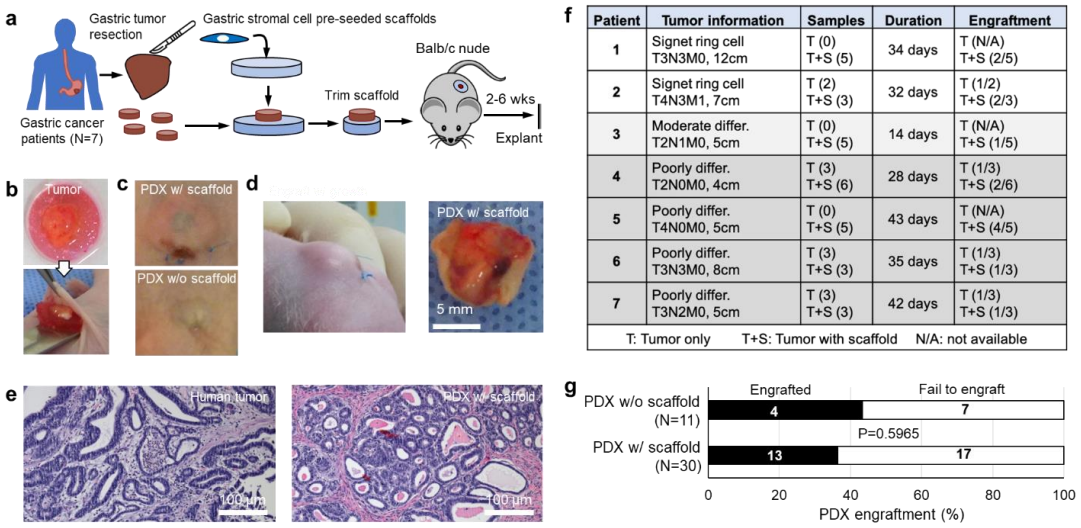

Patient	Tumor information	Samples	Duration	Engraftment
1	Signet ring cell T3N3M0, 12cm	T (0) T+S (5)	34 days	T (N/A) T+S (2/5)
2	Signet ring cell T4N3M1, 7cm	T (2) T+S (3)	32 days	T (1/2) T+S (2/3)
3	Moderate differ. T2N1M0, 5cm	T (0) T+S (5)	14 days	T (N/A) T+S (1/5)
4	Poorly differ. T2N0M0, 4cm	T (3) T+S (6)	28 days	T (1/3) T+S (2/6)
5	Poorly differ. T4N0M0, 5cm	T (0) T+S (5)	43 days	T (N/A) T+S (4/5)
6	Poorly differ. T3N3M0, 8cm	T (3) T+S (3)	35 days	T (1/3) T+S (1/3)
7	Poorly differ. T3N2M0, 5cm	T (3) T+S (3)	42 days	T (1/3) T+S (1/3)
T: Tumor only T+S: Tumor with scaffold N/A: not available				

Figure 3.9. Patient derived tumor transplantation.
a, Experimental schematic of scaffold-assisted human gastric tumor xenograft strategy. **b,** Gross images of scaffold-assisted patient gastric tumor biopsy and subcutaneous transplantation into Balb/c nude mice. **c,** Gross images of PDX implants beneath the skin with and without scaffold. **d,** Gross image of successful PDX engraftment and extracted sample with scaffold removed. **e,** Histological comparison of gastric tumor tissue structure between primary and PDX tumors with H&E staining. **f,** Table of patient tumor information, implantation duration and engraftment success. **g.** Summary of PDX engraftment with and without scaffold.

Multiple microenvironment (mLy6G, endomucin, alpha-smooth muscle actin), human tumor (hVimentin, hCytokeratin, hCD45, hCD44) and mitogenic (Ki67) markers were evaluated in scaffold-assisted and Scaffold-free tumor transplants **(Figure 3.10a)**. Alpha-smooth muscle actin (αSMA) is expressed by activated fibroblasts[174]. Vimentin and cytokeratin are mesenchymal and epithelial cell markers, respectively[175]. hCD45 is a pan-leukocyte marker, and hCD44 is a marker associated with cancer stem cells[176]. Tumors implanted with a scaffold had significantly more proliferative cells ($Ki67^+$), and human immune cells ($hCD45^+$) **(Figure 3.10b)**. There was no difference in other tumor related

markers between the two groups indicating scaffold-assisted transplantation did not negatively affect the tumor phenotype compared to control. Proliferative human immune cells (i.e. double positive Ki67 and hCD45) were rare in both scaffold-free and scaffold-assisted PDX transplants **(Figure 3.11)**. Taken together, IHS results demonstrate higher mitogenic and human immune cell activity in human tumors co-implanted with biomaterials compared scaffold-free controls.

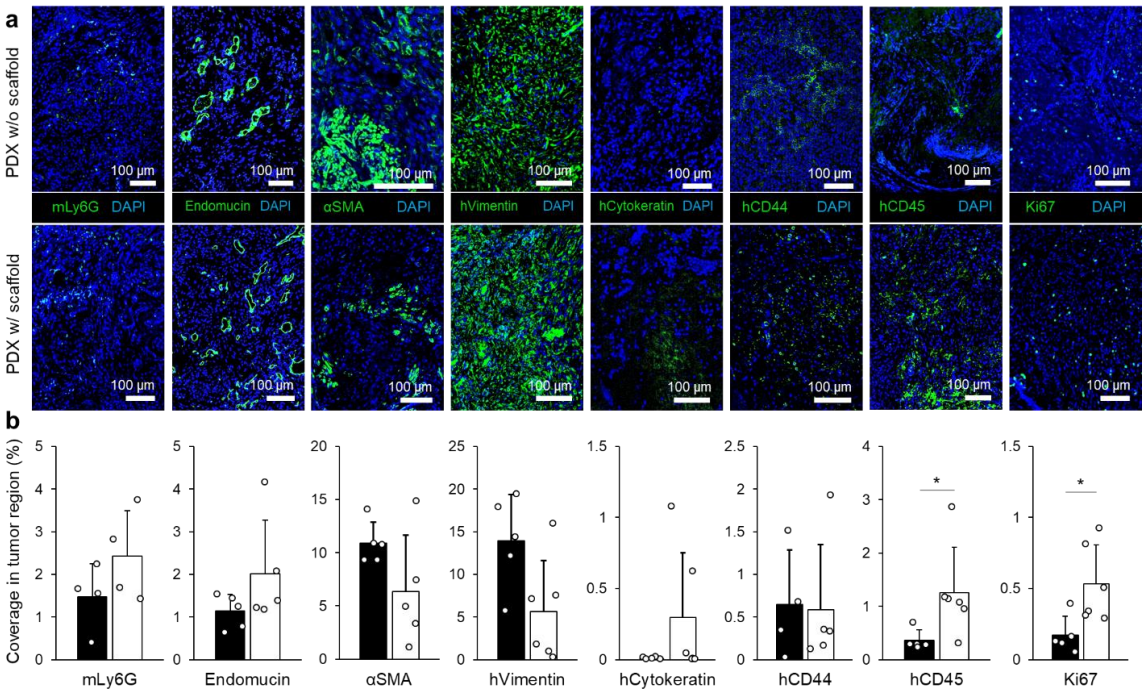

Figure 3.10. Histological analysis of PDX tissue.
a, IHS comparison of mouse cells, human cells, and mitogenic marker expression of patient-derived gastric tumor microenvironments engrafted without and with scaffolds. **b,** Quantitative comparison of each marker in PDX tumors transplanted without and with scaffold. (N=4-5 tumors per group, *P < 0.05)

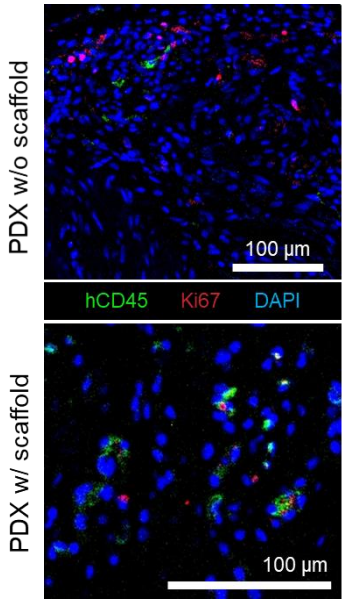

Figure 3.11. Proliferative status of hCD45 cells in PDX samples.
IHS of mitogenic status (Ki67) of tumor resident human immune cells (CD45) transplanted without and with scaffold.

3.4 Discussion

The ability to modulate the biomaterial-host immune response is an exciting enabling step in the realization of many biomedical technologies[154, 156]. For example, biomaterials have widespread success in modulating osteoblast and osteoclast activity during bone tissue repair[177]. Biomaterial encapsulation of islet cells has shown promise in being a functional treatment for diabetic patients[178]. Immunomodulatory nanomaterials have been developed to target inflammatory monocytes and alter lymph node activity *in vivo*[179]. Implantable biomaterial-based cancer vaccines take advantage of the influx of dendritic cells to boost the host immune response against cancer[180-181]. A removable biomaterial strategy after subcutaneous implantation leaves behind a fibrotic tissue pocket that has been exploited for islet cell delivery[143]. Implantable polymeric biomaterials that attract circulating tumor cells have shown the feasibility to reduce the risk of metastasis in vital organs[103-104]. The inversed spherical pore geometry of ICC hydrogel scaffolds directs

the formation of distinct inflammatory microenvironments, with a pro-inflammatory milieu at the pore surface and an immune-suppressive niche within the pore cavity[119]. This phenomenon enables enhanced vascularization with reduced fibrotic encapsulation while maintaining pro-inflammatory immune cell activity[116, 182-183]. Previously we exploited these features in creating humanized metastatic tumor microenvironments consists of human immune, stromal and tumor cells to study systemic investigation of humanized tumor microenvironment and identify critical events in metastatic relapse[96-97, 101]. In the present study, we demonstrate a new translational opportunity of biomaterials to improve ectopic and xenogeneic transplantation of tissues and tumors. The findings of this work can be leveraged to improve preclinical mouse models to better reflect human biology and disease.

A foreign body reaction is a physiological host response to a foreign object within the tissue, whereby the object is encapsulated with a fibrotic capsule, effectively sealing it off from the host[149]. We intended to exploit the angiogenic activity of the foreign body response to improve the transplantation of mature tissue into the subcutaneous space by co-implanting a porous biomaterial scaffold. The effects of this co-implantation strategy were three-fold. First, mechanical deformation of the transplanted tissue was minimized due to the structural stability of the scaffold. ICC scaffolds composed of at least 30 wt% polyacrylamide do not deform when implanted[101]. This property enabled the preservation of original tissue structures, maintaining tissue complexity and heterogeneity compared to collapsed Scaffold-free transplanted tissues. Second, increased inflammatory signaling due to the presence of the biomaterial scaffold modulated the recruitment of innate immune cells by attracting them to the biomaterial rather than within the transplanted tissue. Third,

implantation of biomaterials accelerated vascularization to the transplant by increasing pro-angiogenic signaling molecules such as molecules such as VEGF[184]. The pro-inflammatory and pro-angiogenic milieu generated by co-implanted biomaterial demonstrated a distinct advantage over scaffold-free transplants. The addition of hBMSCs on the surface of the ICC hydrogel scaffolds further enhanced the results of the scaffold-assisted approach. hBMSCs are known to secrete various immunomodulatory and angiogenic molecules[101, 167]. We have previously demonstrated hBMSCs can maintain secretory function after long-term (12 week) subcutaneous implantation[49]. The large surface area of ICC hydrogel scaffolds permits the accommodation of a high density of stromal cells. Seeding of tissue-specific stroma may provide further supportive functions to transplanted tissues.

Neutrophils and macrophages are innate immune cells that play an important role in inflammation, tissue remodeling, and fibrosis. As an early responder, neutrophils create an inflammatory environment through release of cytokines, chemokines, reactive oxygen species, and neutrophil extracellular traps (NETs)[185-186]. Release of reactive oxygen species and tissue digesting enzymes can be particularly disruptive and cause graft tissue damage[187]. However, neutrophil derived matrix metalloproteases and NETs have been implicated in enhancing angiogenesis[188-189]. Synthetic polymer scaffolds have been shown to elicit a strong immunological response compared to extracellular matrix scaffolds[155]. In the presented study scaffold-assisted samples have benefited from pro-angiogenic features of neutrophils without direct, potentially disruptive physical interaction. A recent report suggests that hBMSCs alter neutrophil response toward an immunosuppressive phenotype, which in the context of this study may have further enhanced the viability of transplanted tissues[190]. Our findings suggest hBMSCs were the cause of increased neutrophil

recruitment compared to biomaterial alone, but it is difficult to conclude if this was linked to the increase in angiogenesis. Further transient studies of neutrophils and biomaterial may elucidate their biological function. Macrophages are another important innate immune cell type in the foreign body response and secrete a variety of inflammatory signals that can lead to fibrotic encapsulation[191]. Here macrophages were predominantly localized to the surrounding tissues regardless of the presence of biomaterial. Interestingly, we observed a notable reduction in macrophages derived from donor liver tissue after transplantation, which is potentially due to a migratory response to the strong inflammatory signals in the surrounding tissue. The functional consequence of macrophage attrition in ectopically engrafted liver remains to be determined as tissue resident macrophages play diverse roles in liver function.

In the presented study we explored the application of scaffold-assisted transplantation to improve human PDX models in mice. Due to technical challenges, orthotopic transplantation of PDX tumors is rarely performed therefore subcutaneous implantation is primarily utilized. Although engraftment can still occur, the difference in the local stroma can change tumor behavior and growth. PDX models are also hampered by the rate of engraftment and overall engraftment efficiency. The rate of engraftment normally takes between 2-8 months before developing a preclinical model[130]. The efficiency of gastric cancer engraftment is also low, with over 70 % of xenografts failing to grow[169-171]. Finally, the local stroma of PDX models gradually becomes replaced with mouse cells, leading to a loss of heterogeneity which can skew preclinical testing and result in poor patient efficacy. Based on the ectopic mouse liver tissue transplant experiments we adjusted the strategy for the scaffold-assisted PDX model. First, we utilized nude mice,

which are only deficient in mature T cells to minimize the loss of immunological response on the tumor. A recent study showed that mice reconstituted with human immune progenitor cells prevented genetic drift within engrafted PDX tumors by better recapitulating the tumor microenvironment[133]. Second, we changed the configuration of biomaterial and transplant to increase the interface and subsequent effect of CAFs. The presence of CAFs seeded on the scaffold may have provided supportive cytokines and growth factors to resident human immune cells in addition to tumor cells to maintain a heterogeneous microenvironment. Although the presented results of gastric cancer engraftment were sub-optimal, as tumor engraftment between the two groups was comparable, detailed IHS characterization distinguished higher percentages of $hCD45^+$ and $Ki67^+$ cells within the tumor tissue in scaffold-assisted transplants compared to scaffold-free controls. We believe further exploration into biomaterial strategies of co-implantation with PDX tumors is warranted.

3.5 Conclusion

Our results demonstrate a new approach to aid in the transplantation of mature tissues to an ectopic, subcutaneous location. By leveraging the acute host response to biomaterial implantation, we improved vascularization while keeping potentially disruptive immune cells away from the transplant. The presented biomaterial strategy may be applicable for the xenotransplantation of human tissues such as the liver and lung potentially enabling the study of human disseminated tumors in the context of fully mature human tissues. Additionally, we have highlighted a modulatory effect on the tumor microenvironment of human gastric cancer PDXs via this co-implantation strategy. We anticipate this approach

is an important step in expanding the preclinical value of mouse models and achieve better understanding of human disease and the discovery of effective therapies.

3.6 Materials and Methods

All chemicals and materials were purchased from Sigma Aldrich or Fisher Scientific unless specified. All animal procedures were approved by the Institutional Animal Care and Use Committee at the University of Massachusetts-Amherst and Ajou University Medical Center. Patient-derived samples were approved by the institutional review board of Ajou University Hospital. Informed consent was received from all patients.

3.6.1 Porous hydrogel scaffold fabrication

Interconnected porous hydrogel scaffolds were fabricated as previously described[101]. Soda lime glass beads were sorted using an Advantech Sonic Sifter using 250 µm and 300 µm collection trays. The resulting beads had an average diameter of 275 ± 21 µm. Glass beads were dispersed in deionized water and gradually loaded into an 8 x 35 mm or 12 x 35 mm glass vial to a height of 2 mm. A dense lattice structure was achieved utilizing an ultrasonic water bath. Water was removed in a 60 °C oven prior to thermal annealing of the glass beads in a 664 °C furnace for 4 hours. The annealed glass bead templates were infiltrated with a hydrogel precursor solution via centrifugation. The precursor solution was composed of 30 wt% acrylamide monomer, 1.5 wt% bis-acrylamide crosslinker, 0.2 vol% N,N,N’,N’-tetramethylethylenediamine accelerator, and 0.2 vol% 2-hydroxy-2-methylpropiophenone photoinitiator in nitrogen purged DI water. The precursor solution was immediately polymerized under a 15 W ultraviolet light source for 15 minutes. The next day, excess hydrogel was removed by scraping the glass bead template with a razor blade on all surfaces. Glass beads were selectively dissolved in alternating

washes of an acid solution containing a 1:5 dilution of hydrofluoric acid in 1.2 M hydrochloric acid, and 2.4 M hydrochloric acid. Washes were performed on a shake plate and the solutions were changed every four hours until the beads were removed. Scaffolds were washed with DI water to remove residual acid and lyophilized. Cracked or misshapen scaffolds were removed before proceeding. Scaffolds were sterilized with 70% ethanol and the scaffolds were surface treated with Sulpho-SANPAH to covalently crosslink rat-tail collagen. Scaffolds were stored at 4 °C in sterile phosphate buffered saline.

3.6.2 Cell culture of hBMSCs and seeding onto ICC scaffold

Human bone marrow aspirates were acquired from Lonza and isolation was performed as previously described[101]. Cells were cryogenically frozen in media containing 10% dimethyl sulfoxide (DMSO). Cells were cultured with alpha modified, minimal essential medium (MEM) supplemented with 10% fetal bovine serum (FBS), 2% penicillin-streptomycin, 0.2% gentamicin, and 1 µg/L recombinant human fibroblast growth factor. Half a million hBMSCs were seeded onto partially dehydrated scaffolds and kept in culture for up to one week prior to use. hBMSCs were not used beyond passage 4 and media was changed every 3 days.

3.6.3 Sterile DsRed tissue collection and integration into hBMSC scaffold

A breeding pair of DsRed (005441) was obtained from Dr. Barbara Osbourne. Mice were housed in sterile conditions with unrestricted access to food and water. Mice used in this study were between 6-13 weeks old. DsRed mice were euthanized via carbon dioxide and the liver and lung tissues were harvested in a biosafety cabinet and kept in sterile phosphate buffered saline (PBS) over ice. A sterile 3 mm biopsy punch was used on the harvested liver and lung to generate tissue inserts. Additionally, a 3 mm hole was created

in the center of the hBMSC-seeded scaffolds. The tissue piece was gently inserted inside the hole of the scaffold using sterile forceps. Completed scaffold-assisted implants were kept in PBS on ice until implantation surgery.

3.6.4 Subdermal transplantation into NSG mice

A breeding pair of NOD-scid IL2Rg^{null} mice (005557) was initially obtained from the Jackson Laboratories. Mice were housed in sterile conditions with unrestricted access to food and water. Mice used in this study were between 6-13 weeks old. NSG mice were anesthetized with 1.5 % isoflurane before removing the dorsal hair with electric clippers and Nair. The skin was sterilized using 70 % isopropyl alcohol prep wipes. Mice received 2 mg meloxicam/kg mouse weight subcutaneously prior to surgery. A subcutaneous pocket was created by making a 2 mm horizontal incision in the dorsal space followed by expansion of surgical scissors into the incision and expansion. One Scaffold-free or scaffold-assisted tissue with or without hBMSCs was inserted into the pocket and the incisions were closed with two 7 mm wound clips. Each mouse received four implants. Wound clips were removed after 1 week.

3.6.5 Evans Blue perfusion and quantitative imaging

Prior to euthanization, mice were injected with a 2 wt% Evans Blue dye at a dosage of 2 mL/kg mouse weight. Dye was allowed to perfuse for 20 minutes before euthanization via carbon dioxide. Tissues were harvested from the mice and imaged on an IVIS Spectrum CT using an excitation wavelength of 640 nm and emission wavelength of 680 nm.

3.6.6 MDA-MB-231 cell culture and intravenous injection

MDA-MB-231 human breast cancer cells were cultured with Dulbecco's Modified Eagle Medium (DMEM) supplemented with 10% FBS and 1% penicillin-streptomycin.

For intravenous cell injections 2 x 10^6 cells were suspended in 200 µL of PBS and injected into the lateral tail vein using a 27 gauge needle.

3.6.7 Frozen tissue preparation and sectioning

At the conclusion of the *in vivo* experiment, implants were frozen by embedding the tissue in Cryomatrix ™ and snap-frozen in 2-methylbutane cooled on dry ice. Frozen tissue was cut to 20 µm using a NX70 Cryostat. Frozen tissue blocks and sectioned slides were stored at -80 °C.

3.6.8 Immunohistostaining

Frozen slides were fixed in -20 °C acetone for 10 minutes. Slides were washed with a wash buffer consisting of 0.5 % Tween 20 in PBS (PBST) 3 times before blocking in a solution containing 10 % normal goat or donkey serum, and 1 % bovine serum albumin for 1 hour. Following blocking, primary antibodies diluted in blocking solution were added to the slides and left in a humidified chamber overnight at 4 °C. Slides were washed 3 times with PBST and then incubated with secondary antibodies diluted in blocking solution for 2 hours at room temperature. Prior to imaging, slides were washed 3 times in PBST and stained with a 10 ng/µL solution of DAPI. Fluorescent images were taken on a Zeiss Cell Observer SD. A table of primary and secondary antibodies used in this study has been provided (**Table S3.1**).

Table 3.1. List of antibodies used for immunohistostaining

Target	Vendor	Catalog Number
Rat – anti-Endomucin	Invitrogen	14-5851-81
Rat – anti-Ly6G	Becton Dickinson	557445
Rat – anti-F4/80	Becton Dickinson	565409
Mouse – anti-CD44	Becton Dickinson	550392
Mouse – anti-CD45	Becton Dickinson	550539
Mouse – anti-Vimentin	Dako	M072529-2
Guinea pig – anti-Cytokeratin	Lifespan Biosciences	LS-C193787
Rabbit – anti-Ki67	Abcam	Ab16667
Donkey – anti-Albumin	Bethel Laboratories	A90-134A
Rabbit – anti-α-Smooth Muscle Actin	Abcam	Ab5694
Goat – anti-rat AF488	Life Technologies	A11006
Goat – anti-mouse AF660	Life Technologies	A21054
Goat – anti-mouse AF488	Life Technologies	A32723
Goat – anti-guinea pig AF647	Life Technologies	A21450
Goat – anti-rabbit AF568	Life Technologies	A11011
Donkey – anti-goat AF488	Life Technologies	A11055

3.6.9 Human cancer and fibroblast isolation and transplantation

Human gastric cancer specimens were obtained from patients undergoing tumor resection surgery at the Ajou University Hospital as previously described[172]. Fibroblasts were isolated from gastric cancer tissues and were used within six passages. 2.5 x 10^5 cells were seeded onto 12 mm scaffolds. A human gastric cancer specimen (3-5 mm) was placed on top of cancer associated fibroblast-seeded scaffolds. After removing excess hydrogel matrix, implants were inserted into a subcutaneous pocket made on the dorsal side of Balb/c nude mice. The incision was closed using sutures.

3.6.10 Tissue histology

Formalin-fixed paraffin-embedded tissue samples from PDX experiments were sectioned using a microtome. Sections were cut to a thickness of 6 μm. To deparaffinize

sections, slides were treated sequentially with xylenes, 100 % ethanol, 95 % ethanol, and 50 % ethanol before washing with deionized water. For antigen retrieval, citrate buffer (10 mM, pH 6.0) was preheated to 90-95 °C on a hotplate before slides were immersed and incubated for 20 minutes. The antigen retrieval solution was then removed from the hotplate and allowed to cool to room temperature. Slides were washed with PBST solution before beginning the standard blocking and antibody staining procedure. Hematoxylin and eosin (H&E) staining were performed as previously described[101]. Brightfield images were taken on an EVOS FL Auto microscope.

3.6.11 Image analysis

All image processing and quantitative analysis was performed in ImageJ. For overlapping quantification, DsRed images were used to identify the transplanted tissue area.

3.6.12 Statistics

Unpaired Student's t tests were performed for comparison of the mean values between groups in mouse tissue implantation studies. A logistic regression analysis was used to evaluate the effect of scaffold on PDX engraftment. Mann Whitney U test was performed to analyze the statistical significance of immunohistostaining measurements of markers in PDX tumor experiments. Statistical significance was determined if $p < 0.05$ for two-tailed analysis. All quantitative data represent mean and standard deviation.

CHAPTER 4

IMPLANTABLE PRE-METASTATIC NICHES FOR THE STUDY OF THE MICROENVIRONMENTAL REGULATION OF DISSEMINATED HUMAN TUMOR CELLS

Adapted with permission from Ryan Carpenter, Jun-Goo Kwak, Shelly Peyton, and Jungwoo Lee. *Nature Biomedical Engineering*. **2018** 2, 915-929. DOI: 10.1038/s41551-018-0307-x.

4.1 Abstract

Cancer survivors often carry disseminated tumor cells (DTCs), yet owing to DTC dormancy they do not relapse from treatment. Understanding how the local microenvironment regulates the transition of DTCs from a quiescent state to active proliferation could suggest new therapeutic strategies to prevent or delay the formation of metastases. Here, we show that implantable biomaterial microenvironments incorporating human stromal, immune and cancer cells can be used to examine the post-dissemination phase of the evolution of the tumor microenvironment. After subdermal implantation in mice, porous hydrogel scaffolds seeded with human bone marrow stromal cells form a vascularized niche and recruit human circulating tumor cells released from an orthotopic prostate tumor xenograft. Systemic injection of human peripheral blood mononuclear cells slowed the evolution of the active metastatic niches but did not change the rate of overt metastases, as the ensuing inflammation promoted the formation of DTC colonies. Implantable pre-metastatic niches might enable the study of DTC colonization and proliferation, and facilitate the development of effective anti-metastatic therapies.

4.2 Introduction

Tumor cell dissemination and subsequent metastatic relapse is the leading cause of death from nearly all cancers. This insidious event has often already occurred when a patient is first diagnosed with a tumor. However, not all disseminated tumor cells (DTCs) develop lethal metastases within the lifetime of the patient because the formation of aggressive secondary tumors is inefficient and lengthy [192]. Only a few circulating tumor cells (CTCs) disseminate successfully to vital organs, and the majority of these DTCs undergo apoptosis or clearance by immune cells [193]. Often, CTCs that survive extravasation do not immediately proliferate, but instead lay dormant for months to decades until the surrounding milieu becomes favorable for regrowth [194-195]. Emerging evidence suggests that metastatic relapse may not be explained solely by intrinsic genetic instability of DTCs, instead bi-directional interaction with the surrounding microenvironment needs to be considered [22, 196-197]. Understanding how the local milieu surrounding DTCs prevents or aids in regaining proliferative phenotypes is imperative to developing better therapeutic strategies to prevent or delay lethal metastasis.

CTCs theoretically spread to a wide range of distant organs, but metastasis limitedly occurs in a subset of target organs including the lung, bone, liver, and brain. This non-random development of metastasis has been recognized as the “Seed and Soil” hypothesis [198]. Recently the “Pre-metastatic Niche” hypothesis further posits that CTCs are actively attracted to transiently formed pro-inflammatory microenvironments, driven by signaling from the primary tumor, in these distant organs that better support the survival and growth of DTCs [21]. The key microenvironmental signatures of the pre-metastatic niche include (i) a vascular network [48, 63] and associated oxygen tension (i.e. hypoxia) [199], (ii) altered local

deposition of extracellular matrix [200-202], (iii) recruitment of bone marrow-derived cells [21, 29], and (iv) pro-inflammatory immune cell activity [50-51, 203-204]. These niche factors are believed to attract CTCs and subsequently direct the fate of DTCs to remain in a dormant state or proliferate [205]. However, the detailed mechanisms through which dormant DTCs regain their aggressive phenotype while interacting with the local microenvironment have remained uncertain due to the lack of relevant experimental models that can faithfully simulate the post-dissemination phase of a dormant-to-active transition of DTCs with high analytical power.

Mouse models have been widely used to understand various aspects of cancer biology. For example, spontaneous and experimental metastasis models simulate invasion, circulation and dissemination of cells from solid tumors in a physiologically relevant manner [65-67]. The development of immunodeficient NOD-scid IL2Rg^{null} (NSG) mice has improved the ability to study the biology of human cancer cells in the context of living systems [73]. This has greatly advanced knowledge about early stage events in human tumor metastasis and the functional interplay between human DTCs and the local stromal microenvironment [96]. However, there are major limitations in current models to study metastatic relapse of dormant human DTCs. First, experimental metastasis models always induce both active and dormant DTCs simultaneously, restricting the study of late stage metastatic tumor recurrence. Second, rare dormant DTCs are impractical to detect. Metastatic relapse becomes evident only after reactivated DTCs establish a clinically detectable tumor mass. Third, immunodeficient mice cannot capture the role of the immune system in microenvironmental regulation of DTC survival and outgrowth. Fourth, most of these mouse models rely on xenografts wherein human tumor cells interact with mouse

stromal cells, which does not fully recapitulate human disease. Lastly, these systems offer little opportunity to manipulate individual properties of the niche, constraining the ability to distinguish the role of individual factors of the tumor microenvironment in regulating DTC biology.

Recently, tissue engineering strategies have been applied to address the fundamental limitations of conventional murine metastasis models [160, 206-207]. These efforts can be divided into two different aspects based on the target tissues. Among the four major metastatic prone tissues, bone has been the most successful in tissue engineering. A combination of bone inducing biomaterial selection, porous scaffold design, and osteogenic growth factors have successfully been applied to generate ectopic bone and marrow, mostly beneath the skin [88-89]. The addition of human bone marrow stromal cell (hBMSC)-derived osteogenic cells and subsequently introduced human tumor cells recapitulate humanized bone-specific metastasis [90-94]. The second approach exploits the transient foreign body response triggered by biomaterials that attract immune cells along with CTCs to the site of implantation [96-100]. These approaches have been utilized to distinguish common biological processes that support aggressive metastatic tumor formation [96, 99]. Engineered tumor cell attracting niches have also demonstrated translational potential as they have been shown to significantly reduce metastatic burden in vital organs and resultantly extend the lifespan of tumor bearing mice [103-104, 208]. However, tissue engineered microenvironments have not been applied for detailed investigation of the post-dissemination phase of cancer biology.

In this report, we introduce a new experimental metastasis model to study the evolution of early humanized DTC niches in immunodeficient NSG mice. Functional pre-

metastatic niches can arise in multiple tissue sites and share pro-inflammatory features observed during wound healing and tissue remodeling processes [209]. A recent study demonstrated that repeated injection of tumor-derived exosomes induced a pre-metastatic niche in the liver and lung of mice [210], indicating that a pre-metastatic niche can be generated by exogenously delivered factors. Based on this premise, we have developed a tissue engineered pre-metastatic niche by subdermally implanting inverted colloidal crystal (ICC) hydrogel scaffolds that induce vascularized and pro-inflammatory tissue microenvironments. This niche was humanized with hBMSCs preseeded on the scaffolds, followed by recruitment of CTCs released from an orthotopic human tumor xenograft. The established humanized pre-metastatic niche was applied to determine the long-term impact of inflammation triggered by human peripheral blood mononuclear cells (hPBMCs) in directing the fate of DTCs. Many solid tumor patients suffering metastasized lesions receive chemotherapy and/or radiation therapy and subsequent bone marrow transplantation. In these patients, graft-versus-tumor effects have been clinically observed, whereby grafted cells reduce tumor burden of the recipient [211]. Therefore, we hypothesized that the introduction of hPBMCs would reduce long-term metastatic relapse by decreasing DTCs. Serial transplantation of early humanized DTC niches into syngeneic naive mice permitted prolonged evolution of the tumor microenvironments. Over a 10-week period, the kinetics of metastatic relapse were quantitatively monitored under whole body bioluminescent imaging. At the end of the study, we identified early, intermediate, and overt stages of the metastatic cascade. Deep multiplex imaging and quantitative analysis captured the ability of hPBMCs to reduce the number of single DTCs but did not affect the incidence of overt metastatic tumor development. Additionally, the importance of

vasculature and innate immune cells in regulating the stable-to-active transition of human DTCs was substantiated. The presented tissue engineered, humanized, and analytical niche model may serve as an enabling tool for the study of microenvironmental regulation of the post-dissemination phase of cancer biology and development of targets for anti-metastatic therapies.

4.3 Results

4.3.1 hBMSC-seeded inverted colloidal crystal hydrogel scaffolds induce a vascularized tissue microenvironment *in vivo*

We hypothesized that engineered implantable biomaterials could create pre-metastatic niche-mimicking tissue microenvironments by directing the foreign body response to promote angiogenesis and maintain a pro-inflammatory milieu. An isotropic porous ICC structure fabricated by a simple and tunable procedure was chosen to systematically investigate the role of biomaterial design in directing host tissue response by orthogonally manipulating its physical and chemical properties [212-215]. ICC geometry consists of fully interconnected spherical pore arrays and provides maximal surface area in the given volume, increasing the biomaterial-tissue interface to direct the foreign body response [216]. Cavity diameter and mechanical integrity of the hydrogel matrix were recognized as important parameters to direct angiogenesis and subsequent systemic recruitment of cells including immune and bone marrow cells. Ultimately, we determined that a 6.5 mm diameter, 1 mm thick cylindrical ICC scaffold consisting of 300 ± 15 μm pores with 30 wt% synthetic PAA hydrogel was optimal to generate a controlled humanized vascularized tissue at the subcutaneous site **(Figure 4.1a)**.

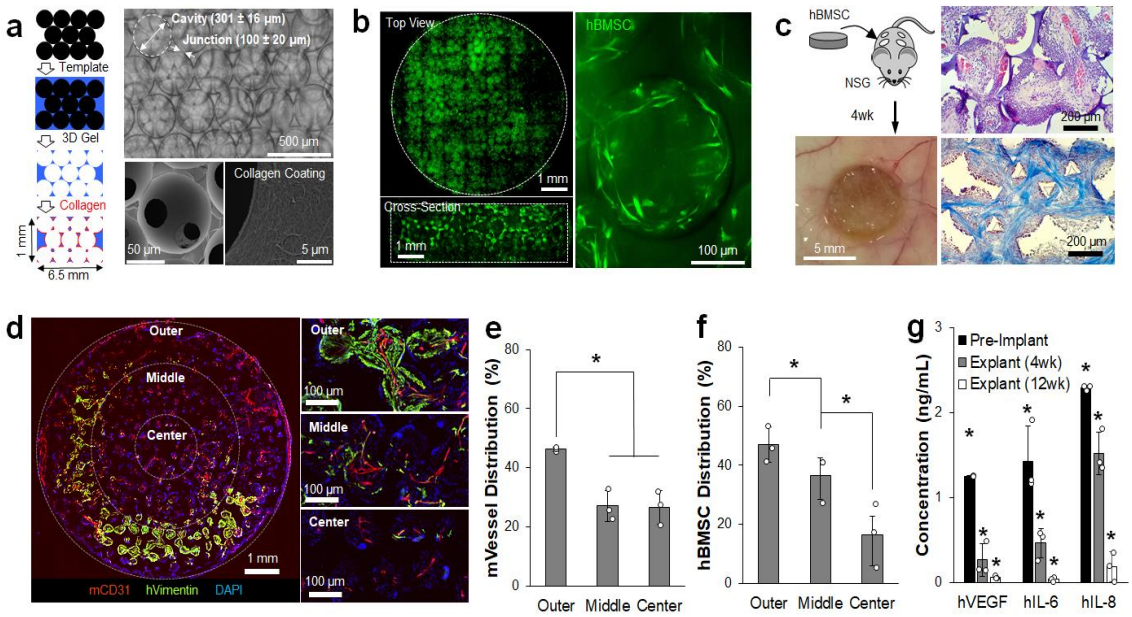

Figure 4.1. Subdermally implanted hBMSC-seeded ICC hydrogel scaffolds develop vascularized humanized niches in immunodeficient NSG mice.
a, Schematic of microsphere template-based fabrication of ICC geometry polyacrylamide hydrogel scaffolds. Bright-field image shows ICC structure through transparent hydrogel matrix (top), and SEM images show interconnecting junctions and surface immobilized type I collagen (bottom). **b,** Confocal images of tiled top and cross-sectioned scaffolds demonstrate homogeneously seeded fluorescently labeled hBMSCs into 3D ICC hydrogel scaffolds with typical mesenchymal morphology after adhesion. **c,** Representative gross and histological images of subdermally implanted hBMSC seeded scaffold after 4 weeks in NSG mice. H&E (top) and trichrome staining (bottom) shows recruitment of stromal and immune cells, and organized collagen architecture, respectively. **d,** Immunohistostaining (IHS) of hVimentin and mCD31 for analyzing spatial characteristics of hBMSCs and vasculature within the scaffold. **e, f,** Quantitative analysis of blood vessels **(e),** and hBMSC localization **(f)** (n=3 independent scaffolds)**. g,** Comparison of key human cytokine secretion from hBMSC-scaffolds before and after implantation for 4 and 12 weeks (n=3 independent scaffolds). *P<0.05.

A humanized stromal niche was created by seeding $5x10^5$ hBMSCs onto an ICC hydrogel scaffold coated with type I collagen. hBMSCs are adherent fibroblastic cells isolated from the human bone marrow that carry multilineage capabilities and high secretory activity **(Figure 4.2)** [167]. Confocal imaging confirmed deep and homogeneous distribution of hBMSCs, displaying a spindle-like cellular morphology **(Figure 4.1b)**. We

previously demonstrated that subdermally implanted ICC scaffolds preseeded with hBMSCs significantly enhanced vascularization and hematopoietic cell recruitment [97]. Four hBMSC-scaffolds were implanted in the dorsal subcutaneous space apart from each other in a NSG mice. ICC hydrogel scaffolds facilitated rapid and deep migration of mouse immune cells, which was in turn followed by near tissue cell migration and inter-scaffold angiogenesis. After 4 weeks, complete inter-scaffold tissue development was confirmed under scanning electron microscopy **(Figure 4.3)**. Histological analysis revealed that pores were filled with organized dense collagen extracellular matrix and populated with various types of hematopoietic cells on the pore surface **(Figure 4.1c)**. Immunohistostaining (IHS) for mouse endothelial cell marker, mCD31, and human mesenchymal marker, hVimentin, revealed a richly vascularized tissue throughout the scaffold with hBMSCs **(Figure 4.1d)**. There was no overlap between mCD31 and hVimentin, indicating that blood vessels were mouse tissue derived and hBMSCs did not incorporate with mouse vessels. Interscaffold angiogenesis was directed by the biomaterial geometry as vasculature took on branched morphology between the scaffold cavities **(Figure 4.4)**. Quantitative analysis revealed that most blood vessels and hBMSCs resided at the outer regions of the scaffold, gradually decreasing in number toward the center **(Figure 4.1e,f)**. This indicates that the survival of hBMSCs was dependent on the rapid formation of inter-scaffold blood vessels. To determine whether engrafted hBMSCs remained functional, we examined *ex vivo* secretion of cytokines from hBMSCs remaining in implanted scaffolds 4 and 12 weeks post implantation. Explanted scaffolds were cultured *ex vivo* for 36 hours before conditioned media was collected and analyzed for a subset of human cytokines (VEGF, IL-6, and IL-8) that have implicated importance in angiogenesis and inflammation [21, 217-219]. Human

cytokine secretion gradually diminished overtime *in vivo* but was still detectable by ELISA (>35 pg/mL) 12 weeks after implantation **(Figure 4.1g)**. The directed foreign body response and hBMSC secretome in ICC hydrogel scaffolds reproducibly form an analytical tissue microenvironment that recapitulates three key features including (i) vascular networks, (ii) bone marrow derived cells, and (iii) inflammatory immune cells.

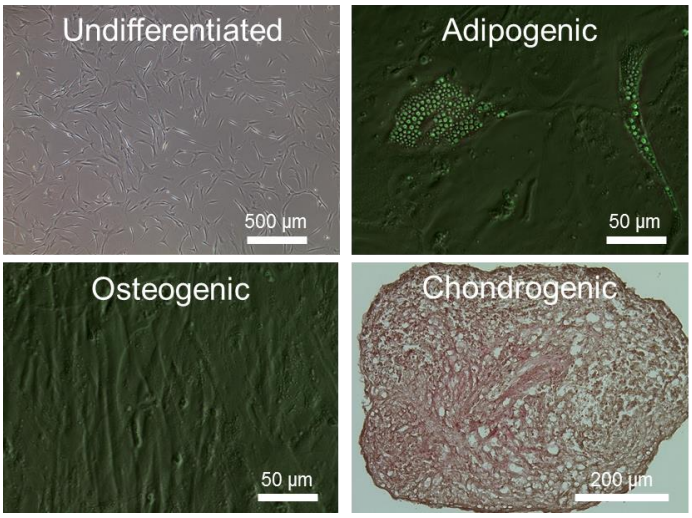

Figure 4.2. Human bone marrow stromal cell (hBMSC) multilineage potential. hBMSCs isolated from human bone marrow aspirate have capability to differentiate into adipogenic, osteogenic, and chondrogenic lineage. Undifferentiated, adipogenic, and osteogenic images are representative brightfield images displaying changes to morphology. Chondrogenic image was taken following Safranin O staining for proteoglycans.

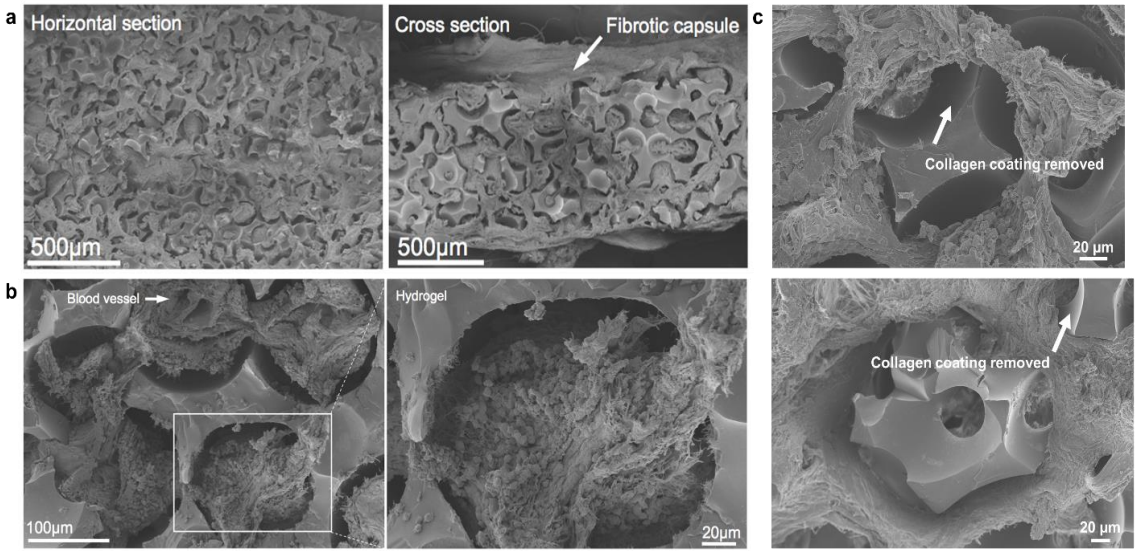

Figure 4.3. Scanning electron microscope images of complete tissue infiltration into PAA ICC hydrogel scaffolds.

a, Complete tissue infiltration with minimal fibrotic encapsulation of the PAA scaffold. **b**, Vascularization and recruitment of immune cells. **c**, Initial collagen coating removed from acrylamide surface.

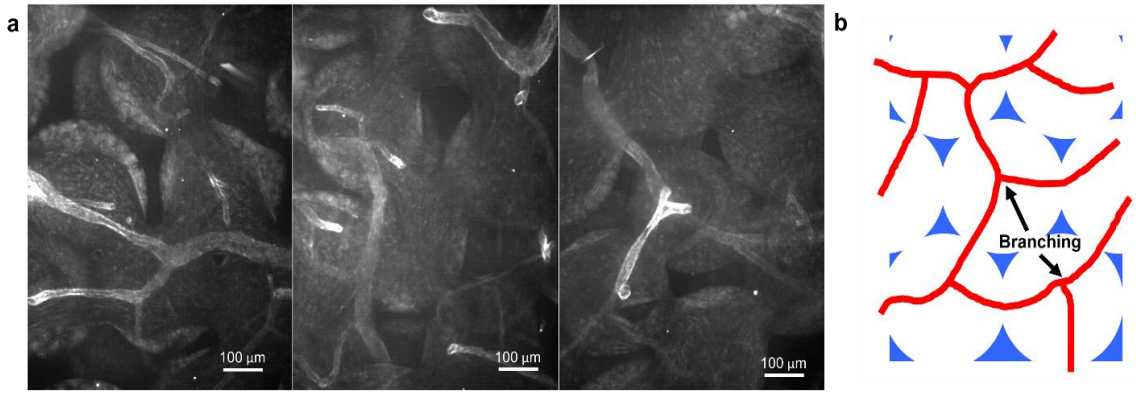

Figure 4.4. Branched vascular morphology through interconnecting pore in the ICC scaffold.

a, Representative immunohistostaining (IHS) of mCD31 through the scaffold. Blood vessels have a branched morphology. **b**, Vascular branching only occurred in the scaffold pores and not at interconnecting junction indicating the vasculature is directed by the biomaterial geometry.

4.3.2 Humanized stromal niches attract human CTCs and permit colonization

We employed an orthotopic xenograft tumor-based experimental metastasis model with PC3 human prostate tumor cells that has demonstrated robust engraftment and

subsequent metastasis [220-222]. After 3 weeks, hBMSC-scaffold implantation, we performed an intra-prostate injection of $2x10^6$ PC3 human prostate tumor cells expressing green fluorescent protein (GFP) and luciferase (Luc). Engraftment and metastatic spread of human tumor cells was non-invasively monitored via whole-body bioluminescent imaging (BLI). The efficiency of successful orthotopic engraftment based on BLI was above 90%. Unsuccessfully engrafted mice were excluded from experiments. BLI+ mice were sacrificed at 8 weeks because mice became moribund due to continuous growth of the primary tumor and aggressive metastasis in vital organs **(Figure 4.5a)**. Previous characterization demonstrated that by this time point, primary tumors grew in weight to about 400 mg and generated roughly 10-50 CTCs per mL of blood [96]. At the end of the study, gross examination of internal organs confirmed overt metastatic tumor nodules in the liver **(Figure 4.5b)**. IHS of explanted tissues confirmed the formation of micro-metastases in the liver and lung whereas DTCs remained individually in the bone marrow and spleen **(Figure 4.5c)**. IHS of humanized stromal niches revealed CTCs had successfully disseminated. DTCs were mostly observed in a single cell state but there were few colonized DTCs **(Figure 4.5d)**. These results verified that the implanted humanized stromal niches recapitulated the microenvironmental complexity, tumor cell attracting, and supportive functions of the pre-metastatic niche.

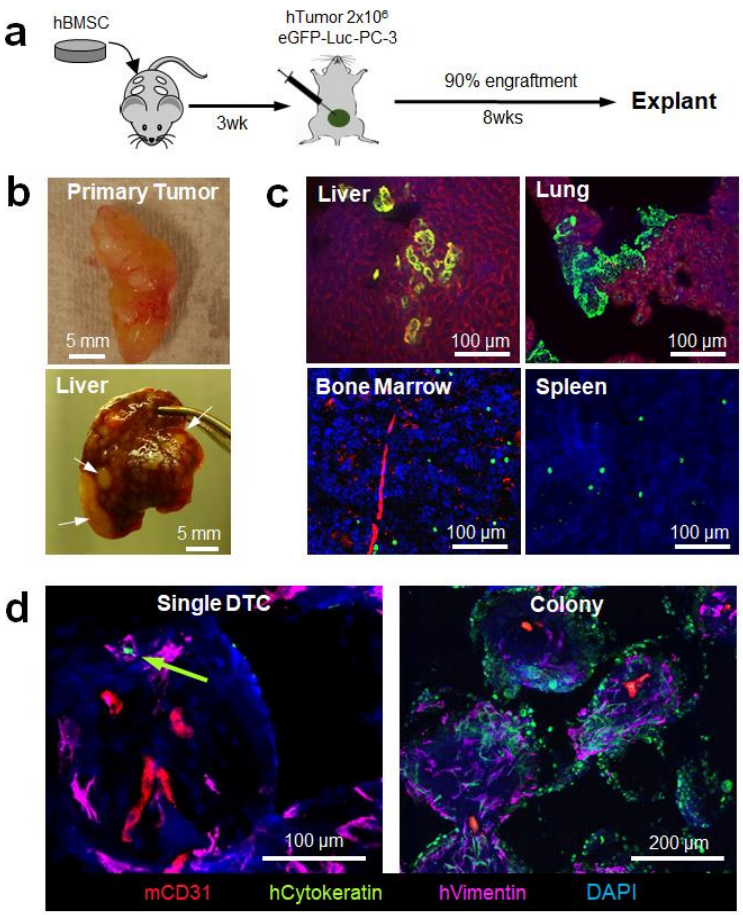

Figure 4.5. Humanized implantable microenvironments recapitulate tumor cell receptive and supportive functions of the pre-metastatic niche.
a, Experimental schematic describing establishment of an orthotopic xenograft tumor and subsequent metastasis. **b,** Gross images of the orthotopic xenograft PC-3 human prostate tumor and liver metastasis. Arrows indicate overt metastatic nodules. **c,** IHS images of dissemination and colonization of DTCs in vital organs including the liver, lung, bone marrow and spleen. Micrometastatses commonly appeared in the liver and lung while DTCs remained mostly in an individual state in the bone marrow and spleen. **d,** IHS of implantable pre-metastatic niche showed both single and colonized DTCs. Green arrow indicates single DTC.

4.3.3 Intravenously delivered hPBMCs increased human immune cell complexity

Immune cells, both innate and adaptive, are important components of the pre-metastatic niche [21, 223]. To add human immune cell complexity, we intravenously injected 1 x 10^7 hPBMCs isolated from healthy adult donors into mice bearing hBMSC-scaffolds 4 weeks after implantation **(Figure 4.6a)**. Initial distribution of hPBMCs was characterized 24 hours after injection. As expected, hPBMCs were primarily localized to the spleen and lung. A relatively low and comparable level of hPBMCs was confirmed across hBMSC-scaffolds, bone marrow, and liver **(Figure 4.6b and Figure 4.7)**. At the same time point, we also determined whether systemically migrated immune cells initiated local tissue inflammation. After 36 hours of *ex vivo* culture, conditioned media for human cytokines representative of inflammation (TNF-α, IL-6, and IL-10) were compared to non-hPBMC injected controls. Increased inflammatory cytokine secretion was observed in the lung, liver, and spleen but not in the bone marrow. hBMSC-scaffolds showed significantly increased pro-inflammatory IL-6 but decreased anti-inflammatory IL-10 compared to hPBMC-free controls **(Figure 4.6c)**. We then examined the long-term effect of human immune cells on tissues and hBMSC-scaffolds by IHS for the pan-leukocyte marker, hCD45, 6 weeks after injection of hPBMCs. $hCD45^+$ cells displayed a single cell morphology and were observed widespread across the scaffold **(Figure 4.6d and Figure 4.8)**. Sublineage analysis of human immune cells confirmed both hCD4 and hCD8 T-lymphocytes were present in the scaffold **(Figure 4.9)**. Diffuse mCD31 endothelial staining in hPBMC-injected mice compared to controls indicated leaky and permeable vasculature, which is the representative vascular morphology in inflamed tissues [224]. Further quantitative image analysis confirmed a significant increase in vascular density in the

scaffold tissue with hPBMCs compared to controls **(Figure 4.6e)**. Taken together, implantable humanized niches gained enhanced inflammatory characteristics after the introduction of hPBMCs, however the host animals developed symptoms of systemic graft-versus-host-disease and became moribund 10-12 weeks post hPBMC injection [225-226].

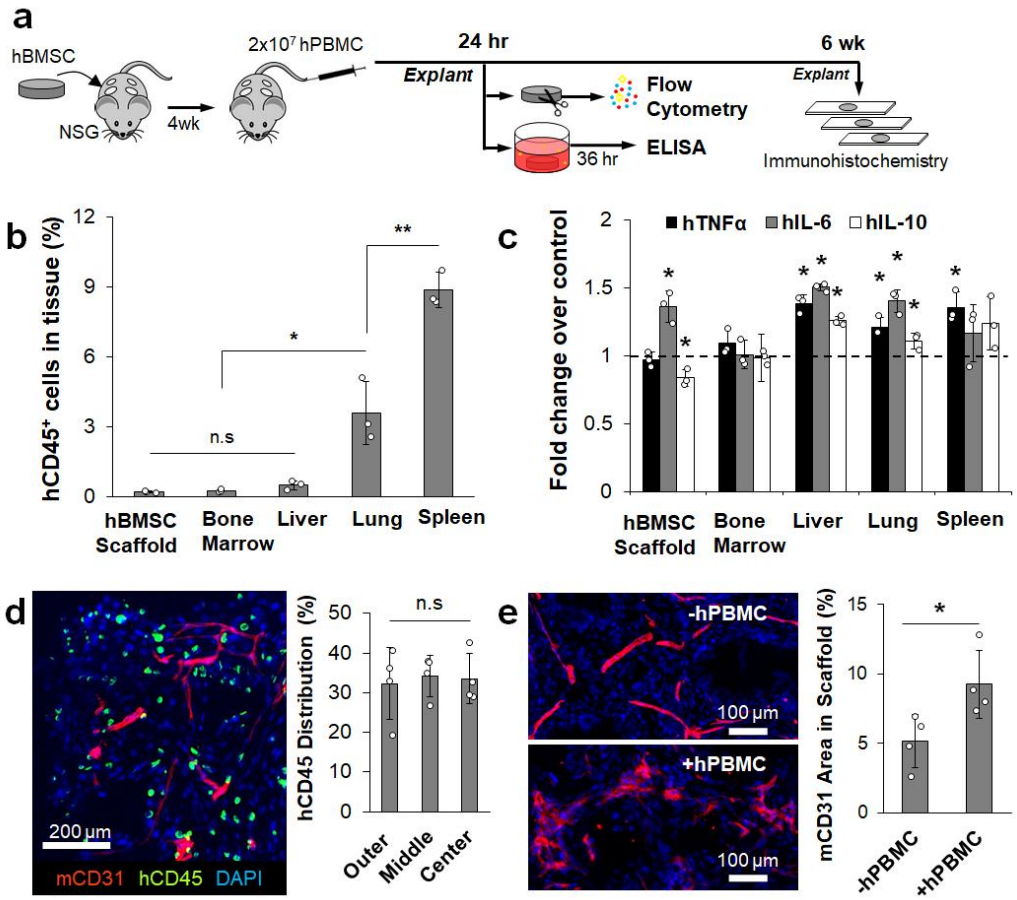

Figure 4.6. Implantable humanized stromal niches attract systemic hPBMCs.
a, Experimental schematic describing systemic introduction of hPBMCs followed by functional and immunohistological characterization. **b,** Flow cytometry analysis of hPBMC distribution 24 hours after intravenous injection (n=3 mice). **c,** Analysis of inflammatory human cytokine secretion from *ex vivo* cultured tissues and scaffolds retrieved 24 hours after injection. Dotted line indicates cytokine levels from control tissue and scaffolds without hPBMCs (n=3 mice). **d,** IHS of hCD45 and mCD31 in scaffolds 6 weeks after hPBMC injection with quantitative characterization of $hCD45^+$ cell distribution within the scaffolds (n=4 independent scaffolds). **e,** IHS of mCD31 6 weeks after hPBMC injection shows leaky vascular morphology when compared to non-injected control and quantitative analysis confirms significantly increased vascular density following hPBMC injection (n=4 independent scaffolds). *P<0.05, **P<0.005.

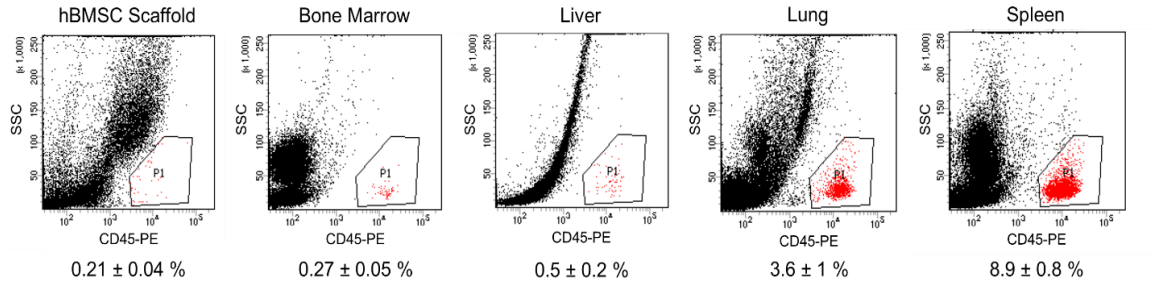

Figure 4.7. Flow cytometry plots of hPBMC migration across various tissue.
N= 3 independent mice.

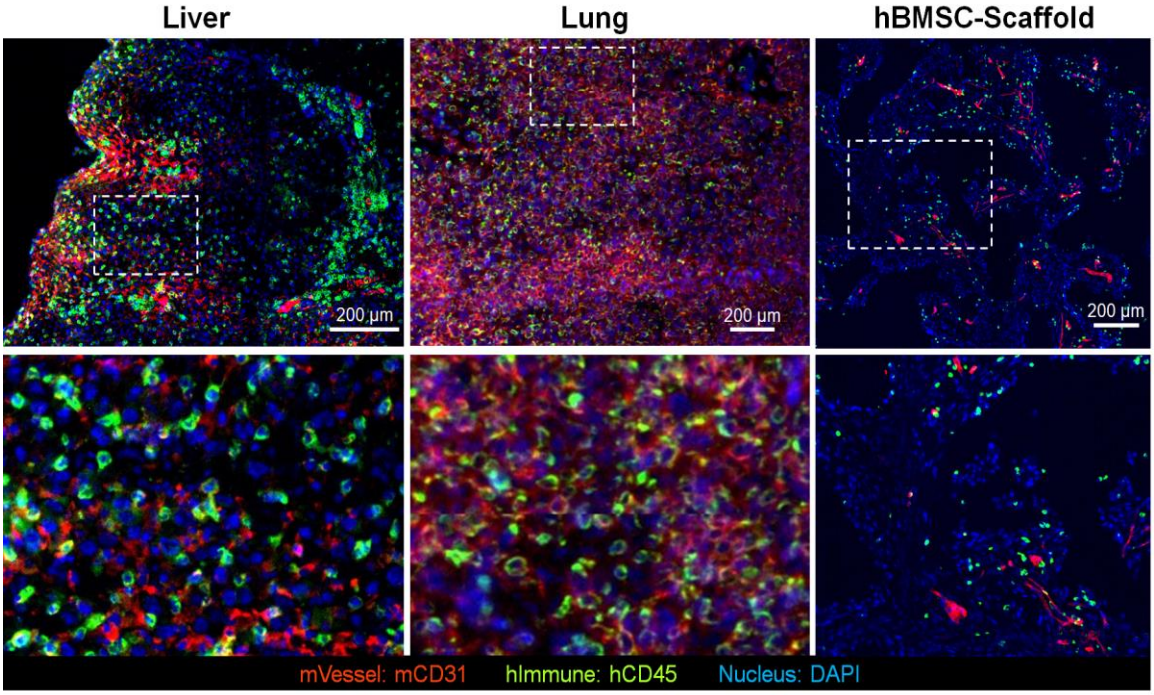

Figure 4.8. Distribution of hCD45 cells in primary mice liver, lung, and implanted hBMSC- scaffold 6 weeks after hPBMC injection.
IHS shows more human immune cells in native mouse tissues than hBMSC-scaffolds. Immune cells in the scaffold remain largely as single cells.

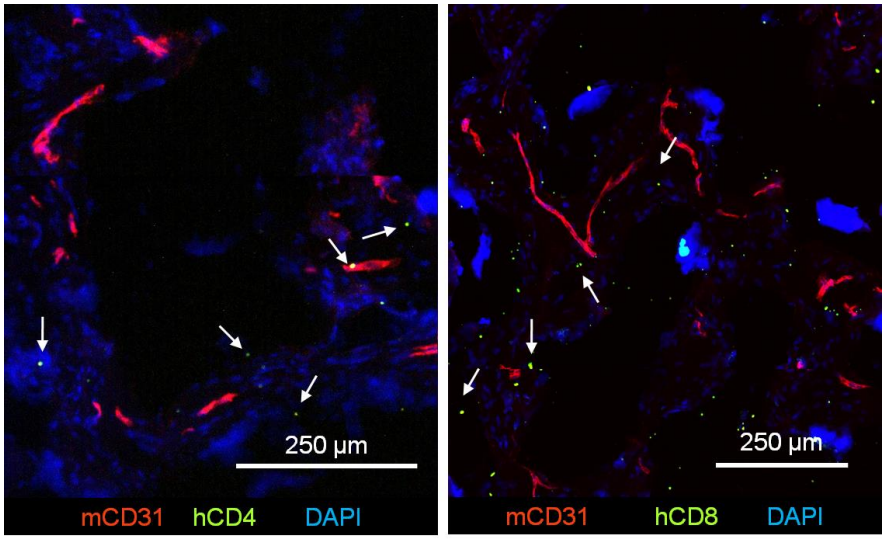

Figure 4.9. Human CD4 and CD8 IHS 6 weeks after hPBMC injection.
Human CD4 and CD8 cells in hBMSC scaffolds.

4.3.4 Systemic delivery of hPBMCs instigates early stage humanized DTC niches

Next, we challenged humanized early DTC niches with hPBMCs under the hypothesis that mature, functional human immune cells would decrease metastasis. After subdermal implantation hBMSC-scaffolds for 3 weeks, $2x10^6$ eGFP-Luc PC3 cells were injected into the mouse prostate to form an orthotopic human prostate tumor xenograft. The primary tumor grew for 6 weeks before intravenous injection of $1x10^7$ hPBMCs to introduce human immune cells to the implanted microenvironments. By this point, the host animals carried substantial primary and metastatic tumor burden. Thus, 5 days after hPBMC injection, we euthanized mice and characterized the establishment of the early humanized metastatic niche in the scaffolds **(Figure 4.10a)**. IHS revealed coexistence of human stromal (hVimentin), human immune (hCD45), and human tumor (hCytokeratin) cells residing in the same microenvironment **(Figure 4.10b)**. BLI analysis of explanted scaffolds revealed 8% of scaffolds produced positive signal from both control (3/36) and hPBMC (4/44) injected mice. There was no significant difference in overall bioluminescent

signal intensity between hPBMC-injected and control mice **(Figure 4.10c)**. We expected hPBMC-induced inflammation of humanized DTC niches altered DTC fate, but these results indicated that a longer period of implantation was necessary to substantiate the functional consequence.

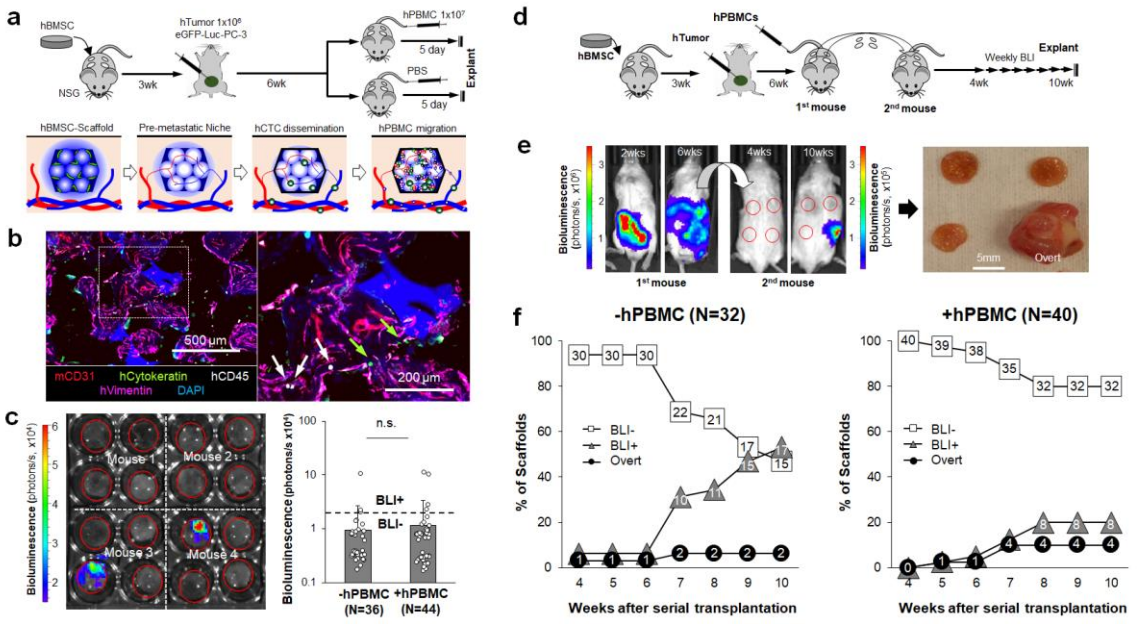

Figure 4.10. Instigation of humanized pre-metastatic niches with hPBMCs and long-term monitoring of DTC niche evolution via serial transplantation.
a, Experimental schematic describing the establishment of early stage humanized DTC niches and subsequent instigation by systemic introduction of hPBMCs. **b,** Representative IHS of humanized early DTC niche including hCytokeratin (tumor), hCD45 (immune), hVimentin (stroma) and mCD31 (vessel). Arrows indicate human immune (white) and tumor (green) cells. **c,** Representative *ex vivo* BLI of explanted scaffolds from primary mice and quantified bioluminescent signal with and without hPBMCS. The dotted line represents a threshold used to define BLI+ and BLI-. **d,** Experimental schematic describing a strategy to monitor the long-term evolution of humanized DTC niches via serial transplantation of intact early metastatic niches to naïve secondary syngeneic mice. **e,** Representative whole body BLI of primary and secondary mice at different time points. Gross image of explanted scaffolds from secondary mice showing an overt metastasis. **f,** Quantitative analysis of human DTC growth in scaffolds after transplantation into secondary mice via weekly BLI. Scaffolds were classified as BLI-, BLI+, or overt based on their bioluminescent intensity. Presented N values are representative of independent scaffolds.

4.3.5 Serial transplantation of humanized DTC niches allowed for long-term monitoring of metastatic evolution

We hypothesized that evolution of the early humanized DTC niches could be continued by intact transplantation of the microenvironment to the same anatomical site of syngeneic mice. We followed the aforementioned experimental schedule to generate humanized DTC niches with and without hPBMCs. Bioluminescent signal from scaffolds retrieved from primary mice was checked *ex vivo*, and BLI negative scaffolds were transplanted immediately to naïve NSG mice 6-12 weeks of age. Subsequent metastatic relapse was non-invasively monitored on a weekly basis via BLI starting 4 weeks after transplantation and continued up to 10 weeks **(Figure 4.10d)**. We did not observe noticeable necrotic tissue areas in histological analysis of serially transplanted scaffolds (data not shown). Gross observation 3 and 7 days after transplantation showed large blood vessels surrounding the scaffolds **(Figure 4.11)**. By the end of the study, serially transplanted microenvironments captured a broad range of the metastatic cascade **(Figure 4.10e)**. Based on bioluminescent intensity and outgrowth beyond the scaffold, we categorized scaffold microenvironments into three groups: (i) BLI-, (ii) BLI+ and (iii) Overt. BLI+ microenvironments were defined by signal at least 3 times greater than the background signal, and the rest were defined as BLI- microenvironments. Background BLI signal was determined from mice without injection of luciferin. Overt growth, a subcategory of BLI+, described aggressive metastases where the tumor expanded outside of the boundary of the scaffold **(Figure 4.10f)**. hPBMC-free mice displayed a gradual increase in the number of BLI+ scaffolds over the 10-week period whereas in mice with hPBMCs the number of BLI+ scaffolds stabilized 8 weeks after transplantation. By the end of the study, 53% (17/32) and 23% (9/40) of scaffolds became BLI+ in hPBMC-free and

hPBMC-injected mice, respectively. There was no significant difference in the percentage of scaffolds with overt metastasis between the two groups; 6.3% (2/32) in hPBMC-free and 10% (4/40) in hPBMC-injected mice. Our results signify the ability of hPBMCs to suppress human DTC growth but did not affect the incidence of aggressively growing metastases.

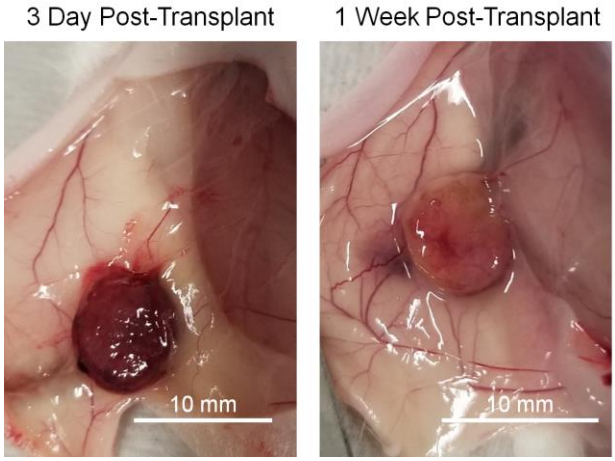

Figure 4.11. Large blood vessel recruitment to the transplanted scaffold after 3 and 7 days in secondary mice.

4.3.6 Complete optical sectioning of BLI- scaffolds captured the impact of hPBMCs on early DTCs

We hypothesized that BLI- scaffolds still attracted CTCs, but the number of DTCs were low and the cells entered a dormant state. Conventional IHS and flow cytometry may not effectively detect rare DTCs due to the technical difficulties of probing entire tissue volumes and representative cell recovery after tissue digestion, respectively. To overcome these challenges, we adapted the recently introduced CLARITY technique through which optically cleared fixed tissues permit microscopic detection of rare cell populations while retaining spatial resolution in the tissue microenvironment [227] **(Figure 4.12a)**. A PAA hydrogel meshwork (4 wt%) between fixed cellular proteins was formed before removal

of light scattering lipids, achieved by passive washing with sodium dodecyl sulfate and boric acid at 37 °C. Transparency dramatically improved in the scaffold, but light scattering was still present, possibly due to ICC geometry, or mismatched hydrogel density between the pore cavities and scaffolds **(Figure 4.12b)**. We cut the scaffolds to a thickness of 250 μm using a cryostat, which allowed complete optical imaging **(Figure 4.12c)**. Sliced scaffolds were stained with antibodies for mouse α-smooth muscle actin and human cytokeratin to visualize vasculature and tumor cells, respectively. Analysis of the images revealed abundant (80-400) single DTCs as well as few (5-30) colonized DTCs throughout the BLI- scaffolds **(Figure 4.12d)**. DTCs were detected in all characterized BLI- (6/6) scaffolds regardless of hPBMC injection. Complete counts of single and colonized DTCs did not show a significant difference between hPBMC-injected and hPBMC-free mice **(Figure 4.12e)**. Further spatial analysis revealed widespread distribution of DTCs across inner and outer regions of the scaffolds **(Figure 4.13)**. The frequency of colonized DTCs in total tumor counts, was two times higher in implants with hPBMCs compared to hPBMC-free implants **(Figure 4.12f)**. There was no significant difference in DTC colony size among BLI- scaffolds with an average size of 3,700 μm^2 **(Figure 4.14)**. These results suggest that the implantable pre-metastatic niches effectively attract CTCs and subsequently maintain the long-term viability of DTCs. hPBMC injection disrupted DTC survival but did not decrease colonization events.

We then extended cytological profiling of the DTCs to determine intrinsic tumor cell properties and proliferative state using standard immunohistostaining. First, we examined CD44 expression in DTCs to identify potential cancer stem cells [228-229]. About 29% of primary tumor cells (N=3 primary tumors) co-expressed hCD44 and hCytokeratin

whereas all observed DTCs (97 DTCs from 4 independent scaffolds) were double positive regardless of being in single or colonized states **(Figure 4.15)**. To confirm cellular dormancy, we examined the functional status of the DTCs. Several studies have reported a subset of markers that are expressed while DTCs are in a dormant state. These markers have been shown to be dependent on the microenvironment [43-45, 230]. For example, NR2F1 was shown to promote dormancy in the lung and spleen, however did not play the same role in DTCs found in the bone marrow [42]. Additionally, the expression of these markers is transient and relative, therefore not necessarily informative to distinguish the functional state of dormancy [40, 231-232]. Thus, we focused on expression of the cell proliferation marker Ki67. All singular DTCs found in the scaffold microenvironments (N=107) were $Ki67^-$, confirming that these cells were not in a proliferative state. In DTCs that formed colonies, only 8.3% (24/252) contained at least one $Ki67^+$ cell. We did not observe any colonies in which all cells expressed Ki67. These results suggest that the majority of initial proliferating DTCs stop growing and enter dormancy indicating that intrinsic properties of early DTCs may be important to initiate metastatic colonization but not sufficient to lead to continuous growth. Comparison between scaffolds with and without hPBMCs revealed no significant differences in the number of $Ki67^+$ DTCs **(Figure 4.12g)**.

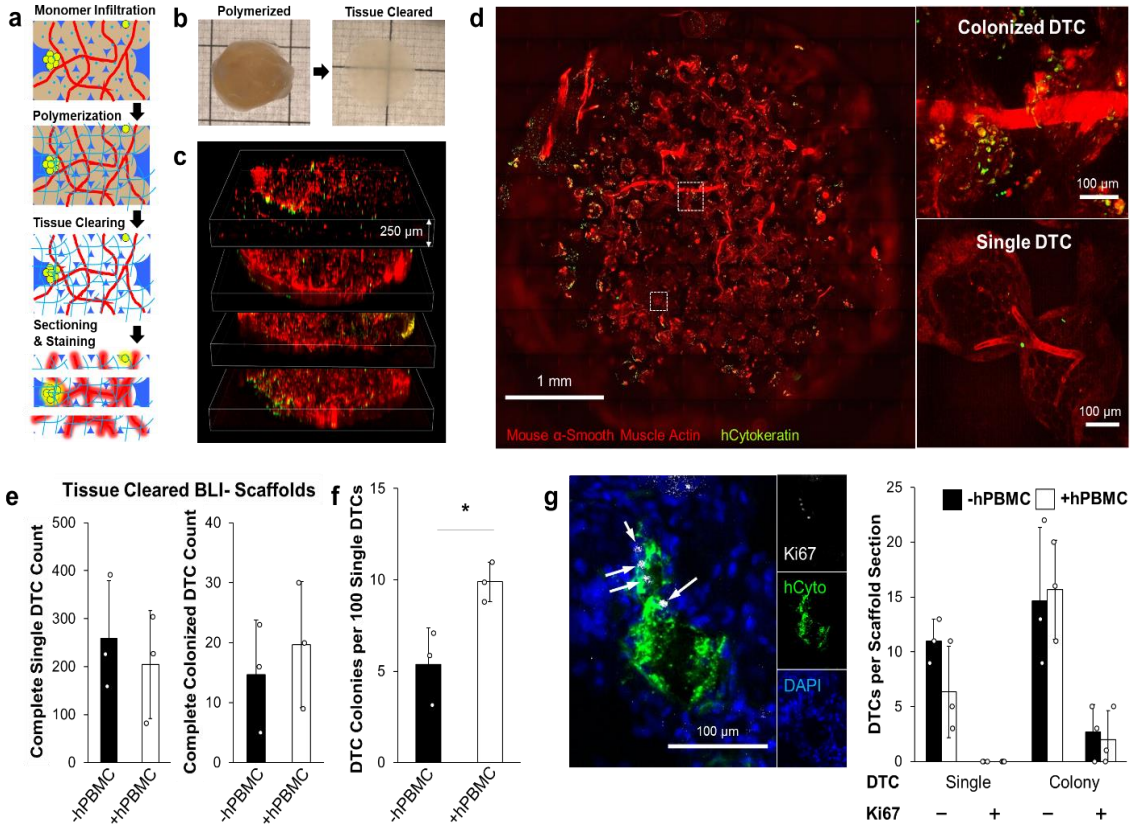

Figure 4.12. Detection of rare dormant DTCs via whole scaffold tissue clearing and optical sectioning.

a, Schematic of tissue clearing process describing hydrogel embedding, tissue clearing, thick sectioning (250 µm), and antibody staining of explanted scaffolds. **b,** Gross images of whole scaffold before and after tissue clearing. **c,** Tiled confocal z-stack images of an entire scaffold sectioned into 4 slices. **d,** Representative tissue cleared scaffold images of DTCs as singular and micro-colonies. **e,** Comparison of complete single and colonized DTC counts between BLI- scaffolds with and without hPBMCs. **f,** Comparison of normalized frequency of DTC colony per 100 DTCs in BLI- scaffolds with and without hPBMCs. **g,** Representative HIS of $Ki67^{+}$ tumor colony (left) and quantitative comparison of $Ki67^{+}$ of single and colonized DTCs between scaffolds with and without hPBMCs (right). White arrows identify $Ki67^{+}$ cells (n= 3 independent scaffolds from mice without and with hPBMCs). *P<0.05

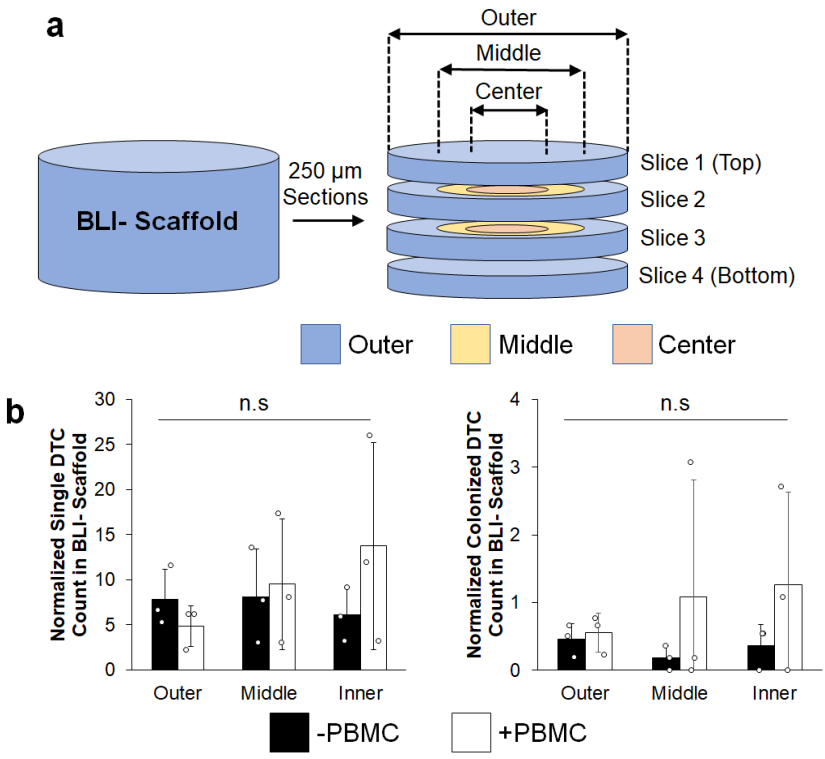

Figure 4.13. Spatial dissection of DTCs in BLI- scaffolds.
a, Schematic of BLI- scaffold processing and region designation. **b**, Normalized distribution of single and colonized DTCs in each region.

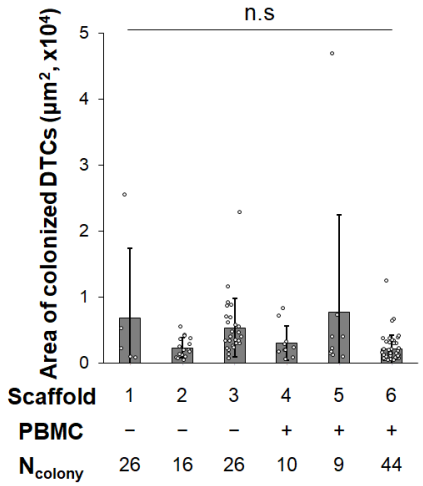

Figure 4.14.Colonized DTC size measurements from SLI- scaffolds via whole tissue analysis.

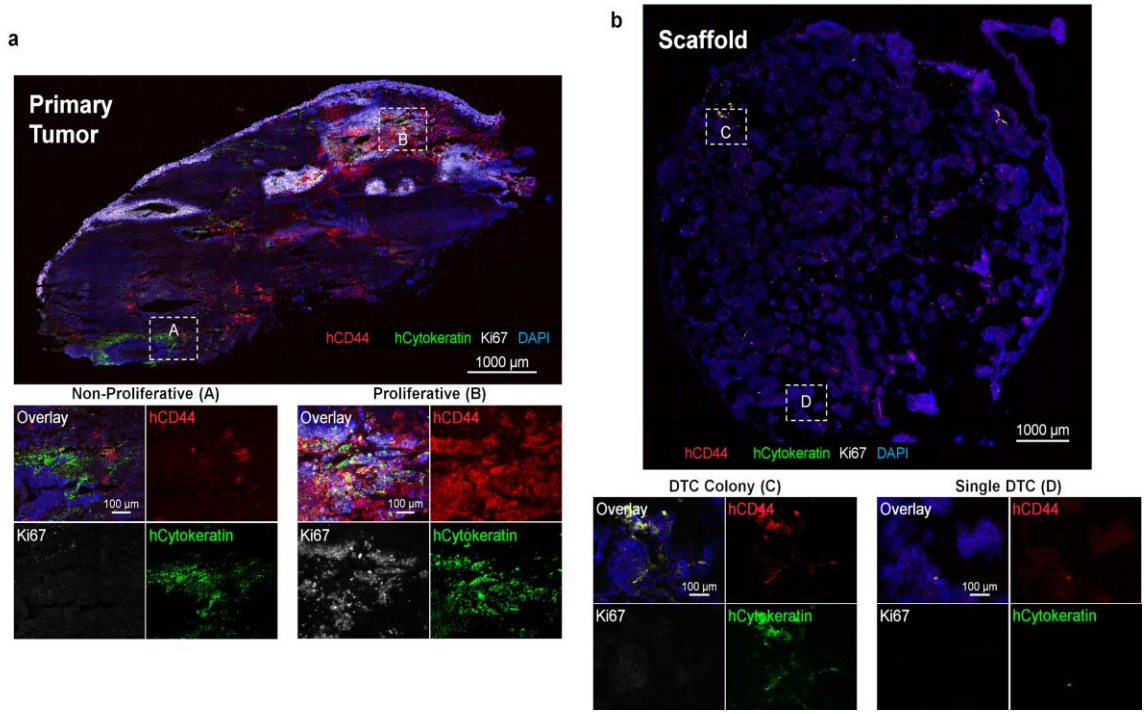

Figure 4.15. IHS of Ki67, hCD44 and hCytokeratin in a primary tumor and an implanted hBMSC-scaffold.
a, Human CD44 and human cytokeratin do not have high overlap in primary tumor. Proliferative regions of the primary tumor had higher overlap than non-proliferative regions. **b**, Nearly all single and colonized DTCs had overlapping human CD44 and human cytokeratin.

4.3.7 Comparative analysis of niche factors identifies key microenvironmental regulation of DTCs in single-to-colony transition

Next, we characterized how early DTC niches evolved by probing the local tumor microenvironments in single and colonized DTCs. By leveraging the uniform pore geometry of the scaffold, we generated a standardized imaging analysis of the microenvironment **(Figure 4.16a)**. Antibodies for IHS were chosen to determine the role of blood vessels (mCD31), human stromal cells (hVimentin), human immune cells (hCD45), and innate mouse immune cells in the single-to-colony transition of DTCs. Snapshots were collected in the tumor microenvironment of single cell and tumor colonies from at least 4 independent scaffolds **(Figure 4.16b)**. We first determined the proximity of

human immune cells to single and colonized DTCs. $hCD45^+$ cells located significantly closer to colonized DTCs. About 25% of tumor colonies were infiltrated with $hCD45^+$ cells. However, colocalization of single tumor cell and human immune cells was rare **(Figure 4.16c)**. Next, we analyzed the correlation between single and colonized DTCs with respect to the distance from blood vessels. In general blood vessels were found within 50 μm of a tumor cell. Without hPBMCs, over 50% of tumor colonies had at least one infiltrating blood vessels, but this phenomenon was observed in less than 35% of tumor colonies in scaffolds with hPBMCs **(Figure 4.16d)**. As expected, the average colony size infiltrated with blood vessels was significantly larger than those without, but there existed no significant correlation between tumor colony size and hPBMCs **(Figure 4.16e)**. Functional characterization between $Ki67^+$ tumor colonies and blood vessel availability revealed that nearly all (8/9) proliferative colonies had infiltrating vasculature. However infiltrating vasculature did not guarantee proliferation, only accounting for 26% (9/35) instances. These observations were not dependent on the presence hPBMCs **(Figure 4.17)**.

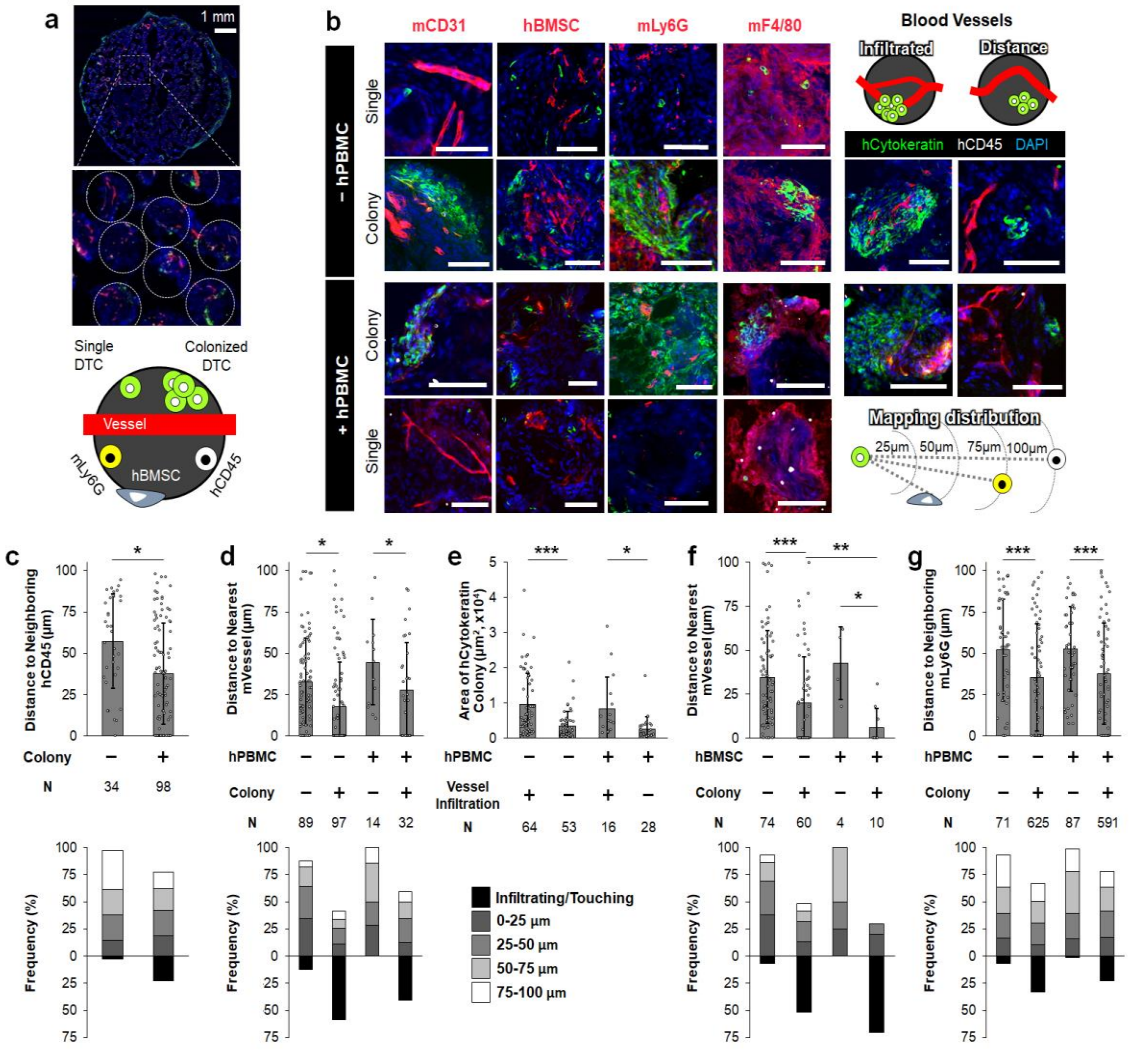

Figure 4.16. Quantitative comparison of vascular, stromal and immune niches between single and colonized DTCs in single pore microenvironment.

a, Representative images of dormant human DTC bearing scaffold and schematic of pore imaging targets. **b,** Representative IHS of microenvironments surrounding single and colonized DTCs with vascular and cellular niche components including hCD45, hBMSCs, mLy6G, and mF4/80. Scale bars 100 µm. **c,** Comparison of distribution profiles of neighboring hCD45$^+$ cells to hTumor cells between single and colonized DTCs (top) and frequency mapping of hCD45$^+$ cells (bottom). **d,** Comparison of distribution profiles of nearest mCD31$^+$ cells to hTumor cells with and without hPBMC injection (top) and frequency mapping of mCD31$^+$ cells (bottom). **e,** Comparison of tumor colony size with and without infiltrating mVessel. **f,** Comparison of distribution profiles of mCD31$^+$ cells to hTumor with and without neighboring hBMSCs (top) and frequency mapping of mCD31$^+$ cells (bottom). **g,** Comparison of distribution profiles of neighboring mLy6G$^+$ cells to hTumor cells with and without hPBMCs (top) and frequency mapping of mLy6G$^+$ cells (bottom). Representative values were plotted, selected by ordering datasets and averaging every 10 points, when N>100. Data collected from 5 biologically independent scaffolds from each group. *P<0.05, **P<0.005, ***P<0.0005.

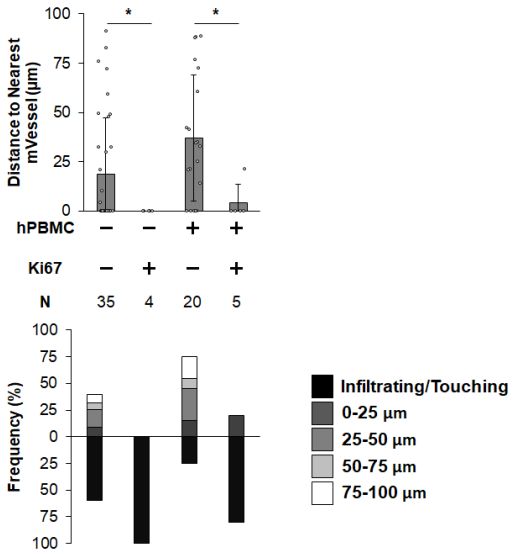

Figure 4.17. Correlation between tumor infiltrating vessels and proliferative tumor colonies.
Proliferative tumor colonies were always within 25 um of mouse blood vessel. *P<0.05

We extended quantitative analysis of IHS images with other microenvironmental components. First, the distance between tumor cells and blood vessels was considered when in the proximity of hBMSCs. Although the existence of DTCs and hBMSCs in the same pore was rare, as cellularity of hBMSCs decreased over the implantation period, tumor colonies that formed near hBMSCs were more likely to be infiltrated with a blood vessel than those not closely associated with human stroma **(Figure 4.16f)**. Next, we characterized the recruitment and distribution of endogenous mLy6G$^+$, mLy6C$^+$, and mF4/80$^+$ cells to determine the role of innate immune cells. Abundant mLy6C$^+$ and mF4/80$^+$ cells were observed at the pore periphery in nearly every pore regardless of experimental condition indicating that their response was dominantly triggered by the biomaterial rather than tumor or human immune cell activities **(Figure 4.18)**. Both mLy6C$^+$ and mF4/80$^+$ cells are known critical players in tissue remodeling, secreting protease enzymes including matrix metallopeptidase 9 (MMP-9) [233]. IHS of MMP-9

confirmed localized tissue remodeling activity at the pore surface **(Figure 4.19)**. Interestingly, mLy6G$^+$ cells were preferentially localized within tumor colonies, compared to single DTCs **(Figure 4.16g)**. The distribution of mLy6G$^+$ cells in tumor colonies was independent of their proliferative status confirmed by Ki67 staining **(Figure 4.20)**. Taken together these results indicate that increasing vascular connection and recruitment mLy6G$^+$ cells are common and could be important changes in DTC niches during single-to-colony transition.

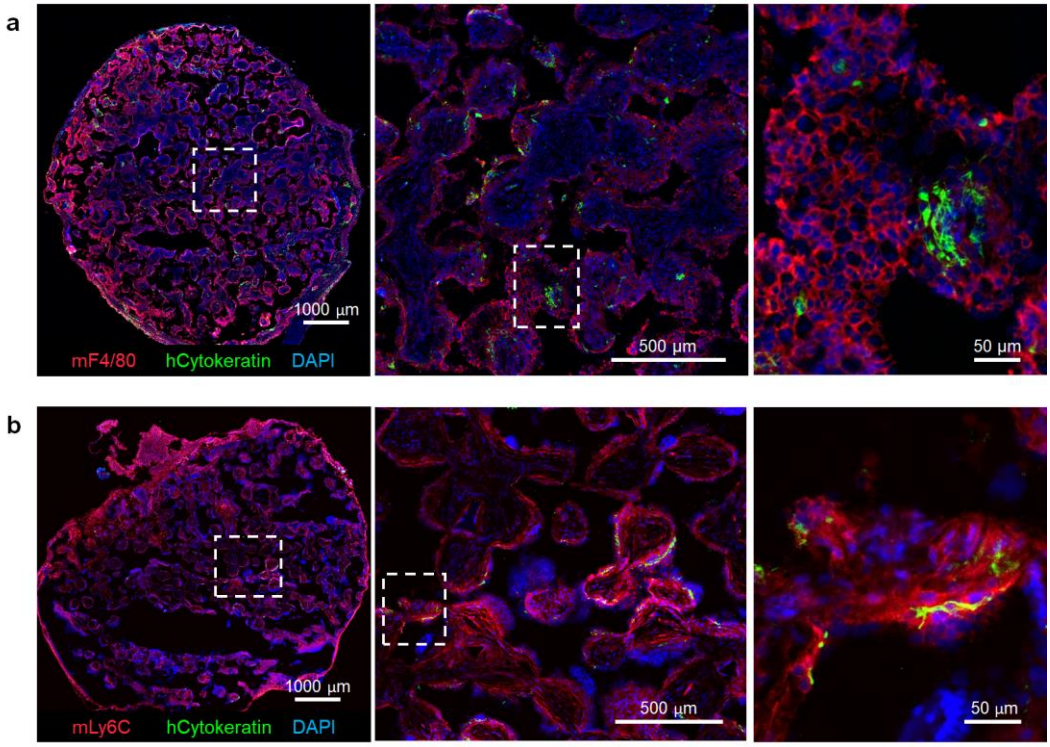

Figure 4.18. HIS of mouse F4/80 and Ly6C in hBMSC-scaffold.
a, Representative IHS images of mF4/80 and **b**, mLy6C staining in disseminated tumor microenvironment. Widespread staining made quantification difficult and non-conclusive.

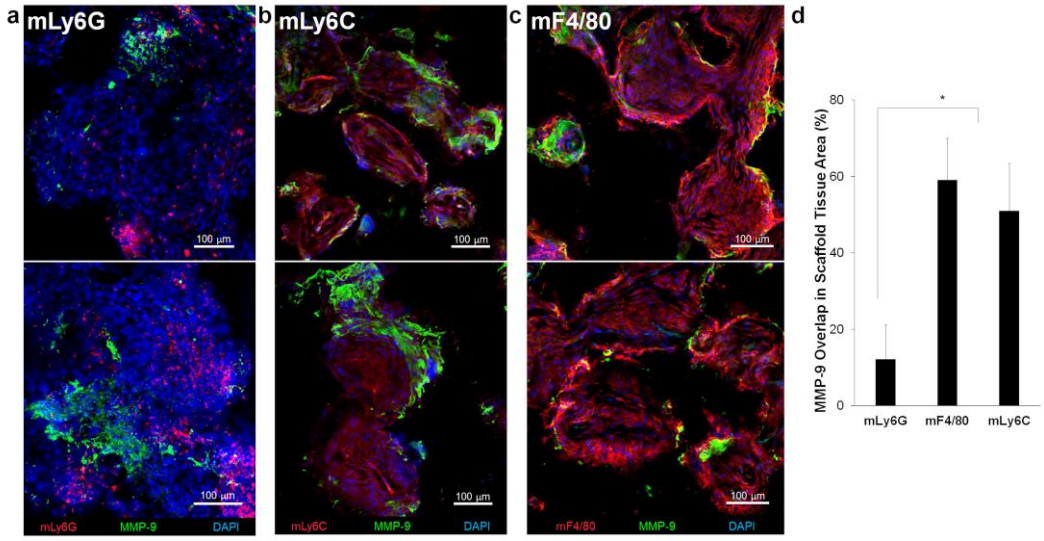

Figure 4.19. IHS of MMP-9 in hBMSC-scaffolds.
Representative IHS images of **a**, mLy6G, **b**, mLy6C, and **c**, mF4/80 staining in scaffold microenvironment. High amounts of MMP-9 at the biomaterial scaffold interface. **d**, Quantification of MMP-9 source reveals mF4/80 and mLy6C cells are main producers.

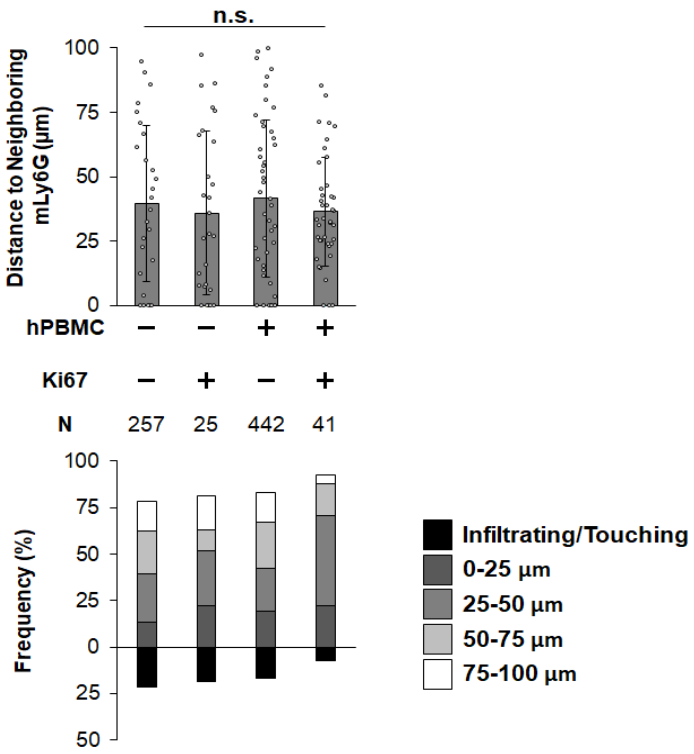

Figure 4.20. Correlation between mLy6G and proliferative tumor colonies.
No change in local mLy6G cell distribution between proliferative and non-proliferative tumor colonies. Addition of hPBMCs did not influence distribution. Characterization was not performed on singular DTCs since all cells were non-proliferative.

4.3.8 Multiplex IHS of overt metastasis substantiates the importance of innate immune cell influx in continuous outgrowth of DTCs

To understand how the early DTC microenvironment evolved during metastatic relapse, we characterized tumors that had progressed beyond the initial awakening events. A panel of 9 different antibodies, hCytokeratin, hVimentin, mCD31, hCD45, Ki67, hCD4, hCD8, mLy6G, and mF4/80, and the nucleus stain DAPI were used to visualize and quantify cellular signatures in the tumor microenvironment **(Table 4.1)**. Eight consecutive histological sections, 20 µm thick, were stained with sets of 3-5 antibodies to generate a multiplexed and comprehensive view of the metastatic tumor heterogeneity **(Figure 4.21)**. Using ImageJ, individual image channels were centered and overlaid. From these cumulative images, eight zones were manually identified that highlighted regions of diversity **(Figure 4.22a)**.

Table 4.1. Antibody reagents.

PRIMARY ANTIBODIES			
Vendor	Catalog Number	Chemical Name	Target
DAKO	M072529-2	Mouse - Anti Human Vimentin	hStroma/hTumor
Abcam	ab5694	Rabbit - Anti Alpha Smooth Muscle Actin	Blood Vessel (CLARITY)
BD Pharmingen	550274	Rat - Anti Mouse CD31	Blood Vessel
BD Pharmingen	555480	Mouse - Anti Human CD45	hImmune
BD Pharmingen	555631	Mouse - Anti Human CD8	hCD8
BD Pharmingen	555344	Mouse - Anti Human CD4	hCD4
Abcam	ab16667	Rabbit - Anti Ki67	Proliferation
Abcam	ab107115	Chicken - Anti Human Cytokeratin 8	hTumor
BD Pharmingen	565409	Rat - anti mouse F4/80	mMacrophage
BD Pharmingen	557445	Rat - anti mouse Ly-6G Ly-6C	mNeutrophil
Lifespan Biosience	LS-C193787-100	Guinea Pig - Anti Human Cytokeratin	hTumor
BD Pharmingen	550392	Mouse - Anti Human CD44	hStem Cell
Abcam	ab15627	Rat - anti Mouse Ly6C	mMonocyte
ThermoFisher	PA513199	Rabbit - anti MMP	MMP-9

SECONDARY ANTIBODIES		
Vendor	Catalog Number	Chemical Name
Life Technology	A-11006	Goat anti-Rat IgG (H+L) Antibody - Alexa Fluor® 488
Life Technology	A-21424	Goat-Anti Mouse IgG (H+L) Antibody - Alexa Fluor® 555
Life Technology	A-11011	Goat Anti-Rabbit IgG (H+L) Antibody, Alexa Fluor® 568
Life Technology	A-21054	Goat-Anti Mouse IgG (H+L) Antibody - Alexa Fluor® 660
Life Technology	A-16058	Goat-Anti Chicken IgY (H+L) Antibody, biotin conjugate
Life Technology	Q10163MP	Qdot 705 Streptavidin Conjugate
Life Technology	A21449	Goat Anti-Chicken IgG (H+L) Antibody - Alexa Fluor® 647
Life Technology	A21450	Goat Anti-Guinea Pig IgG (H+L) Antibody - Alexa Fluor® 647
Life Technology	A10680	Goat Anti-Mouse IgG, IgM (H+L) Antibody - Alexa Fluor® 448

FACS		
Vendor	Catalog Number	Chemical Name
BD Bioscience	555483	Hu CD45 PE

ELISA		
Vendor	Catalog Number	Chemical Name
R&D Systems	DY206	Human IL-6 DuoSet
R&D Systems	DY217B	Human IL-10 DuoSet
R&D Systems	DY210-05	Human TNF-alpha DuoSet
R&D Systems	DY293B	Human VEGF DuoSet
R&D Systems	DY208	Human CXCL8/IL-8 DuoSet

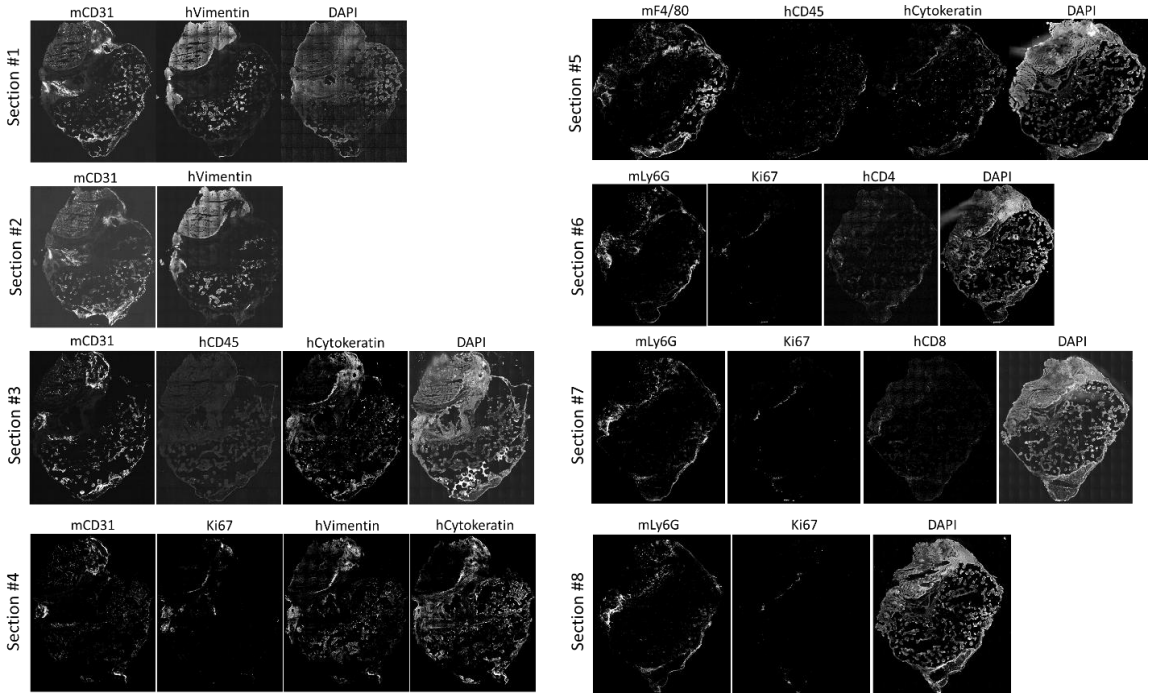

Figure 4.21. IHS of eight consecutive overt metastasis slices with different antibody staining.

Individual monochrome images showing individual antibody staining results on eight consecutive tissue sections.

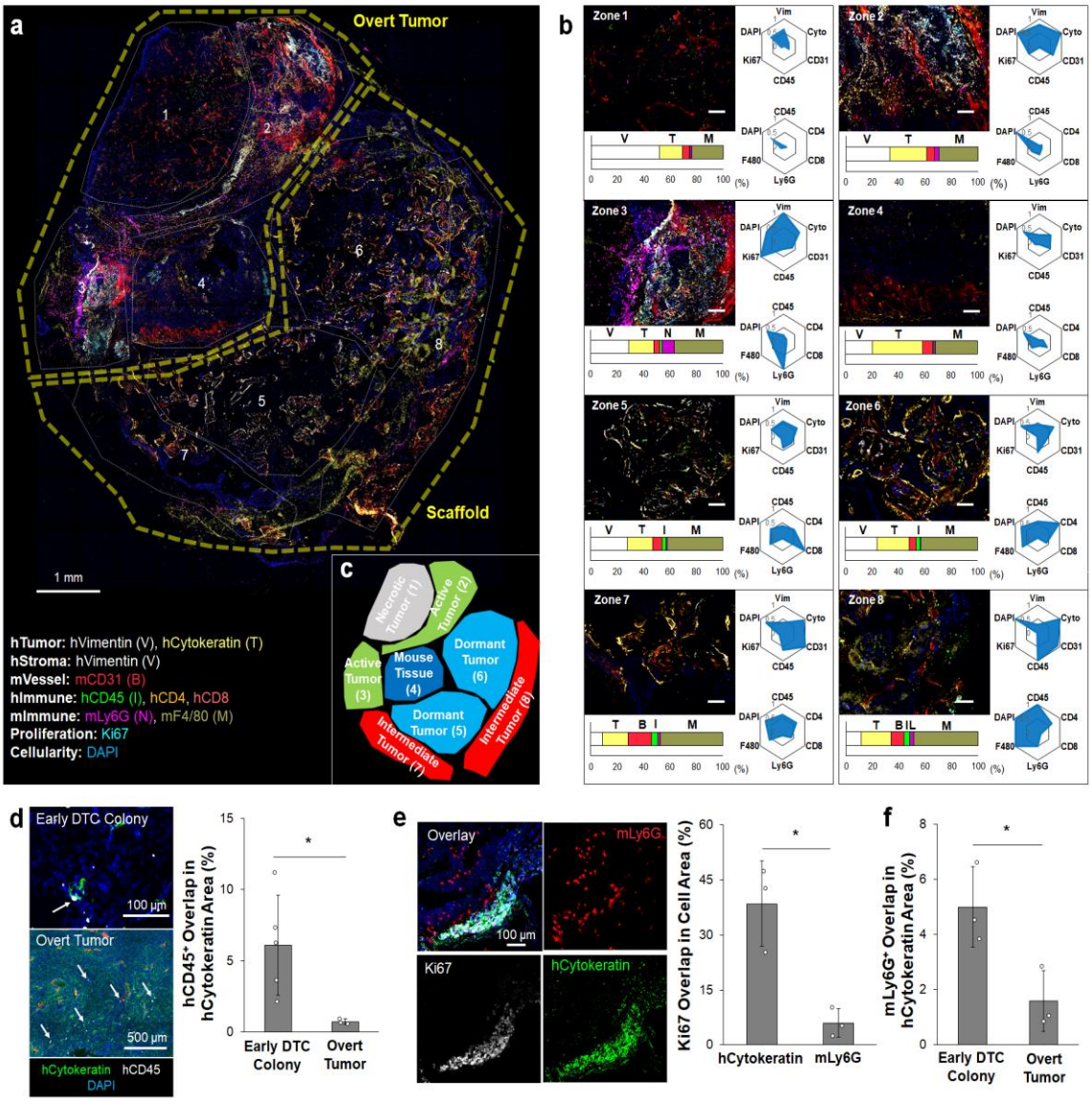

Figure 4.22. Multiplex IHS imaging-based characterization of heterogeneity in overt metastatic microenvironments.

a, Overlaid IHS images from eight consecutive 20 µm thick slices and manually defined zones representing distinct microenvironment profiles with a list of antibodies and their associated targets. **b,** Representative IHS images of each zone with quantitative cellular complexity. Bar graphs display intra-zone composition of quantified antibody staining. Radial plots represent inter-zone comparison of cellular markers normalized to the zone with the highest signal. Top panel highlights human stromal, tumor, and immune celllocalization. Bottom panel highlights human and mouse immune cell subset. **c,** Five functional zones capturing different states of metastatic tumors: (1) necrotic tumor, (2) active tumor, (3) host tissue, (4) dormant tumor, and (5) intermediate tumor. **d,** IHS images of hCD45 cells found within early DTC colonies (n=5) and overt scaffold metastases (n=3) with quantitative representation of overlapping hCD45^{+} cell coverage. Arrows show

infiltrating hCD45$^+$ cells (white). **e,** IHS image of mLy6G$^+$ cell localization at the boundary of an actively growing overt metastasis and quantitative comparison of Ki67 stain overlap with human tumor and mLy6G$^+$ cells (n=3). **f,** Quantitative comparison of overlapping mLy6G$^+$ cells in early DTCs and overt scaffold metastases (n=3). *P<0.05.

To quantitatively determine cellular and functional signatures of each zone, we developed an imaging analysis pipeline. Two different characterizations were considered for quantifying the selected regions **(Figure 4.23)**. The first analysis compared the absolute pixel number of each stain within each zone to highlight the makeup of each region, which was displayed as a bar graph. The second was a comparative analysis between zones, which was plotted on a radial chart broken into two panels; (i) a general overview of cellularity, and (ii) the diversity of immune cells **(Figure 4.22b)**. Comparison of the different zones revealed similar phenotypes that were categorized into five separable regions. Zone 1 highlighted a typical necrotic tumor region consisting largely of weak human tumor and immune cell markers. Mouse macrophages were present but relatively low compared to other regions. A pocket of mouse tissue, zone 4, was characterized by a low signal in human cell markers and weak Ki67 signal. Zones 5 and 6 exhibited similar tissue microenvironments to a dormant DTC niche; a high number of human stromal and immune cells with relatively few mLy6G$^+$ cells were observed, and overall Ki67 signal was weak. On the periphery of the scaffold, zones 7 and 8, an increase in vessels and immune cells was observed **(Figure 4.22c)**. In contrast to our observation of micro-metastases, the frequency of human immune cells in overt tumor regions was significantly lower **(Figure 4.22d)**. This result was possibly caused by reduction in human immune cells, but IHS of spleens revealed the presence of hCD45$^+$ cells suggesting that a subset of human immune cells systemically migrate and proliferate in the secondary host. The frequency of hCD45$^+$

cells in the spleen was not significantly different between secondary mice with and without overt tumors **(Figure 4.24)**. Zone 2 and 3 contained actively growing tumors indicated by high DAPI and Ki67 staining. Zone 2 had higher hCytokeratin signal than zone 3 but only half the relative Ki67. High hVimentin in zone 3 suggests a more mesenchymal tumor phenotype, which was linked with higher proliferation compared to the more epithelial tumor phenotype in zone 2. Colocalization analysis confirmed that Ki67 staining was mostly derived from tumor cells and not mLy6G$^+$ cells that were also observed in these actively growing tumor zones **(Figure 4.22e)**. mLy6G$^+$ cells limitedly infiltrated overt tumor regions and remained on the tumor periphery, opposite to what was observed during the early stages of colonization **(Figure 4.22f.)**. Considering the relatively short lifespan of mLy6G$^+$ cells, about 1 day [234], this result indicates that mLy6G$^+$ cells continuously migrated to actively growing tumors. This phenomenon was repeatedly observed in three independent overt metastatic tumors **(Figure 4.25)**. Together these results demonstrate that the tumor microenvironment evolves during progression to an overt tumor, including phenotypic changes of tumor cells to a more mesenchymal phenotype, and continual recruitment of innate immune cells, especially mLy6G$^+$ cells.

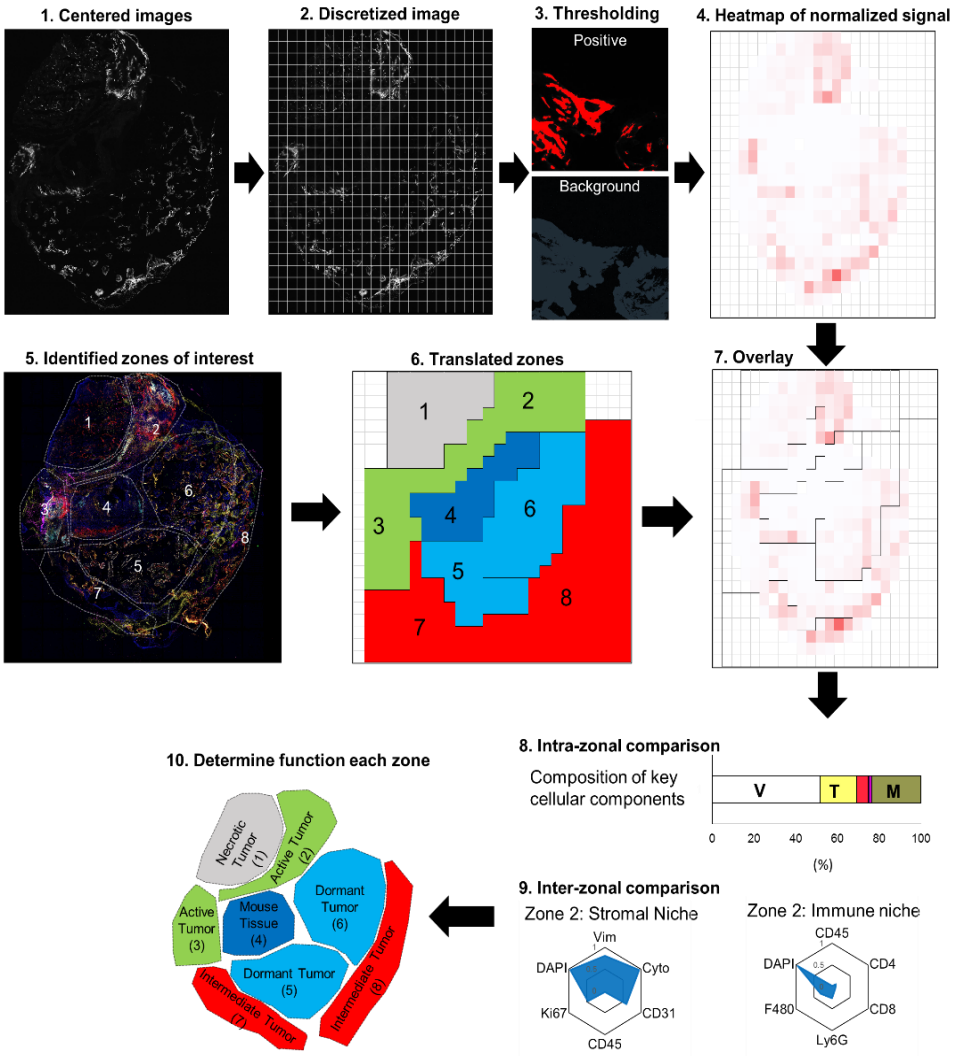

Figure 4.23. Active tumor microenvironment imaging analysis pipeline.

1) Images were centered and canvas size equalized.
2) Scaffold images discretized into 24x24 grid of subimages.
3) For each antibody positive signal separated from background noise. Total tissue area was calculated by increasing background to include autofluorescent tissue.
4) Positive signal from each subimage was normalized to total tissue area and displayed as a heatmap.
5) Visual inspection of images revealed 8 zones that housed unique features.
6) Manually determined zones of interest translated to 24x24 grid.
7) The 8 translated zones were overlaid on images with normalized signal. Normalized signal was recalculated for each of the 8 zones.
8) Intra-zonal composition was performed by dividing the positive pixels for each stain and dividing by the summation of all positive pixels from all staining except Ki67 and DAPI. Stain compositions were plotted on a bar plot.
9) Inter-zonal comparison was performed by taking normalized signal from each zone and dividing by the largest value for each stain. Thusly, the zone with the highest

value for a particular stain would have a value of 1. Quantitative results were displayed on a radial plot broken into two different panels.

10) Results of 8 and 9 analyzed to generate groupings of similar features.

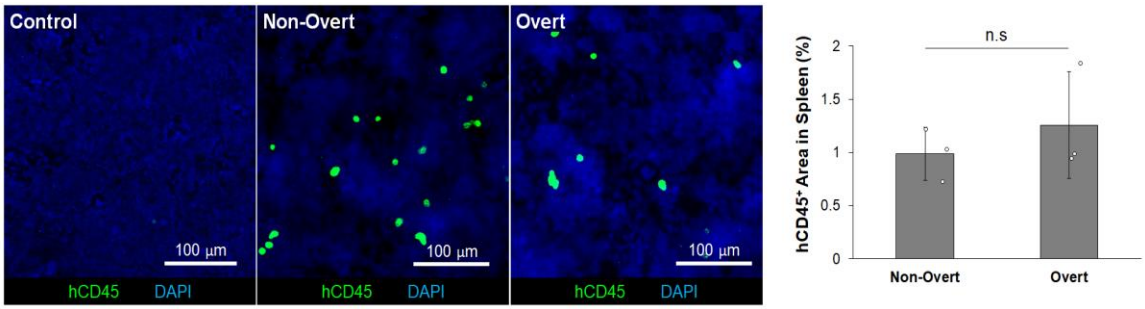

Figure 4.24. Human PBMCs enter circulation in secondary mouse host.
Spleens taken from non-injected (control) and hPBMC-injected mice. Non-overt spleens taken from mice without overt-metastasis bearing scaffolds. Overt spleen taken from mice with a scaffold with an overt metastasis.

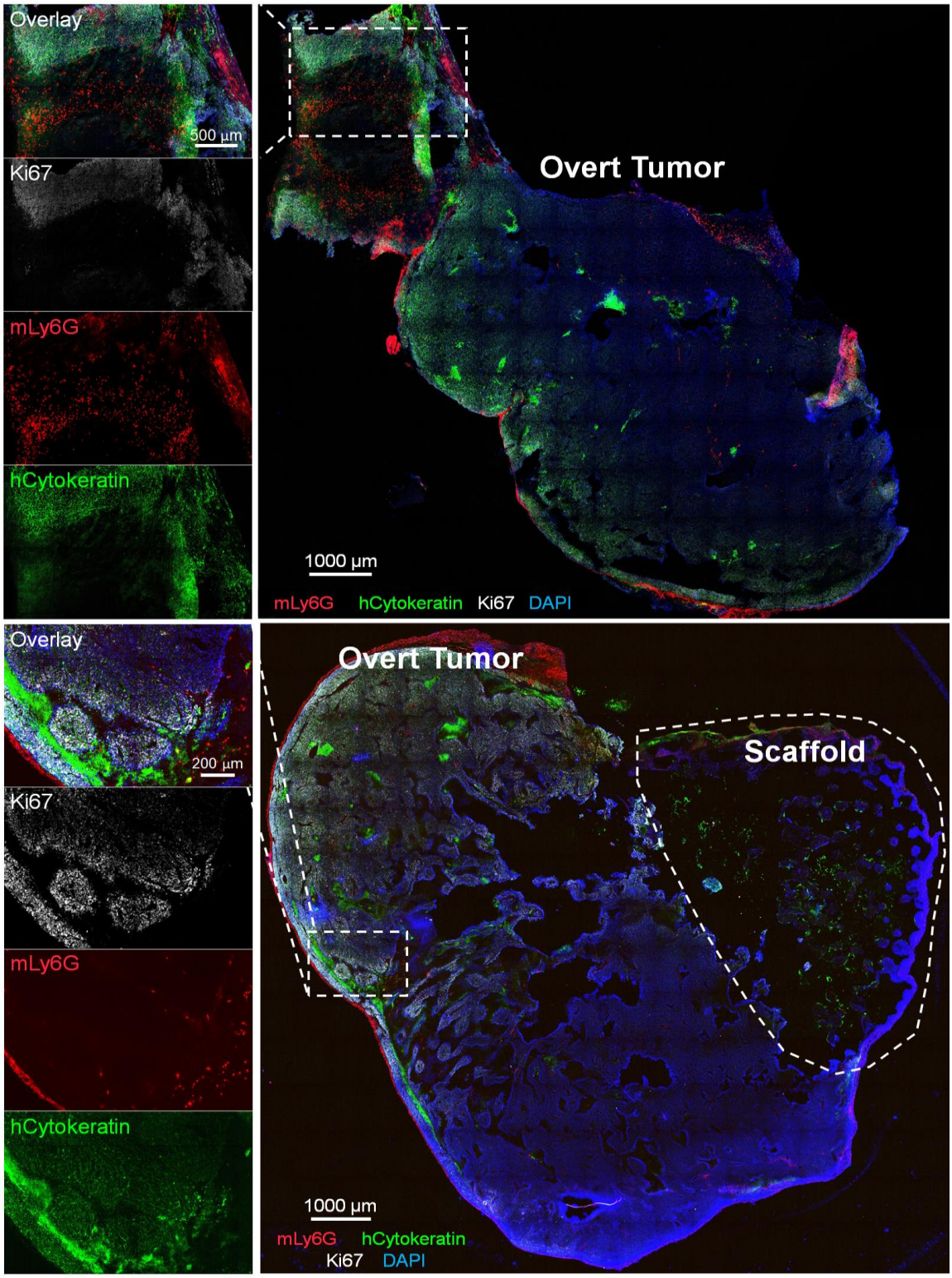

Figure 4.25. IHS of mLy6G, Ki67, and hCytokeratin in independent over metastasis. IHS of Ki67 and mLy6G localization in independent actively growing overt tumors beyond the boundaries of the scaffold.

4.4 Discussion

Accumulating evidence suggests that systemic spread of DTCs may be unavoidable [235], but metastatic relapse can be preventable. For example, low-dosage aspirin [236], canakinumab [237], metformin [238], and cabozantinib [239] have demonstrated significantly reduced risk for metastasis. It is imperative to develop detailed understanding of how these molecules suppress revitalization of dormant DTCs in distant tissue sites. The lack of relevant experimental models that can faithfully determine the long-term functional consequence of therapeutic intervention in the context of humanized tissue microenvironments has been a critical challenge. The presented tissue engineered pre-metastatic niche model represents a new opportunity to study the post-dissemination phase of human cancer biology from three distinct aspects. First, the use of biomaterials to create a pre-metastatic niche allowed controlled and analytical experimentation to quantitatively distinguish key features of microenvironmental regulation in dormant-to-active transition of DTCs. The standardized structure of ICC scaffolds generated reproducible tissue microenvironments and streamlined multiplex imaging and comparative analysis of DTC niches. Additionally, optical transparency of PAA hydrogel permitted whole tissue clearing and complete optical sectioning of tumor microenvironments to detect rare DTCs while retaining spatial resolution. Implantation of biomaterials in a subcutaneous pocket enables easy accessibility to various functional characterizations including direct measurement of tumor growth, BLI, and possible intravital imaging via surgical engraftment of a skinfold window chamber [97, 184]. The tunable design of ICC hydrogel scaffolds permits easy manipulation of physical and geometrical parameters. Recently there has been a substantial progress in understanding the interaction between implantable biomaterials and host tissue

and immune cells [240]. For example, poly-lactic and glycolic acid (PLGA) scaffolds [241] and methacrylated alginate cryogels [242] manipulate dendritic cell homing and immune response; scaffolds composed of extracellular matrix proteins have modulated pro-regenerative systemic immune environments [164]; physical dimensions of biomaterials influence foreign body response [120]. These efforts can further empower an implantable pre-metastatic niche model to study human tumor metastasis.

Second, *in vitro* seeding of stromal cells provided additional capability to create defined and functional implantable pre-metastatic niches. Here hBMSCs were introduced into the scaffold to create humanized stromal niche and modulate foreign body response and interscaffold angiogenesis. hBMSCs are known to secrete immunomodulatory and proangiogenic molecules, which resultantly attenuate foreign body response [166] and enhanced angiogenic activity [97] in previous studies. Similarly, different types and combinations of stromal cells can be introduced into biomaterials to induce defined functionality of microenvironments. For example, genetically engineered stromal cells that secrete specific human cytokines were used to create defined humanized soluble microenvironments [134].

Finally, the transplantation strategy separated early metastatic niches from advanced tumors and prolonged the microenvironment evolution to substantiate functional mechanisms behind metastatic relapse. Serial transplantation has been commonly conducted to maintain intrinsic characteristics of human blood cancer cells and solid tumors (e.g. patient derived xenograft tumors) in the context of living system for extended periods [243-244]. Applying this concept to metastatic tumor microenvironments overcame the fundamental limitation of mouse model for long-term evolution of the DTC niche beyond

the lifespan of primary host mice, which enabled observation of the full spectrum of post-disseminated tumor progression. Here we exploited this feature to determine the functional consequence of acute inflammation triggered by hPBMC injection. Even though the experiment was halted 10 weeks after transplantation, dormant DTC microenvironment studies could continue for longer experimental duration. This capability will facilitate observation of the long-term dormant DTC niche and the screening of drugs for metastasis prevention.

Intravenous injection of hPBMCs instigated early humanized DTCs niches and subsequent metastatic relapse became evident 6 weeks after serial transplantation. The incidence of metastasis was significantly lower and stabilized when compared to hPBMC-free scaffolds. This phenomenon is reminiscent of a graft-versus-tumor response [211, 245-246]. Comparative analysis of single and colonized DTCs revealed a correlation between human immune cells and colonized DTCs, whereas single DTCs did not directly interact with human immune cells **(Fig. 4.16c, d)**. Given the observation of reduced DTCs in mice that received hPBMCs, direct contact between human immune and tumor cells could be a potential mechanism in the elimination of DTCs. Indeed, a previous study showed that systemic delivery of hPBMCs prior to the subcutaneous injection of human PC3 tumor cells in NSG mice significantly decreased ectopic tumor development with increased primary tumor-infiltration of T-lymphocytes [247]. Additional studies reported that T-lymphocytes within patient-derived xenografts continually proliferated and systemically spread to the host NSG mouse [248]. Similarly, we confirmed the presence of $hCD45^{+}$ cells in the spleens of secondary mice, indicating that a subset of human immune cells migrated out from the scaffolds and potentially continued growth. This could be the mechanism that

leads to long-term stabilization of DTC growth in secondary hosts. Although hPBMCs reduced overall metastatic relapse, the incidence to develop overt metastasis was not changed. Additionally, complete optical sectioning of BLI- scaffolds revealed an increased frequency of colonized DTCs in total DTC counts in mice that received hPBMCs **(Fig. 4.12f)**. These results suggest that although hPBMCs decreased DTC burden, during this process they may also increase the chance to initiate colonization of DTCs possibly due to local tissue inflammation. However, detailed mechanisms by which human immune cells promoted colonization of DTCs remains an open question.

Previous studies have highlighted vasculature and immune cell interaction as critical for reactivation of dormant DTCs [32, 63, 249-252]. Our results provide additional evidence to support these findings and quantitatively capture the changes in the local DTC microenvironments from single, to colonized to overt metastasis. The vasculature is initially used by tumor cells to migrate to distant tissues, however during the period of dormancy, DTCs remain distant from the vasculature. Quantitative analysis of the blood vessels surrounding DTCs revealed that tumor cells begin to proliferate without immediate contact with a blood vessel, but their growth could not exceed a cross-sectional area of roughly 4,000 μm^2 without the connection to a blood vessel. It remains unclear if DTCs migrate toward a blood vessel, a vessel is recruited by DTCs, or DTCs and vessels meets opportunistically. Recent studies suggest the source of angiogenic signaling may be derived from local immune and stromal cells that release proinflammatory or proangiogenic factors that initiate endothelial tip cell sprouting [63, 253-254], induce phenotypic switching of perivascular cells to a less differentiated state [28], or transiently enhance vascular remodeling activity.

Additionally, our results substantiate the important role of continuously recruited innate immune cells in forming a supportive microenvironment for awakening dormant DTCs. mLy6G$^+$ cells consist of several myeloid cells including monocytes, granulocytes, and neutrophils. Recent studies have shown that neutrophils are associated with playing a key role in initiating metastatic outgrowth [32, 249-252]. Deep optical characterization of the metastatic niche demonstrated their presence within awakening DTC colonies during initial tumor colonization, however it is unclear how the host neutrophils seek out early stage, reactivated DTCs and their role in promoting or inhibiting growth. Once a tumor colony became an advanced large metastasis, mLy6G$^+$ cells no longer infiltrated but remained on the periphery where they were continually recruited. The lack of infiltrating neutrophils within overt tumors indicates that the tumor may produce a repulsive microenvironment once it has formed a large enough mass. The varying activities of mLy6G$^+$ cells within the different stages of tumor development demonstrate the need for deeper understanding of myeloid cell biology such as neutrophils in the tumor microenvironment, which may lead to more effective anti-metastatic strategies [255]. It is possible, and likely that many budding metastases fail to evade immune response at the initial stages of outgrowth and become terminated. Tumors that can evade microenvironmental control will continue to proliferate and gain control of the microenvironment and dictate bi-directional interactions with surrounding cells. From our data, we demonstrated that overt tumor cell proliferation occurs together with vascularization and exclusion of innate and adaptive immune cells, while selectively attracting a subset of innate immune cells to the actively proliferative boundary, allowing for continuous growth **(Figure 4.26)**.

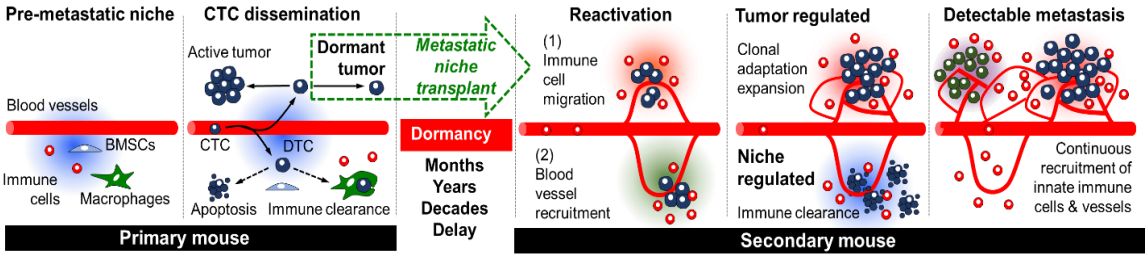

Figure 4.26. Proposed microenvironmental regulation of DTCs during initial dormancy, reactivation, and overt metastasis along with the experimental transplantation strategy from primary to secondary mice for long-term observation.

The presented implantable pre-metastatic niche model has demonstrated enabling features for detailed observation of awakening dormant DTCs *in vivo*, yet there is still room to improve. First, since the established humanized microenvironments are comprised of three different donors, human immune interactions are allogeneic, which limits the study of adaptive immune system mediated tumor microenvironment regulation. Creating donor-matched microenvironments is possible by obtaining different tissue cells from the same patient but this involves clinical and ethical considerations [256]. One alternative solution is to use induced pluripotent stem cells that can differentiate into stromal, hematopoietic, and tumorigenic cells [257]. While the current study has focused on humanized tumor microenvironments keeping in mind translational opportunity, for mechanistic studies the experimental system could be adapted to an entirely mouse-based model. Second, hPBMC injection delivers fully functional human immune cells but the innate immune cell effect is restricted to a short-term period due to their limited lifespan; the average lifespan of monocytes and neutrophils are about 1 week and 24 hours, respectively [234, 258]. Instead, repeated injection of human granulocytes into the humanized mice could replenish short-lived immune cells. Alternatively, the transplantation of human hematopoietic stem cells

could stably provide human innate immune cells, but differentiated human immune cells in the mouse bone marrow may not carry full functionality [259]. Emerging data including our own has demonstrated that innate immune cells play a critical role in regulating the tumor microenvironment [260-262]. Innate immune cell activity does not strictly rely on the highly specific binding required for adaptive immune cells, and thus human tumor and mouse innate immune cell interaction may be clinically relevant. Third, the prolonged local foreign body unnaturally elevated macrophage activity and may not accurately reflect physiological situations. Recent studies have shown that locally implanted biomaterials modulate systemic immune response and host regenerative potential [164, 263-264]. Additionally, biomaterial-induced myeloid cell responses were shown to be tunable by incorporating macrophage selective drugs e.g. clodronate for macrophage depletion [184]. Finally, transplantation of the intact microenvironments possibly caused brief temporal oxygen and nutrient deprivation. Aside from intrinsic changes to DTCs, their fate can be critically influenced by the secondary host cells, especially immune cells. We minimized this potential effect by using syngeneic mice and implanted the microenvironments to the same anatomical locations. However, a similar clinical scenario has been reported in the field of organ transplantation where dormant DTCs in the donor organ developed metastasis in the recipient [49, 265]. Indeed, this feature may provide a new opportunity to investigate the role of local and systemic tissue microenvironments by altering the recipient host animal in terms of age, immune competence, and implantation site.

Mouse models play a critical role in advancing our understanding of cancer metastasis, however their capability to capture the long-term evolution of the metastatic niche and their relevance to humans remains questionable. Tissue engineered humanized

metastasis models can reduce the pre-clinical gap and potentially uncover new biological interactions between human tumors and the surrounding microenvironment. Studies can be readily extended to characterize the extracellular matrix, and molecular and genetic profiles. One promising future direction is to combine comparative analysis based on endpoint IHS characterization with temporal observation of cellular processes via intravital or *ex vivo* imaging, which will enable deeper mechanistic understanding of the DTC niche evolution. The established metastasis model can also be applied to screen the effectiveness of drugs targeting DTCs and secondary outgrowths. Taken together, we envision that tissue engineered strategies will provide an invaluable tool to answer provocative hypotheses emerging in the cancer field and advance clinical translation of anti-metastatic therapeutic strategies.

4.5 Materials and Methods

All chemicals and materials were purchased from Sigma Aldrich or Fisher Scientific unless specified. All animal procedures were approved by the Institutional Animal Care and Use Committee at the University of Massachusetts-Amherst. Experiments and handling of mice were conducted under federal, state and local guidelines.

4.5.1 Type I collagen coated inverted colloidal crystal hydrogel scaffold fabrication

Inverted colloidal crystal hydrogel scaffolds were fabricated following the previously reported methods (33). Soda lime glass beads were sorted using an Advantech Sonic Sifter for each range with ~8% deviation. Beads dispersed in deionized (DI) water were gradually loaded into a glass vial (8 x 35 mm) to a height of 2-2.5 mm and were mechanically packed into a lattice structure in an ultrasonic water bath. Orderly packed

glass beads were dried in a 60 °C oven and then thermally annealed between 650 and 680 °C depending on the bead size for 4 hours in a furnace. A hydrogel precursor solution composed of 5, 15, 30, and 50 wt% acrylamide monomer, 1.5 wt% bis-acrylamide crosslinker, 0.2 vol% N,N,N',N'-tetramethylethylenediamine accelerator, and 0.2 vol% 2-hydroxy-2-methylpropiophenone photoinitiator in nitrogen purged DI water was prepared immediately before use. 150 µL of precursor solution was infiltrated into the glass bead template and centrifuged in a microcentrifuge at 9,000 RPM for 15 min and subsequently polymerized under a 15 W ultraviolet light source for 15 minutes. Polyacrylamide hydrogel-glass templates were removed from the glass vials the next day to ensure complete polymerization. Excess hydrogel was removed by scraping the glass bead template with a razor blade on all surfaces. Glass beads were selectively dissolved in alternating washes of an acid solution containing a 1:5 dilution of hydrofluoric acid in 1.2 M hydrochloric acid and 2.4 M hydrochloric acid (Caution: These chemicals are corrosive and must be used in a fume hood with proper protective gear). Washes were completed on a shake plate and solutions were changed every four hours until the beads were removed. Scaffolds were thoroughly washed with DI water to remove residual acid and lyophilized. Following lyophilization, scaffolds were resuspended in CryomatrixTM embedding resin and cut to 1 mm thickness on a CryoStar NX70. After thorough washing in DI water, scaffolds were sterilized with 70% ethanol and stored at 4 °C in sterile phosphate buffered saline solution (PBS). The final pore dimension of the optimized scaffolds used for the remainder of the study was 300 ± 16 µm. To support stromal cell adhesion on polyacrylamide hydrogel scaffolds, type I collagen extracted from rat tails was covalently immobilized on the pore surface using Sulfo-SANPAH conjugate chemistry.

4.5.2 Human BMSC isolation and culture expansion

50 mL of bone marrow aspirate obtained from a healthy donor was purchased from Lonza. Mononuclear cells were isolated via density gradient based centrifugation using Ficoll Paque (GE) at 1500 RPM for 30 minutes using minimum acceleration and no brake. Mononuclear cells were plated on T-225 flasks with Minimum Essential Medium Eagle, alpha modified (αMEM) supplemented with 20% FBS, 2% penicillin-streptomycin, 0.2% gentamicin, and 1 µg/L recombinant human fibroblast growth factor. After 1 week, colonies of adherent cells were harvested, cryogenically frozen in media containing 10% DMSO, and stored in a cryotank. The multilineage differentiation potential of hBMSCs were tested using standard protocols.

4.5.3 Human BMSC seeding and culture on a 3D hydrogel scaffold

Collagen coated ICC hydrogel scaffolds were partially dehydrated by removing excess PBS and drying in a biosafety cabinet. 5×10^5 hBMSCs suspended in 20 µL of growth media were dropped on top of a partially dehydrated scaffold. The cell suspension was drawn into the dried scaffold, facilitating deep and homogenous cell seeding in the 3D scaffolds. Cell loaded scaffolds were incubated for 20 minutes in a CO2 incubator to allow initial cell adhesion. Cell-scaffolds were transferred to a 48-well plate containing 500 µL of media and allowed to grow for up to one week prior to use. Media was changed every 3 days.

4.5.4 Subdermal implantation of hBMSC-scaffolds in NSG mice

A breeding pair of NOD-scid IL2Rg^{null} mice (005557) was initially obtained from the Jackson Laboratories. NSG mice were housed in sterile conditions with unrestricted

access to food and water. In this study 6-13 week age mice were used for implantation. Mice were anesthetized with 1.5% isoflurane and dorsal hair was removed with electric clippers and Nair. The skin was sterilized using 70% isopropyl alcohol prep wipes. Prior to surgery, 2 mg meloxicam/kg mouse weight was subcutaneously injected. 2 mm horizontal incisions were made in the upper and lower dorsal spaces. A subcutaneous pocket was formed by inserting surgical scissors into the incision and expanding. One scaffold per subcutaneous pocket was implanted and the incisions were closed with 2 Reflex 7 mm wound clips. Four scaffolds were implanted per mouse. Wound clips were removed after 1 week.

4.5.5 Characterization of cytokine secretion of implanted hBMSC-scaffolds

Implanted hBMSC-scaffolds were retrieved at 4 and 12 weeks from NSG mice. Explanted scaffolds were cut into 1-2mm pieces using surgical scissors and cultured in 500 µL of αMEM media supplemented with 1% mouse serum and 1% penicillin-streptomycin for 36 hours. For control samples, 1 week *in vitro* cultured hBMSC-scaffolds were used. Conditioned media was collected and used immediately for characterization human VEGF, IL-6 and, IL-8 secretion by DuoSet® ELISA kits (R&D Systems).

4.5.6 Tail vein injection of human PBMCs

Whole blood was obtained from 3 healthy male donors age 20-38 in BD Vacutainer K2 EDTA blood collection tubes. Mononuclear cells were isolated via density gradient-based centrifugation using Ficoll Paque at 1500 RPM for 30 minutes using minimum acceleration and no brake. From roughly 30 mL of whole blood we extracted 25-30 million PBMCs. Isolated mononuclear cells were counted and re-suspended in PBS to a density of $10x10^6$ or $20x10^6$ cells per 100 µL PBS. Scaffold bearing or scaffold and tumor bearing

mice were warmed under a heat lamp to dilate the tail vein, placed in a restrainer, and intravenously delivered by tail vein injection using a 27 Gauge needle.

4.5.7 Human PBMC distribution and cytokine secretion

Mice 6-13 weeks of age were implanted with BMSC seeded scaffolds. $20x10^6$ PBMCs suspended in 100 µL of PBS were intravenously delivered 5.5 weeks after scaffold implantation. Mice were euthanized 24 hours after PBMC injection. Lung, liver, spleen, bone, and scaffolds were retrieved. Tissue samples were aliquoted for analysis via flow cytometry or ELISA. For flow cytometry experiments, freshly harvested tissue samples were minced with scissors in a 40 µm cell strainer and further digested with Collagenase, Type II. Stock solution (100 U/µL) was diluted in PBS to 200 U/mL and added to the tissue for 15 minutes. Tissue pieces were pushed through the 40 µm cell strainer using the back side of a 1 mL syringe plunger. DMEM media containing 10% FBS was added to quench the enzymatic reaction before spinning down in a centrifuge at 1500 RPM. Cell pellets were resuspended in FACS buffer (PBS containing 1% bovine serum albumin (BSA)) and counted. Cells were spun down again and resuspended to a final concentration of 10^7 cells/mL in FACS buffer. 100 µL of the cell suspension was added to a U-bottom 96 well plate. 100 µL of FACS buffer containing 2.5 µg of Fc Block was added to each well and incubated for 10 minutes at room temperature. The plate was spun down and supernatant removed before adding mouse anti-human CD45-PE diluted in FACS buffer 1:100. Samples were incubated for 30 minutes at room temperature in the dark. Samples were washed 3 times with FACS buffer before being transferred to FACS tubes and analyzed with a BD LSRFortessa. BD FACSDiva software was used for both collection and analysis. For human cytokine secretion, retrieved tissues were kept relatively equal in size and cut

into 1-2 mm pieces using surgical scissors. Conditioned media was prepared 36 hours after plating in 500 μL of αMEM media supplemented with 1% mouse serum and 1% penicillin and streptomycin. Conditioned media was used immediately for characterization using DuoSet® ELISA kits for human TNF-α, IL-6 and IL-10 (R&D Systems)

4.5.8 Orthotopic xenoengraftment of human prostate tumor

Luciferase (Luc) and green fluorescent protein (GFP) transduced PC-3 Human Prostate Cancer cells were obtained from the Center for Engineering in Medicine, Massachusetts General Hospital. Luc-GFP PC3 cells were cultured with DMEM supplemented with 10% FBS and 1% penicillin-streptomycin. Scaffold bearing mice were anesthetized with 2% isoflurane followed by ventral hair removal with Nair. Skin was sterilized with 70% isopropyl alcohol prep wipes. Prior to surgery 2 mg meloxicam/kg mouse weight was subcutaneously injected. A 10 mm vertical incision was made in the lower abdomen of the mouse. The bladder was externalized through the opening to expose the prostate. 2 x 10^6 Luc-GFP PC-3 cells suspended in 50 μL of matrigel were injected to the prostate using a 27 G needle. The bladder was returned to the intraperitoneal cavity, the muscle layer was sutured using polyglycolic acid sutures (Henry Schein), and the skin was clamped with Reflex 7 mm wound clips. Clips were removed after 1 week.

4.5.9 Monitoring human tumor engraftment and metastasis by bioluminescent imaging

Two weeks after orthotopic injection of Luc-GFP PC3 tumor cells, whole body bioluminescent imaging was performed to confirm engraftment and metastasis to distant organs using an IVIS SpectrumCT (Perkin Elmer). Luciferin was prepared by dilution in PBS to a concentration of 15 mg/mL in PBS. Mice were anesthetized with 2% isoflurane

and injected intraperitoneally with 10 µL luciferin solution/g of body weight before being placed in the imaging chamber. Images were taken every 5 minutes until peak values were achieved. 6 weeks after orthotopic tumor injection, mice were euthanized, and scaffolds were retrieved and placed in a 48-well plate. Luciferin stock solution was diluted 1:100 in PBS and 300 µL were loaded into each well. Bioluminescent imaging was performed every 2 minutes until reaching peak values.

4.5.10 Non-invasive long-term monitoring of metastasis in serially transplanted scaffolds

Metastatic tumor microenvironments primed in primary mice were retrieved and immediately transplanted to the same anatomical site in naïve male NSG mice 6-12 weeks of age following the same method as initial scaffold implantation. Wound clips were removed after 1 week. Whole body bioluminescent imaging was started 4 weeks after serial transplantation and continued for an additional 6 weeks with measurements taken weekly. Images were taken every 5 minutes until peak values were achieved.

4.5.11 Scanning electron microscopy imaging

Microfabricated scaffolds coated with type I collagen were fixed with 2% glutaraldehyde, serially dehydrated with 50, 70, 90, and 100% ethanol and lyophilized overnight. The prepared dehydrated samples were deposited with a thin gold film using a sputter-coating machine (208HR, Cressington) and observed using a Zeiss Ultra55 Field Emission Scanning Electron Microscope.

4.5.12 Immunohistological staining and imaging

At the end of *in vivo* experimentation, tissue and scaffold samples were frozen by embedding tissue in CryomatrixTM and snap-frozen in a metal beaker containing 2-methylbutane cooled by dry ice. Frozen samples were sectioned using a Cryostat (NX70). Scaffolds were cut to 20-25 µm, while native tissue were cut to 10 µm thickness and attached to ColorMarkTM Plus glass slides. Remaining frozen tissue blocks and sectioned slides were stored at -80 °C. Frozen tissue was briefly fixed in pre-chilled acetone for 10 minutes. Following 3 wash cycles in 0.05% Tween-20 in PBS (PBST), samples were outlined with a hydrophobic marker and blocked with 10% goat serum and 1% BSA in PBST for 2 hours at room temperature. Primary antibodies were added at a dilution ratio of 1:200 in blocking solution and left overnight in 4 °C. Samples were washed 3 times with 0.05% PBST followed by secondary antibodies at a dilution ratio of 1:200 in blocking solution and left for 2 hours at room temperature. Samples were washed 3 times with PBST prior to addition of 1 µg/mL DAPI solution and a cover slide. When required, streptavidin conjugated Qdot was added to the samples and left for 1 hour prior to the final washing cycle. 10 µL of 10 ng/µL DAPI solution was added to samples before imaging. Images were obtained using a Zeiss Cell Observer SD with 10x and 20x objectives. Tiling was performed with 10% overlap. Human antibodies were validated against relevant mouse tissue to rule out cross-reactivity **(Figure 4.27)**. For hematoxylin & eosin and trichrome staining, frozen tissue sections were fixed with 10% neutral buffered formalin for 10 minutes. After washing with DI water, sides were stained with dye solutions following the protocol provided by the (American Master Tech).

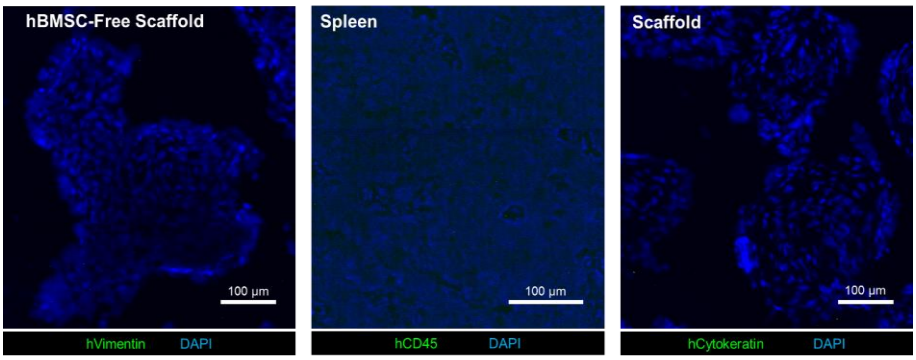

Figure 4.27. IHS of hVimentin, hC45, and hCytokeratin against relevant mouse tissue to rule out cross-reactivity.

4.5.13 Optical tissue clearing and complete optical sectioning of the scaffolds

Mice were transcardially perfused with 20 mL of ice cold PBS followed by 20 mL of ice cold monomer solution containing 4% acrylamide, 0.05% bis-acrylamide, 0.25% VA-044 (thermal initiator) and 4% paraformaldehyde in PBS. Tissue samples were collected and incubated in fresh monomer solution at 4 °C for 48 hours. Air in the tubes was replaced with nitrogen gas prior to incubation at 37 °C for 3-4 hours to polymerize the monomer solution. Excess polymer was removed and samples were left in either PBS or tissue clearing solution (4% SDS, 200 mM boric acid, pH 8.5). Scaffold samples required thick sectioning to achieve whole tissue imaging. Samples were frozen in CryomatrixTM and cut to a thickness of 250 µm with a cryostat for a total of 4 slices per scaffold. Sections were washed thoroughly in 0.1 vol% Triton X-100 in PBS prior to antibody staining. All of the staining procedures were performed at room temperature. Samples were blocked with 10% normal goat serum (NGS) and 1% BSA in PBST overnight. Samples were incubated for 36 hours in primary antibody solution containing chicken anti-human cytokeratin and rabbit anti-mouse smooth muscle actin diluted 1:200 in blocking solution. Samples were washed thoroughly with Triton X-100 PBS for 24 hours. Samples were

incubated in secondary antibody solution containing goat anti-chicken Alexa Fluor 647 and goat anti-rabbit Alexa Fluor 568 diluted 1:200 in blocking solution for 36 hours. Samples were washed thoroughly with Triton X-100 PBS before imaging. Refractive index matching solutions did not enhance scaffold imaging depth, so samples were imaged in PBS. Samples were transferred to a glass slide with silicone isolators and covered with a cover slip. Whole tissue Z-stack images were taken with a Zeiss Cell Observer SD with a 10x objective at a 10 μm z-step. Optical slices were observed and compiled in ImageJ. Single cells and tumor colonies were manually counted and concentric circles were drawn as previously described. Nikon Elements AR v4.5 was used for 3D rendering and creation of videos. The videos were annotated in Adobe Premiere Pro CC 2014 and encoded in Adobe Media Encoder CC 2014.

4.5.14 Image analysis

For characterization of mCD31 and hVimentin distribution in 4-week *in vivo* scaffolds, concentric circles were drawn in ImageJ. Three circles were drawn with 1/3 R-Total (Total Radius), 2/3 R-Total and R-Total. Background signal of each individual channel were removed before measuring the pixel density. Values were normalized by the zone area and the signal measured from the entire scaffold to generate a relative distribution across the scaffold. The same analysis was performed for hCD45 distribution in hPBMC injected mice 6 weeks after intravenous injection. Percent coverage analysis (mCD31, hCD44, hCD45, Ki67, and mLy6G) was calculated by measuring the overlap between positive signal and the total area of the appropriate tissue (entire scaffold, hCytokeratin, or $mLy6G^{+}$).

For in depth characterization of the local tumor microenvironment, single cell and tumor colonies were manually identified by examining tiled images of stained tissue sections. Nearest vessel, vessel diameter, tumor colony diameter, and nearest cell distance were measured in ImageJ for all of the identified tumor cells. Data was binned to generate histograms.

4.5.15 Multiple antibody staining of overt metastatic tumor bearing scaffold

8 consecutive tissue slices, each 20 μm thick, from a single scaffold were stained with multiple combinations of antibodies, for a total of 11 different stains. All of the images were aligned in ImageJ. Images were then divided into a grid of 24x24 images, thresholded and pixel density was measured for each channel. Total tissue area was determined by setting a low threshold to include background signal. Values from each individual channel were normalized by total tissue area within each and plotted in a 24x24 heatmap. 10 color images were generated by combining images from different staining combinations. From these composite images, regions of interest were manually determined to highlight heterogeneity. Regions of interest were translated to the 24x24 heatmaps and pixel density was recalculated for the 8 zones. Pixel densities from each of the zones of interest were normalized to the maximum value from the 8 zones. Channels that had more than one replicate were averaged together before plotting on a radar chart. Cellular composition within each zone was achieved by normalizing the absolute pixel count of each channel by the total pixel count of the zone.

4.5.16 Statistics

Unpaired Student's t tests were performed for comparison of the mean values between two groups. Statistical significance was determined if $p<0.05$ for two-tailed analysis. All quantitative data represent mean and standard deviation.

CHAPTER 5

INVESTIGATION OF THERAPY-INDUCED METASTATIC RELAPSE VIA ENGINEERED DISSEAMINTED TUMOR CELL NICHES

5.1 Abstract

The treatment of most primary tumor types has greatly improved, however metastatic disease remains a substantial clinical hurdle. Disseminated tumor cells (DTCs) are impractical to detect in patients and can develop resistance to treatment options that successfully treated the primary tumor. It is widely accepted that DTCs undergo periods of dormancy that can last years to decades after primary tumor treatment. However, several clinical and preclinical studies have shown greatly accelerated metastatic recurrence after the administration of chemotherapy and surgical intervention. The direct causes of metastatic relapse remain largely unknown and represent a critical gap in understanding to produce effective treatments. Here we present a biomaterial scaffold driven *in vivo* model to understand the implications current treatment strategies have on DTCs and their local microenvironment. Tissue engineering approaches have been shown to enable the long-term observation of non-metastatic DTCs and provide high analytical assessment of the cellular and molecular factors that drive metastatic relapse. Investigation of implantable niches shortly after an adjuvant chemotherapy regimen suggested that DTCs were eradicated in 50% of treated samples, however long-term analysis revealed all niches had undergone relapse to the same degree as non-treated implants. Secretome analysis of the scaffold tissue revealed significant increases in SDF-1 and leptin, and decreases in proMMP9, MMP8, VEGF, IP-10, IL-10, IL-15, and IFNy following chemotherapy. Direct surgical manipulation of long-term dormant niches revealed a significant increase in tumor

burden and an increase in angiogenic and inflammatory cell recruitment. These results demonstrate the translational potential of implantable niches to uncover mechanisms of DTC activation in a clinically relevant manner.

5.2 Introduction

Although primary tumor treatments have improved, the overall five-year survival rate for patients diagnosed with cancer remains under 70%. The main cause of this is the dissemination of tumor cells to distant tissues and the eventual relapse into metastatic disease. Treatment of the metastatic disease is challenging due to several factors. First, metastatic disease can be asymptomatic and is usually detected late into tumor progression. Second, disseminated tumor cells (DTCs) can develop new mutations and interact with different stromal cell populations that may aid in resistance to therapies. Third, metastatic tumors generally proliferate in organs vital to survival, specifically the lung, liver, bone, and brain. A better understanding of DTC biology is needed to create effective treatments against metastasis.

Chemotherapeutic agents have been used for the last few decades with successful application across several tumor types. Chemotherapies aim to interfere with the proliferation pathways of cancer cells. Following tumor removal, adjuvant chemotherapy may be administered with the goal of removing residual tumor cells. The ability to monitor the success or failure of these therapies is difficult in patients. Clinical studies examining the efficacy of adjuvant therapies tend to demonstrate marginal increases in reducing remission and prolonging survival[266-267]. The nature of chemotherapies is not tumor specific, and the systemic delivery of these drugs yields several off-target effects[268-270]. A recent study demonstrated that administration of chemotherapeutic agents in a neoadjuvant

regimen mobilized bone marrow derived cells and increased angiogenesis leading to tumor regrowth and relapse[271]. The local microenvironment has been shown to plays a critical role in regulating chemosensitivity during adjuvant therapy and can be targeted to improve treatment effectiveness[272]. These provocative findings have led to the questioning of adjuvant and neoadjuvant therapies and their potential negative responses in accelerating metastatic relapse.

Metastatic recurrence is commonly observed shortly after the surgical removal of the primary tumor. The act of surgery triggers a wound healing response that can activate systemic inflammation, and in turn awaken dormant DTCs in distant tissues. A recent study has demonstrated that surgery can lead to the outgrowth of immunologically restricted tumors by increasing circulating neutrophils and inflammatory monocytes through IL-6, G-CSF, and CCL2 signaling. The increased monocyte activity was shown to directly counter T cell-mediated growth restriction of the tumor[273]. Additional evidence suggests that primary tumors themselves may prevent metastatic relapse by releasing systemic factors[106]. Although these studies provide mechanisms of escape for larger tumor colonies, it is unclear how surgery or the wound response to surgery may aid in changing the phenotype of DTCs that are actively dormant.

Chemotherapy and surgery provide substantial clinical benefits, however they both induce systemic immune responses that may trigger metastatic relapse. Specifically, we hypothesized that these treatments stimulate systemic inflammatory pathways and cause dormant DTC niches to undergo tissue remodeling and trigger metastatic relapse. Mouse models that are capable of investigating DTC dormancy generally utilize specialized cell lines that may misrepresent patient phenomenon. We have recently developed a tissue-

engineered metastasis model using micro-fabricated porous hydrogel scaffolds subdermally implanted into mice. The scaffold induces the formation of vascularized tissue microenvironments that recruit bone marrow-derived cells, an emulating key feature of the premetastatic niche. Circulating tumor cells are attracted to the implants and DTC niches can be retrieved intact and re-implanted to a secondary tumor-free mouse enabling the observation of the full spectrum of the metastatic cascade from single DTCs to a fully metastasized tumor. Isolation of the DTC niche provides high experimental control without confounding factors such as multiple metastases or diminishing health of the host. The standardized 3D structure and synthetic hydrogel impart high analytical power when combined with conventional immunohistostaining and recently introduced tissue-clearing techniques for whole tissue imaging. Here we use this biomaterial approach to investigate the impact of adjuvant chemotherapy and local surgery on long-term dormant DTCs.

5.3 Results

5.3.1 Circulating tumor cells from an orthotopic MMTV-PyMT transplant model home to implantable biomaterial niches

Four ICC hydrogel scaffolds were implanted subcutaneously into immunocompetent FVB mice to begin niche tissue development. Two weeks later a fragment of syngeneic MMTV-PyMT breast tumor was orthotopically transplanted into the mammary fat pad. This approach was taken to increase the experimental throughput, as one MMTV-PyMT primary tumor could be split into 15-20 pieces **(Figure 5.1A)**. The primary tumor was grown until a critical size of 1,000 mm^3 was reached. Only tumors that achieved this size within 10 weeks of implantation (82.1%) were considered for further experiments **(Figure 5.1B)**. Scaffolds were removed and analyzed for the presence of

DTCs. Immunohistostaining revealed 100% of scaffolds were positive for DTCs, however colony development was rare at the time of sacrifice **(Figure 5.1C)**. These results suggest implantable scaffold niches retain their tumor cell capture abilities in fully immunocompetent syngeneic tumor models.

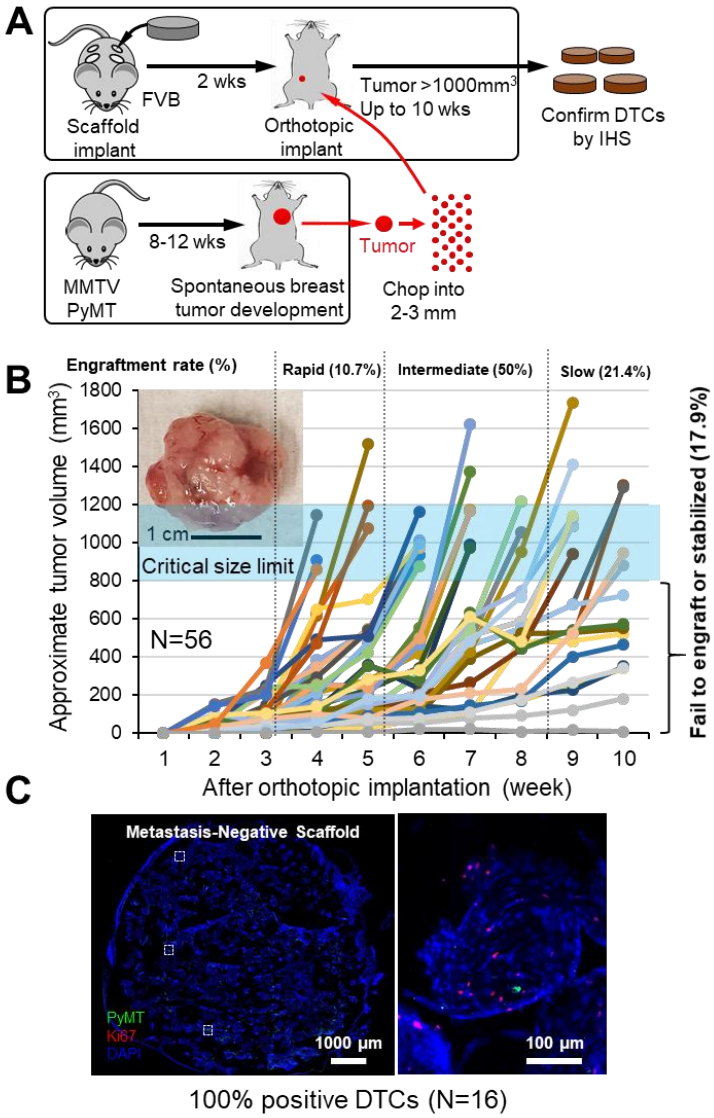

Figure 5.1. Orthotopic MMTV-PyMT tumor transplant model generates DTCs in implantable niches.
a, Experimental schematic of scaffold implantation and orthotopic breast tumor generation. **b,** Orthotopic primary tumor growth kinetics and engraftment efficiency. **c,** Immunohistostaining revealed all scaffold niches contained DTCs.

5.3.2 Adjuvant chemotherapy reduces initial DTC burden but does not prevent relapse

DTC-containing scaffolds were transplanted to secondary tumor-free FVB hosts to prolong the observation window of cancer cell progression. One week after transplantation, adjuvant chemotherapy, consisting of doxorubicin and cyclophosphamide, or PBS was administered intraperitoneally once a week for three weeks **(Figure 5.2A)**. Twenty-four hours after the final dose of chemotherapy scaffolds were removed from mice to assess the short-term results of therapy. Microscopic analysis of the scaffolds revealed the presence of single DTCs and early stage colonies in both experimental groups **(Figure 5.2B)**. Quantification of DTCs in the scaffolds revealed a significant decrease in cancer cells in mice given chemotherapy **(Figure 5.2C)**. Additionally, 50% of chemotherapy-treated scaffolds did not contain any DTCs.

A separate group of mice were sacrificed 10 weeks after the final dose of chemotherapy to assess long-term impact of adjuvant therapy on DTCs. Surprisingly all analyzed scaffolds contained an increased tumor burden regardless of treatment **(Figure 5.2D)**. Quantification revealed no significant difference between the final tumor burden observed in the scaffolds after the 10 week period **(Figure 5.2E)**.

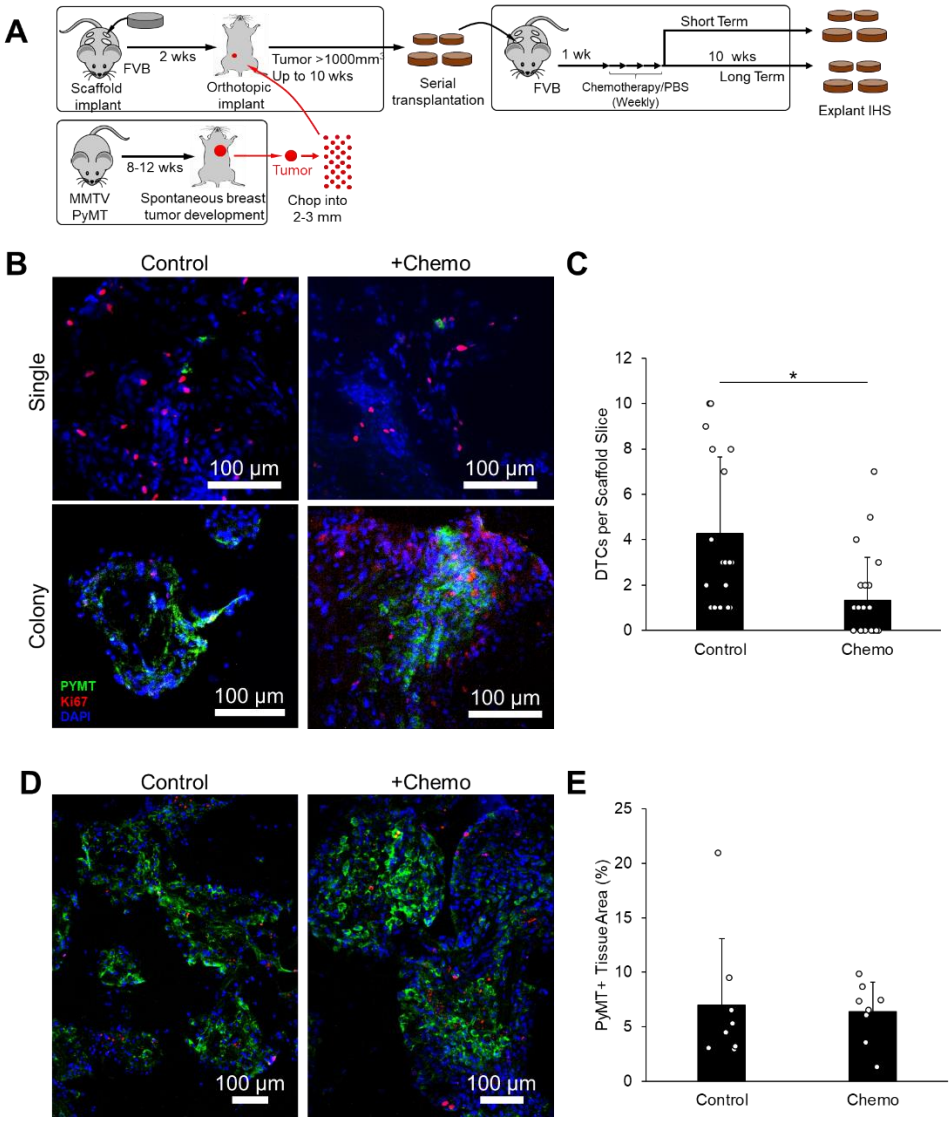

Figure 5.2. Short and long-term effects of adjuvant chemotherapy in transplantable niche model.
a, Experimental schematic to investigate the role of adjuvant chemotherapy on DTC niches. **b,** Immunohistostaining of samples retrieved 24 hours after the final dose of adjuvant chemotherapy. **c,** Quantitative image analysis of DTCs in scaffolds retrieved 24 hours after the final dose of adjuvant chemotherapy. **d,** Immunohistostaining of samples after long-term, 10 week, observation. **e,** Quantitative analysis of total tumor positive area in long-term samples. (*P<0.05)

5.3.3 Chemotherapy alters soluble factors in local microenvironment

Next, we assessed changes to the soluble microenvironments within the scaffolds following chemotherapy. Four scaffolds were subcutaneously implanted into FVB mice

and left for three weeks before starting chemotherapy. Twenty-four hours after the final dose of chemotherapy scaffolds were harvested and cultured *ex vivo* for 36 hours **(Figure 5.3A)**. Conditioned media was analyzed with a panel of 45 cytokines **(Figure 5.3B)**. Secretion of SDF-1 and leptin were significantly increased, while proMMP-9, MMP-8, VEGF, IP-10, IL-15, IL-10, and IFNγ were significantly decreased **(Figure 5.3C)**. SDF-1 is a ligand connected to immune cell homing. Leptin has been implicated as leading to chronic inflammation and a pro-tumor factor. The decreases observed appear likely due to a decrease in immunogenic activity within the scaffold niche due to therapy. The change in soluble factors may lead to altered immune cell homing and trigger rapid tissue remodeling once the effects of chemotherapy subside.

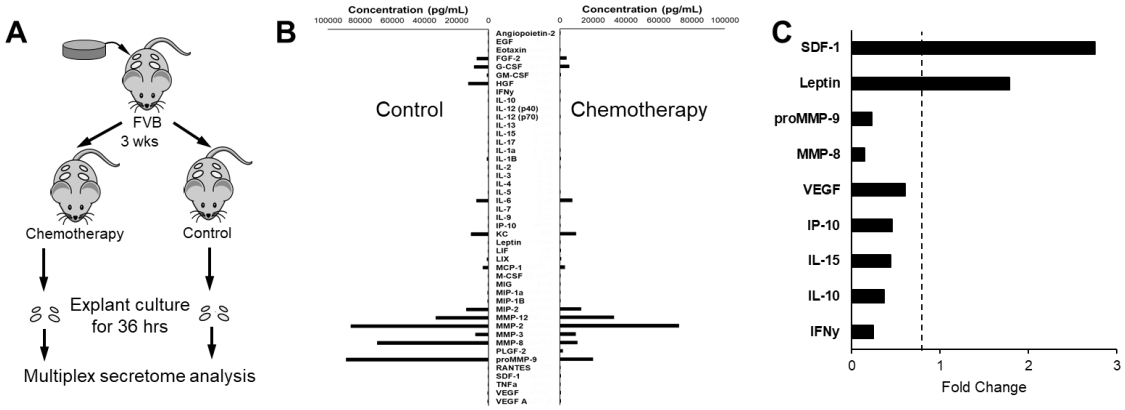

Figure 5.3. Secretome analysis of implantable niche tissue following chemotherapy. a, Experimental schematic of procedure to generate conditioned media for multiplex secretome analysis. **b,** Secretion profile of scaffold niches from mice without and with chemotherapy. **c,** Subset of cytokines that displayed significant up- or downregulation following therapy compared to control.

5.3.4 Local surgical intervention increases tumor growth

Surgical intervention was modeled by performing a 4mm biopsy in the center of the implant tissue and replacing it with an empty ICC hydrogel scaffold. Long-term DTC niches were generated using the transplantation strategy described above, however

scaffolds were untreated and left for 15 weeks prior to intervention **(Figure 5.4A)**. Two of the four scaffolds underwent biopsy surgery and the remaining two remained untouched **(Figure 5.4B)**. Five weeks after the surgery scaffolds were explanted and analyzed via immunohistostaining **(Figure 5.4C and 5.4D)**. Tumor burden was over three-fold higher in scaffolds that underwent surgical intervention **(Figure 5.4E)**. Characterization of the local microenvironment revealed increases in vasculature (CD31), leptin, MMP9 and Ly6G in the surgically activated scaffolds **(Figure 5.4F)**. Analysis on the biopsy samples was performed on the original tissue area and did not include the area accounting for the newly implanted scaffold. Collectively these results indicate that local surgical intervention significantly increased tissue remodeling and tumor burden from DTCs.

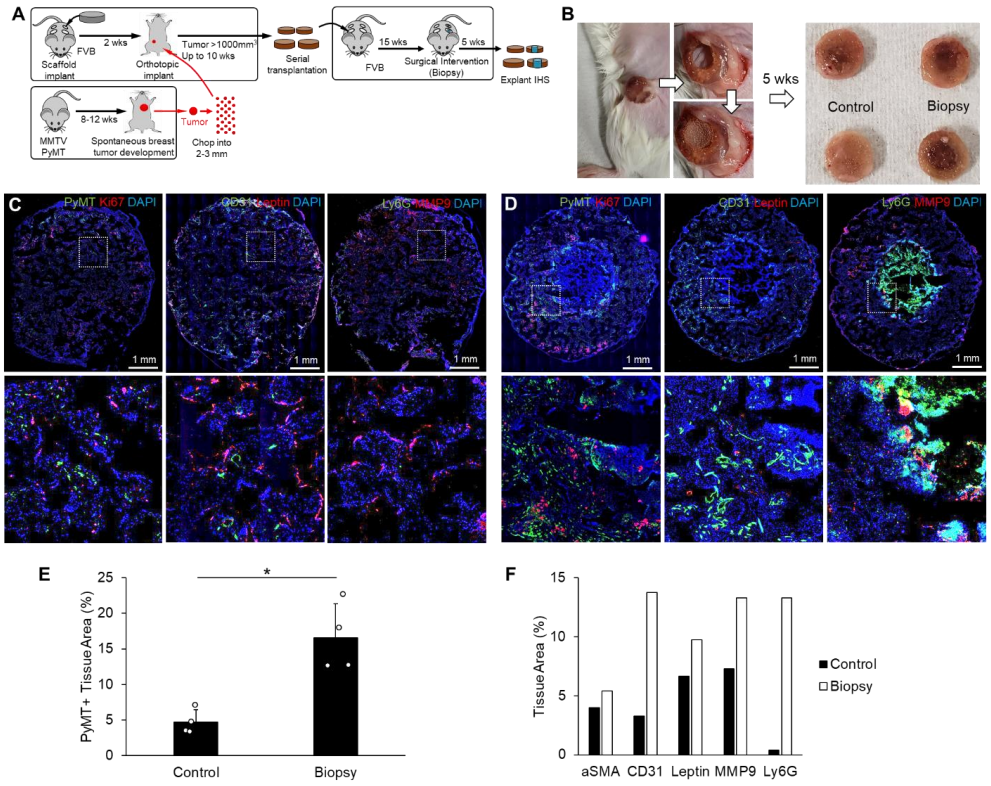

Figure 5.4. Surgical intervention of long-term DTC niches.
a, Experimental schematic of procedure to generate controlled surgical disruption using a 4 mm biopsy punch. **b,** Gross images of surgical procedure and explanted scaffolds 5 weeks after surgery. **c,** Immunohistostaining of long-term control DTC niches.

d, Immunohistostaining of samples that received surgical intervention. **e,** Quantitative analysis of $PyMT^+$ tumor burden in scaffolds without and with surgery. **f,** Quantitative image analysis of tissue nice components found in the original scaffold area. (*P<0.05)

5.4 Discussion

The observation that metastatic relapse can occur years after the removal of primary tumors has provoked extensive research into the understanding of DTC biology. Multiple efforts have been made to uncover pathways that enabled DTCs to escape a quiescent state and proliferate into a metastatic tumor. However, this is a challenging phenomenon to model and reproduce consistently in traditional mouse models. Here we provide evidence that implantable scaffold niches can reduce this gap and enable the long-term analysis of DTCs. Transplantation of scaffold niches housing DTCs to tumor-free mice enables complete isolation of the microenvironment with the added benefit of niche control via tissue engineering principles. In this study we have applied two stimuli to the niches, adjuvant chemotherapy and surgery, to provide mechanistic insight toward metastatic relapse. Although adjuvant chemotherapy showed promise in removing DTCs in the short-term, long-term observation following the end of adjuvant therapy suggests a substantial number of DTCs were able to survive and proliferate. In modeling local tissue surgical intervention, we demonstrated a robust increase in tumor growth in the surrounding tissue via activation of inflammatory signaling.

Adjuvant chemotherapy given after the resection of a primary tumor is a common strategy to remove residual DTCs. These methods have recently come under question as treatment is ultimately unsuccessful over time[274]. Chemotherapy by nature of the drug mechanism of action relies on interfering with the proliferative state of the tumor cells. Most DTCs are believed to be held in a dormant state making these therapies only effective

once they start growing. However, evidence has been provided that demonstrates chemotherapy can have negative side-effects such as increased remodeling and inflammation[271]. Secretome analysis performed on scaffold microenvironments confirmed the upregulation of SDF-1 and leptin following chemotherapy. Both molecules have been implicated as pro-tumor and may accelerate metastatic relapse[275-276]. The local microenvironment is believed to be a key regulator in maintenance of DTC dormancy, and disruption may have unexpected effects[107, 272, 277]. Short- and long-term histological characterization following chemotherapy may provide clues as to how the niche evolves over time with and without therapy. However, it may be challenging to capture key biological events without increasing the sampling rate following the end of therapeutic intervention. The heterogeneous makeup of tumor cells can also lead to drug resistance as tumor cells can gain resistance to therapy once disseminated[278]. The findings in this study confirm the notion that adjuvant chemotherapy is not effective in the prevention of long-term DTC relapse. However, additional factors such as increasing the length of treatment may yield significant decreases in relapse. An additional aspect that remains unexplored is the cyclical nature of adjuvant therapy and the associated fluctuations of immune cell populations. Myeloid and myeloid precursor cells are dramatically reduced during chemotherapy. Interestingly, the onset of neutropenia after therapy is correlated with antitumor efficacy and good patient prognosis[279]. A recent study has shown that repeated dosing of inflammatory lipopolysaccharide was necessary to aggressively reactivate DTCs in the lung[251]. Understanding how the body changes on a systemic level after subsequent doses of chemotherapy may unveil new drivers of metastatic relapse[107].

Clinical observation of patients after tumor resection has revealed a sharp increase in risk of metastatic recurrence shortly after surgery[280]. This early spike in relapse appears to undermine the concept of DTC dormancy, yet the act of surgery provokes wound healing responses that may reactivate DTCs. This notion is confirmed by patients that undergo elective surgeries and an observed increase in metastatic relapse[281-282]. Aside from surgery, reports that the primary tumor can maintain dormancy have also been made[106]. A recent study however has shown that surgical wounding can disrupt immunologically regulated tumor dormancy by altering systemic immune cell responses[273]. Here we demonstrate local metastatic relapse due to proinflammatory signaling due to surgery including increased vascular density, leptin, MMP9 and Ly6G. Additional work is necessary to validate the role of the increased soluble factors. Due to the broad nature of the response stemming from tissue remodeling, targeting these factors with pan anti-inflammatory molecules may reduce metastatic spread. In addition to systemic administration of anti-inflammatory molecules, replacement scaffold inserts can be loaded with drug to increase the effect on the local tissue.

Additional questions regarding DTCs and potential mechanisms that activate relapse remain. For example, the effect of aging and senescence of local tissue cells and hematopoietic cells has not been fully explored. New therapeutic approaches to combat relapse have been made but will require further investigation before application in patients. Antibodies have been developed against remodeled laminin to prevent $\alpha_3\beta_1$ integrin signaling and DTC proliferation[107]. Direct blocking of integrin function has also achieved better adjuvant chemotherapy results[272]. Previously we used ICC hydrogel scaffolds to demonstrate the modulation of inflammatory signaling with an IL-1 antagonist altered the

fate of DTCs within the niche[96]. In addition to understanding fundamental mechanisms, the standardized tissue-engineered metastasis model presented in this study provides a unique opportunity to screen anti-metastatic drug candidates. We believe implantable DTC microenvironments will serve as an indispensable tool across several aspects of metastatic relapse.

5.5 Materials and Methods

All chemicals and materials were purchased from Sigma Aldrich or Fisher Scientific unless specified. All animal procedures were approved by the Institutional Animal Care and Use Committee at the University of Massachusetts-Amherst.

5.5.1 Porous hydrogel scaffold fabrication

ICC hydrogel scaffolds were fabricated using soda lime glass beads with sizes ranging from 250 μm to 300 μm as previously described[101]. The polyacrylamide hydrogel was made from a precursor solution composed of 30 wt% acrylamide monomer, 1.5 wt% bis-acrylamide crosslinker, 0.2 vol% N,N,N',N'-tetramethylethylenediamine accelerator, and 0.2 vol% 2-hydroxy-2-methylpropiophenone photoinitiator in nitrogen purged DI water. The solution was polymerized under an ultraviolet light. Beads were removed with alternating acid washes of hydrofluoric and hydrochloric acid. Scaffolds were thoroughly washed with DI water to remove residual acid and lyophilized. Scaffolds were sterilized with 70% ethanol before they were surface treated with Sulpho-SANPAH to covalently crosslink rat-tail collagen. Scaffolds were stored at 4 °C in sterile phosphate buffered saline.

5.5.2 Mouse colony

MMTV-PyMT mice on the FVB/N background (002374 bred in house from a colony initially obtained from the Jackson Laboratory. Wild type FVB/N were acquired from MMTV-PyMT breeding. Mice were housed in sterile conditions with unrestricted access to food and water.

5.5.3 Orthotopic MMTV-PyMT tumor model implantation of scaffolds

FVB mice at an age between 6 and 12 weeks old were implanted with four scaffolds subcutaneously. Mice were anesthetized with 1.5% isoflurane before removing the dorsal hair with electric clippers and Nair. The skin was sterilized using 70% isopropyl alcohol prep wipes. Mice received 2 mg meloxicam/kg mouse weight subcutaneously prior to surgery. A subcutaneous pocket was formed and implanted with an ICC hydrogel scaffold. The incisions with Reflex 7 mm wound clips. Two weeks after scaffold implantation mice were given a fragment of primary tumor from an MMTV-PyMT mouse. Large tumors were retrieved from 8 to 12 week old MMTV-PyMT mice and chopped into 2-3 mm pieces using a scalpel. Tumor fragments were immediately implanted into a subcutaneous pocket located at the right abdominal mammary gland. Incisions were closed with wound clips. Tumor measurements were taken weekly using digital calipers and volume was calculated using the formula $V = (Width^2 \times Length)/2$. Once the primary tumor reached 1,000 mm^3 scaffolds were harvested for immunohistostaining or orthotopically transplanted to secondary FVB mice. Transplantation surgery was the same as initial implantation of the scaffold.

5.5.4 Adjuvant chemotherapy regimen

Doxorubicin was dissolved in phosphate buffered saline to a final concentration of 0.2 mg/mL. Cyclophosphamide was dissolved in 0.9% NaCl to a final concentration of 12 mg/mL. Drug solutions were stored at -80 °C. One week after transplantation mice received intraperitoneal doses of doxorubicin (2 mg/kg) and cyclophosphamide (60 mg/kg) once a week for three weeks.

5.5.5 Multiplex soluble factor analysis

FVB mice were implanted with four scaffolds subcutaneously as described above. Three weeks after implantation, mice received the adjuvant chemotherapy regimen. Twenty-four hours after the final dose scaffolds were harvested and cultured *ex vivo* in serum-free alpha-Modified Eagle Medium supplemented with 1% penicillin-streptomycin. Conditioned media was harvested thirty-six hours later and stored at -80 °C. Samples were shipped on dry ice to Eve Technologies for multiplex cytokine analysis (MD31, MAGP-08-107, and MMO-C,O).

5.5.6 Surgical intervention of DTC niches

Fifteen weeks after transplantation DTC niches were subjected to surgical disruption. An incision was made close to the implant and the connective tissue was broken on the muscle side of the implant. The scaffold was carefully exposed through the incision and a 4 mm biopsy punch was used to remove the central region of the implant. A new 4 mm ICC hydrogel scaffold was placed in the void and the scaffold was carefully returned to its original location. The incision was closed with wound clips.

5.5.7 Frozen tissue preparation and sectioning

At the conclusion of the *in vivo* experiment, implants were frozen by embedding the tissue in Cryomatrix ™ and snap-frozen in 2-methylbutane cooled on dry ice. Frozen tissue was cut to 20 µm using a NX70 Cryostat. Frozen tissue blocks and sectioned slides were stored at -80 °C.

5.5.8 Immunohistostaining

Frozen slides were fixed in -20 °C acetone for 10 minutes. Slides were washed with PBST solution 3 times before blocking in a solution containing 10% normal goat serum, and 1% bovine serum albumin for 1 hour. Following blocking primary antibodies diluted in blocking solution were added to the slides and left in a humidified chamber overnight at 4 °C. Slides were washed 3 times with PBST and then incubated with secondary antibodies diluted in blocking solution for 2 hours at room temperature. Prior to imaging, slides were washed 3 times in PBST and stained with a 10 ng/uL solution of DAPI. Fluorescent images were taken on a Zeiss Cell Observer SD. PyMT (ab15085), Ki67 (ab16667) A-smooth muscle actin (ab5694), CD31 (550274), Leptin (PA1-052), MMP9 (PA513199), and Ly6G (557445) primary antibodies. Anti-rabbit Alexa Fluor Plus 488 (A32731), and anti-rat Alexa Fluor 647 (A21247) secondary antibodies were used in this study.

5.5.9 Image analysis

All image processing and quantitative analysis was performed in ImageJ. Total tissue area was determined using the DAPI image for all relevant analysis. DTC counts were tabulated by assuming small colonies were formed from a single DTC.

5.5.10 Statistics

Unpaired Student's t tests were performed for comparison of the mean values between two groups. Statistical significance was determined if $p<0.05$ for two-tailed analysis. All quantitative data represent mean and standard deviation.

CHAPTER 6

FABRICATION OF BIOACTIVE INVERTED COLLOIDAL CRYSTAL SCAFFOLDS USING EXPANDED POLYSTYRENE BEADS

Adapted with permission from Ryan Carpenter, Dalton Macres, Jun-Goo Kwak, Katherine Daniel, and Jungwoo Lee. *Tissue Engineering Part C: Methods*. **2020**. DOI: 10.1089/ten.TEC.2019.0333.

6.1 Abstract

Inverted colloidal crystal (ICC) hydrogel scaffolds have emerged as a new class of 3D cell culture matrix that represents a unique opportunity to reproduce lymphoid tissue microenvironments. ICC geometry promotes the formation of stromal cell networks and their interaction with hematopoietic cells, a core cellular process in lymphoid tissues. When subdermally implanted, ICC hydrogel scaffolds direct unique foreign body responses to form a vascularized stromal tissue with prolonged attraction of hematopoietic cells, which together resemble lymphoid tissue microenvironments. While conceptually simple, fabrication of ICC hydrogel scaffold requires multiple steps and laborious handling of delicate materials. Here, we introduce a facile route for ICC hydrogel scaffold fabrication using expanded polystyrene (EPS) beads making the process cheaper, faster, and safer. EPS beads shrink and fuse in a tunable manner under pressurized thermal conditions, which serves as colloidal crystal templates for ICC scaffold fabrication. Inclusion of collagen in the precursor solution greatly simplified preparation of bioactive hydrogel scaffolds. The resultant EPS-templated bioactive ICC hydrogel scaffolds demonstrate characteristic features required for lymphoid tissue modeling in both *in vitro* and *in vivo* settings. We

envision that the presented method will facilitate widespread implementation of ICC hydrogel scaffolds for lymphoid tissue engineering and other emerging applications.

6.2 Introduction

Three-dimensional (3D) cell culture matrices also known as scaffolds are an essential component of tissue engineering that provide the biophysical framework and biochemical complexity to reproduce essential tissue structure and function[160]. As each tissue represents different cellular and extracellular matrix (ECM) composition and organization, biomaterial selection and structural design of scaffolds have been specialized to reproduce key cellular processes in target tissues[283-285]. Inverted colloidal crystal (ICC) hydrogel scaffolds have been developed to reproduce lymphoid tissue microenvironments[286-288]. ICC geometry consisting of fully interconnected spherical pore arrays provides a large surface area for adherent stromal cells and the formation of an intricate stromal network[289]. Spherical cavities connected via small channels transiently entrap hematopoietic cells and facilitate their intimate interactions with stromal cells[290], which is a core cellular process in lymphoid tissues. ICC hydrogel scaffolds have demonstrated biological significance in simulating bone marrow[291-292], thymus[293] and lymph nodes[214] *in vitro*. When subdermally implanted in mouse models, ICC hydrogel scaffolds rapidly induced interscaffold vascularization and attract local and systemic hematopoietic cells[97, 101, 294], which together function as a lymphoid tissue analogue.

The fabrication of ICC scaffolds involves four steps: (i) preparation of colloidal crystal templates via partial fusion of microspheres with narrow size distribution, (ii) infiltration of a hydrogel precursor solution and subsequent polymerization, (iii) selective

removal of the template microbeads, and (iv) if necessary, modification of the pore surface to support stromal cell adhesion[295] **(Figure 6.1A)**. The most critical consideration is the selection of template bead material as it determines the possible range of pore sizes and conditions for template preparation and dissociation. Current ICC scaffold fabrication can be categorized into five groups based on template materials **(Figure 6.2B)**. The first group is solid polymeric beads synthesized by emulsion polymerization including poly(methylmethacrylate) (PMMA) and polystyrene (PS) [291, 293, 296-301]. ICC geometry was initially developed for nanostructured photonic crystal materials using submicron PMMA and PS beads. By increasing the bead size, ICC structures can be utilized for 3D cell culture experiments. While PMMA and PS beads are commercially available, they are expensive and limited in size selection, with an upper limit of 160 μm due to the decreasing stability of emulsions with increasing size. Addition of crosslinkers allows synthesis of larger beads, but cross-linked beads cannot be dissolved. The second group is polymeric beads prepared by solvent evaporation from emulsion droplets including polycaprolactone (PCL)[302]. Polymers dissolved in organic solvents are microfluidically processed into uniform size emulsion droplets that in turn solidify as the solvent evaporates[303]. This method increases template bead sizes in a cost-effective manner, but the resultant polymeric beads exhibit a narrow window for thermal and mechanical stability, requiring exceptional care to process into colloidal crystal templates and ICC scaffold fabrication. The third group is hydrogel beads generated by in situ gelation including alginate and gelatin. Formation and dissociation of alginate beads are exploited by ionic cross-linking and a chelating agent, ethylenediaminetetraacetic acid, respectively[304-305]. Synthesis and solubilization of gelatin beads take advantage of their temperature-dependent reversible sol-gel transition[306-309].

Although hydrogel beads made from biocompatible materials are removable without using toxic chemicals, their weak mechanical properties make them difficult to process and handle. The fourth group is microbubbles including air and nitrogen gases[310-313]. Microbubbles suspended in a precursor solution generated by a flow-focusing microfluidic device are collected in a confined container and solidified under negative pressure, which opens the closed pores and enables formation of an open porous ICC structure. This method is simple, fast, and essentially non-toxic, but requires significant optimization due to the intrinsic instability of the microbubbles. The last group is glass beads. Glass beads are commercially available with a broad range of sizes and represents high thermal and mechanical stability that facilitates streamlined fabrication of ICC hydrogel scaffolds[96-97, 101, 134, 314-316]. However, requirement of toxic chemicals (i.e. hydrofluoric acid) to dissolve the glass beads has been a critical issue. Currently there exists no practical and cost-effective method to produce ICC hydrogel scaffolds at high scale under good manufacturing practices. The development of a better fabrication method remains an active area of research.

Here, we introduce a simple and robust method to fabricate bioactive ICC hydrogel scaffolds using expanded polystyrene (EPS) beads, the raw material commonly used for packaging and insulation products. EPS beads are a closed cell foam material composed of 95-98% air, with robust mechanical and thermal stability[317]. We have developed a method to shrink and fuse EPS beads into a free-standing construct that functions as a colloidal crystal template for fabrication of ICC hydrogel scaffolds. Pore size is tunable by adjusting the degree of EPS bead shrinkage. Surface modification for bioactive ICC hydrogel scaffolds was simplified by introducing collagen fibers into the hydrogel precursor solution

and polymerizing in a single step. The biological significance of EPS-templated ICC hydrogel scaffolds was demonstrated *in vitro* via conducting a hematopoietic colony-foaming assay in the presence of bone marrow stromal cells (BMSCs). The ability to form vascularized tissue and attract hematopoietic cells after subdermal implantation was comparatively demonstrated using glass bead-templated ICC hydrogel scaffolds. We envision that this simple and cost-effective fabrication strategy will facilitate usage of ICC hydrogel scaffolds for lymphoid tissue modeling and other emerging novel biological applications.

A

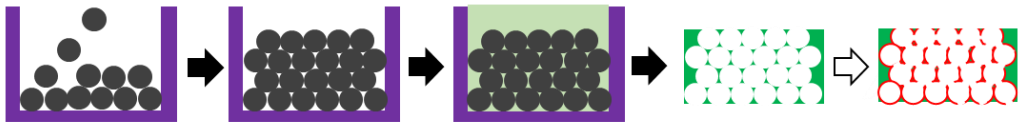

B

Bead materials	Synthesis	Dissolution	Scaffold materials	References
PMMA **PS**	Emulsion polymerization	Organic solvents (THF, DCM, etc.)	Hydrogel: PAA, PEG Polymer: n/a	10, 12, 18-23
	+ : available commercial beads - : limited size selection below 160 μm, cost to obtain a large quantity of beads			
PCL	Solvent evaporation in polymer solution	Organic solvents (THF, DCM, etc.)	Hydrogel: Gelatin Polymer: n/a	24, 25
	+ : custom manufacturing and flexible size control, significantly reduced costs - : weak mechanical and thermal stability to handle and process			
Alginate **Gelatin**	In situ ionic & thermal crosslinking	Chelate (EDTA) Temp. change	Hydrogel: Gelatin, Chitosan Polymer: PCL, PLGA	26, 27 (alginate) 28-31 (gelatin)
	+ : non-toxic chemical for template structure dissolution - : weak mechanical property to handle and process			
Microbubbles **(N_2, air)**	Flow focusing microfluidic devices	n/a (negative pressure)	Hydrogel: Gelatin Polymer: n/a	32-35
	+ : No need to dissolve templates - : requires significant optimization due to floating and instable nature of microbubbles			
Glass	Flame flotation	Hydrofluoric acid, Hydrochloric acid	Hydrogel: PAA, PEG Polymer: PCL, PLGA	14, 15, 36-40
	+ : streamline, reproducible fabrication with thermal & mechanical stability, available commercial beads - : require toxic chemical to dissolve			

Figure 6.1. Summary of the state-of-the-art inverted colloidal crystal hydrogel scaffold fabrication methods.
(A) Schematic illustration of the procedure to fabricate bioactive inverted colloidal crystal hydrogel scaffolds starting from microbead-based colloidal crystal templates. **(B)** The fabrication of ICC hydrogel scaffolds can be divided into five groups based on microbead materials used for template preparation. (THF: tetrahydrofuran, DCM: dichloromethane)

6.3 Results

6.3.1 Preparation of colloidal crystal templates using expanded polystyrene (EPS) beads

For some polystyrene foam products, EPS beads are subjected to steamed mechanical compression to make a densely packed foam structure without interstitial space. We hypothesized that EPS beads with increased interstitial space could serve as colloidal crystal templates for ICC hydrogel scaffold fabrication. To test this hypothesis, we used a pressure cooker to apply vapor phase water and ethanol solutions to EPS beads without mechanical compression **(Figure 6.2A)**. Water and ethanol were used as the source of vapor because they are cheap and relatively safe for scaled operation. EPS beads (diameters = 1.6 ± 0.19 mm) were placed in a perforated metal container and processed in an electric pressure cooker for 5, 10, 15, and 30 min. The perforated metal container was elevated to prevent contact with the liquid phase at the bottom of the cooker. Electronic pressure cookers are regulated by a pressure setpoint. On the Chefman unit used for these experiments a gauge pressure of roughly 0.5-0.7 bar is achieved during operation. Evaluation of the vapor pressure as a function of temperature reveals that the chamber reaches a temperature of 110-114 °F with water compared to 89-93 °C with pure ethanol. Pressurized thermal conditions directed shrinkage and fusion of EPS beads to create a free-standing colloidal crystal-like structure. The shape of the template remained identical, indicating isotropic shrinkage of EPS beads **(Figure 6.2B)**. In pure ethanol, beads underwent rapid and uneven size reduction, evident by a wider base compared to top. The overall size reduction was directly correlated to operation time for all ethanol:water solutions. Increasing ethanol concentration was observed to increase the degree of shrinkage. Interestingly a 50:50 mixture had less shrinking ability compared to pure water.

Size reduction was greatest at early timepoints and the rate of reduction gradually slowed down over time **(Figure 6.2C)**.

We next characterized the size and shape change of the individual EPS beads under optical microscopy. Increasing operation time and ethanol concentration reduced the size of EPS beads in an isotropic manner. The interface between the fused beads exhibited elongated necking. In the pure ethanol condition, uneven shrinkage of templates caused different size reduction of EPS beads between the top and bottom surface; EPS beads in the top side showed densely fused morphology whereas EPS beads in the bottom showed significantly elongated necks **(Figure 6.2D)**. The dynamic shrinking of porous EPS beads during bead-bead fusion presents a significantly different annealing process. We further conducted micro-CT scans to visualize the internal packing structure and quantify the interstitial area. While EPS beads have regular sphericity and about 10 % of size distribution, their packing density was lower compared to solid beads and microbubbles. The characteristic interstitial area was about 26.2 % **(Figure 6.2E)**. Quantitative analysis of EPS beads substantiated rapid and significant reduction of size with increasing concentrations of ethanol and time **(Figure 6.2F)**.

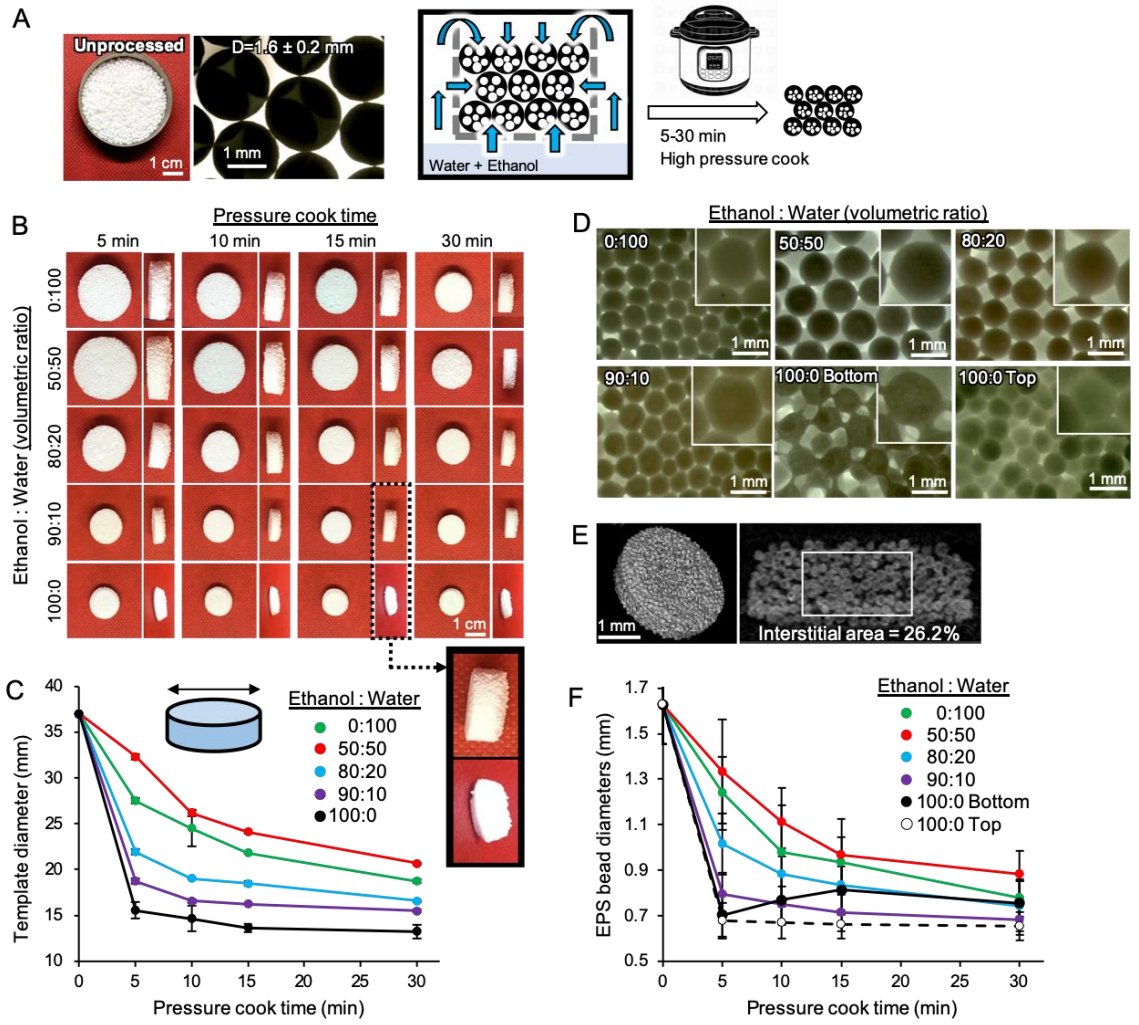

Figure 6.2. Preparation of colloidal crystal templates using expanded polystyrene (EPS) beads.

(A) Gross image of EPS beads in a perforated metal container (Left) and schematic of experimental set-up and process to fuse EPS beads using a pressure cooker (Right). **(B)** Images of free-standing fused EPS beads after a pressurized thermal process in 5 different ethanol solutions and 4 operating times. Zoomed-in images of side view show non-isotropic size reduction of EPS beads processed with pure ethanol. **(C)** Quantitative analysis of overall template diameters (n=4, * $P<0.05$). **(D)** Microscopy images of fused EPS beads after 15 minutes of operation in varying compositions of ethanol solution. **(E)** 3D reconstruction of micro-CT scanned EPS bead-templated colloidal crystal structure and quantitative measurement of interstitial area (n=5). **(F)** Quantitative analysis of shrunken EPS bead diameters. Due to anisotropic shrinkage of templates, top and bottom side templates exhibit different size reduction (n=75-100, * $P<0.05$).

6.3.2 Fabrication of ICC hydrogel scaffolds using EPS bead-based templates

Complete infiltration of hydrogel precursor solution into the interstitial space of colloidal crystal templates requires centrifugation, and the templates should endure the gravitational force. Two critical considerations in using EPS bead-based colloidal crystal templates include flotation of the structure and insufficient mechanical stability. We addressed the flotation issue with a laser-cut acrylic structure designed to fit a standard 50 mL centrifuge tube, consisting of thin rings that support a disk with holes which are then held down with long bracing pieces that become wedged once the cap is screwed on **(Figure 6.3A)**. In this study, we used a hydrogel precursor solution composed of acrylamide monomer and bis-arylamide crosslinker activated by ammonium persulfate and TEMED. After overnight polymerization at room temperature, the polymerized hydrogel and EPS template were taken out from the tube and excess hydrogel was removed. Finally, hydrogel-EPS templates were soaked in chloroform for 4-6 hours during which EPS beads were selectively dissolved, leaving behind an ICC polyacrylamide hydrogel matrix **(Figure 6.3B)**. EPS templates prepared in solutions with less than 80 % ethanol were broken during precursor infiltration, in which the characteristic ultimate mechanical strength was 1.8 ± 0.2 megapascals (MPa). EPS templates prepared in pure ethanol exhibited the highest mechanical strength (10.3 ± 1.2 MPa) but were difficult to infiltrate with precursor solution due to limited interstitial space **(Figure 6.3C)**. When this mechanical correlation was plotted as a function of the overall template size, it turned out that more than 50 % size reduction was required to maintain mechanical strength necessary for centrifugation **(Figure 6.3D)**. Based on these data, we determined that templates processed with 90 %

ethanol solution were optimal for fabrication of EPS-templated ICC polyacrylamide scaffolds.

EPS-templated ICC hydrogel scaffolds exhibited spherical pore cavities and optical transparency comparable to ICC hydrogel scaffolds prepared with glass beads of comparable sizes **(Figure 6.3E)**. Scaffold pore size was found to be tunable based on the duration of EPS-templated processing. For example, pore diameters were 1.05 ± 0.2 mm, 9.27 ± 0.18 mm and 8.23 ± 0.15 mm for ICC hydrogel scaffolds fabricated from templates made with 90% ethanol for 5 min, 15 min and 30 min operation, respectively **(Figure 6.3F)**. The EPS-templated ICC hydrogel scaffold fabrication strategy is flexible and rapid, enabling creation of different prototypes demonstrated by triangular, square, and hexagonal shapes of ICC hydrogel scaffolds by changing the initial mold design **(Figure 6.3G)**.

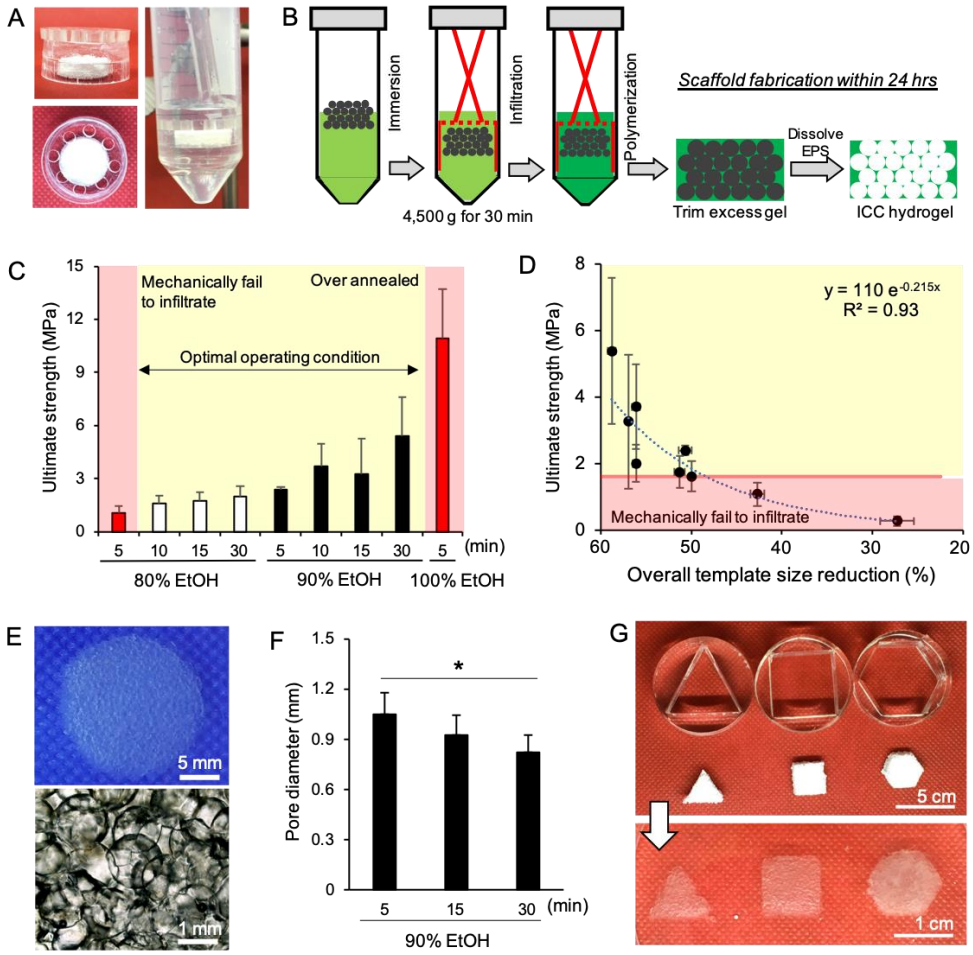

Figure 6.3. Preparation of EPS-templated ICC polyacrylamide hydrogel scaffolds. **(A)** Acrylic structures designed to keep EPS bead-based colloidal crystal templates submerged during the infiltration of precursor solution and subsequent polymerization. **(B)** Schematic of experimental procedures to obtain a hydrogel with an ICC structure. **(C)** Quantitative analysis of the ultimate strength of fused EPS beads under varying conditions and an indication of the optimal operating range. **(D)** Quantitative correlation of ultimate strength and diameter change highlighting the minimum mechanical strength to endure mechanical stress of centrifugation. **(E)** Camera (top) and microscope (bottom) images of EPS-templated ICC hydrogel scaffolds. **(F)** Quantitative analysis of pore diameters of ICC hydrogel scaffolds fabricated with three different operating periods and 90% ethanol. (n=4, *P<0.05). **(G)** Demonstration of conserved EPS template shrinking, and subsequent ICC hydrogel scaffolds fabricated with varying initial mold shapes.

6.3.3 Preparation of bioactive ICC hydrogel scaffolds via type I collagen integration in bulk hydrogel

Polyacrylamide hydrogel is not conductive for cell adhesion and requires immobilization of collagen fibers or RGD peptides to become bioactive. However, reagents for the conjugate chemistry are expensive and this procedure is laborious. Instead we hypothesized that inclusion of collagen fibers directly in the precursor solution would simplify fabrication of bioactive ICC hydrogel scaffolds. To test this hypothesis, we fabricated ICC hydrogel scaffolds with precursor solution containing type I collagen fibers at a final concentration of 2 mg/mL and compared them to scaffolds prepared by attaching collagen fibers using Sulfo-SANPAH conjugate chemistry **(Figure 6.4A)**. Collagen fibers in the hydrogel matrix were visualized via second harmonic generation in a multiphoton microscope. As expected, the conventional method immobilized collagen exclusively on the pore surface whereas collagen dispersed in the precursor solution appeared both on the surface and within the bulk hydrogel. Collagen fibers exhibited different morphologies; stretched thin fibers when surface conjugated and coiled bundles when mixed directly in the polymer precursor solution **(Figure 6.4B)**. Collagen fibers are known to undergo a reversible conformational change depending on the surrounding pH [318]. For example, at low pH, collagen fibers adopt an elongated morphology whereas at high pH, collagen fibers coil. Our results indicate that the alkaline reaction pH of acrylamide polymerization via addition of ammonium persulfate and TEMED could direct collagen fibers to adopt a more coiled morphology[319].

We next examined whether the collagen embedded within the polyacrylamide of an ICC hydrogel scaffold could support stromal cell adhesion. Primary BMSCs retrieved from the femurs of eGFP mice were used to easily visualize stromal cells seeded on the

scaffold. Fluorescence images taken 3 days after seeding showed that most stromal cells adhered and displayed an elongated, spread morphology on scaffolds with collagen, whereas the stromal cells that adhered on control collagen-free hydrogel scaffolds had a round morphology, indicating poor surface adhesion **(Figure 6.4C)**. Quantitative analysis of stromal cell morphology revealed 85 % had an elongated morphology on collagen scaffolds whereas only 15 % of cells adhered on collagen-free scaffolds **(Figure 6.4D)**. These results indicate that direct introduction of collagen fibers in precursor solution promotes stromal cell adhesion comparable to conventional conjugate chemistry.

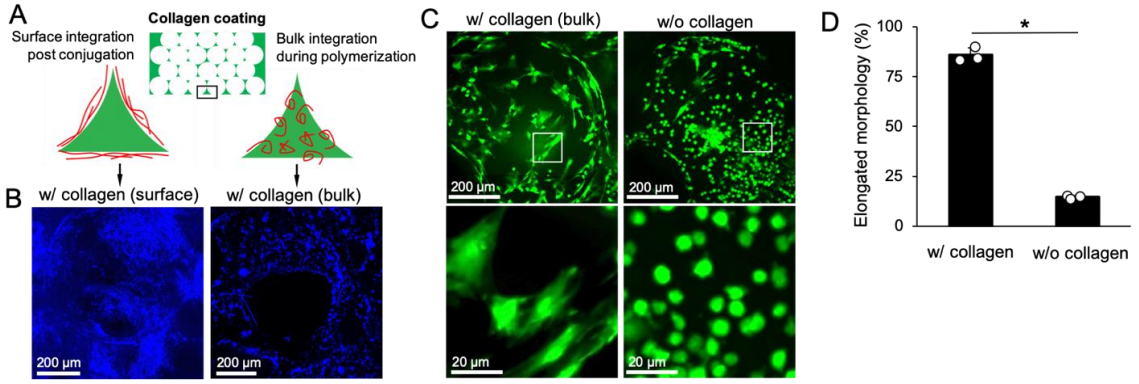

Figure 6.4. Hybridization of collagen and polyacrylamide to achieve bioactive hydrogel scaffolds.
(A) Schematic illustration of conventional surface modification using conjugation chemistry and dispersion in precursor solution for direct integration within the hydrogel matrix during polymerization. **(B)** Second harmonic generation images of collagen on polyacrylamide hydrogel scaffolds using multiphoton microscopy. **(C)** Comparison of fluorescent confocal images of eGFP BMSCs on the pore surface of ICC hydrogel scaffolds with and without bulk collagen integration. **(D)** Quantitative comparison of stromal cell adhesion morphology. (n=3, *P < 0.05)

6.3.4 *In vitro* modeling of bone marrow tissue microenvironments

For an *in vitro* functional demonstration, we applied EPS-templated ICC hydrogel scaffolds to model the bone marrow tissue microenvironment focusing on hematopoietic cell activity as a function of BMSCs. BMSCs are known to secrete a variety of soluble factors that support and direct hematopoietic activity in the bone marrow[320-322]. By changing the availability of collagen we hypothesized that the BMSCs seeded on ICC hydrogel scaffolds would adopt distinctive soluble factor profiles and differentially direct hematopoietic colony forming activity. A critical issue in characterizing hematopoietic colonies in 3D scaffolds is deciphering stroma from hematopoietic cells and their progenitors using traditional microscopy techniques. To overcome this challenge, we employed cells from eGFP and DsRed reporter mice that facilitate fluorescent monitoring of stromal and hematopoietic cell activity while preserving the intrinsic phenotype of both cell types **(Figure 6.5A)**. We first examined the secretion profile of BMSCs focusing on key factors involved in bone remodeling: IL-6, osteoprotegerin (OPG), and receptor activator of nuclear factor kappa-B ligand (RANKL). Increased RANKL and IL-6 stimulate osteoblasts and osteoclasts to promote bone remodeling activity, whereas OPG secretion suppresses remodeling activity. ELISA data showed that BMSCs secreted significantly more IL-6 and RANKL and notably lower OPG on collagen-free ICC hydrogel scaffolds than collagen embedded hydrogel scaffolds **(Figure 6.5B-D)**. These results indicate that BMSCs seeded on hydrogel matrix with embedded collagen suppress bone remodeling activity.

We next evaluated if the different soluble environments could direct hematopoietic colony forming activity. After 1-week culture of eGFP BMSCs on collagen-coated and

control ICC hydrogel scaffolds, we introduced freshly harvested femoral bone marrow cells retrieved from DsRed mice. Before loading, bone marrow cells were dispersed in methylcellulose medium without hematopoietic cytokines. Subsequent hematopoietic colony development was monitored with fluorescence microscopy over a 16-day period. DsRed fluorescent colonies gradually emerged in and around BMSC seeded scaffolds **(Figure 6.5E)**. This unconventional three-dimensional colony forming assay makes it difficult to distinguish specific types of hematopoietic colonies. Instead, we focused on the number of emerging colonies by taking advantage of the endogenous fluorescence. In stromal cell-free control cultures without essential hematopoietic cytokines, no hematopoietic colonies emerged, indicating stromal cells play a vital role in supporting the survival and function of hematopoietic cells *ex vivo*. Quantitative monitoring of colony number over the experimental period showed an increased number of hematopoietic colonies when cocultured with BMSCs seeded on scaffolds with embedded collagen, whereas the number of colonies stabilized after 1-week of coculture with BMSCs on collagen-free scaffolds **(Figure 6.5F).** 3D confocal imaging at the end of the study revealed the spatial distribution of BMSCs and hematopoietic cells, with some in physical contact with each other **(Figure 6.5G)**. Collectively these results indicate that the different soluble milieus produced by BMSCs with and without collagen stimulation can affect hematopoietic colony forming activity. This also demonstrated that EPS-templated ICC hydrogel scaffolds are capable of identifying dynamic functional interactions between hematopoietic and stromal cells *ex vivo*.

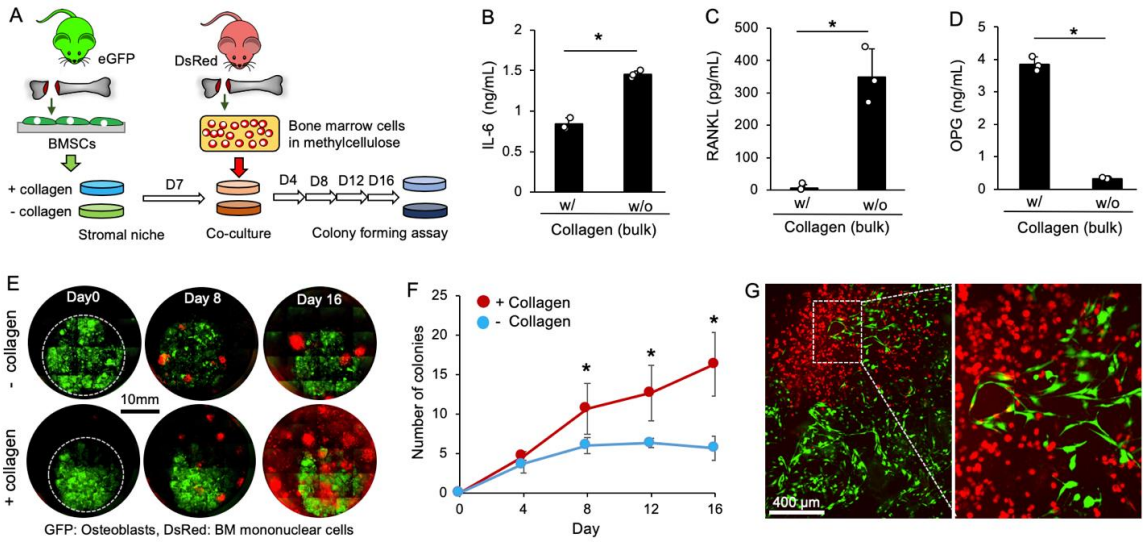

Figure 6.5. ***In vitro*** **demonstration of functional bone marrow tissue model using EPS-templated ICC hydrogel scaffolds.**

(A) Schematic of bone marrow tissue model with eGFP stromal cells and subsequent introduction of bone marrow cells from DsRed mice dispersed in methylcellulose medium for colony-forming assay. **(B-D)** Comparative ELISA of **(B)** IL-6, **(C)** osteoprotegerin (OPG), and **(D)** RANKL secretion by BMSCs seeded on collagen and collagen-free ICC hydrogel scaffolds. **(E)** Representative fluorescence microscope images of time course hematopoietic colony-forming activity in BMSC seeded scaffolds on collagen and collagen-free ICC hydrogel scaffolds. **(F)** Time course quantification of hematopoietic colony count (n=3, * P<0.05). **(G)** Z-projection of 3D confocal microscope images of stromal (green) and hematopoietic (red) cell spatial distribution in EPS-templated ICC hydrogel scaffolds.

6.3.5 Formation of lymphoid mimicking tissue microenvironments *in vivo*

Subdermal implantation of ICC hydrogel scaffolds has been shown to direct unique foreign body responses leading to a richly vascularized stromal tissue with prolonged hematopoietic cell activity. We evaluated if EPS-templated ICC hydrogel scaffolds induced comparable tissue development to hydrogel scaffolds made with glass beads after subdermal implantation in FVB mice **(Figure 6.6A)**. Scaffolds fabricated from glass beads were chosen for comparison because they are commercially available in sizes close to those achieved with the EPS fabrication technique. Gross observation after four weeks of implantation revealed EPS and glass-templated ICC hydrogel scaffolds showed similar tissue development and attraction of large blood vessels **(Figure 6.6B)**. H&E staining confirmed complete interscaffold tissue development and a comparable pattern of spatial tissue microenvironments directed by the ICC geometry. In general, fibrotic tissue is formed within the central region of each pore whereas hematopoietic cells are localized near the pore surface **(Figure 6.6C)**.

We further characterized the vascular network and attraction of macrophages and neutrophils via immunohistostaining for CD31, F4/80 and Ly6G, respectively. Tissues developed in EPS-templated ICC hydrogel scaffolds contained an extensive vascular network similar to glass-templated ICC scaffolds **(Figure 6.6D)**. Non-degradable synthetic hydrogels direct macrophage response throughout the entire scaffolds **(Figure 6.6E).** Distinct from the widespread vasculature and macrophages, neutrophils were highly localized in 2-3 sites of each tissue section **(Figure 6.6F).** Overlaid CD31, F4/80, Ly6G, and nuclei staining substantiates the spatial distribution of vascular, stromal and immune cells in an ICC pore cavity **(Figure 6.6G).** Quantitative analysis of CD31, F4/80, and Ly6G

positive areas confirmed comparable tissue development between EPS- and glass-templated ICC hydrogel scaffolds **(Figure 6.6H-I)**. Overall our results indicate that EPS-templated ICC hydrogel scaffolds retain comparable ability to induce characteristic vascularized and hematopoietic cell attracting lymphoid tissue-mimicking microenvironments to glass-templated ICC hydrogel scaffolds.

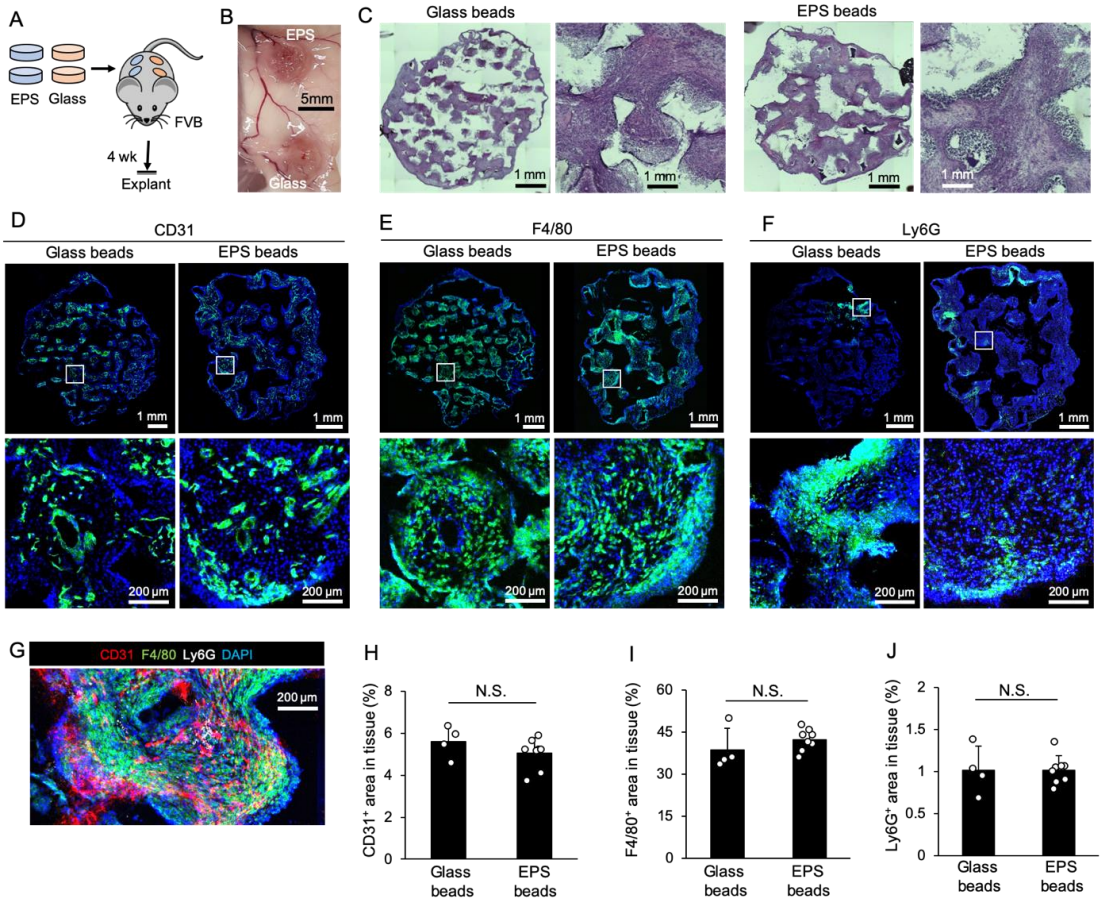

Figure 6.6. Comparison of tissue microenvironment formed in ICC hydrogel scaffolds made from glass and EPS beads after subdermal implantation.
(A) Experimental schematic of EPS and glass-templated ICC hydrogel scaffold implantation for *in vivo* tissue microenvironment formation. **(B)** Gross images of glass- and EPS-templated ICC hydrogel scaffolds in FVB mice after 4 weeks of subdermal implantation. **(C)** Comparison of hematoxylin and eosin stained tissue microenvironments. **(D-F)** Comparison of immunohistostaining (IHS) for **(D)** blood vessels (CD31), **(E)** macrophages (F4/80) and **(F)** neutrophils (Ly6G). **(G)** Overlaid IHS image of blood vessels, macrophages, neutrophils, and nucleus (DAPI) to visualize the spatial resolution in the lymphoid tissue mimicking microenvironment. **(H-J)** Quantitative imaging analysis of **(H)** $CD31^+$, **(I)** $F4/80^+$, and **(J)** $Ly6G^+$ positive areas (%) (n=6, *P<0.05).

6.4 Discussion

In this report, we introduced EPS bead-based ICC hydrogel scaffold fabrication. EPS beads are widely available at low cost. From a material aspect, EPS beads exhibit intermediate characteristics between solid beads and microbubbles while retaining mechanical integrity and flexibility. These properties facilitate the production of the intricate geometry of ICC scaffolds in a fast, cost-effective, and less toxic manner when compared to existing template materials. In addition, direct inclusion of type I collagen in the precursor solution has greatly simplified the manufacturing procedure for bioactive hydrogel scaffolds. These features represent great potential to reduce the technical and cost barriers in fabricating bioactive ICC hydrogel scaffolds. The presented method for EPS-templated hydrogel scaffolds can be improved further. First, the dimension of EPS beads is not ideal for modeling trabecular bone cavities in hematopoietic bone marrow and other lymphoid tissues. This issue can be resolved by reducing the size of expandable polystyrene resins that are being processed into EPS. Second, the packing of EPS beads is suboptimal as the low density of EPS beads makes it difficult to apply centrifugation and agitation-assisted packing methods. This can be improved by benchmarking the previous methods in building colloidal crystal templates at the air-water interface[323-324]. Lastly, the coiled morphology of in situ collagen integration is also suboptimal to maximize the function of collagen for stromal cell adhesion. Collagen fibers undergo pH dependent conformational change; collagen fibers are relaxed in an acidic environment whereas they are coiled configuration in basic solutions[325]. Alkaline precursor solution likely causes the collagen fibers to undergo a conformational change. By adjusting the pH in the precursor

solution, more aligned collagen fibers and better coverage of hydrogel matrix may be achieved.

Water and ethanol were used to generate the pressurized heated vapor phase responsible for EPS shrinkage and fusion to form a free-standing template structure. Although the theoretical temperature of the chamber was lower in pure ethanol samples, the size reduction was the greatest. This phenomenon may be explained by the solubility of polystyrene in ethanol and water. Solubility parameters can be estimated from physical properties, as described by the Hildebrand solubility parameter and Hansen solubility parameter[326]. The Hildebrand model defines the parameter δ as the square root of the cohesive energy density. Cohesive energy density is the negative value of the internal energy commonly defined *U*, divided by the molar volume. The Hansen model provides expansion of application to polar systems via empirical observations to determine dispersive, polar, and hydrogen-bonding terms. Solubility parameters provide input on whether polymers will dissolve in solvents, effectively if solubility parameters are similar the two components are predicted to be miscible. The Hansen solubility parameters δ $(MPa)^{1/2}$ for water, ethanol, and polystyrene are 47.9, 26.0, and 18.7, respectively. For comparison the solubility parameter for the solvent used to dissolve the template, chloroform is 19 $(MPa)^{1/2}$. The increased, though overall poor, solubility of polystyrene in ethanol may provide faster collapse of the foam structure within EPS beads. The beads do not appear to lose their spherical geometry indicating these changes may occur on a very small scale. Electron microscopy may provide details on pore structure of EPS beads processed with different solvents. Additionally, means to calculate solubility parameters of mixtures are not straightforward. However, other than samples processed with a 50:50

mixture, this assessment provides evidence for the two extreme cases of EPS shrinkage as seen by use of pure vapor phase solutions. Evaluation with solvents with similar solubility parameter values may further substantiate these claims.

Besides lymphoid tissue modeling, ICC hydrogel scaffolds have been previously demonstrated to be advantageous in other tissue engineering applications. For example, ICC geometry made with cell-repulsive hydrogel matrix directed formation of multicellular hepatocyte and stem cell spheroids with narrow size distribution[327-328]. Hepatic and embryonic spheroids demonstrated *in vivo* relevant cellular processes in toxic nanoparticle exposure[316] and differentiation into lineage cells[329], respectively. ICC hydrogel scaffolds have demonstrated additional *in vitro* success modeling cartilage[330], bone[314] and neuronal[331] tissues taking advantage of their unique geometry with tailored biomaterials in each target application. ICC hydrogel scaffolds have also demonstrated exceptional capability for rapid vascularization as a function of pore size[298]. This capability has been applied for cardiac tissue engineering and wound healing medical devices. The presented EPS-templated ICC hydrogel scaffold fabrication will leverage these abilities to broader academic and industrial communities.

ICC hydrogel scaffolds with controlled isotropic spherical pore arrays of hydrogel matrix has emerged as an important class of biomaterials for tissue engineering. Originally in the context of lymphoid tissue engineering, ICC scaffolds have many promising applications both *in vitro* and *in vivo*. An important next step in the advancement of ICC hydrogel scaffolds is improved fabrication techniques that facilitate effective scale up. Currently, there are no commercial ICC hydrogel scaffolds due to material cost, time, and safety. The presented work provides a cheaper, faster, and safer method for ICC hydrogel

fabrication by using EPS and directly mixing collagen fibers within the synthetic hydrogel matrix. ICC hydrogel scaffolds have already demonstrated many promising applications in lymphoid tissue engineering and beyond. We envision that the presented EPS beads-based scaffold fabrication will greatly facilitate broad and practical applications of ICC hydrogel scaffolds to the research community and enable exploration into translational opportunities for patients.

6.5 Materials and Methods

All chemicals and cell culture reagents were purchased from Thermo Fisher Scientific unless otherwise specified. The animal protocol was approved by the University of Massachusetts Amherst Institutional Animal Care and Use Committee.

6.5.1 Pressurized thermal annealing of EPS beads

EPS beads (Diameter = 1,626 ± 195 μm) obtained from Amazon were loaded into a perforated stainless-steel mesh container (Diameter = 38 mm, Height = 44 mm) to a height of 1 cm. The mesh container was transferred to an elevated rack in a 2.5-quart electric pressure cooker and the cooker was filled with 200 mL of ethanol and water mixture. Using the “High Pressure” setting on the cooker, an annealing time was set between 5-30 minutes. The lid was attached, and the pressure valve was closed to prevent loss of vapor. At the end of annealing, built-up pressure was released before carefully removing the lid and steel mesh containers. Annealed EPS templates were kept at room temperature prior to further processing. Template images were acquired with an inverted tissue culture microscope. Pore size analysis was performed in ImageJ.

6.5.2 Micro-CT imaging and porosity characterization

Templates fabricated using different annealing conditions and times were scanned using the CT imager on an IVIS SpectrumCT with a voxel size of 75 μm. Calculation of void fraction based on micro-CT imaging was performed in MATLAB.

6.5.3 EPS bead-templated ICC hydrogel scaffold fabrication

An acrylamide precursor solution was made with 30 wt% acrylamide monomer and 1.5 wt% bis-acrylamide crosslinker dissolved in nitrogen-purged deionized (DI) water. For collagen experiments, nitrogen purged DI water was displaced with a 4 mg/mL rat-tail collagen solution to obtain a final collagen concentration of 2 mg/mL. Prior to polymerization of the EPS template, a 50 mL centrifuge tube was prepared with laser-cut acrylic inserts to keep the template fully submerged during polymerization. 10 wt/vol% ammonium persulfate and N,N,N',N'-tetramethyl-ethylenediamine (TEMED) were added to the acrylamide precursor solution such that both were at a final concentration of 0.1 %. The solution was added to the EPS template-containing centrifuge tube and centrifuged at 4,500 xg for 20 minutes at 4 °C. Tubes were carefully removed from the centrifuge and left at room temperature to polymerize. Once polymerized, infiltrated EPS templates were retrieved from the centrifuge tubes and carefully scraped on all sides with a razor blade to remove excess polymer. Infiltrated EPS templates were placed in chloroform and left overnight to dissolve EPS beads. A second wash with fresh chloroform was performed to remove residual EPS before thorough washing with water. Hydrogel gel scaffolds were sterilized by submerging in 70 % ethanol for 30 minutes. For *in vitro* and *in vivo* applications scaffolds fabricated with 90 % ethanol and annealing time of 30 minutes were

used. Initially large scaffolds were cut down (Diameter = 6 mm x Height = 2.5 mm) using a 6 mm biopsy punch and a razor blade. Sterile scaffolds were stored in phosphate-buffered saline at 4 °C.

6.5.4 Rat tail type I collagen isolation

Type I collagen was isolated from rat tails using serial salt precipitation and dissolution in acetic acid[97]. Briefly, tendons were extracted from rat tails using hemostats and a razor blade, and then dissolved in 3 % (v/v) acetic acid overnight. The resulting solution was passively filtered through a 500 μm mesh and centrifuged for 2 hours at 13,000 xg at 4 ^{o}C to remove debris and impurities. Next, the supernatant was collected and diluted 1:4 by volume in a 30 % (wt/v) NaCl solution at a rate of 350 mL/hr and then left still for 2 hours. To collect the collagen, the resulting solution was spun down at 8,500 xg for 45 min at 4 ^{o}C, and the precipitated gelatinous collagen harvested. Addition of salt solution and precipitation was repeated until no more collagen was extracted from the solution after centrifugation, upon which all collagen material was combined and resuspended in 0.6 % (v/v) acetic acid. The collagen solution was then dialyzed in 1 mN HCl, and the concentration determined using lyophilization.

6.5.5 Glass bead-templated ICC hydrogel scaffold fabrication

Soda lime glass beads (Diameter = 650 ± 65 μm) were sorted using an Advantech Sonic Sifter. Beads dispersed in DI water were gradually loaded into a glass vial (8×35mm) to a height of 2–2.5mm and were mechanically packed into a lattice structure in an ultrasonic water bath. Orderly packed glass beads were dried in a 60 °C oven and then thermally annealed for 4 h in a furnace between 650 and 680 °C. A hydrogel precursor solution composed of 30 wt% acrylamide monomer, 1.5wt% bis-acrylamide crosslinker,

0.2 vol% N,N,N′,N′-tetramethylethylenediamine accelerator, and 0.2 vol% 2-hydroxy-2-methylpropiophenone photoinitiator in nitrogen-purged DI water was prepared immediately before use. Precursor solution (150 μl) was infiltrated into the glass bead template and centrifuged in a microcentrifuge at 8,500 xg for 15min and subsequently polymerized under a 15W ultraviolet light source for 15min. Polyacrylamide hydrogel–glass templates were removed from the glass vials the next day to ensure complete polymerization. Excess hydrogel was removed by scraping the glass bead template with a razor blade on all surfaces. Glass beads were selectively dissolved in alternating washes of an acid solution containing a 1:5 dilution of hydrofluoric acid in 1.2M hydrochloric acid and 2.4M hydrochloric acid (caution: these chemicals are corrosive and must be used in a fume hood with proper protective gear). Washes were completed on a shake plate, and solutions were changed every 4h until the beads were removed. Scaffolds were thoroughly washed with DI water to remove residual acid and lyophilized. Type I collagen isolated from rat tails was covalently immobilized on the pore surface using Sulfo-SANPAH conjugate chemistry as previously described[101].

6.5.6 Mechanical testing of EPS templates

Mechanical properties were measured using an ElectroForce 5500 (TA Instruments) equipped with a 50 lb-load cell. A strain rate of 0.02 mm/sec was applied with a 3 mm platen. Ultimate strength was calculated by taking the maximal force before failure.

6.5.7 Multiphoton microscopy imaging of collagen fibers via second-harmonic generation

Collagen fibers on the surface and embedded within hydrogel scaffolds were imaged using a Nikon A1MP multiphoton microscope equipped with a tunable Ti:Sapphire laser source set at an excitation wavelength of 850 nm and a 492 nm shortpass filter.

6.5.8 Primary mouse bone marrow stromal cell isolation and culture expansion

A breeding pair of eGFP mice (006567) were purchased from Jackson Laboratories. A breeding pair of DsRed (005441) was obtained from Dr. Barbara Osbourne. Femurs and tibias were collected from DsRed or eGFP mice. Bone marrow stromal cells (BMSCs) were isolated from the bone by centrifugation and cultured in alpha-Modified Eagle Medium supplemented with 10 % fetal bovine serum and 1 % penicillin-streptomycin. Adherent cells were cultured for a maximum of 4 passages.

6.5.9 ELISA of mouse IL-6, OPG, and RANKL

EPS scaffolds with and without collagen were seeded with 500,000 adherent eGFP BMSCs and cultured in the wells of a 48 well plate. The culture was maintained until cells spread and covered the scaffold surface. 2D tissue culture plastic controls were seeded at a density of 50,000 cells per well and grown until confluence. Medium was changed every 3 days for the duration of the experiment. At the end of the experiment conditioned media was collected 48 hours after a media change and frozen at -80 °C. ELISAs were performed on thawed conditioned media samples using ELISA kits acquired from R&D Systems.

6.5.10 Methylcellulose colony-forming assay

EPS scaffolds were seeded with 500,000 adherent eGFP stromal cells and cultured in wells of a 48 well plate until all surfaces were covered. Freshly isolated bone marrow

cells from DsRed mice were resuspended to a concentration of 500 cells/μL in methylcellulose media (1.27 % alpha-Modified Eagle Medium methylcellulose, 10% fetal bovine serum, and 1% penicillin-streptomycin). 50,000 cells were carefully added to the wells containing eGFP BMSCs pre-seeded EPS-templated ICC hydrogel scaffolds and empty EPS scaffolds. Full well scans were acquired using an EVOS fluorescent microscope on day 1, 4, 8, 12 and 16. Fluorescent z-stack images were taken by confocal microscope (Zeiss Cell Observer) and 3D reconstructed images were generated and animated in Nikon Elements AR v5.2.0. FFMPEG was utilized to downsample and compress the 3D reconstructions.

6.5.11 Subdermal implantation of scaffolds in mouse models

6-week old FVB mice (001800) were obtained from Jackson Laboratory. Mice were anesthetized with 1.5% isoflurane before removing dorsal hair with electric clippers and Nair. 70% of isopropanol wipes were used to sterilize the skin. Mice received 2 mg of meloxicam/kg mouse weight subcutaneously prior to surgery. Four subcutaneous pockets were formed in mice and EPS and Glass-templated ICC hydrogel scaffolds were immediately place within. Wounds were closed with two 7 mm wound clips. Wound clips were removed after one week. Four weeks after implantation scaffolds were retrieved and flash frozen in Shandon Cryomatrix embedding resin. Tissue blocks were stored at -80 °C until use.

6.5.12 Histological characterization

Frozen tissue blocks were sectioned on an NX70 cryostat at a thickness of 20 μm. Hematoxylin and eosin, and immunohistostaining procedures were performed as previously described[101]. CD31 (550274), F4/80 (565409), and Ly6G (557445) primary

antibodies and anti-Rat AlexaFluor 647 (A21247) secondary antibodies were used in this study. Brightfield images were acquired on an EVOS FL Auto microscope and fluorescent images were acquired on a Zeiss Cell Observer SD.

6.5.13 Statistics

Unpaired Student's t-test was performed for comparison of the mean values in all quantitative analysis. Statistical significance was determined if $p<0.05$ for a two-tailed analysis. All quantitative data represent mean and standard deviation.

CHAPTER 7

CONCLUSION AND FUTURE DIRECTIONS

7.1 Conclusion

Metastasis remains a critical problem in clinics and therapeutic strategies have not made significant impact on patient health. The work presented here provides an enabling tool to better understand disseminated tumor cells (DTCs) and their progression to lethal metastases and potentially provide translational results to improve patient health. Inverted colloidal crystal (ICC) hydrogel scaffolds produce standardized and controlled *in vivo* niches for a wide variety of studies. The flexibility of ICC scaffolds and implantable niche models can be leveraged for further tunability. First, the physical and bulk properties of the scaffold can be altered by changing the pore size, the polymer material, and polymer properties such as crosslinking density. For example, pore size was shown to alter vasculature formation and control the diameter of blood vessels. Second, *ex vivo* cell seeding enables new cell populations to be directly added to the tissue niche. Here I have utilized human bone marrow stromal cells to generate niches that actively secrete human cytokines and more closely model human tissue. Third, changing the implant location drastically changes the local cell populations and impacts the final cellular and molecular niche that forms within the pores. Finally, the transplantable capabilities enable extended experimental duration and open the door to the development of new strategies to model disease. Here we transplanted to syngeneic hosts of similar age, however one exciting possibility is transplantation into significantly older hosts to understand how ageing affects the niche and metastasis.

The immunomodulatory properties of ICC hydrogel scaffolds prevent fibrotic encapsulation, typically associated with the later stages of the foreign body response. Instead a highly vascularize tissue rich in bone marrow derived cells is formed. Here I heavily relied on these properties to create a receptive niche for circulating tumor cells. Additionally, I have demonstrated the ability to leverage the benefits of increased vascularization and altered immune response to transplant lung and liver tissue ectopically to the subcutaneous space. Maintenance of native tissue properties is an exciting result and provides evidence that xenotransplantation of mature human tissue may benefit from the scaffold-assisted approach. Out of patient study of fully mature human tissues in an *in vivo* setting could prove to be powerful preclinical models for drug screening and probing basic biological questions about human tissue.

The central goal of this work was to create new *in vivo* models that overcome the limitations present in traditional models of metastasis. I have shown the versatility of implantable models across several mouse strains: FVB, C57BL/6, and NSG. Additionally, the implantable niche strategy has been successful in multiple methods of tumor generation including intravenous, orthotopic, xenografts, and genetically engineered spontaneous cancer models. The work has addressed very critical problems in DTC dormancy and metastatic relapse. DTC dormancy models were formed using a transplantable niche strategy. Primary tumor burden and aggressive metastases in vital organs prevents the effective study of long-term dormant DTCs. Transplantation of DTC containing niches enabled long-term observation and identified critical niche components that are associated with maintenance and activation of dormancy. This was furthered by instigating the niche to try and force an escape from dormancy. I found that adjuvant therapy, while effective at

reducing burden initially did not prevent DTC growth long-term. Surgical intervention was also shown to play a role in increasing the growth of DTCs. These results demonstrate that ICC scaffolds can capture long-term DTC phenomenon and may reveal targetable factors that activate metastatic progression.

Finally, I have demonstrated a new fabrication scheme for ICC hydrogel scaffolds. The entirety of the *in vivo* metastasis studies performed in this work were performed with glass beads, however the manufacturing process is laborious, dangerous, and ultimately costly. Changing to expanded polystyrene beads provided a more scalable approach that may utilize existing infrastructure for large scale production of ICC hydrogel scaffolds.

7.2 Future Directions

Although several milestones were achieved with the presented work, implantable niches to study metastasis are still relatively underutilized and the translational potential remains unmet. The microenvironment is finally being recognized as a key driver of DTC fate, and new characterization techniques enable deeper analysis into components of the niche. Single cell RNA sequencing has provided an unparalleled level of cellular detail but has not been utilized to understand niche evolution around DTCs[332]. Part of this challenge has been in capturing DTCs and their immediate niche for analysis. This process requires total disruption of the tissue, therefore it is not practical to capture the local niche for analysis. Efforts have been made to adapt single cell RNA sequencing to histological slides enabling spatial mapping of RNA sequencing data[333]. This is an exciting direction to detect minute differences in the DTC niche as cells undergo the transition from dormancy to a proliferative state and could be applied to long-term dormant DTC containing scaffold niches. Similar spatial analysis should be performed on the local matrix proteins.

Techniques such as imaging mass spectrometry provide spatial proteomic analysis and have been used to understand protein regulation of tumor expansion[334]. A final analysis to continue to pursue is of the local secretome. I have provided evidence of changing secretome after chemotherapy in this work. However, temporal monitoring would provide a better idea as to how the niche is evolving and provide further mechanistic understanding of cytokine signaling and inflammatory pathways associated with metastatic progression. In regard to cytokines and soluble molecules, exosomes are another exciting class of molecule that should be investigated in the DTC niche. Understanding exosome signaling during the foreign body response may enable further immune modulation.

The tunable nature of tissue engineered niches can reduce the gap in species-species differences between mice and human when using animal models. As described here a humanized niche was formed by pre-seeding the scaffold with human bone marrow stroma cells. Although not fully representative of the bone marrow, this approach may be used as a starting point to generate human-relevant stromal niches to study their interaction in an *in vivo* setting. For example, human lung stromal cells or human kidney stromal cells could be seeded onto scaffolds to identify potential differences driven by the stromal cells that substantiate the altered metastatic growth in typically high and low metastatic tissues, respectively. In addition to probing the interaction of specific cellular components, extracellular matrix proteins can be directly investigated using implantable scaffold niches. For example, fibronectin has been identified as a potential marker for the pre-metastatic niche development. Increased integration of fibronectin into the scaffold via surface coating or bulk integration within the polymer matrix may yield significantly different tissue formation and metastatic potential within the scaffold niches. This approach could

be applied to other extracellular matrix proteins including specific collagens beyond type I found in rat tails, elastins, and laminins. I expect that this high level of microenvironment control will aid in the identification of cellular and molecular factors that drive metastatic relapse. In addition to changing the potential metastatic capabilities of the scaffolds, unique translational opportunities may arise from the formation of different tissue microenvironments by changing the initial cellular and molecular composition of the scaffolds prior to implantation.

Deeper mechanistic understanding of the DTC niche will ultimately produce targetable cellular and molecular pathways that enable metastatic growth. Previous work has demonstrated the ability for scaffold metastasis models to act as a screening platform based on microarray analysis of the niche. In this dissertation work I have developed new methods to test syngeneic models in high throughput via transplantation of primary MMTV-PyMT tumor fragments. Further development as a preclinical screening model should be pursued and implemented based on literature and future findings. For example, checkpoint inhibitors are an exciting therapeutic option that have been relatively unexplored mechanistically within the context of metastatic relapse. This future research direction using biomaterial DTC niches is important in validating potential mechanisms of metastatic relapse and maintenance of dormancy, and screening of pre-clinical candidates.

Intravital imaging is a powerful technique that enables real-time observation of cellular events in a living organism. Extravasation and tracking of disseminated tumor cells into the brain microvasculature has been shown using a chronic cranial window[48]. This model also identified necessary steps that were necessary for metastasis formation including extravasation out of circulation and remaining in the perivascular space. Another

approach has been performed to examine the lung microenvironment using a vacuum stabilized window directly on the lung of a mouse[107, 335-336]. These windows have been critical in observing extravasation of cancer cells into the lung tissue and early immune cell interaction. For example, they have enabled visualization of neutrophil extracellular traps around pro-metastasis cancer cell lines that had extravasated into the lungs[251]. Previously our lab has utilized a dorsal-skin fold window chamber to observe tumor cells extravasating into the scaffold niche[97]. I have started to implement this technique with moderate success. First, scaffolds are implanted to allow for tissue development. During window engraftment, the skin is stretched around the scaffold such that it is sandwiched between the skin. Titanium supports are installed over the scaffold and held with a combination of screws and sutures. One side of the skin is removed, revealing the scaffold and a cover slip is installed **(Figure 7.1a)**. During imaging red fluorescent dextran is intravenously administered to visualize blood vessels. Intravenous injection of eGFP-MDA-MB-231 or eGFP-PC-3 tumor cells enables observation of tumor cells. Preliminary results reveal the ability to observe tumor cells and the local vasculature via the window chamber **(Figure 7.1b)**. Plans have been made to apply an intravital window to chimeric eGFP mice and introduce fluorescent cancer cells to observe bone marrow cell interaction with DTCs. Combining this study with adjuvant chemotherapy or surgical intervention may provide new insight on the dynamic interactions between DTCs and the surrounding niche during stimuli relevant to patients.

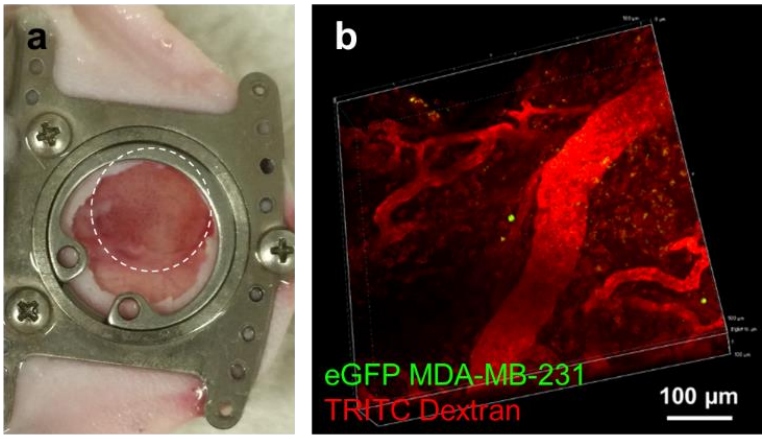

Figure 7.1. Intravital imaging.
a, Gross image of window chamber engraftment around implanted scaffold. **b,** Intravital image of DTC (green) and vessel (red).

Although I have investigated local immune modulation, systemic changes to immune cell behavior have not been investigated. Previous work in biomaterial implantation has had success in manipulating dendritic cell homing and immune response [120, 164, 240-242]. Implantable biomaterials have also been observed to reduce metastatic tumor burden in vital organs by altering CTC recruitment patterns [103-104]. Additionally, an experiment involving the implantation of human fetal tissue revealed a renewal in metastatic potential following either radiotherapy or injection of IL-1β [87]. I hypothesize that implantation of ICC scaffolds has unexplored systemic immunomodulatory properties that could be utilized for basic biological understanding or leveraged for translational use in patients. The potential for this research thrust has been demonstrated by the experiments performed by Krall *et. al.* whereby dormant tumors were reawakened following implantation of a biomaterial by mobilization of inflammatory bone marrow cells[273]. Similar strategies may provide therapeutic benefit for disease such as chronic fibrosis by redirecting bone marrow cell activity. Evidence highlighting the important interactions between the immune system and the intestinal microbiota have become increasingly

prevalent. Investigation of the role biomaterial implantation has on the microbiome and vice versa may uncover important immunomodulatory behavior that could have therapeutic benefit in unforeseen diseases.

I hope the work presented here will convince the community that tissue engineering approaches and specifically implantable ICC scaffold strategies are powerful tools to address provocative hypotheses that are challenging to study in traditional systems. I believe these approaches are still early in their development and their potential has not yet been realized.

BIBLIOGRAPHY

1. Hanahan, D.; Weinberg, R. A., Hallmarks of cancer: the next generation. *Cell* **2011,** *144* (5), 646-74.

2. Howlader N, N. A., Krapcho M, Miller D, Brest A, Yu M, Ruhl J, Tatalovich Z, Mariotto A, Lewis DR, Chen HS, Feuer EJ, Cronin KA (eds), SEER Cancer Statistics Review, 1975-2016. *National Cancer Institute. Bethesda, MD*.

3. Steeg, P. S., Tumor metastasis: mechanistic insights and clinical challenges. *Nat Med* **2006,** *12* (8), 895-904.

4. Braun, S.; Kentenich, C.; Janni, W.; Hepp, F.; de Waal, J.; Willgeroth, F.; Sommer, H.; Pantel, K., Lack of effect of adjuvant chemotherapy on the elimination of single dormant tumor cells in bone marrow of high-risk breast cancer patients. *J Clin Oncol* **2000,** *18* (1), 80-6.

5. Janni, W.; Vogl, F. D.; Wiedswang, G.; Synnestvedt, M.; Fehm, T.; Juckstock, J.; Borgen, E.; Rack, B.; Braun, S.; Sommer, H.; Solomayer, E.; Pantel, K.; Nesland, J.; Friese, K.; Naume, B., Persistence of disseminated tumor cells in the bone marrow of breast cancer patients predicts increased risk for relapse--a European pooled analysis. *Clin Cancer Res* **2011,** *17* (9), 2967-76.

6. Pan, H.; Gray, R.; Braybrooke, J.; Davies, C.; Taylor, C.; McGale, P.; Peto, R.; Pritchard, K. I.; Bergh, J.; Dowsett, M.; Hayes, D. F.; Ebctcg, 20-Year Risks of Breast-Cancer Recurrence after Stopping Endocrine Therapy at 5 Years. *N Engl J Med* **2017,** *377* (19), 1836-1846.

7. Smith, T. J.; Hillner, B. E., Explaining marginal benefits to patients, when "marginal" means additional but not necessarily small. *Clin Cancer Res* **2010,** *16* (24), 5981-6.

8. Lamouille, S.; Xu, J.; Derynck, R., Molecular mechanisms of epithelial-mesenchymal transition. *Nat Rev Mol Cell Biol* **2014,** *15* (3), 178-96.

9. Chaffer, C. L.; Weinberg, R. A., A perspective on cancer cell metastasis. *Science* **2011,** *331* (6024), 1559-64.

10. Aceto, N.; Bardia, A.; Miyamoto, D. T.; Donaldson, M. C.; Wittner, B. S.; Spencer, J. A.; Yu, M.; Pely, A.; Engstrom, A.; Zhu, H.; Brannigan, B. W.; Kapur, R.; Stott, S. L.; Shioda, T.; Ramaswamy, S.; Ting, D. T.; Lin, C. P.; Toner, M.; Haber, D. A.; Maheswaran, S., Circulating tumor cell clusters are oligoclonal precursors of breast cancer metastasis. *Cell* **2014,** *158* (5), 1110-1122.

11. Paget, S., The distribution of secondary growths in cancer of the breast

Lancet **1889,** *1*, 571-573

12. Obenauf, A. C.; Massague, J., Surviving at a Distance: Organ-Specific Metastasis. *Trends Cancer* **2015,** *1* (1), 76-91.

13. Tabaries, S.; Dupuy, F.; Dong, Z.; Monast, A.; Annis, M. G.; Spicer, J.; Ferri, L. E.; Omeroglu, A.; Basik, M.; Amir, E.; Clemons, M.; Siegel, P. M., Claudin-2 promotes breast cancer liver metastasis by facilitating tumor cell interactions with hepatocytes. *Mol Cell Biol* **2012,** *32* (15), 2979-91.

14. Zhao, L.; Lim, S. Y.; Gordon-Weeks, A. N.; Tapmeier, T. T.; Im, J. H.; Cao, Y.; Beech, J.; Allen, D.; Smart, S.; Muschel, R. J., Recruitment of a myeloid cell subset (CD11b/Gr1 mid) via CCL2/CCR2 promotes the development of colorectal cancer liver metastasis. *Hepatology* **2013,** *57* (2), 829-39.

15. Reticker-Flynn, N. E.; Bhatia, S. N., Aberrant glycosylation promotes lung cancer metastasis through adhesion to galectins in the metastatic niche. *Cancer Discov* **2015,** *5* (2), 168-81.

16. Weilbaecher, K. N.; Guise, T. A.; McCauley, L. K., Cancer to bone: a fatal attraction. *Nat Rev Cancer* **2011,** *11* (6), 411-25.

17. Malanchi, I.; Santamaria-Martinez, A.; Susanto, E.; Peng, H.; Lehr, H. A.; Delaloye, J. F.; Huelsken, J., Interactions between cancer stem cells and their niche govern metastatic colonization. *Nature* **2011,** *481* (7379), 85-9.

18. Kim, S. J.; Kim, J. S.; Park, E. S.; Lee, J. S.; Lin, Q.; Langley, R. R.; Maya, M.; He, J.; Kim, S. W.; Weihua, Z.; Balasubramanian, K.; Fan, D.; Mills, G. B.; Hung, M. C.; Fidler, I. J., Astrocytes upregulate survival genes in tumor cells and induce protection from chemotherapy. *Neoplasia* **2011,** *13* (3), 286-98.

19. Kim, S. W.; Choi, H. J.; Lee, H. J.; He, J.; Wu, Q.; Langley, R. R.; Fidler, I. J.; Kim, S. J., Role of the endothelin axis in astrocyte- and endothelial cell-mediated chemoprotection of cancer cells. *Neuro Oncol* **2014,** *16* (12), 1585-98.

20. Kang, Y.; Siegel, P. M.; Shu, W.; Drobnjak, M.; Kakonen, S. M.; Cordon-Cardo, C.; Guise, T. A.; Massague, J., A multigenic program mediating breast cancer metastasis to bone. *Cancer Cell* **2003,** *3* (6), 537-49.

21. Kaplan, R. N.; Riba, R. D.; Zacharoulis, S.; Bramley, A. H.; Vincent, L.; Costa, C.; MacDonald, D. D.; Jin, D. K.; Shido, K.; Kerns, S. A.; Zhu, Z.; Hicklin, D.; Wu, Y.; Port, J. L.; Altorki, N.; Port, E. R.; Ruggero, D.; Shmelkov, S. V.; Jensen, K. K.; Rafii, S.; Lyden, D., VEGFR1-positive haematopoietic bone marrow progenitors initiate the pre-metastatic niche. *Nature* **2005,** *438* (7069), 820-7.

22. Peinado, H.; Zhang, H.; Matei, I. R.; Costa-Silva, B.; Hoshino, A.; Rodrigues, G.; Psaila, B.; Kaplan, R. N.; Bromberg, J. F.; Kang, Y.; Bissell, M. J.; Cox, T. R.; Giaccia, A. J.; Erler, J. T.; Hiratsuka, S.; Ghajar, C. M.; Lyden, D., Pre-metastatic niches: organ-specific homes for metastases. *Nat Rev Cancer* **2017,** *17* (5), 302-317.

23. Tominaga, N.; Kosaka, N.; Ono, M.; Katsuda, T.; Yoshioka, Y.; Tamura, K.; Lotvall, J.; Nakagama, H.; Ochiya, T., Brain metastatic cancer cells release microRNA-181c-containing extracellular vesicles capable of destructing blood-brain barrier. *Nat Commun* **2015,** *6*, 6716.

24. Huang, Y.; Song, N.; Ding, Y.; Yuan, S.; Li, X.; Cai, H.; Shi, H.; Luo, Y., Pulmonary vascular destabilization in the premetastatic phase facilitates lung metastasis. *Cancer Res* **2009,** *69* (19), 7529-37.

25. Hoshino, A.; Costa-Silva, B.; Shen, T. L.; Rodrigues, G.; Hashimoto, A.; Tesic Mark, M.; Molina, H.; Kohsaka, S.; Di Giannatale, A.; Ceder, S.; Singh, S.; Williams, C.; Soplop, N.; Uryu, K.; Pharmer, L.; King, T.; Bojmar, L.; Davies, A. E.; Ararso, Y.; Zhang, T.; Zhang, H.; Hernandez, J.; Weiss, J. M.; Dumont-Cole, V. D.; Kramer, K.; Wexler, L. H.; Narendran, A.; Schwartz, G. K.; Healey, J. H.; Sandstrom, P.; Labori, K. J.; Kure, E. H.; Grandgenett, P. M.; Hollingsworth, M. A.; de Sousa, M.; Kaur, S.; Jain, M.; Mallya, K.; Batra, S. K.; Jarnagin, W. R.; Brady, M. S.; Fodstad, O.; Muller, V.; Pantel, K.; Minn, A. J.; Bissell, M. J.; Garcia, B. A.; Kang, Y.; Rajasekhar, V. K.; Ghajar, C. M.; Matei, I.; Peinado, H.; Bromberg, J.; Lyden, D., Tumour exosome integrins determine organotropic metastasis. *Nature* **2015,** *527* (7578), 329-35.

26. Bresnick, A. R.; Weber, D. J.; Zimmer, D. B., S100 proteins in cancer. *Nat Rev Cancer* **2015,** *15* (2), 96-109.

27. Hiratsuka, S.; Watanabe, A.; Sakurai, Y.; Akashi-Takamura, S.; Ishibashi, S.; Miyake, K.; Shibuya, M.; Akira, S.; Aburatani, H.; Maru, Y., The S100A8-serum amyloid A3-TLR4 paracrine cascade establishes a pre-metastatic phase. *Nat Cell Biol* **2008,** *10* (11), 1349-55.

28. Murgai, M.; Ju, W.; Eason, M.; Kline, J.; Beury, D. W.; Kaczanowska, S.; Miettinen, M. M.; Kruhlak, M.; Lei, H.; Shern, J. F.; Cherepanova, O. A.; Owens, G. K.; Kaplan, R. N., KLF4-dependent perivascular cell plasticity mediates pre-metastatic niche formation and metastasis. *Nat Med* **2017,** *23* (10), 1176-1190.

29. Erler, J. T.; Bennewith, K. L.; Cox, T. R.; Lang, G.; Bird, D.; Koong, A.; Le, Q. T.; Giaccia, A. J., Hypoxia-induced lysyl oxidase is a critical mediator of bone marrow cell recruitment to form the premetastatic niche. *Cancer Cell* **2009,** *15* (1), 35-44.

30. Yan, H. H.; Pickup, M.; Pang, Y.; Gorska, A. E.; Li, Z.; Chytil, A.; Geng, Y.; Gray, J. W.; Moses, H. L.; Yang, L., Gr-1+CD11b+ myeloid cells tip the balance of immune protection to tumor promotion in the premetastatic lung. *Cancer Res* **2010,** *70* (15), 6139-49.

31. Liu, Y.; Gu, Y.; Han, Y.; Zhang, Q.; Jiang, Z.; Zhang, X.; Huang, B.; Xu, X.; Zheng, J.; Cao, X., Tumor Exosomal RNAs Promote Lung Pre-metastatic Niche Formation by Activating Alveolar Epithelial TLR3 to Recruit Neutrophils. *Cancer Cell* **2016,** *30* (2), 243-256.

32. Wculek, S. K.; Malanchi, I., Neutrophils support lung colonization of metastasis-initiating breast cancer cells. *Nature* **2015,** *528* (7582), 413-7.

33. Chery, L.; Lam, H. M.; Coleman, I.; Lakely, B.; Coleman, R.; Larson, S.; Aguirre-Ghiso, J. A.; Xia, J.; Gulati, R.; Nelson, P. S.; Montgomery, B.; Lange, P.; Snyder, L. A.; Vessella, R. L.; Morrissey, C., Characterization of single disseminated prostate cancer cells reveals tumor cell heterogeneity and identifies dormancy associated pathways. *Oncotarget* **2014,** *5* (20), 9939-51.

34. Linde, N.; Fluegen, G.; Aguirre-Ghiso, J. A., The Relationship Between Dormant Cancer Cells and Their Microenvironment. *Adv Cancer Res* **2016,** *132*, 45-71.

35. Polzer, B.; Klein, C. A., Metastasis awakening: the challenges of targeting minimal residual cancer. *Nat Med* **2013,** *19* (3), 274-5.

36. Guttery, D. S.; Page, K.; Hills, A.; Woodley, L.; Marchese, S. D.; Rghebi, B.; Hastings, R. K.; Luo, J.; Pringle, J. H.; Stebbing, J.; Coombes, R. C.; Ali, S.; Shaw, J. A., Noninvasive detection of activating estrogen receptor 1 (ESR1) mutations in estrogen receptor-positive metastatic breast cancer. *Clin Chem* **2015,** *61* (7), 974-82.

37. Shaw, J. A.; Page, K.; Blighe, K.; Hava, N.; Guttery, D.; Ward, B.; Brown, J.; Ruangpratheep, C.; Stebbing, J.; Payne, R.; Palmieri, C.; Cleator, S.; Walker, R. A.; Coombes, R. C., Genomic analysis of circulating cell-free DNA infers breast cancer dormancy. *Genome Res* **2012,** *22* (2), 220-31.

38. Page, K.; Guttery, D. S.; Fernandez-Garcia, D.; Hills, A.; Hastings, R. K.; Luo, J.; Goddard, K.; Shahin, V.; Woodley-Barker, L.; Rosales, B. M.; Coombes, R. C.; Stebbing, J.; Shaw, J. A., Next Generation Sequencing of Circulating Cell-Free DNA for Evaluating Mutations and Gene Amplification in Metastatic Breast Cancer. *Clin Chem* **2017,** *63* (2), 532-541.

39. Yeh, A. C.; Ramaswamy, S., Mechanisms of Cancer Cell Dormancy--Another Hallmark of Cancer? *Cancer Res* **2015,** *75* (23), 5014-22.

40. Aguirre-Ghiso, J. A.; Estrada, Y.; Liu, D.; Ossowski, L., ERK(MAPK) activity as a determinant of tumor growth and dormancy; regulation by p38(SAPK). *Cancer Res* **2003,** *63* (7), 1684-95.

41. Jo, H.; Jia, Y.; Subramanian, K. K.; Hattori, H.; Luo, H. R., Cancer cell-derived clusterin modulates the phosphatidylinositol 3'-kinase-Akt pathway through attenuation of insulin-like growth factor 1 during serum deprivation. *Mol Cell Biol* **2008,** *28* (13), 4285-99.

42. Sosa, M. S.; Parikh, F.; Maia, A. G.; Estrada, Y.; Bosch, A.; Bragado, P.; Ekpin, E.; George, A.; Zheng, Y.; Lam, H. M.; Morrissey, C.; Chung, C. Y.; Farias, E. F.; Bernstein, E.; Aguirre-Ghiso, J. A., NR2F1 controls tumour cell dormancy via SOX9- and RARbeta-driven quiescence programmes. *Nat Commun* **2015,** *6*, 6170.

43. Taichman, R. S.; Patel, L. R.; Bedenis, R.; Wang, J.; Weidner, S.; Schumann, T.; Yumoto, K.; Berry, J. E.; Shiozawa, Y.; Pienta, K. J., GAS6 receptor status is associated with dormancy and bone metastatic tumor formation. *PLoS One* **2013,** *8* (4), e61873.

44. Kobayashi, A.; Okuda, H.; Xing, F.; Pandey, P. R.; Watabe, M.; Hirota, S.; Pai, S. K.; Liu, W.; Fukuda, K.; Chambers, C.; Wilber, A.; Watabe, K., Bone morphogenetic protein 7 in dormancy and metastasis of prostate cancer stem-like cells in bone. *The Journal of Experimental Medicine* **2012,** *209* (3), 639-639.

45. Bragado, P.; Estrada, Y.; Parikh, F.; Krause, S.; Capobianco, C.; Farina, H. G.; Schewe, D. M.; Aguirre-Ghiso, J. A., TGF-beta2 dictates disseminated tumour cell fate in target organs through TGF-beta-RIII and p38alpha/beta signalling. *Nat Cell Biol* **2013,** *15* (11), 1351-61.

46. Gimbrone, M. A., Jr.; Leapman, S. B.; Cotran, R. S.; Folkman, J., Tumor dormancy in vivo by prevention of neovascularization. *J Exp Med* **1972,** *136* (2), 261-76.

47. Al-Mehdi, A. B.; Tozawa, K.; Fisher, A. B.; Shientag, L.; Lee, A.; Muschel, R. J., Intravascular origin of metastasis from the proliferation of endothelium-attached tumor cells: a new model for metastasis. *Nat Med* **2000,** *6* (1), 100-2.

48. Kienast, Y.; von Baumgarten, L.; Fuhrmann, M.; Klinkert, W. E.; Goldbrunner, R.; Herms, J.; Winkler, F., Real-time imaging reveals the single steps of brain metastasis formation. *Nat Med* **2010,** *16* (1), 116-22.

49. MacKie, R. M.; Reid, R.; Junor, B., Fatal melanoma transferred in a donated kidney 16 years after melanoma surgery. *N Engl J Med* **2003,** *348* (6), 567-8.

50. Eyles, J.; Puaux, A. L.; Wang, X.; Toh, B.; Prakash, C.; Hong, M.; Tan, T. G.; Zheng, L.; Ong, L. C.; Jin, Y.; Kato, M.; Prevost-Blondel, A.; Chow, P.; Yang, H.; Abastado, J. P., Tumor cells disseminate early, but immunosurveillance limits metastatic outgrowth, in a mouse model of melanoma. *J Clin Invest* **2010,** *120* (6), 2030-9.

51. Muller-Hermelink, N.; Braumuller, H.; Pichler, B.; Wieder, T.; Mailhammer, R.; Schaak, K.; Ghoreschi, K.; Yazdi, A.; Haubner, R.; Sander, C. A.; Mocikat, R.; Schwaiger, M.; Forster, I.; Huss, R.; Weber, W. A.; Kneilling, M.; Rocken, M., TNFR1 signaling and IFN-gamma signaling determine whether T cells induce tumor dormancy or promote multistage carcinogenesis. *Cancer Cell* **2008,** *13* (6), 507-18.

52. Kagan, M.; Howard, D.; Bendele, T.; Mayes, J.; Silvia, J.; Repollet, M.; Doyle, J.; Allard, J.; Tu, N.; Bui, T.; Russell, T.; Rao, C.; Hermann, M.; Rutner, H.; Terstappen, L. W. M. M., A sample preparation and analysis system for identification of circulating tumor cells. *J Clin Ligand Assay* **2002,** *25* (1), 104-110.

53. Cristofanilli, M.; Budd, G. T.; Ellis, M. J.; Stopeck, A.; Matera, J.; Miller, M. C.; Reuben, J. M.; Doyle, G. V.; Allard, W. J.; Terstappen, L. W.; Hayes, D. F., Circulating tumor cells, disease progression, and survival in metastatic breast cancer. *N Engl J Med* **2004,** *351* (8), 781-91.

54. Zhang, Z.; Shiratsuchi, H.; Lin, J.; Chen, G. A.; Reddy, R. M.; Azizi, E.; Fouladdel, S.; Chang, A. C.; Lin, L.; Jiang, H.; Waghray, M.; Luker, G.; Simeone, D. M.; Wicha, M. S.; Beer, D. G.; Ramnath, N.; Nagrath, S., Expansion of CTCs from early stage lung cancer patients using a microfluidic co-culture model. *Oncotarget* **2014,** *5* (23), 12383-12397.

55. Yu, M.; Bardia, A.; Aceto, N.; Bersani, F.; Madden, M. W.; Donaldson, M. C.; Desai, R.; Zhu, H.; Comaills, V.; Zheng, Z.; Wittner, B. S.; Stojanov, P.; Brachtel, E.; Sgroi, D.; Kapur, R.; Shioda, T.; Ting, D. T.; Ramaswamy, S.; Getz, G.; Iafrate, A. J.; Benes, C.; Toner, M.; Maheswaran, S.; Haber, D. A., Cancer therapy. Ex vivo culture of circulating breast tumor cells for individualized testing of drug susceptibility. *Science* **2014,** *345* (6193), 216-20.

56. Cayrefourcq, L.; Mazard, T.; Joosse, S.; Solassol, J.; Ramos, J.; Assenat, E.; Schumacher, U.; Costes, V.; Maudelonde, T.; Pantel, K.; Alix-Panabieres, C., Establishment and characterization of a cell line from human circulating colon cancer cells. *Cancer Res* **2015,** *75* (5), 892-901.

57. Khoo, B. L.; Lee, S. C.; Kumar, P.; Tan, T. Z.; Warkiani, M. E.; Ow, S. G.; Nandi, S.; Lim, C. T.; Thiery, J. P., Short-term expansion of breast circulating cancer cells predicts response to anti-cancer therapy. *Oncotarget* **2015,** *6* (17), 15578-93.

58. Zhang, L.; Ridgway, L. D.; Wetzel, M. D.; Ngo, J.; Yin, W.; Kumar, D.; Goodman, J. C.; Groves, M. D.; Marchetti, D., The identification and characterization of breast cancer CTCs competent for brain metastasis. *Sci Transl Med* **2013,** *5* (180), 180ra48.

59. Khoo, B. L.; Grenci, G.; Lim, Y. B.; Lee, S. C.; Han, J.; Lim, C. T., Expansion of patient-derived circulating tumor cells from liquid biopsies using a CTC microfluidic culture device. *Nat Protoc* **2018,** *13* (1), 34-58.

60. Baccelli, I.; Schneeweiss, A.; Riethdorf, S.; Stenzinger, A.; Schillert, A.; Vogel, V.; Klein, C.; Saini, M.; Bauerle, T.; Wallwiener, M.; Holland-Letz, T.; Hofner, T.; Sprick, M.; Scharpff, M.; Marme, F.; Sinn, H. P.; Pantel, K.; Weichert, W.; Trumpp, A., Identification of a population of blood circulating tumor cells from breast cancer patients that initiates metastasis in a xenograft assay. *Nat Biotechnol* **2013,** *31* (6), 539-44.

61. Pradhan, S.; Sperduto, J. L.; Farino, C. J.; Slater, J. H., Engineered In Vitro Models of Tumor Dormancy and Reactivation. *J Biol Eng* **2018,** *12*, 37.

62. Katt, M. E.; Placone, A. L.; Wong, A. D.; Xu, Z. S.; Searson, P. C., In Vitro Tumor Models: Advantages, Disadvantages, Variables, and Selecting the Right Platform. *Front Bioeng Biotechnol* **2016,** *4*, 12.

63. Ghajar, C. M.; Peinado, H.; Mori, H.; Matei, I. R.; Evason, K. J.; Brazier, H.; Almeida, D.; Koller, A.; Hajjar, K. A.; Stainier, D. Y.; Chen, E. I.; Lyden, D.; Bissell, M. J., The perivascular niche regulates breast tumour dormancy. *Nat Cell Biol* **2013,** *15* (7), 807-17.

64. Jeon, J. S.; Bersini, S.; Gilardi, M.; Dubini, G.; Charest, J. L.; Moretti, M.; Kamm, R. D., Human 3D vascularized organotypic microfluidic assays to study breast cancer cell extravasation. *Proc Natl Acad Sci U S A* **2015,** *112* (1), 214-9.

65. Kang, Y.; Pantel, K., Tumor cell dissemination: emerging biological insights from animal models and cancer patients. *Cancer Cell* **2013,** *23* (5), 573-81.

66. Francia, G.; Cruz-Munoz, W.; Man, S.; Xu, P.; Kerbel, R. S., Mouse models of advanced spontaneous metastasis for experimental therapeutics. *Nat Rev Cancer* **2011,** *11* (2), 135-41.

67. Bos, P. D.; Nguyen, D. X.; Massague, J., Modeling metastasis in the mouse. *Curr Opin Pharmacol* **2010,** *10* (5), 571-7.

68. Deroose, C. M.; De, A.; Loening, A. M.; Chow, P. L.; Ray, P.; Chatziioannou, A. F.; Gambhir, S. S., Multimodality imaging of tumor xenografts and metastases in mice with combined small-animal PET, small-animal CT, and bioluminescence imaging. *J Nucl Med* **2007,** *48* (2), 295-303.

69. Seemann, M. D.; Beck, R.; Ziegler, S., In vivo tumor imaging in mice using a state-of-the-art clinical PET/CT in comparison with a small animal PET and a small animal CT. *Technol Cancer Res Treat* **2006,** *5* (5), 537-42.

70. Bradner, W. T.; Clarke, D. A.; Stock, C. C., Stimulation of host defense against experimental cancer. I. Zymosan and sarcoma 180 in mice. *Cancer Res* **1958,** *18* (3), 347-51.

71. Mantel, N.; Bryan, W. R., "Safety" Testing of Carcinogenic Agents. *JNCI: Journal of the National Cancer Institute* **1961,** *27* (2), 455-470.

72. Suggitt, M.; Bibby, M. C., 50 years of preclinical anticancer drug screening: empirical to target-driven approaches. *Clin Cancer Res* **2005,** *11* (3), 971-81.

73. Shultz, L. D.; Ishikawa, F.; Greiner, D. L., Humanized mice in translational biomedical research. *Nat Rev Immunol* **2007,** *7* (2), 118-30.

74. Johnson, J. I.; Decker, S.; Zaharevitz, D.; Rubinstein, L. V.; Venditti, J. M.; Schepartz, S.; Kalyandrug, S.; Christian, M.; Arbuck, S.; Hollingshead, M.; Sausville, E. A., Relationships between drug activity in NCI preclinical in vitro and in vivo models and early clinical trials. *Br J Cancer* **2001,** *84* (10), 1424-31.

75. Sharpless, N. E.; Depinho, R. A., The mighty mouse: genetically engineered mouse models in cancer drug development. *Nat Rev Drug Discov* **2006,** *5* (9), 741-54.

76. Sikder, H.; Huso, D. L.; Zhang, H.; Wang, B.; Ryu, B.; Hwang, S. T.; Powell, J. D.; Alani, R. M., Disruption of Id1 reveals major differences in angiogenesis between transplanted and autochthonous tumors. *Cancer Cell* **2003,** *4* (4), 291-9.

77. Daniel, V. C.; Marchionni, L.; Hierman, J. S.; Rhodes, J. T.; Devereux, W. L.; Rudin, C. M.; Yung, R.; Parmigiani, G.; Dorsch, M.; Peacock, C. D.; Watkins, D. N., A primary xenograft model of small-cell lung cancer reveals irreversible changes in gene expression imposed by culture in vitro. *Cancer Res* **2009,** *69* (8), 3364-73.

78. Hidalgo, M.; Amant, F.; Biankin, A. V.; Budinska, E.; Byrne, A. T.; Caldas, C.; Clarke, R. B.; de Jong, S.; Jonkers, J.; Maelandsmo, G. M.; Roman-Roman, S.; Seoane, J.; Trusolino, L.; Villanueva, A., Patient-derived xenograft models: an emerging platform for translational cancer research. *Cancer Discov* **2014,** *4* (9), 998-1013.

79. Izumchenko, E.; Paz, K.; Ciznadija, D.; Sloma, I.; Katz, A.; Vasquez-Dunddel, D.; Ben-Zvi, I.; Stebbing, J.; McGuire, W.; Harris, W.; Maki, R.; Gaya, A.; Bedi, A.; Zacharoulis, S.; Ravi, R.; Wexler, L. H.; Hoque, M. O.; Rodriguez-Galindo, C.; Pass, H.; Peled, N.; Davies, A.; Morris, R.; Hidalgo, M.; Sidransky, D., Patient-derived xenografts effectively capture responses to oncology therapy in a heterogeneous cohort of patients with solid tumors. *Ann Oncol* **2017,** *28* (10), 2595-2605.

80. Hidalgo, M.; Bruckheimer, E.; Rajeshkumar, N. V.; Garrido-Laguna, I.; De Oliveira, E.; Rubio-Viqueira, B.; Strawn, S.; Wick, M. J.; Martell, J.; Sidransky, D., A pilot clinical study of treatment guided by personalized tumorgrafts in patients with advanced cancer. *Mol Cancer Ther* **2011,** *10* (8), 1311-6.

81. Gengenbacher, N.; Singhal, M.; Augustin, H. G., Preclinical mouse solid tumour models: status quo, challenges and perspectives. *Nat Rev Cancer* **2017,** *17* (12), 751-765.

82. Hanahan, D.; Wagner, E. F.; Palmiter, R. D., The origins of oncomice: a history of the first transgenic mice genetically engineered to develop cancer. *Genes Dev* **2007,** *21* (18), 2258-70.

83. Guy, C. T.; Cardiff, R. D.; Muller, W. J., Induction of mammary tumors by expression of polyomavirus middle T oncogene: a transgenic mouse model for metastatic disease. *Mol Cell Biol* **1992,** *12* (3), 954-61.

84. Kersten, K.; de Visser, K. E.; van Miltenburg, M. H.; Jonkers, J., Genetically engineered mouse models in oncology research and cancer medicine. *EMBO Mol Med* **2017,** *9* (2), 137-153.

85. Singh, M.; Murriel, C. L.; Johnson, L., Genetically engineered mouse models: closing the gap between preclinical data and trial outcomes. *Cancer Res* **2012,** *72* (11), 2695-700.

86. Simmons, J. K.; Hildreth, B. E., 3rd; Supsavhad, W.; Elshafae, S. M.; Hassan, B. B.; Dirksen, W. P.; Toribio, R. E.; Rosol, T. J., Animal Models of Bone Metastasis. *Vet Pathol* **2015,** *52* (5), 827-41.

87. Shtivelman, E.; Namikawa, R., Species-specific metastasis of human tumor cells in the severe combined immunodeficiency mouse engrafted with human tissue. *Proc Natl Acad Sci U S A* **1995,** *92* (10), 4661-5.

88. Seib, F. P.; Berry, J. E.; Shiozawa, Y.; Taichman, R. S.; Kaplan, D. L., Tissue engineering a surrogate niche for metastatic cancer cells. *Biomaterials* **2015,** *51*, 313-319.

89. Stiers, P.-J.; van Gastel, N.; Moermans, K.; Stockmans, I.; Carmeliet, G., An Ectopic Imaging Window for Intravital Imaging of Engineered Bone Tissue. *JBMR Plus* **2018,** *2* (2), 92-102.

90. Holzapfel, B. M.; Wagner, F.; Loessner, D.; Holzapfel, N. P.; Thibaudeau, L.; Crawford, R.; Ling, M. T.; Clements, J. A.; Russell, P. J.; Hutmacher, D. W., Species-specific homing mechanisms of human prostate cancer metastasis in tissue engineered bone. *Biomaterials* **2014,** *35* (13), 4108-4115.

91. Moreau, J. E.; Anderson, K.; Mauney, J. R.; Nguyen, T.; Kaplan, D. L.; Rosenblatt, M., Tissue-engineered bone serves as a target for metastasis of human breast cancer in a mouse model. *Cancer Res* **2007,** *67* (21), 10304-8.

92. Schuster, J.; Zhang, J.; Longo, M., A novel human osteoblast-derived severe combined immunodeficiency mouse model of bone metastasis. *J Neurosurg Spine* **2006,** *4* (5), 388-91.

93. Thibaudeau, L.; Taubenberger, A. V.; Holzapfel, B. M.; Quent, V. M.; Fuehrmann, T.; Hesami, P.; Brown, T. D.; Dalton, P. D.; Power, C. A.; Hollier, B. G.; Hutmacher, D. W., A tissue-engineered humanized xenograft model of human breast cancer metastasis to bone. *Dis Model Mech* **2014,** *7* (2), 299-309.

94. Reinisch, A.; Thomas, D.; Corces, M. R.; Zhang, X.; Gratzinger, D.; Hong, W. J.; Schallmoser, K.; Strunk, D.; Majeti, R., A humanized bone marrow ossicle xenotransplantation model enables improved engraftment of healthy and leukemic human hematopoietic cells. *Nat Med* **2016,** *22* (7), 812-21.

95. Chen, A. A.; Thomas, D. K.; Ong, L. L.; Schwartz, R. E.; Golub, T. R.; Bhatia, S. N., Humanized mice with ectopic artificial liver tissues. *Proc Natl Acad Sci U S A* **2011,** *108* (29), 11842-7.

96. Bersani, F.; Lee, J.; Yu, M.; Morris, R.; Desai, R.; Ramaswamy, S.; Toner, M.; Haber, D. A.; Parekkadan, B., Bioengineered Implantable Scaffolds as a Tool to Study Stromal-Derived Factors in Metastatic Cancer Models. *Cancer Research* **2014,** *74* (24), 7229-7238.

97. Lee, J.; Li, M.; Milwid, J.; Dunham, J.; Vinegoni, C.; Gorbatov, R.; Iwamoto, Y.; Wang, F. J.; Shen, K. Y.; Hatfield, K.; Enger, M.; Shafiee, S.; McCormack, E.; Ebert, B. L.; Weissleder, R.; Yarmush, M. L.; Parekkadan, B., Implantable microenvironments to attract hematopoietic stem/cancer cells. *P Natl Acad Sci USA* **2012,** *109* (48), 19638-19643.

98. Ko, C. Y.; Wu, L.; Nair, A. M.; Tsai, Y. T.; Lin, V. K.; Tang, L., The use of chemokine-releasing tissue engineering scaffolds in a model of inflammatory response-mediated melanoma cancer metastasis. *Biomaterials* **2012,** *33* (3), 876-85.

99. Aguado, B. A.; Wu, J. J.; Azarin, S. M.; Nanavati, D.; Rao, S. S.; Bushnell, G. G.; Medicherla, C. B.; Shea, L. D., Secretome identification of immune cell factors mediating metastatic cell homing. *Sci Rep* **2015,** *5*, 17566.

100. Vaiselbuh, S. R.; Edelman, M.; Lipton, J. M.; Liu, J. M., Ectopic human mesenchymal stem cell-coated scaffolds in NOD/SCID mice: an in vivo model of the leukemia niche. *Tissue Eng Part C Methods* **2010,** *16* (6), 1523-31.

101. Carpenter, R. A.; Kwak, J. G.; Peyton, S. R.; Lee, J., Implantable pre-metastatic niches for the study of the microenvironmental regulation of disseminated human tumour cells. *Nat Biomed Eng* **2018,** *2* (12), 915-929.

102. Oakes, R. S.; Bushnell, G. G.; Orbach, S. M.; Kandagatla, P.; Zhang, Y.; Morris, A. H.; Hall, M. S.; LaFaire, P.; Decker, J. T.; Hartfield, R. M.; Brooks, M. D.; Wicha, M. S.; Jeruss, J. S.; Shea, L. D., Metastatic conditioning of myeloid cells at a subcutaneous synthetic niche reflects disease progression and predicts therapeutic outcomes. *Cancer Res* **2019**.

103. Rao, S. S.; Bushnell, G. G.; Azarin, S. M.; Spicer, G.; Aguado, B. A.; Stoehr, J. R.; Jiang, E. J.; Backman, V.; Shea, L. D.; Jeruss, J. S., Enhanced Survival with Implantable Scaffolds That Capture Metastatic Breast Cancer Cells In Vivo. *Cancer Res* **2016,** *76* (18), 5209-18.

104. Azarin, S. M.; Yi, J.; Gower, M.; Aguado, B. A.; Sullivan, M. E.; Goodman, A. G.; Jiang, E. J.; Rao, S. S.; Ren, Y. Y.; Tucker, S. L.; Backman, V.; Jeruss, J. S.; Shea, L. D., In vivo capture and label-free detection of early metastatic cells. *Nat Commun* **2015,** *6*.

105. de la Fuente, A.; Alonso-Alconada, L.; Costa, C.; Cueva, J.; Garcia-Caballero, T.; Lopez-Lopez, R.; Abal, M., M-Trap: Exosome-Based Capture of Tumor Cells as a New Technology in Peritoneal Metastasis. *J Natl Cancer Inst* **2015,** *107* (9).

106. Holmgren, L.; O'Reilly, M. S.; Folkman, J., Dormancy of micrometastases: balanced proliferation and apoptosis in the presence of angiogenesis suppression. *Nat Med* **1995,** *1* (2), 149-53.

107. Albrengues, J.; Shields, M. A.; Ng, D.; Park, C. G.; Ambrico, A.; Poindexter, M. E.; Upadhyay, P.; Uyeminami, D. L.; Pommier, A.; Kuttner, V.; Bruzas, E.; Maiorino, L.; Bautista, C.; Carmona, E. M.; Gimotty, P. A.; Fearon, D. T.; Chang, K.; Lyons, S. K.; Pinkerton, K. E.; Trotman, L. C.; Goldberg, M. S.; Yeh, J. T.; Egeblad, M., Neutrophil extracellular traps produced during inflammation awaken dormant cancer cells in mice. *Science* **2018,** *361* (6409).

108. Linde, N.; Casanova-Acebes, M.; Sosa, M. S.; Mortha, A.; Rahman, A.; Farias, E.; Harper, K.; Tardio, E.; Reyes Torres, I.; Jones, J.; Condeelis, J.; Merad, M.; Aguirre-Ghiso, J. A., Macrophages orchestrate breast cancer early dissemination and metastasis. *Nat Commun* **2018,** *9* (1), 21.

109. Armstrong, E.; O'Dwyer, C., Artificial opal photonic crystals and inverse opal structures – fundamentals and applications from optics to energy storage. *Journal of Materials Chemistry C* **2015,** *3* (24), 6109-6143.

110. Kinoshita, S.; Yoshioka, S., Structural Colors in Nature: The Role of Regularity and Irregularity in the Structure. *ChemPhysChem* **2005,** *6* (8), 1442-1459.

111. Kotov, N. A.; Liu, Y.; Wang, S.; Cumming, C.; Eghtedari, M.; Vargas, G.; Motamedi, M.; Nichols, J.; Cortiella, J., Inverted Colloidal Crystals as Three-Dimensional Cell Scaffolds. *Langmuir* **2004,** *20* (19), 7887-7892.

112. Simpson, B. J., Hydron: a hydrophilic polymer. *Biomed Eng* **1969,** *4* (2), 65-8.

113. Calnan, J. S.; Pflug, J. J.; Chhabra, A. S.; Raghupati, N., Clinical and experimental studies of polyhydroxyethylmethacrylate gel ("Hydron") for reconstructive surgery. *Br J Plast Surg* **1971,** *24* (2), 113-24.

114. Winter, G. D., Transcutaneous implants: reactions of the skin-implant interface. *J Biomed Mater Res* **1974,** *8* (3), 99-113.

115. Isenhath, S. N.; Fukano, Y.; Usui, M. L.; Underwood, R. A.; Irvin, C. A.; Marshall, A. J.; Hauch, K. D.; Ratner, B. D.; Fleckman, P.; Olerud, J. E., A mouse model to evaluate the interface between skin and a percutaneous device. *J Biomed Mater Res A* **2007,** *83* (4), 915-22.

116. Madden, L. R.; Mortisen, D. J.; Sussman, E. M.; Dupras, S. K.; Fugate, J. A.; Cuy, J. L.; Hauch, K. D.; Laflamme, M. A.; Murry, C. E.; Ratner, B. D., Proangiogenic scaffolds as functional templates for cardiac tissue engineering. *Proc Natl Acad Sci U S A* **2010,** *107* (34), 15211-6.

117. Cai, X.; Zhang, Y.; Li, L.; Choi, S. W.; MacEwan, M. R.; Yao, J.; Kim, C.; Xia, Y.; Wang, L. V., Investigation of neovascularization in three-dimensional porous scaffolds in vivo by a combination of multiscale photoacoustic microscopy and optical coherence tomography. *Tissue Eng Part C Methods* **2013,** *19* (3), 196-204.

118. Feng, B.; Jinkang, Z.; Zhen, W.; Jianxi, L.; Jiang, C.; Jian, L.; Guolin, M.; Xin, D., The effect of pore size on tissue ingrowth and neovascularization in porous bioceramics of controlled architecture in vivo. *Biomed Mater* **2011,** *6* (1), 015007.

119. Sussman, E. M.; Halpin, M. C.; Muster, J.; Moon, R. T.; Ratner, B. D., Porous implants modulate healing and induce shifts in local macrophage polarization in the foreign body reaction. *Ann Biomed Eng* **2014,** *42* (7), 1508-16.

120. Veiseh, O.; Doloff, J. C.; Ma, M.; Vegas, A. J.; Tam, H. H.; Bader, A. R.; Li, J.; Langan, E.; Wyckoff, J.; Loo, W. S.; Jhunjhunwala, S.; Chiu, A.; Siebert, S.; Tang, K.; Hollister-Lock, J.; Aresta-Dasilva, S.; Bochenek, M.; Mendoza-Elias, J.; Wang, Y.; Qi, M.; Lavin, D. M.; Chen, M.; Dholakia, N.; Thakrar, R.; Lacik, I.; Weir, G. C.; Oberholzer, J.; Greiner, D. L.; Langer, R.; Anderson, D. G., Size- and shape-dependent foreign body

immune response to materials implanted in rodents and non-human primates. *Nat Mater* **2015,** *14* (6), 643-51.

121. Coussens, L. M.; Tinkle, C. L.; Hanahan, D.; Werb, Z., MMP-9 supplied by bone marrow-derived cells contributes to skin carcinogenesis. *Cell* **2000,** *103* (3), 481-90.

122. Takao, K.; Miyakawa, T., Genomic responses in mouse models greatly mimic human inflammatory diseases. *Proc Natl Acad Sci U S A* **2015,** *112* (4), 1167-72.

123. Day, C. P.; Merlino, G.; Van Dyke, T., Preclinical mouse cancer models: a maze of opportunities and challenges. *Cell* **2015,** *163* (1), 39-53.

124. Gould, S. E.; Junttila, M. R.; de Sauvage, F. J., Translational value of mouse models in oncology drug development. *Nat Med* **2015,** *21* (5), 431-9.

125. Webster, S. J.; Bachstetter, A. D.; Nelson, P. T.; Schmitt, F. A.; Van Eldik, L. J., Using mice to model Alzheimer's dementia: an overview of the clinical disease and the preclinical behavioral changes in 10 mouse models. *Front Genet* **2014,** *5*, 88.

126. Gkouskou, K. K.; Deligianni, C.; Tsatsanis, C.; Eliopoulos, A. G., The gut microbiota in mouse models of inflammatory bowel disease. *Front Cell Infect Microbiol* **2014,** *4*, 28.

127. Brehm, M. A.; Shultz, L. D.; Greiner, D. L., Humanized mouse models to study human diseases. *Curr Opin Endocrinol Diabetes Obes* **2010,** *17* (2), 120-5.

128. Spade, D. J.; McDonnell, E. V.; Heger, N. E.; Sanders, J. A.; Saffarini, C. M.; Gruppuso, P. A.; De Paepe, M. E.; Boekelheide, K., Xenotransplantation models to study the effects of toxicants on human fetal tissues. *Birth Defects Res B Dev Reprod Toxicol* **2014,** *101* (6), 410-22.

129. Wimmer, R. A.; Leopoldi, A.; Aichinger, M.; Wick, N.; Hantusch, B.; Novatchkova, M.; Taubenschmid, J.; Hammerle, M.; Esk, C.; Bagley, J. A.; Lindenhofer, D.; Chen, G.; Boehm, M.; Agu, C. A.; Yang, F.; Fu, B.; Zuber, J.; Knoblich, J. A.; Kerjaschki, D.; Penninger, J. M., Human blood vessel organoids as a model of diabetic vasculopathy. *Nature* **2019,** *565* (7740), 505-510.

130. Jung, J.; Seol, H. S.; Chang, S., The Generation and Application of Patient-Derived Xenograft Model for Cancer Research. *Cancer Res Treat* **2018,** *50* (1), 1-10.

131. Brehm, M. A.; Wiles, M. V.; Greiner, D. L.; Shultz, L. D., Generation of improved humanized mouse models for human infectious diseases. *J Immunol Methods* **2014,** *410*, 3-17.

132. Karpel, M. E.; Boutwell, C. L.; Allen, T. M., BLT humanized mice as a small animal model of HIV infection. *Curr Opin Virol* **2015,** *13*, 75-80.

133. Morton, J. J.; Bird, G.; Keysar, S. B.; Astling, D. P.; Lyons, T. R.; Anderson, R. T.; Glogowska, M. J.; Estes, P.; Eagles, J. R.; Le, P. N.; Gan, G.; McGettigan, B.; Fernandez, P.; Padilla-Just, N.; Varella-Garcia, M.; Song, J. I.; Bowles, D. W.; Schedin, P.; Tan, A. C.; Roop, D. R.; Wang, X. J.; Refaeli, Y.; Jimeno, A., XactMice: humanizing mouse bone marrow enables microenvironment reconstitution in a patient-derived xenograft model of head and neck cancer. *Oncogene* **2016,** *35* (3), 290-300.

134. Lee, J.; Heckl, D.; Parekkadan, B., Multiple genetically engineered humanized microenvironments in a single mouse. *Biomater Res* **2016,** *20*, 19.

135. Das Thakur, M.; Salangsang, F.; Landman, A. S.; Sellers, W. R.; Pryer, N. K.; Levesque, M. P.; Dummer, R.; McMahon, M.; Stuart, D. D., Modelling vemurafenib resistance in melanoma reveals a strategy to forestall drug resistance. *Nature* **2013,** *494* (7436), 251-5.

136. Jimeno, A.; Amador, M. L.; Kulesza, P.; Wang, X.; Rubio-Viqueira, B.; Zhang, X.; Chan, A.; Wheelhouse, J.; Kuramochi, H.; Tanaka, K.; Danenberg, K.; Messersmith, W. A.; Almuete, V.; Hruban, R. H.; Maitra, A.; Yeo, C. J.; Hidalgo, M., Assessment of celecoxib pharmacodynamics in pancreatic cancer. *Mol Cancer Ther* **2006,** *5* (12), 3240-7.

137. Heid, I.; Steiger, K.; Trajkovic-Arsic, M.; Settles, M.; Esswein, M. R.; Erkan, M.; Kleeff, J.; Jager, C.; Friess, H.; Haller, B.; Steingotter, A.; Schmid, R. M.; Schwaiger, M.; Rummeny, E. J.; Esposito, I.; Siveke, J. T.; Braren, R. F., Co-clinical Assessment of Tumor Cellularity in Pancreatic Cancer. *Clin Cancer Res* **2017,** *23* (6), 1461-1470.

138. Choi, Y.; Lee, S.; Kim, K.; Kim, S. H.; Chung, Y. J.; Lee, C., Studying cancer immunotherapy using patient-derived xenografts (PDXs) in humanized mice. *Exp Mol Med* **2018,** *50* (8), 99.

139. Owonikoko, T. K.; Zhang, G.; Kim, H. S.; Stinson, R. M.; Bechara, R.; Zhang, C.; Chen, Z.; Saba, N. F.; Pakkala, S.; Pillai, R.; Deng, X.; Sun, S. Y.; Rossi, M. R.; Sica, G. L.; Ramalingam, S. S.; Khuri, F. R., Patient-derived xenografts faithfully replicated clinical outcome in a phase II co-clinical trial of arsenic trioxide in relapsed small cell lung cancer. *J Transl Med* **2016,** *14* (1), 111.

140. Pompili, L.; Porru, M.; Caruso, C.; Biroccio, A.; Leonetti, C., Patient-derived xenografts: a relevant preclinical model for drug development. *J Exp Clin Cancer Res* **2016,** *35* (1), 189.

141. Siolas, D.; Hannon, G. J., Patient-derived tumor xenografts: transforming clinical samples into mouse models. *Cancer Res* **2013,** *73* (17), 5315-9.

142. Shultz, L. D.; Goodwin, N.; Ishikawa, F.; Hosur, V.; Lyons, B. L.; Greiner, D. L., Subcapsular transplantation of tissue in the kidney. *Cold Spring Harb Protoc* **2014,** *2014* (7), 737-40.

143. Pepper, A. R.; Gala-Lopez, B.; Pawlick, R.; Merani, S.; Kin, T.; Shapiro, A. M., A prevascularized subcutaneous device-less site for islet and cellular transplantation. *Nat Biotechnol* **2015,** *33* (5), 518-23.

144. Ward, W. K.; Slobodzian, E. P.; Tiekotter, K. L.; Wood, M. D., The effect of microgeometry, implant thickness and polyurethane chemistry on the foreign body response to subcutaneous implants. *Biomaterials* **2002,** *23* (21), 4185-92.

145. Helton, K. L.; Ratner, B. D.; Wisniewski, N. A., Biomechanics of the sensor-tissue interface-effects of motion, pressure, and design on sensor performance and the foreign body response-part I: theoretical framework. *J Diabetes Sci Technol* **2011,** *5* (3), 632-46.

146. Griffin, M. F.; Leung, B. C.; Premakumar, Y.; Szarko, M.; Butler, P. E., Comparison of the mechanical properties of different skin sites for auricular and nasal reconstruction. *J Otolaryngol Head Neck Surg* **2017,** *46* (1), 33.

147. Jaalouk, D. E.; Lammerding, J., Mechanotransduction gone awry. *Nat Rev Mol Cell Biol* **2009,** *10* (1), 63-73.

148. Akhtar, M. Z.; Sutherland, A. I.; Huang, H.; Ploeg, R. J.; Pugh, C. W., The role of hypoxia-inducible factors in organ donation and transplantation: the current perspective and future opportunities. *Am J Transplant* **2014,** *14* (7), 1481-7.

149. Anderson, J. M.; Rodriguez, A.; Chang, D. T., Foreign body reaction to biomaterials. *Semin Immunol* **2008,** *20* (2), 86-100.

150. Ben-David, U.; Ha, G.; Tseng, Y. Y.; Greenwald, N. F.; Oh, C.; Shih, J.; McFarland, J. M.; Wong, B.; Boehm, J. S.; Beroukhim, R.; Golub, T. R., Patient-derived xenografts undergo mouse-specific tumor evolution. *Nat Genet* **2017,** *49* (11), 1567-1575.

151. Vishwakarma, A.; Bhise, N. S.; Evangelista, M. B.; Rouwkema, J.; Dokmeci, M. R.; Ghaemmaghami, A. M.; Vrana, N. E.; Khademhosseini, A., Engineering Immunomodulatory Biomaterials To Tune the Inflammatory Response. *Trends Biotechnol* **2016,** *34* (6), 470-482.

152. Hubbell, J. A.; Thomas, S. N.; Swartz, M. A., Materials engineering for immunomodulation. *Nature* **2009,** *462* (7272), 449-60.

153. Singh, A.; Peppas, N. A., Hydrogels and scaffolds for immunomodulation. *Adv Mater* **2014,** *26* (38), 6530-41.

154. Hotaling, N. A.; Tang, L.; Irvine, D. J.; Babensee, J. E., Biomaterial Strategies for Immunomodulation. *Annu Rev Biomed Eng* **2015,** *17*, 317-49.

155. Sadtler, K.; Wolf, M. T.; Ganguly, S.; Moad, C. A.; Chung, L.; Majumdar, S.; Housseau, F.; Pardoll, D. M.; Elisseeff, J. H., Divergent immune responses to synthetic and biological scaffolds. *Biomaterials* **2019,** *192*, 405-415.

156. Boehler, R. M.; Graham, J. G.; Shea, L. D., Tissue engineering tools for modulation of the immune response. *Biotechniques* **2011,** *51* (4), 239-40, 242, 244 passim.

157. Wang, H.; Mooney, D. J., Biomaterial-assisted targeted modulation of immune cells in cancer treatment. *Nat Mater* **2018,** *17* (9), 761-772.

158. Vegas, A. J.; Veiseh, O.; Doloff, J. C.; Ma, M.; Tam, H. H.; Bratlie, K.; Li, J.; Bader, A. R.; Langan, E.; Olejnik, K.; Fenton, P.; Kang, J. W.; Hollister-Locke, J.; Bochenek, M. A.; Chiu, A.; Siebert, S.; Tang, K.; Jhunjhunwala, S.; Aresta-Dasilva, S.; Dholakia, N.; Thakrar, R.; Vietti, T.; Chen, M.; Cohen, J.; Siniakowicz, K.; Qi, M.; McGarrigle, J.; Graham, A. C.; Lyle, S.; Harlan, D. M.; Greiner, D. L.; Oberholzer, J.; Weir, G. C.; Langer, R.; Anderson, D. G., Combinatorial hydrogel library enables identification of materials that mitigate the foreign body response in primates. *Nat Biotechnol* **2016,** *34* (3), 345-52.

159. Chen, S.; Jones, J. A.; Xu, Y.; Low, H. Y.; Anderson, J. M.; Leong, K. W., Characterization of topographical effects on macrophage behavior in a foreign body response model. *Biomaterials* **2010,** *31* (13), 3479-91.

160. Lee, J.; Cuddihy, M. J.; Kotov, N. A., Three-dimensional cell culture matrices: state of the art. *Tissue Eng Part B Rev* **2008,** *14* (1), 61-86.

161. Jansen, L. E.; Amer, L. D.; Chen, E. Y.; Nguyen, T. V.; Saleh, L. S.; Emrick, T.; Liu, W. F.; Bryant, S. J.; Peyton, S. R., Zwitterionic PEG-PC Hydrogels Modulate the Foreign Body Response in a Modulus-Dependent Manner. *Biomacromolecules* **2018,** *19* (7), 2880-2888.

162. Matlaga, B. F.; Yasenchak, L. P.; Salthouse, T. N., Tissue response to implanted polymers: the significance of sample shape. *J Biomed Mater Res* **1976,** *10* (3), 391-7.

163. Zhang, L.; Cao, Z.; Bai, T.; Carr, L.; Ella-Menye, J. R.; Irvin, C.; Ratner, B. D.; Jiang, S., Zwitterionic hydrogels implanted in mice resist the foreign-body reaction. *Nat Biotechnol* **2013,** *31* (6), 553-6.

164. Sadtler, K.; Estrellas, K.; Allen, B. W.; Wolf, M. T.; Fan, H.; Tam, A. J.; Patel, C. H.; Luber, B. S.; Wang, H.; Wagner, K. R.; Powell, J. D.; Housseau, F.; Pardoll, D. M.; Elisseeff, J. H., Developing a pro-regenerative biomaterial scaffold microenvironment requires T helper 2 cells. *Science* **2016,** *352* (6283), 366-70.

165. Sadtler, K.; Allen, B. W.; Estrellas, K.; Housseau, F.; Pardoll, D. M.; Elisseeff, J. H., The Scaffold Immune Microenvironment: Biomaterial-Mediated Immune Polarization in Traumatic and Nontraumatic Applications<sup/>. *Tissue Eng Part A* **2017,** *23* (19-20), 1044-1053.

166. Swartzlander, M. D.; Blakney, A. K.; Amer, L. D.; Hankenson, K. D.; Kyriakides, T. R.; Bryant, S. J., Immunomodulation by mesenchymal stem cells combats the foreign body response to cell-laden synthetic hydrogels. *Biomaterials* **2015,** *41*, 79-88.

167. Parekkadan, B.; Milwid, J. M., Mesenchymal stem cells as therapeutics. *Annu Rev Biomed Eng* **2010,** *12*, 87-117.

168. Tan, Z.; Dini, D.; Rodriguez y Baena, F.; Forte, A. E., Composite hydrogel: A high fidelity soft tissue mimic for surgery. *Materials & Design* **2018,** *160*, 886-894.

169. Zhang, T.; Zhang, L.; Fan, S.; Zhang, M.; Fu, H.; Liu, Y.; Yin, X.; Chen, H.; Xie, L.; Zhang, J.; Gavine, P. R.; Gu, Y.; Ni, X.; Su, X., Patient-Derived Gastric Carcinoma Xenograft Mouse Models Faithfully Represent Human Tumor Molecular Diversity. *PLoS One* **2015,** *10* (7), e0134493.

170. Choi, Y. Y.; Lee, J. E.; Kim, H.; Sim, M. H.; Kim, K. K.; Lee, G.; Kim, H. I.; An, J. Y.; Hyung, W. J.; Kim, C. B.; Noh, S. H.; Kim, S.; Cheong, J. H., Establishment and characterisation of patient-derived xenografts as paraclinical models for gastric cancer. *Sci Rep* **2016,** *6*, 22172.

171. Wang, H.; Lu, J.; Tang, J.; Chen, S.; He, K.; Jiang, X.; Jiang, W.; Teng, L., Establishment of patient-derived gastric cancer xenografts: a useful tool for preclinical evaluation of targeted therapies involving alterations in HER-2, MET and FGFR2 signaling pathways. *BMC Cancer* **2017,** *17* (1), 191.

172. Ham, I. H.; Oh, H. J.; Jin, H.; Bae, C. A.; Jeon, S. M.; Choi, K. S.; Son, S. Y.; Han, S. U.; Brekken, R. A.; Lee, D.; Hur, H., Targeting interleukin-6 as a strategy to overcome stroma-induced resistance to chemotherapy in gastric cancer. *Mol Cancer* **2019,** *18* (1), 68.

173. Ham, I.-H.; Lee, D.; Hur, H., Role of Cancer-Associated Fibroblast in Gastric Cancer Progression and Resistance to Treatments. *Journal of Oncology* **2019,** *2019*, 11.

174. Fuyuhiro, Y.; Yashiro, M.; Noda, S.; Kashiwagi, S.; Matsuoka, J.; Doi, Y.; Kato, Y.; Muguruma, K.; Sawada, T.; Hirakawa, K., Myofibroblasts are associated with the progression of scirrhous gastric carcinoma. *Exp Ther Med* **2010,** *1* (4), 547-551.

175. Mani, S. A.; Guo, W.; Liao, M. J.; Eaton, E. N.; Ayyanan, A.; Zhou, A. Y.; Brooks, M.; Reinhard, F.; Zhang, C. C.; Shipitsin, M.; Campbell, L. L.; Polyak, K.; Brisken, C.; Yang, J.; Weinberg, R. A., The epithelial-mesenchymal transition generates cells with properties of stem cells. *Cell* **2008,** *133* (4), 704-15.

176. Takaishi, S.; Okumura, T.; Tu, S.; Wang, S. S.; Shibata, W.; Vigneshwaran, R.; Gordon, S. A.; Shimada, Y.; Wang, T. C., Identification of gastric cancer stem cells using the cell surface marker CD44. *Stem Cells* **2009,** *27* (5), 1006-20.

177. Lee, J.; Byun, H.; Madhurakkat Perikamana, S. K.; Lee, S.; Shin, H., Current Advances in Immunomodulatory Biomaterials for Bone Regeneration. *Adv Healthc Mater* **2019,** *8* (4), e1801106.

178. Soon-Shiong, P.; Heintz, R. E.; Merideth, N.; Yao, Q. X.; Yao, Z.; Zheng, T.; Murphy, M.; Moloney, M. K.; Schmehl, M.; Harris, M.; et al., Insulin independence in a

type 1 diabetic patient after encapsulated islet transplantation. *Lancet* **1994,** *343* (8903), 950-1.

179. Getts, D. R.; Terry, R. L.; Getts, M. T.; Deffrasnes, C.; Muller, M.; van Vreden, C.; Ashhurst, T. M.; Chami, B.; McCarthy, D.; Wu, H.; Ma, J.; Martin, A.; Shae, L. D.; Witting, P.; Kansas, G. S.; Kuhn, J.; Hafezi, W.; Campbell, I. L.; Reilly, D.; Say, J.; Brown, L.; White, M. Y.; Cordwell, S. J.; Chadban, S. J.; Thorp, E. B.; Bao, S.; Miller, S. D.; King, N. J., Therapeutic inflammatory monocyte modulation using immune-modifying microparticles. *Sci Transl Med* **2014,** *6* (219), 219ra7.

180. Ali, O. A.; Emerich, D.; Dranoff, G.; Mooney, D. J., In situ regulation of DC subsets and T cells mediates tumor regression in mice. *Sci Transl Med* **2009,** *1* (8), 8ra19.

181. Kim, J.; Li, W. A.; Choi, Y.; Lewin, S. A.; Verbeke, C. S.; Dranoff, G.; Mooney, D. J., Injectable, spontaneously assembling, inorganic scaffolds modulate immune cells in vivo and increase vaccine efficacy. *Nat Biotechnol* **2015,** *33* (1), 64-72.

182. Galperin, A.; Oldinski, R. A.; Florczyk, S. J.; Bryers, J. D.; Zhang, M.; Ratner, B. D., Integrated bi-layered scaffold for osteochondral tissue engineering. *Adv Healthc Mater* **2013,** *2* (6), 872-83.

183. Choi, S. W.; Zhang, Y.; Macewan, M. R.; Xia, Y., Neovascularization in biodegradable inverse opal scaffolds with uniform and precisely controlled pore sizes. *Adv Healthc Mater* **2013,** *2* (1), 145-54.

184. Dondossola, E.; Holzapfel, B. M.; Alexander, S.; Filippini, S.; Hutmacher, D. W.; Friedl, P., Examination of the foreign body response to biomaterials by nonlinear intravital microscopy. *Nature Biomedical Engineering* **2016,** *1* (1), 0007.

185. Wynn, T. A.; Ramalingam, T. R., Mechanisms of fibrosis: therapeutic translation for fibrotic disease. *Nat Med* **2012,** *18* (7), 1028-40.

186. Kolaczkowska, E.; Kubes, P., Neutrophil recruitment and function in health and inflammation. *Nat Rev Immunol* **2013,** *13* (3), 159-75.

187. Scozzi, D.; Ibrahim, M.; Menna, C.; Krupnick, A. S.; Kreisel, D.; Gelman, A. E., The Role of Neutrophils in Transplanted Organs. *Am J Transplant* **2017,** *17* (2), 328-335.

188. Aldabbous, L.; Abdul-Salam, V.; McKinnon, T.; Duluc, L.; Pepke-Zaba, J.; Southwood, M.; Ainscough, A. J.; Hadinnapola, C.; Wilkins, M. R.; Toshner, M.; Wojciak-Stothard, B., Neutrophil Extracellular Traps Promote Angiogenesis: Evidence From Vascular Pathology in Pulmonary Hypertension. *Arterioscler Thromb Vasc Biol* **2016,** *36* (10), 2078-87.

189. Christoffersson, G.; Vagesjo, E.; Vandooren, J.; Liden, M.; Massena, S.; Reinert, R. B.; Brissova, M.; Powers, A. C.; Opdenakker, G.; Phillipson, M., VEGF-A recruits a proangiogenic MMP-9-delivering neutrophil subset that induces angiogenesis in transplanted hypoxic tissue. *Blood* **2012,** *120* (23), 4653-62.

190. Su, X.; Yang, L.; Yin, Y.; Huang, J.; Qiao, F.; Fang, Y.; Yu, L.; Wang, Y.; Zhou, K.; Wang, J., Bone marrow mesenchymal stem cells tune the differentiation of myeloid-derived suppressor cells in bleomycin-induced lung injury. *Stem Cell Res Ther* **2018,** *9* (1), 253.

191. Wynn, T. A.; Vannella, K. M., Macrophages in Tissue Repair, Regeneration, and Fibrosis. *Immunity* **2016,** *44* (3), 450-462.

192. Luzzi, K. J.; MacDonald, I. C.; Schmidt, E. E.; Kerkvliet, N.; Morris, V. L.; Chambers, A. F.; Groom, A. C., Multistep nature of metastatic inefficiency - Dormancy of solitary cells after successful extravasation and limited survival of early micrometastases. *Am J Pathol* **1998,** *153* (3), 865-873.

193. Chambers, A. F.; Groom, A. C.; MacDonald, I. C., Dissemination and growth of cancer cells in metastatic sites. *Nat Rev Cancer* **2002,** *2* (8), 563-72.

194. Aguirre-Ghiso, J. A., Models, mechanisms and clinical evidence for cancer dormancy. *Nat Rev Cancer* **2007,** *7* (11), 834-46.

195. Meng, S.; Tripathy, D.; Frenkel, E. P.; Shete, S.; Naftalis, E. Z.; Huth, J. F.; Beitsch, P. D.; Leitch, M.; Hoover, S.; Euhus, D.; Haley, B.; Morrison, L.; Fleming, T. P.; Herlyn, D.; Terstappen, L. W.; Fehm, T.; Tucker, T. F.; Lane, N.; Wang, J.; Uhr, J. W., Circulating tumor cells in patients with breast cancer dormancy. *Clin Cancer Res* **2004,** *10* (24), 8152-62.

196. Sosa, M. S.; Bragado, P.; Aguirre-Ghiso, J. A., Mechanisms of disseminated cancer cell dormancy: an awakening field. *Nat Rev Cancer* **2014,** *14* (9), 611-22.

197. He, F.; Chiou, A. E.; Loh, H. C.; Lynch, M.; Seo, B. R.; Song, Y. H.; Lee, M. J.; Hoerth, R.; Bortel, E. L.; Willie, B. M.; Duda, G. N.; Estroff, L. A.; Masic, A.; Wagermaier, W.; Fratzl, P.; Fischbach, C., Multiscale characterization of the mineral phase at skeletal sites of breast cancer metastasis. *P Natl Acad Sci USA* **2017,** *114* (40), 10542-10547.

198. Paget, S., The distribution of secondary growths in cancer of the breast. *Lancet* **1889,** *1*, 571-573.

199. Wong, C. C.; Gilkes, D. M.; Zhang, H.; Chen, J.; Wei, H.; Chaturvedi, P.; Fraley, S. I.; Wong, C. M.; Khoo, U. S.; Ng, I. O.; Wirtz, D.; Semenza, G. L., Hypoxia-inducible factor 1 is a master regulator of breast cancer metastatic niche formation. *Proc Natl Acad Sci U S A* **2011,** *108* (39), 16369-74.

200. Oskarsson, T.; Acharyya, S.; Zhang, X. H.; Vanharanta, S.; Tavazoie, S. F.; Morris, P. G.; Downey, R. J.; Manova-Todorova, K.; Brogi, E.; Massague, J., Breast cancer cells produce tenascin C as a metastatic niche component to colonize the lungs. *Nat Med* **2011,** *17* (7), 867-74.

201. Barkan, D.; El Touny, L. H.; Michalowski, A. M.; Smith, J. A.; Chu, I.; Davis, A. S.; Webster, J. D.; Hoover, S.; Simpson, R. M.; Gauldie, J.; Green, J. E., Metastatic growth

from dormant cells induced by a col-I-enriched fibrotic environment. *Cancer Res* **2010,** *70* (14), 5706-16.

202. Levental, K. R.; Yu, H.; Kass, L.; Lakins, J. N.; Egeblad, M.; Erler, J. T.; Fong, S. F.; Csiszar, K.; Giaccia, A.; Weninger, W.; Yamauchi, M.; Gasser, D. L.; Weaver, V. M., Matrix crosslinking forces tumor progression by enhancing integrin signaling. *Cell* **2009,** *139* (5), 891-906.

203. Koebel, C. M.; Vermi, W.; Swann, J. B.; Zerafa, N.; Rodig, S. J.; Old, L. J.; Smyth, M. J.; Schreiber, R. D., Adaptive immunity maintains occult cancer in an equilibrium state. *Nature* **2007,** *450* (7171), 903-7.

204. Hanna, R. N.; Cekic, C.; Sag, D.; Tacke, R.; Thomas, G. D.; Nowyhed, H.; Herrley, E.; Rasquinha, N.; McArdle, S.; Wu, R.; Peluso, E.; Metzger, D.; Ichinose, H.; Shaked, I.; Chodaczek, G.; Biswas, S. K.; Hedrick, C. C., Patrolling monocytes control tumor metastasis to the lung. *Science* **2015,** *350* (6263), 985-90.

205. Lambert, A. W.; Pattabiraman, D. R.; Weinberg, R. A., Emerging Biological Principles of Metastasis. *Cell* **2017,** *168* (4), 670-691.

206. Villasante, A.; Vunjak-Novakovic, G., Tissue-engineered models of human tumors for cancer research. *Expert Opin Drug Discov* **2015,** *10* (3), 257-68.

207. Hutmacher, D. W.; Loessner, D.; Rizzi, S.; Kaplan, D. L.; Mooney, D. J.; Clements, J. A., Can tissue engineering concepts advance tumor biology research? *Trends Biotechnol* **2010,** *28* (3), 125-133.

208. Aguado, B. A.; Bushnell, G. G.; Rao, S. S.; Jeruss, J. S.; Shea, L. D., Engineering the pre-metastatic niche. *Nature Biomedical Engineering* **2017,** *1* (6), 0077.

209. Dvorak, H. F., Tumors: wounds that do not heal. Similarities between tumor stroma generation and wound healing. *N Engl J Med* **1986,** *315* (26), 1650-9.

210. Costa-Silva, B.; Aiello, N. M.; Ocean, A. J.; Singh, S.; Zhang, H.; Thakur, B. K.; Becker, A.; Hoshino, A.; Mark, M. T.; Molina, H.; Xiang, J.; Zhang, T.; Theilen, T. M.; Garcia-Santos, G.; Williams, C.; Ararso, Y.; Huang, Y.; Rodrigues, G.; Shen, T. L.; Labori, K. J.; Lothe, I. M.; Kure, E. H.; Hernandez, J.; Doussot, A.; Ebbesen, S. H.; Grandgenett, P. M.; Hollingsworth, M. A.; Jain, M.; Mallya, K.; Batra, S. K.; Jarnagin, W. R.; Schwartz, R. E.; Matei, I.; Peinado, H.; Stanger, B. Z.; Bromberg, J.; Lyden, D., Pancreatic cancer exosomes initiate pre-metastatic niche formation in the liver. *Nat Cell Biol* **2015,** *17* (6), 816-26.

211. Inoue, M.; Nakano, T.; Yoneda, A.; Nishikawa, M.; Nakayama, M.; Yumura-Yagi, K.; Sakata, N.; Yasui, M.; Okamura, T.; Kawa, K., Graft-versus-tumor effect in a patient with advanced neuroblastoma who received HLA haplo-identical bone marrow transplantation. *Bone Marrow Transplant* **2003,** *32* (1), 103-6.

212. Lee, J.; Shanbhag, S.; Kotov, N. A., Inverted colloidal crystals as three-dimensional microenvironments for cellular co-cultures. *Journal of Materials Chemistry* **2006,** *16* (35), 3558.

213. Bryers, J. D.; Giachelli, C. M.; Ratner, B. D., Engineering biomaterials to integrate and heal: the biocompatibility paradigm shifts. *Biotechnol Bioeng* **2012,** *109* (8), 1898-911.

214. Stachowiak, A. N.; Bershteyn, A.; Tzatzalos, E.; Irvine, D. J., Bioactive hydrogels with an ordered cellular structure combine interconnected macroporosity and robust mechanical properties. *Adv Mater* **2005,** *17* (4), 399-+.

215. Kotov, N. A.; Liu, Y. F.; Wang, S. P.; Cumming, C.; Eghtedari, M.; Vargas, G.; Motamedi, M.; Nichols, J.; Cortiella, J., Inverted colloidal crystals as three-dimensional cell scaffolds. *Langmuir* **2004,** *20* (19), 7887-7892.

216. Joao, C. F.; Vasconcelos, J. M.; Silva, J. C.; Borges, J. P., An overview of inverted colloidal crystal systems for tissue engineering. *Tissue Eng Part B Rev* **2014,** *20* (5), 437-54.

217. Rutkowski, M. R.; Stephen, T. L.; Svoronos, N.; Allegrezza, M. J.; Tesone, A. J.; Perales-Puchalt, A.; Brencicova, E.; Escovar-Fadul, X.; Nguyen, J. M.; Cadungog, M. G.; Zhang, R.; Salatino, M.; Tchou, J.; Rabinovich, G. A.; Conejo-Garcia, J. R., Microbially driven TLR5-dependent signaling governs distal malignant progression through tumor-promoting inflammation. *Cancer Cell* **2015,** *27* (1), 27-40.

218. Li, A.; Dubey, S.; Varney, M. L.; Dave, B. J.; Singh, R. K., IL-8 Directly Enhanced Endothelial Cell Survival, Proliferation, and Matrix Metalloproteinases Production and Regulated Angiogenesis. *The Journal of Immunology* **2003,** *170* (6), 3369-3376.

219. Lee, E.; Fertig, E. J.; Jin, K.; Sukumar, S.; Pandey, N. B.; Popel, A. S., Breast cancer cells condition lymphatic endothelial cells within pre-metastatic niches to promote metastasis. *Nat Commun* **2014,** *5*, 4715.

220. Havens, A. M.; Pedersen, E. A.; Shiozawa, Y.; Ying, C.; Jung, Y.; Sun, Y.; Neeley, C.; Wang, J.; Mehra, R.; Keller, E. T.; K. McCauley, L.; Loberg, R. D.; Pienta, K. J.; Taichman, R. S., An In Vivo Mouse Model for Human Prostate Cancer Metastasis. *Neoplasia* **2008,** *10* (4), 371-IN4.

221. Magnon, C.; Hall, S. J.; Lin, J.; Xue, X.; Gerber, L.; Freedland, S. J.; Frenette, P. S., Autonomic nerve development contributes to prostate cancer progression. *Science* **2013,** *341* (6142), 1236361.

222. Tai, S.; Sun, Y.; Squires, J. M.; Zhang, H.; Oh, W. K.; Liang, C. Z.; Huang, J., PC3 is a cell line characteristic of prostatic small cell carcinoma. *Prostate* **2011,** *71* (15), 1668-79.

223. Kitamura, T.; Qian, B. Z.; Pollard, J. W., Immune cell promotion of metastasis. *Nat Rev Immunol* **2015,** *15* (2), 73-86.

224. Nakahara, T.; Norberg, S. M.; Shalinsky, D. R.; Hu-Lowe, D. D.; McDonald, D. M., Effect of inhibition of vascular endothelial growth factor signaling on distribution of extravasated antibodies in tumors. *Cancer Res* **2006,** *66* (3), 1434-45.

225. Levine, J. E., Implications of TNF-alpha in the pathogenesis and management of GVHD. *Int J Hematol* **2011,** *93* (5), 571-577.

226. Zeiser, R.; Blazar, B. R., Acute Graft-versus-Host Disease - Biologic Process, Prevention, and Therapy. *N Engl J Med* **2017,** *377* (22), 2167-2179.

227. Chung, K.; Wallace, J.; Kim, S. Y.; Kalyanasundaram, S.; Andalman, A. S.; Davidson, T. J.; Mirzabekov, J. J.; Zalocusky, K. A.; Mattis, J.; Denisin, A. K.; Pak, S.; Bernstein, H.; Ramakrishnan, C.; Grosenick, L.; Gradinaru, V.; Deisseroth, K., Structural and molecular interrogation of intact biological systems. *Nature* **2013,** *497* (7449), 332-7.

228. Visvader, J. E.; Lindeman, G. J., Cancer stem cells in solid tumours: accumulating evidence and unresolved questions. *Nat Rev Cancer* **2008,** *8* (10), 755-68.

229. McFarlane, S.; Coulter, J. A.; Tibbits, P.; O'Grady, A.; McFarlane, C.; Montgomery, N.; Hill, A.; McCarthy, H. O.; Young, L. S.; Kay, E. W.; Isacke, C. M.; Waugh, D. J., CD44 increases the efficiency of distant metastasis of breast cancer. *Oncotarget* **2015,** *6* (13), 11465-76.

230. Gao, H.; Chakraborty, G.; Lee-Lim, A. P.; Mo, Q.; Decker, M.; Vonica, A.; Shen, R.; Brogi, E.; Brivanlou, A. H.; Giancotti, F. G., The BMP inhibitor Coco reactivates breast cancer cells at lung metastatic sites. *Cell* **2012,** *150* (4), 764-79.

231. Yumoto, K.; Eber, M. R.; Wang, J.; Cackowski, F. C.; Decker, A. M.; Lee, E.; Nobre, A. R.; Aguirre-Ghiso, J. A.; Jung, Y.; Taichman, R. S., Axl is required for TGF-beta2-induced dormancy of prostate cancer cells in the bone marrow. *Sci Rep* **2016,** *6*, 36520.

232. Ruppender, N.; Larson, S.; Lakely, B.; Kollath, L.; Brown, L.; Coleman, I.; Coleman, R.; Nguyen, H.; Nelson, P. S.; Corey, E.; Snyder, L. A.; Vessella, R. L.; Morrissey, C.; Lam, H. M., Cellular Adhesion Promotes Prostate Cancer Cells Escape from Dormancy. *PLoS One* **2015,** *10* (6), e0130565.

233. Novak, M. L.; Koh, T. J., Phenotypic transitions of macrophages orchestrate tissue repair. *Am J Pathol* **2013,** *183* (5), 1352-1363.

234. McCracken, J. M.; Allen, L. A., Regulation of human neutrophil apoptosis and lifespan in health and disease. *J Cell Death* **2014,** *7*, 15-23.

235. Hosseini, H.; Obradovic, M. M.; Hoffmann, M.; Harper, K. L.; Sosa, M. S.; Werner-Klein, M.; Nanduri, L. K.; Werno, C.; Ehrl, C.; Maneck, M.; Patwary, N.; Haunschild, G.; Guzvic, M.; Reimelt, C.; Grauvogl, M.; Eichner, N.; Weber, F.; Hartkopf, A. D.; Taran, F. A.; Brucker, S. Y.; Fehm, T.; Rack, B.; Buchholz, S.; Spang, R.; Meister,

G.; Aguirre-Ghiso, J. A.; Klein, C. A., Early dissemination seeds metastasis in breast cancer. *Nature* **2016**.

236. Rothwell, P. M.; Wilson, M.; Price, J. F.; Belch, J. F. F.; Meade, T. W.; Mehta, Z., Effect of daily aspirin on risk of cancer metastasis: a study of incident cancers during randomised controlled trials. *The Lancet* **2012,** *379* (9826), 1591-1601.

237. Ridker, P. M.; MacFadyen, J. G.; Thuren, T.; Everett, B. M.; Libby, P.; Glynn, R. J.; Ridker, P.; Lorenzatti, A.; Krum, H.; Varigos, J.; Siostrzonek, P.; Sinnaeve, P.; Fonseca, F.; Nicolau, J.; Gotcheva, N.; Genest, J.; Yong, H.; Urina-Triana, M.; Milicic, D.; Cifkova, R.; Vettus, R.; Koenig, W.; Anker, S. D.; Manolis, A. J.; Wyss, F.; Forster, T.; Sigurdsson, A.; Pais, P.; Fucili, A.; Ogawa, H.; Shimokawa, H.; Veze, I.; Petrauskiene, B.; Salvador, L.; Kastelein, J.; Cornel, J. H.; Klemsdal, T. O.; Medina, F.; Budaj, A.; Vida-Simiti, L.; Kobalava, Z.; Otasevic, P.; Pella, D.; Lainscak, M.; Seung, K.-B.; Commerford, P.; Dellborg, M.; Donath, M.; Hwang, J.-J.; Kultursay, H.; Flather, M.; Ballantyne, C.; Bilazarian, S.; Chang, W.; East, C.; Everett, B.; Forgosh, L.; Glynn, R.; Harris, B.; Libby, P.; Ligueros, M.; Thuren, T.; Bohula, E.; Charmarthi, B.; Cheng, S.; Chou, S.; Danik, J.; McMahon, G.; Maron, B.; Ning, M.; Olenchock, B.; Pande, R.; Perlstein, T.; Pradhan, A.; Rost, N.; Singhal, A.; Taqueti, V.; Wei, N.; Burris, H.; Cioffi, A.; Dalseg, A. M.; Ghosh, N.; Gralow, J.; Mayer, T.; Rugo, H.; Fowler, V.; Limaye, A. P.; Cosgrove, S.; Levine, D.; Lopes, R.; Scott, J.; Thuren, T.; Ligueros, M.; Hilkert, R.; Tamesby, G.; Mickel, C.; Manning, B.; Woelcke, J.; Tan, M.; Manfreda, S.; Ponce, T.; Kam, J.; Saini, R.; Banker, K.; Salko, T.; Nandy, P.; Tawfik, R.; O'Neil, G.; Manne, S.; Jirvankar, P.; Lal, S.; Nema, D.; Jose, J.; Collins, R.; Bailey, K.; Blumenthal, R.; Colhoun, H.; Gersh, B.; Glynn, R. J., Effect of interleukin-1β inhibition with canakinumab on incident lung cancer in patients with atherosclerosis: exploratory results from a randomised, double-blind, placebo-controlled trial. *The Lancet* **2017,** *390* (10105), 1833-1842.

238. Jacob, L.; Kostev, K.; Rathmann, W.; Kalder, M., Impact of metformin on metastases in patients with breast cancer and type 2 diabetes. *J Diabetes Complications* **2016,** *30* (6), 1056-9.

239. Yakes, F. M.; Chen, J.; Tan, J.; Yamaguchi, K.; Shi, Y.; Yu, P.; Qian, F.; Chu, F.; Bentzien, F.; Cancilla, B.; Orf, J.; You, A.; Laird, A. D.; Engst, S.; Lee, L.; Lesch, J.; Chou, Y. C.; Joly, A. H., Cabozantinib (XL184), a novel MET and VEGFR2 inhibitor, simultaneously suppresses metastasis, angiogenesis, and tumor growth. *Mol Cancer Ther* **2011,** *10* (12), 2298-308.

240. Nair, A.; Tang, L., Influence of scaffold design on host immune and stem cell responses. *Semin Immunol* **2017,** *29*, 62-71.

241. Ali, O. A.; Huebsch, N.; Cao, L.; Dranoff, G.; Mooney, D. J., Infection-mimicking materials to program dendritic cells in situ. *Nat Mater* **2009,** *8* (2), 151-8.

242. Bencherif, S. A.; Warren Sands, R.; Ali, O. A.; Li, W. A.; Lewin, S. A.; Braschler, T. M.; Shih, T. Y.; Verbeke, C. S.; Bhatta, D.; Dranoff, G.; Mooney, D. J., Injectable cryogel-based whole-cell cancer vaccines. *Nat Commun* **2015,** *6*, 7556.

243. Tentler, J. J.; Tan, A. C.; Weekes, C. D.; Jimeno, A.; Leong, S.; Pitts, T. M.; Arcaroli, J. J.; Messersmith, W. A.; Eckhardt, S. G., Patient-derived tumour xenografts as models for oncology drug development. *Nat Rev Clin Oncol* **2012,** *9* (6), 338-50.

244. White, L.; Meyer, P. R.; Benedict, W. F., Establishment and characterization of a human T-cell leukemia line (LALW-2) in nude mice. *J Natl Cancer Inst* **1984,** *72* (5), 1029-38.

245. Baron, F.; Maris, M. B.; Sandmaier, B. M.; Storer, B. E.; Sorror, M.; Diaconescu, R.; Woolfrey, A. E.; Chauncey, T. R.; Flowers, M. E.; Mielcarek, M.; Maloney, D. G.; Storb, R., Graft-versus-tumor effects after allogeneic hematopoietic cell transplantation with nonmyeloablative conditioning. *J Clin Oncol* **2005,** *23* (9), 1993-2003.

246. Korngold, R.; Marini, J. C.; de Baca, M. E.; Murphy, G. F.; Giles-Komar, J., Role of tumor necrosis factor-α in graft-versus-host disease and graft-versus-leukemia responses. *Biology of Blood and Marrow Transplantation* **2003,** *9* (5), 292-303.

247. Roth, M. D.; Harui, A., Human tumor infiltrating lymphocytes cooperatively regulate prostate tumor growth in a humanized mouse model. *J Immunother Cancer* **2015,** *3*, 12.

248. Simpson-Abelson, M. R.; Sonnenberg, G. F.; Takita, H.; Yokota, S. J.; Conway, T. F.; Kelleher, R. J.; Shultz, L. D.; Barcos, M.; Bankert, R. B., Long-Term Engraftment and Expansion of Tumor-Derived Memory T Cells Following the Implantation of Non-Disrupted Pieces of Human Lung Tumor into NOD-scid IL2R null Mice. *The Journal of Immunology* **2008,** *180* (10), 7009-7018.

249. El Rayes, T.; Catena, R.; Lee, S.; Stawowczyk, M.; Joshi, N.; Fischbach, C.; Powell, C. A.; Dannenberg, A. J.; Altorki, N. K.; Gao, D. C.; Mittal, V., Lung inflammation promotes metastasis through neutrophil protease-mediated degradation of Tsp-1. *P Natl Acad Sci USA* **2015,** *112* (52), 16000-16005.

250. De Cock, J. M.; Shibue, T.; Dongre, A.; Keckesova, Z.; Reinhardt, F.; Weinberg, R. A., Inflammation Triggers Zeb1-Dependent Escape from Tumor Latency. *Cancer Res* **2016,** *76* (23), 6778-6784.

251. Park, J.; Wysocki, R. W.; Amoozgar, Z.; Maiorino, L.; Fein, M. R.; Jorns, J.; Schott, A. F.; Kinugasa-Katayama, Y.; Lee, Y.; Won, N. H.; Nakasone, E. S.; Hearn, S. A.; Kuttner, V.; Qiu, J.; Almeida, A. S.; Perurena, N.; Kessenbrock, K.; Goldberg, M. S.; Egeblad, M., Cancer cells induce metastasis-supporting neutrophil extracellular DNA traps. *Sci Transl Med* **2016,** *8* (361).

252. Engblom, C.; Pfirschke, C.; Zilionis, R.; Da Silva Martins, J.; Bos, S. A.; Courties, G.; Rickelt, S.; Severe, N.; Baryawno, N.; Faget, J.; Savova, V.; Zemmour, D.; Kline, J.; Siwicki, M.; Garris, C.; Pucci, F.; Liao, H. W.; Lin, Y. J.; Newton, A.; Yaghi, O. K.; Iwamoto, Y.; Tricot, B.; Wojtkiewicz, G. R.; Nahrendorf, M.; Cortez-Retamozo, V.; Meylan, E.; Hynes, R. O.; Demay, M.; Klein, A.; Bredella, M. A.; Scadden, D. T.;

Weissleder, R.; Pittet, M. J., Osteoblasts remotely supply lung tumors with cancer-promoting SiglecF(high) neutrophils. *Science* **2017,** *358* (6367).

253. Rahbari, N. N.; Kedrin, D.; Incio, J.; Liu, H.; Ho, W. W.; Nia, H. T.; Edrich, C. M.; Jung, K.; Daubriac, J.; Chen, I.; Heishi, T.; Martin, J. D.; Huang, Y.; Maimon, N.; Reissfelder, C.; Weitz, J.; Boucher, Y.; Clark, J. W.; Grodzinsky, A. J.; Duda, D. G.; Jain, R. K.; Fukumura, D., Anti-VEGF therapy induces ECM remodeling and mechanical barriers to therapy in colorectal cancer liver metastases. *Sci Transl Med* **2016,** *8* (360), 360ra135.

254. Sainson, R. C.; Johnston, D. A.; Chu, H. C.; Holderfield, M. T.; Nakatsu, M. N.; Crampton, S. P.; Davis, J.; Conn, E.; Hughes, C. C., TNF primes endothelial cells for angiogenic sprouting by inducing a tip cell phenotype. *Blood* **2008,** *111* (10), 4997-5007.

255. Coffelt, S. B.; Wellenstein, M. D.; de Visser, K. E., Neutrophils in cancer: neutral no more. *Nat Rev Cancer* **2016,** *16* (7), 431-46.

256. Jespersen, H.; Lindberg, M. F.; Donia, M.; Soderberg, E. M. V.; Andersen, R.; Keller, U.; Ny, L.; Svane, I. M.; Nilsson, L. M.; Nilsson, J. A., Clinical responses to adoptive T-cell transfer can be modeled in an autologous immune-humanized mouse model. *Nat Commun* **2017,** *8* (1), 707.

257. Marin Navarro, A.; Susanto, E.; Falk, A.; Wilhelm, M., Modeling cancer using patient-derived induced pluripotent stem cells to understand development of childhood malignancies. *Cell Death Discov* **2018,** *4*, 7.

258. Patel, A. A.; Zhang, Y.; Fullerton, J. N.; Boelen, L.; Rongvaux, A.; Maini, A. A.; Bigley, V.; Flavell, R. A.; Gilroy, D. W.; Asquith, B.; Macallan, D.; Yona, S., The fate and lifespan of human monocyte subsets in steady state and systemic inflammation. *J Exp Med* **2017,** *214* (7), 1913-1923.

259. Drake, A. C.; Chen, Q.; Chen, J., Engineering humanized mice for improved hematopoietic reconstitution. *Cell Mol Immunol* **2012,** *9* (3), 215-24.

260. Powell, D. R.; Huttenlocher, A., Neutrophils in the Tumor Microenvironment. *Trends Immunol* **2016,** *37* (1), 41-52.

261. Reichman, H.; Karo-Atar, D.; Munitz, A., Emerging Roles for Eosinophils in the Tumor Microenvironment. *Trends Cancer* **2016,** *2* (11), 664-675.

262. Qian, B. Z.; Pollard, J. W., Macrophage diversity enhances tumor progression and metastasis. *Cell* **2010,** *141* (1), 39-51.

263. Green, J. J.; Elisseeff, J. H., Mimicking biological functionality with polymers for biomedical applications. *Nature* **2016,** *540* (7633), 386-394.

264. Aguado, B. A.; Hartfield, R. M.; Bushnell, G. G.; Decker, J. T.; Azarin, S. M.; Nanavati, D.; Schipma, M. J.; Rao, S. S.; Oakes, R. S.; Zhang, Y.; Jeruss, J. S.; Shea, L.

D., Biomaterial Scaffolds as Pre-metastatic Niche Mimics Systemically Alter the Primary Tumor and Tumor Microenvironment. *Adv Healthc Mater* **2018**.

265. Strauss, D. C.; Thomas, J. M., Transmission of donor melanoma by organ transplantation. *The Lancet Oncology* **2010,** *11* (8), 790-796.

266. Powles, T.; Paterson, A.; McCloskey, E.; Schein, P.; Scheffler, B.; Tidy, A.; Ashley, S.; Smith, I.; Ottestad, L.; Kanis, J., Reduction in bone relapse and improved survival with oral clodronate for adjuvant treatment of operable breast cancer [ISRCTN83688026]. *Breast Cancer Res* **2006,** *8* (2), R13.

267. Early Breast Cancer Trialists' Collaborative, G.; Peto, R.; Davies, C.; Godwin, J.; Gray, R.; Pan, H. C.; Clarke, M.; Cutter, D.; Darby, S.; McGale, P.; Taylor, C.; Wang, Y. C.; Bergh, J.; Di Leo, A.; Albain, K.; Swain, S.; Piccart, M.; Pritchard, K., Comparisons between different polychemotherapy regimens for early breast cancer: meta-analyses of long-term outcome among 100,000 women in 123 randomised trials. *Lancet* **2012,** *379* (9814), 432-44.

268. Daenen, L. G.; Roodhart, J. M.; van Amersfoort, M.; Dehnad, M.; Roessingh, W.; Ulfman, L. H.; Derksen, P. W.; Voest, E. E., Chemotherapy enhances metastasis formation via VEGFR-1-expressing endothelial cells. *Cancer Res* **2011,** *71* (22), 6976-85.

269. Ebos, J. M.; Lee, C. R.; Cruz-Munoz, W.; Bjarnason, G. A.; Christensen, J. G.; Kerbel, R. S., Accelerated metastasis after short-term treatment with a potent inhibitor of tumor angiogenesis. *Cancer Cell* **2009,** *15* (3), 232-9.

270. Shaked, Y.; Henke, E.; Roodhart, J. M.; Mancuso, P.; Langenberg, M. H.; Colleoni, M.; Daenen, L. G.; Man, S.; Xu, P.; Emmenegger, U.; Tang, T.; Zhu, Z.; Witte, L.; Strieter, R. M.; Bertolini, F.; Voest, E. E.; Benezra, R.; Kerbel, R. S., Rapid chemotherapy-induced acute endothelial progenitor cell mobilization: implications for antiangiogenic drugs as chemosensitizing agents. *Cancer Cell* **2008,** *14* (3), 263-73.

271. Karagiannis, G. S.; Pastoriza, J. M.; Wang, Y.; Harney, A. S.; Entenberg, D.; Pignatelli, J.; Sharma, V. P.; Xue, E. A.; Cheng, E.; D'Alfonso, T. M.; Jones, J. G.; Anampa, J.; Rohan, T. E.; Sparano, J. A.; Condeelis, J. S.; Oktay, M. H., Neoadjuvant chemotherapy induces breast cancer metastasis through a TMEM-mediated mechanism. *Sci Transl Med* **2017,** *9* (397).

272. Carlson, P.; Dasgupta, A.; Grzelak, C. A.; Kim, J.; Barrett, A.; Coleman, I. M.; Shor, R. E.; Goddard, E. T.; Dai, J.; Schweitzer, E. M.; Lim, A. R.; Crist, S. B.; Cheresh, D. A.; Nelson, P. S.; Hansen, K. C.; Ghajar, C. M., Targeting the perivascular niche sensitizes disseminated tumour cells to chemotherapy. *Nat Cell Biol* **2019,** *21* (2), 238-250.

273. Krall, J. A.; Reinhardt, F.; Mercury, O. A.; Pattabiraman, D. R.; Brooks, M. W.; Dougan, M.; Lambert, A. W.; Bierie, B.; Ploegh, H. L.; Dougan, S. K.; Weinberg, R. A., The systemic response to surgery triggers the outgrowth of distant immune-controlled tumors in mouse models of dormancy. *Sci Transl Med* **2018,** *10* (436).

274. Wolmark, N.; Mamounas, E. P.; Baehner, F. L.; Butler, S. M.; Tang, G.; Jamshidian, F.; Sing, A. P.; Shak, S.; Paik, S., Prognostic Impact of the Combination of Recurrence Score and Quantitative Estrogen Receptor Expression (ESR1) on Predicting Late Distant Recurrence Risk in Estrogen Receptor-Positive Breast Cancer After 5 Years of Tamoxifen: Results From NRG Oncology/National Surgical Adjuvant Breast and Bowel Project B-28 and B-14. *J Clin Oncol* **2016,** *34* (20), 2350-8.

275. Wang, J.; Loberg, R.; Taichman, R. S., The pivotal role of CXCL12 (SDF-1)/CXCR4 axis in bone metastasis. *Cancer Metastasis Rev* **2006,** *25* (4), 573-87.

276. Ray, A.; Cleary, M. P., The potential role of leptin in tumor invasion and metastasis. *Cytokine Growth Factor Rev* **2017,** *38*, 80-97.

277. Aguirre-Ghiso, J. A.; Bragado, P.; Sosa, M. S., Metastasis awakening: targeting dormant cancer. *Nat Med* **2013,** *19* (3), 276-7.

278. Sun, Y.; Nelson, P. S., Molecular pathways: involving microenvironment damage responses in cancer therapy resistance. *Clin Cancer Res* **2012,** *18* (15), 4019-25.

279. Di Maio, M.; Gridelli, C.; Gallo, C.; Shepherd, F.; Piantedosi, F. V.; Cigolari, S.; Manzione, L.; Illiano, A.; Barbera, S.; Robbiati, S. F.; Frontini, L.; Piazza, E.; Ianniello, G. P.; Veltri, E.; Castiglione, F.; Rosetti, F.; Gebbia, V.; Seymour, L.; Chiodini, P.; Perrone, F., Chemotherapy-induced neutropenia and treatment efficacy in advanced non-small-cell lung cancer: a pooled analysis of three randomised trials. *Lancet Oncol* **2005,** *6* (9), 669-77.

280. Cheng, L.; Swartz, M. D.; Zhao, H.; Kapadia, A. S.; Lai, D.; Rowan, P. J.; Buchholz, T. A.; Giordano, S. H., Hazard of recurrence among women after primary breast cancer treatment--a 10-year follow-up using data from SEER-Medicare. *Cancer Epidemiol Biomarkers Prev* **2012,** *21* (5), 800-9.

281. Dillekas, H.; Transeth, M.; Pilskog, M.; Assmus, J.; Straume, O., Differences in metastatic patterns in relation to time between primary surgery and first relapse from breast cancer suggest synchronized growth of dormant micrometastases. *Breast Cancer Res Treat* **2014,** *146* (3), 627-36.

282. Dillekas, H.; Demicheli, R.; Ardoino, I.; Jensen, S. A. H.; Biganzoli, E.; Straume, O., The recurrence pattern following delayed breast reconstruction after mastectomy for breast cancer suggests a systemic effect of surgery on occult dormant micrometastases. *Breast Cancer Res Treat* **2016,** *158* (1), 169-178.

283. Zhang, B.; Skelly, J. D.; Maalouf, J. R.; Ayers, D. C.; Song, J., Multifunctional scaffolds for facile implantation, spontaneous fixation, and accelerated long bone regeneration in rodents. *Sci Transl Med* **2019,** *11* (502).

284. Koffler, J.; Zhu, W.; Qu, X.; Platoshyn, O.; Dulin, J. N.; Brock, J.; Graham, L.; Lu, P.; Sakamoto, J.; Marsala, M.; Chen, S.; Tuszynski, M. H., Biomimetic 3D-printed scaffolds for spinal cord injury repair. *Nat Med* **2019,** *25* (2), 263-269.

285. MacQueen, L. A.; Sheehy, S. P.; Chantre, C. O.; Zimmerman, J. F.; Pasqualini, F. S.; Liu, X.; Goss, J. A.; Campbell, P. H.; Gonzalez, G. M.; Park, S. J.; Capulli, A. K.; Ferrier, J. P.; Kosar, T. F.; Mahadevan, L.; Pu, W. T.; Parker, K. K., A tissue-engineered scale model of the heart ventricle. *Nat Biomed Eng* **2018,** *2* (12), 930-941.

286. Lee, J.; Shanbhag, S.; Kotov, N. A., Inverted colloidal crystals as three-dimensional microenvironments for cellular co-cultures. *J Mater Chem* **2006,** *16* (35), 3558-3564.

287. Zhang, Y. S.; Zhu, C. L.; Xia, Y. N., Inverse Opal Scaffolds and Their Biomedical Applications. *Adv Mater* **2017,** *29* (33).

288. Irvine, D. J.; Stachowiak, A. N.; Hori, Y., Lymphoid tissue engineering: Invoking lymphoid tissue neogenesis in immunotherapy and models of immunity. *Semin Immunol* **2008,** *20* (2), 137-146.

289. Bajenoff, M.; Egen, J. G.; Koo, L. Y.; Laugier, J. P.; Brau, F.; Glaichenhaus, N.; Germain, R. N., Stromal cell networks regulate lymphocyte entry, migration, and territoriality in lymph nodes. *Immunity* **2006,** *25* (6), 989-1001.

290. Shanbhag, S.; Woo Lee, J.; Kotov, N., Diffusion in three-dimensionally ordered scaffolds with inverted colloidal crystal geometry. *Biomaterials* **2005,** *26* (27), 5581-5.

291. Nichols, J. E.; Cortiella, J. Q.; Lee, J.; Niles, J. A.; Cuddihy, M.; Wang, S. P.; Bielitzki, J.; Cantu, A.; Mlcak, R.; Valdivia, E.; Yancy, R.; McClure, M. L.; Kotov, N. A., In vitro analog of human bone marrow from 3D scaffolds with biomimetic inverted colloidal crystal geometry. *Biomaterials* **2009,** *30* (6), 1071-1079.

292. Cuddihy, M. J.; Wang, Y. C.; Machi, C.; Bahng, J. H.; Kotov, N. A., Replication of Bone Marrow Differentiation Niche: Comparative Evaluation of Different Three-Dimensional Matrices. *Small* **2013,** *9* (7), 1008-1015.

293. Lee, J.; Kotov, N. A., Notch Ligand Presenting Acellular 3D Microenvironments for ex vivo Human Hematopoietic Stem-Cell Culture made by Layer-By-Layer Assembly. *Small* **2009,** *5* (9), 1008-1013.

294. Bersani, F.; Lee, J.; Yu, M.; Morris, R.; Desai, R.; Ramaswamy, S.; Toner, M.; Haber, D. A.; Parekkadan, B., Bioengineered implantable scaffolds as a tool to study stromal-derived factors in metastatic cancer models. *Cancer Res* **2014,** *74* (24), 7229-38.

295. Joao, C. F. C.; Vasconcelos, J. M.; Silva, J. C.; Borges, J. P., An Overview of Inverted Colloidal Crystal Systems for Tissue Engineering. *Tissue Eng Part B-Re* **2014,** *20* (5), 437-454.

296. Nichols, J. E.; Cortiella, J.; Lee, J.; Niles, J. A.; Cuddihy, M.; Wang, S.; Bielitzki, J.; Cantu, A.; Mlcak, R.; Valdivia, E.; Yancy, R.; McClure, M. L.; Kotov, N. A., In vitro analog of human bone marrow from 3D scaffolds with biomimetic inverted colloidal crystal geometry. *Biomaterials* **2009,** *30* (6), 1071-9.

297. Stachowiak, A. N.; Irvine, D. J., Inverse opal hydrogel-collagen composite scaffolds as a supportive microenvironment for immune cell migration. *J Biomed Mater Res A* **2008,** *85a* (3), 815-828.

298. Madden, L. R.; Mortisen, D. J.; Sussman, E. M.; Dupras, S. K.; Fugate, J. A.; Cuy, J. L.; Hauch, K. D.; Laflamme, M. A.; Murry, C. E.; Ratner, B. D., Proangiogenic scaffolds as functional templates for cardiac tissue engineering. *P Natl Acad Sci USA* **2010,** *107* (34), 15211-15216.

299. Wang, Y. C.; Jan, E.; Cuddihy, M.; Bahng, J. H.; Kotov, N., Layered biomimetic nanocomposites replicate bone surface in three-dimensional cell cultures. *Nanocomposites* **2018,** *4* (4), 156-166.

300. Wu, L. Y.; Ferracci, G.; Wang, Y.; Fan, T. F.; Cho, N. J.; Chow, P. K. H., Porcine hepatocytes culture on biofunctionalized 3D inverted colloidal crystal scaffolds as an in vitro model for predicting drug hepatotoxicity. *Rsc Adv* **2019,** *9* (31), 17995-18007.

301. Zhang, Y. J.; Wang, S. P.; Eghtedari, M.; Motamedi, M.; Kotov, N. A., Inverted-colloidal-crystal hydrogel matrices as three-dimensional cell scaffolds. *Adv Funct Mater* **2005,** *15* (5), 725-731.

302. Choi, S. W.; Zhang, Y.; Xia, Y. N., Three-Dimensional Scaffolds for Tissue Engineering: The Importance of Uniformity in Pore Size and Structure. *Langmuir* **2010,** *26* (24), 19001-19006.

303. Choi, S. W.; Cheong, I. W.; Kim, J. H.; Xia, Y. N., Preparation of Uniform Microspheres Using a Simple Fluidic Device and Their Crystallization into Close-Packed Lattices. *Small* **2009,** *5* (4), 454-459.

304. Kim, J.; Bencherif, S. A.; Li, W. A.; Mooney, D. J., Cell-friendly inverse opal-like hydrogels for a spatially separated co-culture system. *Macromol Rapid Commun* **2014,** *35* (18), 1578-86.

305. Wang, C. C.; Yang, K. C.; Lin, K. H.; Liu, Y. L.; Liu, H. C.; Lin, F. H., Cartilage regeneration in SCID mice using a highly organized three-dimensional alginate scaffold. *Biomaterials* **2012,** *33* (1), 120-127.

306. Zhang, Y. S.; Choi, S. W.; Xia, Y. N., Inverse opal scaffolds for applications in regenerative medicine. *Soft Matter* **2013,** *9* (41), 9747-9754.

307. Choi, S. W.; Zhang, Y.; Thomopoulos, S.; Xia, Y. N., In Vitro Mineralization by Preosteoblasts in Poly(DL-lactide-co-glycolide) Inverse Opal Scaffolds Reinforced with Hydroxyapatite Nanoparticles. *Langmuir* **2010,** *26* (14), 12126-12131.

308. Zhu, C.; Pongkitwitoon, S.; Qiu, J.; Thomopoulos, S.; Xia, Y., Design and Fabrication of a Hierarchically Structured Scaffold for Tendon-to-Bone Repair. *Adv Mater* **2018,** *30* (16), e1707306.

309. Zhang, Y. S.; Regan, K. P.; Xia, Y. N., Controlling the Pore Sizes and Related Properties of Inverse Opal Scaffolds for Tissue Engineering Applications. *Macromol Rapid Comm* **2013,** *34* (6), 485-491.

310. Lin, J. Y.; Lin, W. J.; Hong, W. H.; Hung, W. C.; Nowotarski, S. H.; Gouveia, S. M.; Cristo, I.; Lin, K. H., Morphology and organization of tissue cells in 3D microenvironment of monodisperse foam scaffolds. *Soft Matter* **2011,** *7* (21), 10010-10016.

311. Wang, C. C.; Yang, K. C.; Lin, K. H.; Liu, Y. L.; Yang, Y. T.; Kuo, T. F.; Chen, I. H., Expandable Scaffold Improves Integration of Tissue-Engineered Cartilage: An In Vivo Study in a Rabbit Model. *Tissue Eng Pt A* **2016,** *22* (11-12), 873-884.

312. Wang, C. C.; Yang, K. C.; Lin, K. H.; Wu, C. C.; Liu, Y. L.; Lin, F. H.; Chen, I. H., A Biomimetic Honeycomb-Like Scaffold Prepared by Flow-Focusing Technology for Cartilage Regeneration. *Biotechnol Bioeng* **2014,** *111* (11), 2338-2348.

313. Wang, C. C.; Yang, K. C.; Lin, K. H.; Liu, H. C.; Lin, F. H., A highly organized three-dimensional alginate scaffold for cartilage tissue engineering prepared by microfluidic technology. *Biomaterials* **2011,** *32* (29), 7118-26.

314. Cuddihy, M. J.; Kotov, N. A., Poly(lactic-co-glycolic acid) Bone Scaffolds with Inverted Colloidal Crystal Geometry. *Tissue Eng Pt A* **2008,** *14* (10), 1639-1649.

315. Lee, J.; Lilly, G. D.; Doty, R. C.; Podsiadlo, P.; Kotov, N. A., In vitro toxicity testing of nanoparticles in 3D cell culture. *Small* **2009,** *5* (10), 1213-21.

316. Lee, J.; Cuddihy, M. J.; Cater, G. M.; Kotov, N. A., Engineering liver tissue spheroids with inverted colloidal crystal scaffolds. *Biomaterials* **2009,** *30* (27), 4687-94.

317. Products, U. F. Polystyrene or styrofoam beads. https://univfoam.com/polystyrene-or-styrofoam-beads.

318. Bianchi, E.; Conio, G.; Ciferri, A.; Puett, D.; Rajagh, L., The role of pH, temperature, salt type, and salt concentration on the stability of the crystalline, helical, and randomly coiled forms of collagen. *J Biol Chem* **1967,** *242* (7), 1361-9.

319. Caglio, S.; Righetti, P. G., On the pH dependence of polymerization efficiency, as investigated by capillary zone electrophoresis. *Electrophoresis* **1993,** *14* (5-6), 554-8.

320. Dazzi, F.; Ramasamy, R.; Glennie, S.; Jones, S. P.; Roberts, I., The role of mesenchymal stem cells in haemopoiesis. *Blood Rev* **2006,** *20* (3), 161-71.

321. Mendez-Ferrer, S.; Michurina, T. V.; Ferraro, F.; Mazloom, A. R.; Macarthur, B. D.; Lira, S. A.; Scadden, D. T.; Ma'ayan, A.; Enikolopov, G. N.; Frenette, P. S., Mesenchymal and haematopoietic stem cells form a unique bone marrow niche. *Nature* **2010,** *466* (7308), 829-34.

322. Ding, L.; Saunders, T. L.; Enikolopov, G.; Morrison, S. J., Endothelial and perivascular cells maintain haematopoietic stem cells. *Nature* **2012,** *481* (7382), 457-62.

323. Liu, Y. F.; Wang, S. P.; Lee, J. W.; Kotov, N. A., A floating self-assembly route to colloidal crystal templates for 3D cell scaffolds. *Chem Mater* **2005,** *17* (20), 4918-4924.

324. Ye, X.; Huang, J.; Zeng, Y.; Sun, L. X.; Geng, F.; Liu, H. J.; Wang, F. R.; Jiang, X. D.; Wu, W. D.; Zheng, W. G., Monolayer Colloidal Crystals by Modified Air-Water Interface Self-Assembly Approach. *Nanomaterials (Basel)* **2017,** *7* (10).

325. Rajan, N.; Habermehl, J.; Cote, M. F.; Doillon, C. J.; Mantovani, D., Preparation of ready-to-use, storable and reconstituted type I collagen from rat tail tendon for tissue engineering applications. *Nat Protoc* **2006,** *1* (6), 2753-8.

326. Zeng, W.; Du, Y.; Xue, Y.; Frisch, H. L., Solubility Parameters. In *Physical Properties of Polymers Handbook*, Mark, J. E., Ed. Springer New York: New York, NY, 2007; pp 289-303.

327. Wang, Y. C.; Bahng, J. H.; Kotov, N. A., Three-dimensional biomimetic scaffolds for hepatic differentiation of size-controlled embryoid bodies. *J Mater Res* **2019,** *34* (8), 1371-1380.

328. Ng, S. S.; Saeb-Parsy, K.; Blackford, S. J. I.; Segal, J. M.; Serra, M. P.; Horcas-Lopez, M.; No, D. Y.; Mastoridis, S.; Jassem, W.; Frank, C. W.; Cho, N. J.; Nakauchi, H.; Glenn, J. S.; Rashid, S. T., Human iPS derived progenitors bioengineered into liver organoids using an inverted colloidal crystal poly (ethylene glycol) scaffold. *Biomaterials* **2018,** *182*, 299-311.

329. Zhang, Y.; Xia, Y. N., Formation of Embryoid Bodies with Controlled Sizes and Maintained Pluripotency in Three-Dimensional Inverse Opal Scaffolds. *Adv Funct Mater* **2012,** *22* (1), 121-129.

330. Kuo, Y. C.; Tsai, Y. T., Inverted Colloidal Crystal Scaffolds for Uniform Cartilage Regeneration. *Biomacromolecules* **2010,** *11* (3), 731-739.

331. Kuo, Y. C.; Chiu, K. H., Inverted colloidal crystal scaffolds with laminin-derived peptides for neuronal differentiation of bone marrow stromal cells. *Biomaterials* **2011,** *32* (3), 819-831.

332. Lawson, D. A.; Kessenbrock, K.; Davis, R. T.; Pervolarakis, N.; Werb, Z., Tumour heterogeneity and metastasis at single-cell resolution. *Nat Cell Biol* **2018,** *20* (12), 1349-1360.

333. Rodriques, S. G.; Stickels, R. R.; Goeva, A.; Martin, C. A.; Murray, E.; Vanderburg, C. R.; Welch, J.; Chen, L. M.; Chen, F.; Macosko, E. Z., Slide-seq: A scalable technology for measuring genome-wide expression at high spatial resolution. *Science* **2019,** *363* (6434), 1463-1467.

334. Mendes, M.; Pelaez-Garcia, A.; Lopez-Lucendo, M.; Bartolome, R. A.; Calvino, E.; Barderas, R.; Casal, J. I., Mapping the Spatial Proteome of Metastatic Cells in Colorectal Cancer. *Proteomics* **2017,** *17* (19).

335. Looney, M. R.; Thornton, E. E.; Sen, D.; Lamm, W. J.; Glenny, R. W.; Krummel, M. F., Stabilized imaging of immune surveillance in the mouse lung. *Nat Methods* **2011,** *8* (1), 91-6.

336. Entenberg, D.; Rodriguez-Tirado, C.; Kato, Y.; Kitamura, T.; Pollard, J. W.; Condeelis, J., In vivo subcellular resolution optical imaging in the lung reveals early metastatic proliferation and motility. *Intravital* **2015,** *4* (3).